The effects of industrial processing and chemical variation on the near-surface properties of poly(ethylene terephthalate) films and bottles

Matthew Robert Smith

The effects of industrial processing and chemical variation on the near-surface properties of poly(ethylene terephthalate) films and bottles

Matthew Robert Smith

A thesis submitted for the degree of Doctor of Philosophy at the

University of Durham

Department of Chemistry

2004

Table of contents

List of figures

Figures in chapter 1 - *General introduction*

Figures in chapter 2 - *Literature review*

Figures in chapter 3 - *Materials*

Figures in chapter 4 - *FTIR spectroscopy*

Figures in chapter 5 - *Molecular modelling*

Figures in chapter 6 - *X-ray diffraction*

Figures in *Appendix 1*

List of tables

Tables in chapter 2 - *Literature review*

Tables in chapter 3 - *Materials*

Tables in chapter 4 - *FTIR spectroscopy*

Tables in chapter 5 - *Molecular modelling*

Tables in chapter 6 - *X-ray diffraction*

Tables in - *Appendix 2*

Matthew Robert Smith

The effects of industrial processing and chemical variation on the near-surface properties of poly(ethylene terephthalate) films and bottles

The sub-micron surface region of poly(ethylene terephthalate) (PET) films and bottles has been investigated. Uniaxially drawn and annealed PET films were characterised by bulk and grazing incidence X-ray diffraction (GIXD). Surface-specific diffraction patterns collected below the critical angle (α_c) for total external reflection reveal a radial shift in diffraction peaks, whereas bulk signals collected above this critical angle occur at the predicted locations. It is calculated that this shift can be described by a ~5 % reduction of the a, b and c unit cell parameters for PET crystals within the sub-micron surface region. This shift is less apparant in the un-oriented specimens. The crystallite orientation is consistently higher within the surface region of the drawn PET films than the bulk. There is a good agreement between the X-ray diffraction and FTIR orientation measurement over the range of films analysed.

Polarised FTIR-ATR spectroscopy was used to map the molecular orientation along the inner and outer surfaces of stretch-blown PET bottles. This work reveals complex orientation trends. For 2-litre bottles, the inner surface shows consistently higher orientation levels than the outer surface. There are also two orientation switches at the shoulder and base regions on the outer surface, but only one switch on the inner wall. In all cases, the maximum orientation occurs on the inner surface at 4-6 cm from the base. This analysis was repeated for various bottles, including examples produced from various polyester co-polymers and a series of bottles stretch-blown after different preform heating times. Heating for 5 seconds longer than the recommended time prior to the stretch seriously reduces the orientation in the finished bottle. Lowering the polymer molecular weight has a similar effect.

The use of the popular 1340 cm^{-1} PET IR band for crystallinity evaluation was questioned. It is concluded that the use of this band for crystallinity calculation is erroneous if the specimen possesses molecular orientation. It is shown that the 1340 cm^{-1} band height reveals the orientation trends in highly drawn specimens of low crystallinity. Simple measurements reveal that the 1340 cm^{-1} transition moment for this band lies approximately in the chain direction.

Acknowledgements

My Durham supervisor, Dr. Sharon Cooper, has been exceptional throughout the course of this project. Sharon took an active role at all stages, from first arranging this Industrial C.A.S.E. collaboration to securing funding for excellent apparatus, explaining the science and reading through the many draughts of my thesis. Without her continued patience and understanding, this thesis would not have been possible. Thanks Sharon. I would also like to acknowledge my industrial supervisors; Dr. Mark Hodgson, Dr. Bill Macdonald (DuPont Teijin Films) and Dr. Derek Winter (DuPont Polyester Technologies). Not only did they supply all the PET resins films and bottles, but also their encouragement and useful discussions during the C.A.S.E meetings were instrumental to the success of the project. Thanks also to Dr. Neil Everall (ICI plc) for showing an interest in my work and sharing with me some of his Infrared expertise. Thanks to Miss Katja Nevalainen for stretching the PET films and Mr Phil Bullock for blowing the PET bottles and getting them to me so quickly.

I would like to take this opportunity to acknowledge three influential people who played a key role in my decision to study polymers. Thank you Dr. Mahendrasingam and Dr. Chris Martin (Keele University) for first arousing my interest in polymer science and Dr. Guy Eeckhaut (Huntsman Polyurethanes, Belgium) for furthering this interest during the summer projects of 1999 and 2000. Your unwavering enthusiasm for polymer science and technology has been truly inspirational.

My final words of appreciation are aimed towards my family and loved-ones who provided limitless support and encouragement throughout the course of my doctorate, especially towards the difficult latter stages of writing up. I am forever indebted.

Memorandum

The work reported in this thesis was carried out in the department of chemistry at the University of Durham and at DuPont Teijin films at the Wilton centre, Cleveland. This work was completed between the dates of October 2000 and September 2003. The work has not been submitted for any other degree and is the original work of the author except where acknowledged by the appropriate reference.

Statement of copyright

Financial support

I would like to acknowledge the EPSRC for their financial support. Thanks also the DuPont Polyester Technologies and DuPont Teijin Films UK for their financial contributions to the C.A.S.E. award.

1 General introduction

1.1 Background

Poly(ethylene terephthalate) (PET) is a versatile semi-crystalline polymer which is used in many commercial products. The chemical structure of the repeat unit is shown in Figure 1-1.

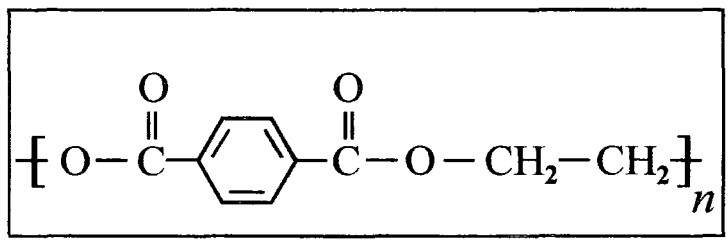

Figure 1-1: The chemical structure of a PET repeat unit

Besides fibres used in textiles and carpets, the most common uses belong to the packaging industry in the form of shatter-proof beverage bottles and strong transparent films, typically 50-400 μm thick.

It has been shown that the top 1 μm surface layer of a polymer film can exhibit different characteristics to the remaining 'bulk' of the film. The surface can possess a higher level of crystallinity[1], a change in molecular orientation[2,3] and even a lower thermodynamic transition temperature[4]. Properties such as the crystallinity and chain orientation of the bulk material dictate the tensile properties of the processed film and have been well documented[5-9]. Far less characterisation work has been done on the narrow sub-micron surface region of the film. This bias towards bulk measurement is largely due to;

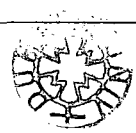

a) Many film characterisation techniques being intrinsically insensitive to surfaces. (eg. standard X-ray diffraction and cross-polarizer optical birefringence measurements)

b) The sub-micron surface layer having negligible effect on the overall mechanical properties of the finished film, making bulk characterisation more desirable.

For an increasing number of applications, which involve the adhesion of laminates or inks to the PET surface, a thorough understanding of the film surface becomes essential. The permanence of a coating will depend more on the surface than the bulk.

The two primary analytical techniques used in this study are Fourier Transform Infrared (FTIR) spectroscopy and a variation of X-ray diffraction (XRD).

FTIR spectroscopy studies the interaction between infra-red radiation and matter. The technique can be made surface selective via the popular Attenuated Total Reflection (FTIR-ATR) modification[10-12]. This technique involves reflecting the IR beam off the interface formed between a highly refractive ATR crystal and the specimen, retrieving spectroscopic information from the top 0.5 μm layer of a PET film[2], as described fully in chapter 4. Jarvis[13] and Everall[14] have made recent advances in this field. By incorporating an infrared polarizer with the FTIR-ATR setup, they have shown that it is possible to deduce accurate molecular orientation information from the sub-micron surface region of PET films. To date, this method has been applied to; a) uniaxially drawn PET films, which showed a convincing correlation between the IR results and those expected by theory[14,15], and b) PET bottles that were probed at the 'shoulder' and

'side' regions[15]. Interestingly for these bottles, the majority of the chains pointed in opposite directions at these two bottle positions. In addition, both bottle positions showed an orientation discrepancy between the inner and outer surfaces.

Wide angle X-ray scattering (WAXS) is commonly used to characterise the crystalline properties of semi-crystalline polymers such as PET. It is a powerful technique as it gives a direct indication of the crystallinity rather than infrared spectroscopy, where the crystallinity is typically inferred by properties such as the distribution of chain conformers[16-18]. The relatively weak interaction between X-rays and polymers (compared to electrons for example) dictate that X-ray diffraction techniques typically retrieve information averaged throughout the whole thickness of the sample. Recent developments have seen the appearance of a new surface selective XRD variation, called Grazing-incidence X-ray Diffraction (GIXD)[19-21]. Theoretically, by directing the beam at very shallow angles of incidence (less than 0.2° for PET[4]) we satisfy the conditions required for total external reflection (TER) and thus can extract diffraction information from the first ~10 nm into the samples surface.

Although the initial GIXD studies on polymers looks promising, the samples used in these studies have been idealised thin, flat films, carefully spin-coated onto highly polished silicon wafers[1,4]. These pioneering discoveries are of great scientific importance, but spin-coated films are very different from PET films produced in industry, which are typically much thicker, highly stretched and exposed to temperatures of around 200°C to increase crystallinity[22].

1.2 Aims of the project

The aim of the project is to determine the surface properties of the PET bottles and films supplied by DuPont Polyester Technologies and DuPont Teijin Films – the C.A.S.E. sponsors of this research. The focus will be on the molecular orientation and crystallinity at the surface region and how this is affected by changes in processing conditions, chemical additives and co-polymer content. This objective encompasses the following studies.

1.2.1 Mapping the near-surface molecular orientation of PET bottles

PET bottles are formed via the stretch-blow process which involves stretching a small straight-walled 'preform' tube into the recognizable 2-litre bottle, resulting in unpredictable orientation trends. Where possible, the orientation trends will be mapped at regularly spaced intervals for the inner and outer bottle wall. This will detail if there is a difference between the two surfaces and how the orientation changes from the shoulder, side and base regions. Once this method has been developed, it can also be applied to bottles made from different polyester resins and stretch-blown under different conditions as described in sections 1.2.1.1 and 1.2.1.2.

1.2.1.1 The effect of processing condition on near surface orientation

Bottle production involves heating the preform for around 60 seconds and then blowing this to full size when the resin is suitably pliable. The heating time is precisely defined for a given bottle type. Any deviation from this can quickly result in a deterioration of the optical clarity of the finished bottle. However, it would be useful to characterise how different preform heating times can affect the surface properties and overall bottle orientation. A sudden loss of orientation for example, might indicate that tensile

strength may be jeopardised. However, if there is no observable orientation loss in the bottles drawn after a shorter heating time, it may give scope for reducing costs and bottle production times.

1.2.1.2 The effect of chemical modifications on near surface molecular orientation

The resin used to make shatter-proof beverage bottles is typically made from a PET resin which contains isophthalic acid (IPA) as an additive. Compared to pure PET, the modified resin exhibits a slower crystallisation rate[23-25], which preserves optical clarity after unavoidable exposure to high processing temperatures. Little work has been done to see if the inclusion of IPA has a marked effect on the surface properties. In addition, there are other modifications which are sometimes used in PET manufacture to enhance the properties or processability of the resin, some of which are new and still in the development stage[26] (see chapter 3). One aim of this research is to establish how the different additives and co-polymer content affects the surface structure after mechanical deformation. This information is of industrial importance as the tensile properties of the finished artefact are directly related to the amount and direction of molecular orientation. It is important that bottles blown from the new resins exhibit a similar orientation trend to the standard well-tested bottles to assess the industrial suitability of the resins. Reduced levels of orientation in the new resins could well indicate that mechanical strength is lost, resulting in bottles that are likely to fail.

1.2.2 Grazing incidence X-ray diffraction (GIXD)

The usefulness of GIXD will be explored as a tool for the surface characterisation of industrially-drawn PET films, rather than the idealised spin-coated specimens found in the literature. The key advantage of these samples is that films with high levels of

orientation can be produced whereas only the film thickness and crystallinity can be varied with spin-coated alternatives.

1.2.3 The heat-setting of PET artefacts

The manufacture of PET films typically includes a heating phase after the biaxial stretch, which increases levels of crystallinity within the film[22]. For films, this 'heat-setting' phase is known to improve the dimensional stability of the finished film. Several authors have characterised how the bulk crystallinity levels in PET films are affected by drawing at elevated temperatures, but it is not known if there are any discrepancies between the nature of the bulk and surface crystallites.

The heat setting process is starting to make an appearance in the production of PET bottles. Some substances, such as orange juice, need to be heated just before bottling in order to prevent bacterial fouling. It is thus advantageous to develop bottles that can withstand these higher filling temperatures. One approach for this is to heat the bottle mould (which is usually at ambient temperature) and keep the bottle at this elevated temperature to increase the levels of crystallinity in the bottle walls. The bottles with higher crystallinity can withstand hotter fill temperatures which can speed up filling times. It is not known whether this additional processing has a marked effect on the orientation properties and so this will be investigated where possible.

1.2.4 Investigating the properties of the 1340 cm^{-1} infra-red band

The 1340 cm^{-1} band is attributed to the CH_2 wagging mode of the *trans* chain conformation. This band is often used to calculate sample crystallinity on the premise that only *trans* chains can pack into crystals and amorphous regions contain chains

exhibiting mainly *gauche* conformations. This research aims to address whether this band gives an accurate portrayal of the crystallinity. The direction of the transition dipole moment of this mode is thought to lie approximately along the chain direction. This work also considers if it can be used as an orientation indicator.

1.3 The structure of this thesis

Chapter 2 contains the literature review summarising the current state of knowledge in the most relevant research fields. The literature review briefly addresses the more fundamental aspects and current knowledge of the science and techniques used in this study. The literature review also directs the reader to more in-depth descriptions in the relevant chapters. Chapter 3 includes more information about the nature of poly(ethylene terephthalate). It details common synthesis routes, commercial uses and some of the many chemical modifications used in the polyester industry. The manufacture of PET films and bottles is also summarised. The research performed using infrared and X-ray methods are encapsulated within the separate chapters, 4 and 6, which contain the relevant background, theory, experiments, results and conclusions. Some molecular modelling is provided in chapter 5. This work complements the X-ray work by modelling PET crystals and calculating expected diffraction patterns. This chapter contains listings of the most intense diffraction peaks expected from an idealised model PET crystal and visualisations of the Miller planes that give rise to the most intense peaks.

The most prominent discoveries resulting from this work are summarised in the conclusions chapter, which also includes recommendations for future work in this field.

1.4 References for chapter 1

(1) Factor, B. J.; Russell, T. P.; Toney, M. F. *Macromolecules* **1993**, *26*, 2847-2859.

(2) Walls, D. J. *Applied Spectroscopy* **1991**, *45*, 1193-1198.

(3) Hobbs, J. P.; Sung, C. S. P. *Macromolecules* **1983**, *16*, 193-199.

(4) Durell, M.; MacDonald, J. E.; Trolley, D.; Wehrum, A.; Jukes, P. C.; Jones, R. A. L.; Walker, C. J.; Brown, S. *Europhysics Letters* **2002**, *58*, 844-850.

(5) Mahendrasingam, A.; Blundell, D. J.; Wright, A. K.; Urban, V.; Narayanan, T.; Fuller, W. *Polymer* **2003**, *44*, 5915-5925.

(6) Göschel, U. *Polymer* **1996**, *37*, 4049-4059.

(7) Lapersonne, P.; Bower, D. I.; Ward, I. M. *Polymer* **1992**, *33*, 1277-1283.

(8) Cunningham, A.; Ward, I. M. *Polymer* **1974**, *15*, 749-756.

(9) Ashford, E.; Bachmann, M. A.; Jones, D. P.; MacKerron, D. H. *Trans IChemE* **2000**, *78*, 33-38.

(10) Fahrenfort, J.; Visser, W. M. *Spectrochimica Acta* **1962**, *18*, 1103-1116.

(11) Hind, A. R.; Bhargava, S. K.; McKinnon, A. *Advances in Colloid and Interface Science* **2001**, *93*, 91-114.

(12) Flournoy, P. A.; Schaffers, W. J. *Spectrochimica Acta* **1966**, *22*, 5-13.

(13) Jarvis, D. A.; Hutchinson, I. J.; Bower, D. I.; Ward, I. M. *Polymer* **1979**, *21*, 41-54.

(14) Everall, N. J.; Bibby, A. *Applied Spectroscopy* **1997**, *51*, 1083-1091.

(15) Everall, N.; MacKerron, D.; Winter, D. *Polymer* **2002**, *43*, 4217-4223.

(16) Belali, R.; Vigoureux, J. M. *Applied Spectroscopy* **1994**, *48*, 465-471.

(17) Sammon, C.; Yarwood, J.; Everall, N. *Polymer* **2000**, *41*, 2521-2534.

(18) Kazarian, S. G.; Brantley, N. H.; Eckert, C. A. *Vibrational Spectroscopy* **1999**, *19*, 277-283.

(19) Murthy, N. S.; Bednarczyk, C.; Minor, H. *Polymer* **2000**, *41*, 277-284.

(20) Jensen, T. R.; Balashev, K.; Bjørnholm, T.; Kjaer, K. *Biochimie* **2001**, *83*, 399-408.

(21) Chang, S.-L. *Journal of Physics and Chemistry of Solids* **2001**, *62*, 1765-1775.

(22) Hodgson, M. R. In *Chemistry - Ph.D. Thesis*; University of Durham, 2000.

(23) Lee, B.; Shin, T. J.; Lee, S. W.; Yoon, J.; Kim, J.; Youn, H. S.; Ree, M. *Polymer* **2003**, *44*, 2509-2518.

(24) Li, B.; Yu, J.; Lee, S.; Ree, M. *European Polymer Journal* **1999**, *35*, 1607-1610.

(25) Li, B.; Yu, J.; Lee, S.; Ree, M. *Polymer* **1999**, *40*, 5371-5375.

(26) Kint, D. P. R.; Rudé, E.; Llorens, J.; Muñoz-Guerra, S. *Polymer* **2002**, *43*, 7529-7537.

2 Literature review

2.1 The nature of PET

PET has proven to be a popular polymer to study, largely due to its abundant usage in industry. The literature is plentiful and covers many diverse issues including an analysis of thermal degradation[1,2], the gas barrier properties of drawn PET sheets[3] and an analysis of contaminants in terephthalic acid, which has colour implications in PET resins[4]. Some of the most important studies have been those that characterise the nature of crystallinity[5,6] and molecular orientation[7-9] in processed PET artefacts. Both these properties are known to have a marked effect on the tensile and optical properties exhibited by the finished products[10].

2.1.1 Techniques used to characterise PET

Bulk crystallinity in PET is commonly assessed using density measurements, wide-angle X-ray diffraction (WAXD) or by using thermal techniques such as differential scanning caliometery (DSC)[11,12]. Gould *et al.*[13] have used atomic force microscopy (AFM) to capture 5 nm X 5 nm atomic-scale images of a PET film surface. These images appear to show a distinction between amorphous and crystalline domains. However, one problem with AFM operating in contact mode is that it is an invasive technique and the AFM tip is capable of changing the PET surface topology.

Two of the most frequently used techniques employed are Fourier transform Infrared (FTIR) spectroscopy and wide-angle X-ray diffraction, the most prominent discoveries of which will be described in sections 2.2 and 2.3.

2.1.2 The 'spin-coating' method of sample preparation

It is possible to obtain thin polymer films using a 'spin-coating' method. This involves preparing a dilute solution of PET resin in a suitable solvent and pipetting this solution onto a spinning mica[14] or silicon[15,16] substrate. The solution rapidly coats the available surface and the solvent is left to evaporate, producing a flat thin polymer film. These substrate materials are chosen as they can posses an extremely flat surface. Mica can be cleaved[14] to reveal an atomically smooth surface and silicon can be grown as large single crystals that are commercially available in the form of highly polished discs or wafers. By experimenting with the solution concentration, solvent type, and spin speed, it is possible to achieve films of various thicknesses and uniformities. Hayes[15] favoured using a 1 % solution (w/w) of PET in hexafluoroisopropanol (HFIP). Amorphous films were then produced by spin-casting 15 ml of solution onto a polished silicon disc spinning at 1500 rpm. This method reportedly gave films ~150 nm thick. Alternatively, Durell *et al.*[16] produced films of the same thickness by spin-coating a solution of PET in trifluroacetic acid onto silicon.

After spin-coating, the polymer films are generally characterised *in situ* on the substrate. The flatness of the coated silicon surface means that these samples have been the chosen specimen for the early grazing incidence XRD work on polymers[16,17]. Although these spin-coated samples are often convenient for scientific investigation, they bear little resemblance to industrially produced PET films, which are typically bi-axially stretched in a film stenter process[18] (See Materials chapter).

2.2 IR studies of PET

Fourier Transform Infrared (FTIR) spectroscopy has proven to be a useful tool for the characterisation of polymers. Various infrared (IR) sampling methods have been

employed to probe the properties of polymers, including PET. The simplest is the transmission mode[19-26], which involves passing the IR beam through the sample. As with any transmission-based arrangement, it probes the specimen at every depth through the thickness of the film and therefore is used to determine the bulk properties. One of the biggest problems associated with transmission experiments on polyaromatic materials such as PET is that they are limited to film thicknesses of less than 10 μm to avoid saturation of highly absorbing bands in the IR spectra[27,28]. Films of these dimensions have little tensile strength and are limited to only a few industrial applications.

Thin PET films of around 150 nm that have been prepared by spin-coating onto a reflective substrate can be explored using reflection absorption infra-red spectroscopy (RAIRS)[29,30]. This technique requires the film to be deposited on a flat surface, which has been specially coated with a ~200 nm layer of gold. The IR beam travels through the sample and reflects off the substrate. Sammon[29] used glass substrates, which were first coated with chromium and then gold. It was found that the chromium acted as a 'primer' for the gold layer as it could bind strongly with both the glass and the gold. However, RAIRS gives a bulk measurement[15] and will not be employed in this study.

Many authors have favoured Attenuated Total Reflection (ATR) as a robust means of retrieving surface-specific information from polymers[31-43]. This sampling technique is based on the principle of *total internal reflection* between an ATR crystal and the sample[30,42], which is described fully in the FTIR Spectroscopy chapter, chapter 4. The most relevant PET IR absorption bands for this study are shown in Table 2-1, these have been extracted from the summary presented by Sammon[28].

Table 2-1: The most relevant PET IR bands for this study, taken from reference 28

Band position / cm^{-1}	Morphology	Assignment
1734	A	ν (C=O)
1722	C	ν (C=O)
1720	A	ν (C=O)
1714	C	ν (C=O)
1410	A/C	in plane δ (C-H)
1385	C	in plane δ (C-H)
1370	A	w (CH_2)
1339	C	w (CH_2)
1019	A	in plane δ (C-H)
875	A/C	out-of-plane δ (C-H)

2.2.1 IR normalisation bands in PET

When collecting an IR spectrum on any given sample using any given sampling geometry, the overall absorbance can fluctuate from spectrum to spectrum. This may be due to factors including slight sample thickness variations across the sample region in transmission mode or the quality of sample – crystal contact in the ATR technique. It is therefore not adequate to compare an IR band from different spectra without first normalising each spectrum by an internal reference band. It is important that the chosen band has been proven not to depend on the amount and direction of molecular orientation (i.e. it must be non-dichroic) or the degree of crystallinity in the specimen. Since Walls[35] identified the 1410 cm^{-1} band as being non-dichroic, it has become generally accepted as a robust normalisation band for IR studies on PET. In these experiments, Walls took peak height ratios from spectra taken with the IR radiation selectively polarised in the draw and transverse-draw sample directions, from PET films drawn by different amounts up to draw ratio 4 (Throughout this work, the draw ratio is defined as the final length divided by the original length). This work also discredited the use of alternative reference bands at 790 cm^{-1} and 1510 cm^{-1}, as they were found to depend on the degree of orientation within the sample.

2.2.2 Determining molecular orientation using IR spectroscopy

Polarised FTIR spectroscopy has long been used to study molecular orientation. A simplified example of how this is possible is shown in Figure 2-1. In this example, two states of the same samples are considered. Each is probed sequentially with IR radiation plane-polarised parallel and then perpendicular to the draw direction. Although the incident IR beam would contain a range of frequencies, the frequency considered here corresponds to that of a species whose transition dipole moment lies along the chain direction. For the un-oriented polymer, there are equal numbers of these dipole moments in both the draw and transverse draw direction. The transmitted intensity from both polarisations in this case will therefore be diminished similarly in both cases. On the orientated sample however, far more dipole moments will coincide with the excitation illustrated in part iii of Figure 2-1 than part iv. The higher absorbance in part iii will thus indicate a greater level of orientation in the draw direction.

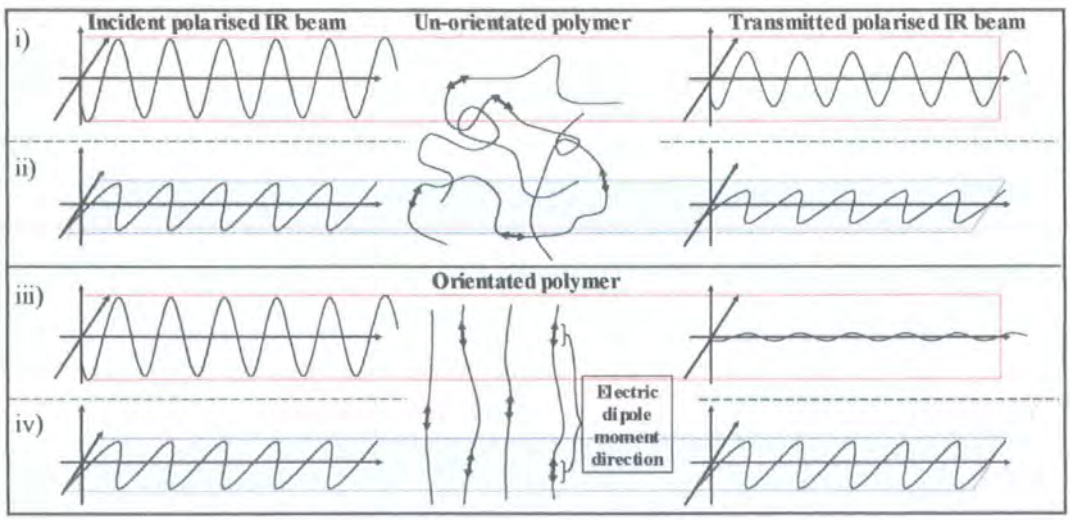

Figure 2-1: How a polarised IR beam can identify orientation in a sample

A dichroic ratio is usually obtained from spectra recorded sequentially with the infrared radiation polarised parallel and perpendicular to a reference direction in the sample

(usually the draw direction in stretched films). Matthews *et al.*[44] defined the dichroic ratio as the ratio of peak areas obtained with the polarisation parallel and perpendicular to the draw direction.

Ideally, one would consider the orientation of a dipole transition moment that lies along the chain axis (as shown in Figure 2-1) or exactly perpendicular to it. This would simplify the analysis as a determination of the dipole direction gives a determination of the chain orientation. In practice, transition moments point at an angle β from the chain axis, where β is rarely 0° or 90°.

It has long been noted that determining molecular orientation using the attenuated total reflection technique would be advantageous, as it would retrieve a surface specific measurement of awkward or highly absorbing specimens. Retrieving IR measurements from the draw and transverse-draw directions necessitates the sample to be unclamped from the ATR crystal, rotated by 90° and re-clamped to the crystal. Unfortunately, this re-clamping procedure will never be able to re-create exactly the original contact between the sample and crystal and thus, the band absorbencies may vary dramatically from spectrum to spectrum. Everall and Bibby[37] have made recent advances in this field. Their work uses two bands associated with ring vibrations and the 1410 cm^{-1} normalisation band, which eliminates the need for identical contact areas. This technique will be detailed in the experimental section of the FTIR spectroscopy chapter. The work of Everall and Bibby built on the earlier work of Sung and co-workers[36,39], who attempted to solve problems associated with sample-crystal contact problems by using a modified revolving sample/crystal holder.

2.2.3 Calculating percentage crystallinity using IR spectroscopy

Using FTIR spectroscopy, sample crystallinity information has to be inferred by observing the bands sensitive to the conformational changes of the ethylene glycol linkages. Assumptions are then made about the proportions of *trans* and *gauche* conformers found in the crystalline and amorphous regions.

2.2.3.1 Conformations of the ethylene glycol linkages in PET chains

It has been noted by many authors that the ethylene glycol linkages can exist in one of two different rotational conformational states, *trans* or *gauche*[6,10,45-48]. The *trans* conformation gives rise to a straight PET chain whereas the *gauche* conformer introduces a bend in the chain. The conformation can switch between *trans* and *gauche* by a partial rotation about the C-C bond as shown in Figure 2-2.

All workers have recognised that for PET chain sections to pack into crystalline regions, they must be straight and thus exhibit an all-*trans* conformation. The chains in the amorphous state bend and curve randomly and are thought to contain a combination of *gauche* and *trans* conformers. Although many authors have studied conformational changes in PET, the proportion of these conformers in the amorphous domain is not fully understood. Schmidt-Rohr *et al.*[46] have performed a detailed study of chain conformations in PET using nuclear magnetic resonance (NMR) in which the average *gauche* torsional angle was found to be ± 70° (with an error of ± 9°) and the amorphous phase contains 14% (± 5%) *trans* conformers. However, from the specular reflectance FTIR data presented by Ajji *et al.*[49], it appears that the unorientated PET film of 5 % crystallinity, consists of 10 % *trans* and 90 % *gauche* conformers, corresponding to ~5% *trans* conformers in the amorphous regions. This uncertainty of conformation

populations in the amorphous regions will obviously have an impact on any FTIR crystallinity calculations based on this quantity.

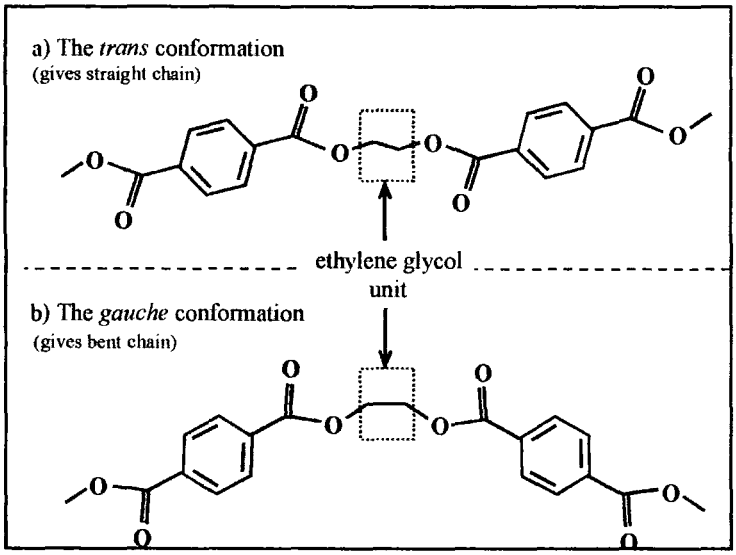

Figure 2-2: The *trans* and *gauche* conformations of the ethylene glycol linkages in PET

In order to assess the proportions of these conformers in a given sample, the absorbencies of bands associated with each conformer need to be measured. Bands related to each of the conformations often exist in pairs[48], namely 1453 and 1456 cm^{-1}, 1370 and 1340 cm^{-1}, 1042 and 973 cm^{-1}. It has been said that the bands at 1340 and 1370 cm^{-1} are most commonly used for crystallinity determination[32]. All parties agree that the band at around 1340 cm^{-1} corresponds to the *trans* conformation and the component at 1370 cm^{-1} is assigned to the gauche conformation of the ethylene glycol moiety. Sammon[29] further states that this band pair is assigned to CH_2 wagging modes. A calculation for the crystallinity determination, χ_c, in semi-crystalline polymers has been derived by Belali and Vigourex[34] and is presented in Equation 2-1.

$$\chi_c = \frac{a_i - a_j(A_i / A_j)}{(c_j - a_j)A_i / A_j - (c_i - a_i)}$$ **Equation 2-1**

where the *a* and *c* parameters are the molar absorption coefficients of the amorphous and crystalline phases at band frequencies ν_i and ν_j and A is the absorption at ν_i or ν_j as indicated in the subscript.

Spectroscopic data collected using an ATR accessory requires special consideration, as the depth of penetration into the sample is inversely proportional to the IR frequency (see the penetration depth discussion in chapter 4). For this reason, an ATR correction can be applied[34] to get Equation 2-2.

$$\chi_c = \frac{a_i - a_j(A_i/A_j)(\upsilon_i/\upsilon_j)}{(c_j - a_j)(A_i/A_j)(\upsilon_i/\upsilon_j) - (c_i - a_i)} \qquad \textbf{Equation 2-2}$$

The molar absorption coefficients used in these equations are obtained from samples with known crystallinity values. Popular values are those of Zajeck[50], which are also published by Belali and Vigoureux[34].

Table 2-2: The *a* and *c* parameters needed for Equations 2-1 and 2-2

IR band (cm^-1)	*a*	*c*
1340	0.080	0.900
1370	0.160	0.050

2.2.4 The use of the 1340 cm^{-1} band

There is ambiguity and conflicting opinion in the literature about the use of the 1340 cm^{-1} band in the analysis of IR spectra collected from PET. This band has been investigated in this study in order to determine the extent to which it can be used for quantitative FTIR analysis in PET. This section summarises how it has been used to-date.

The 1340 cm^{-1} band is attributed to a CH_2 wag mode of a *trans* conformer[28,38,44]. The approximate form of the CH_2 wagging mode is shown in Figure 2-3.

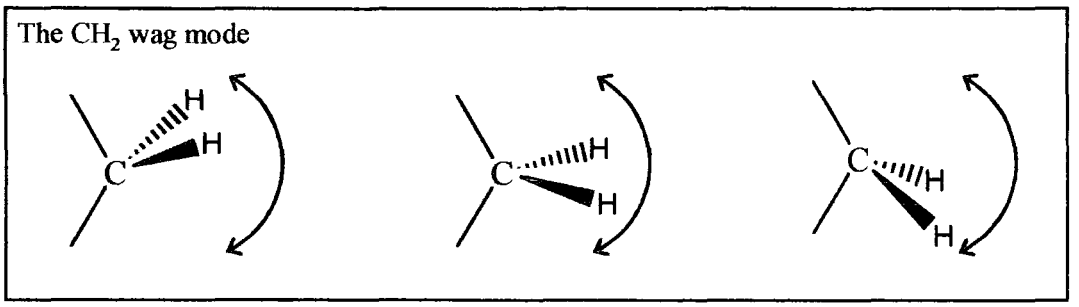

Figure 2-3: The approximate form of a CH_2 wagging that gives rise to the 1340 cm^{-1} IR signal

The majority of authors using the 1340 cm^{-1} band believe that the number of *trans* conformers is a measure of crystallinity. It is particularly convenient in ATR experiments to use the 1340 cm^{-1} band after normalisation by the popular 1410 cm^{-1} reference signal, as both bands occur at a similar wavelength will probe very similar depths.

When considering the integrity of crystallinity analysis involving the 1340 cm^{-1} band, Kazarian[32] concedes that:

"...we cannot exclude the possible contribution to this band of the trans conformer associated with the appearance of ordered amorphous PET as a precursor to the true crystalline structures with three dimensional order."

The orientation properties of the 1340 cm^{-1} are almost exclusively overlooked. However, Walls and Coburn[38] mention that the transition moment of the 1340 cm^{-1} wagging vibration is predominantly parallel to the polymer chain axis. This orientation analysis was brief, but they mentioned that a simple test, involving polarised IR radiation and incremental rotations of an oriented PET sample on an ATR accessory, reveals an absorption maxima coinciding with the draw direction. The use the ATR technique with IR polarisers will be described in the IR chapter. This simple transition moment-characterisation test will be repeated in the IR experimental section of this

thesis, for films drawn to different draw ratios. A comprehensive analysis of the 1340 cm^{-1} band as an orientation indicator could not be found in the literature.

2.2.5 ATR depth profiling

The Walls and Coburn[38] study compared the results gathered from two FTIR attenuated total reflection configurations, which revealed useful structural information about drawn PET films. Walls and Coburn exploited the fact that the sampling depth obtained when using the ATR technique is a function of the angle of incidence and the crystal type used. Walls selected a Germanium ATR crystal at 45° and a KRS-5 crystal at 51°, which he estimated to probe 0.5 μm and 1 μm, respectively, into the PET surface. The most significant discovery was that the measurements taken at these two depths revealed that the films showed higher levels of molecular orientation closer to the film surface.

2.3 X-ray diffraction studies of PET

A large amount of X-ray work on PET involves passing the beam through the sample in transmission mode[51-54]. This type of measurement is generally thought of as a bulk characterisation technique, as any signal from the sub-micron surface region is swamped by the signal from the remaining material. Some of the most striking discoveries in the field of transmission XRD on PET films have been made by the team led by Mahendrasingam *et al.*[55-57]. This team used a custom-built drawing camera[58,59] to observe in real time, strain-induced crystallisation kinetics during fast deformation rates. One of the most interesting discoveries was that that the crystallisation process was found not to start until after the completion of the draw[55].

2.3.1 The unit cell for PET crystals

The unit cell parameters for PET crystals were determined in 1954 by Daubeny[53]. Although various authors have repeated this experiment, Daubeny's parameters are considered generally accepted and are referenced in the majority of the PET X-ray literature. The positions and relative intensities of X-ray diffraction signals from a highly oriented, crystalline sample lead to a determination of the unit cell parameters and atomic coordinates. The unit cell for a PET crystal is triclinic (i.e. $a \neq b \neq c$, $\alpha \neq \beta \neq \gamma$) and has the parameters shown in Table 2-3.

Table 2-3: The generally accepted unit cell parameters of Daubeny *et al.*[53]

Unit cell parameter	Value
a	4.56 Å
b	5.94 Å
c	10.75 Å
α	98.5°
β	118°
γ	112°

The atomic co-ordinates were also determined by Daubeny *et al.* and are presented in Table 2-4. This information is useful as modern software packages such as Cirius2 can simulate a model, build crystals, and calculate the expected X-ray diffraction pattern (see the *Molecular modelling* chapter).

Table 2-4: The atomic co-ordinates within a PET crystal unit cell, as determined by Daubeny *et al.*.

	Atom	x/a	y/b	z/c	x/Å	y/Å	z/Å
1	C	0.000	- 0.078	+ 0.371	0.00	-0.47	+ 3.99
2	C	0.000	- 0.181	+ 0.237	0.00	- 1.08	+ 2.55
3	C (of CH)	+ 0.100	+ 0.170	+ 0.438	+ 0.46	+1.01	+ 4.71
4	C (of CH)	- 0.117	- 0.257	+ 0.433	- 0.53	- 1.53	+ 4.66
5	C (of CH2)	+ 0.045	- 0.085	+ 0.040	+ 0.21	- 0.51	+ 0.43
6	O (of C=O)	- 0.098	- 0.415	+ 0.170	- 0.45	- 2.47	+ 1.83
7	O	+ 0.052	0.000	+ 0.175	+ 0.24	0.00	+ 1.88

The atomic co-ordinate data shown in Table 2-4 display atomic fractional co-ordinates on the left-hand side and the corresponding Cartesian co-ordinates on the right.

2.3.2 Determining crystallite orientation from 2D XRD images

There are two alternative methods in the literature for determining orientation of PET crystallites using WAXS. These are direct measurements of the $(10\bar{5})$ signal[60] and the more complicated method of extrapolating orientation parameters from the (100), (010) and $(1\bar{1}0)$ equatorial signals[52,61]. Both these methods are described later in chapters 5 and 6 of this thesis.

2.3.3 Grazing incidence X-ray diffraction (GIXD)

The phenomenon of total external reflection (TER) can be observed when the angle of incidence is reduced to small angles. For a polished silicon surface, the critical angle (α_c) for TER is 0.4° for copper K_α X-rays of λ = 1.5418 Å , and α_c = 0.2°.for a flat PET surface when using an X-ray wavelength λ = 1.6 Å at the ESRF Synchrotron[16]. Diffraction patterns taken at these small incident angles retrieve surface specific structural information. For PET, the initial GIXD work has been undertaken at the ESRF by Durell *et al.*[16]. In this work, three incident angles (α) were selected which were used to probe spin-coated PET samples of thickness 0.15 μm, annealed over a range of temperatures. The chosen angles and their reported sampling depths were:

$\alpha = 0.6°$	Considered a 'bulk' measurement
$\alpha = 0.2°$	Critical angle: scattering depth $\tau \approx 340$ Å into surface
$\alpha = 0.18°$	Below critical angle: $\tau \approx 80$ Å

The first observation made during this study was that all the peak positions collected above and below the critical angle, were consistent with the expected bulk crystalline structure of Daubeny *et al.*[53]. Interestingly for samples annealed at 95°C, crystallinity was observed at the surface region, but not the bulk. This was attributed to the surface region having a lower glass-transition temperature due to the surface chains being constrained not to cross the interface between the polymer and air. The second primary discovery of this work was that for all annealing temperatures, there was a strong preference for the benzene rings to orientate parallel to the plane of the surface. This was true for both the bulk and surface measurements. No equivalent data was available for stretched PET films. Early GIXD measurements on polymers were performed by Factor *et al.*[17]. In these studies the surface properties of spin-coated aromatic polyimide, poly(pryomellitic dianhydrideoxydianaline) (PMDA-ODA) films were characterised. The study revealed that enhanced order exists near the air surface.

Having detailed the current state of knowledge for the IR and X-ray diffraction studies of PET, chapter 3 will now describe relevant information concerning the PET samples analysed in this study.

2.4 References for chapter 2

(1) Chiu, S. J.; Cheng, W. H. *Polymer Degradation and Stability* **1999**, *63*, 407-412.

(2) Villain, F.; Coudane, J.; Vert, M. *Polymer Degradation and Stability* **1995**, *49*, 393-397.

(3) Lewis, E. L. V.; Duckett, R. A.; Ward, I. M.; Fairclough, J. P. A.; Ryan, A. J. *Polymer* **2003**, *44*, 1631-1640.

(4) Allen, N. S.; Edge, M.; Daniels, J.; Royala, D. *Polymer Degradation and Stability* **1998**, *62*, 373-383.

(5) Wang, Z.-G.; Hsiao, B. S.; Sauer, B. B.; Kampert, W. G. *Polymer* **1999**, *40*, 4615-4627.

(6) McGonigle, E.-A.; Daly, J. H.; Gallagher, S.; Jemkins, S. D.; Liggat, J. J.; Olsson, I.; Pethrick, R. A. *Polymer* **1999**, *40*, 4977-4982.

(7) Jarvis, D. A.; Hutchinson, I. J.; Bower, D. I.; Ward, I. M. *Polymer* **1979**, *21*, 41-54.

(8) Pézolet, M.; Pellerin, C.; Prud'homme, R. E.; Buffeteau, T. *Vibrational Spectroscopy* **1998**, *18*, 103-110.

(9) Lapersonne, P.; Bower, D. I.; Ward, I. M. *Polymer* **1992**, *33*, 1277-1283.

(10) Pereira, J. C.; Porter, R. S. *Journal of Polymer Science: Polymer Physics Edition* **1983**, *21*, 1133-1145.

(11) Kong, Y.; Hay, J. N. *Polymer* **2003**, *44*, 623-633.

(12) Fakirov, S.; Fischer, E. W.; Hoffmann, R.; Schmidt, G. F. *Polymer* **1977**, *18*, 1121-1129.

(13) Gould, S. A. C.; Schiraldi, D. A.; Occelli, M. L. **1996**, 1237-1243.

(14) Freure, C.; Chen, G.; Horton, J. H. *Surface Science* **1999**, *437*, 231-238.

(15) Hayes, N. W.; Beamson, G.; Clark, D. T.; Law, D. S.-L.; Raval, R. *Surface and Interface analysis* **1996**, *24*, 723-728.

(16) Durell, M.; MacDonald, J. E.; Trolley, D.; Wehrum, A.; Jukes, P. C.; Jones, R. A. L.; Walker, C. J.; Brown, S. *Europhysics Letters* **2002**, *58*, 844-850.

(17) Factor, B. J.; Russell, T. P.; Toney, M. F. *Macromolecules* **1993**, *26*, 2847-2859.

(18) Hodgson, M. R. In *Chemistry - Ph.D. Thesis*; University of Durham, 2000.

(19) Middleton, A. C.; Duckett, R. A.; Ward, I. M.; Mahendrasingam, A.; Martin, C. *Journal of Applied Polymer Science* **2001**, *79*, 1825-1837.

(20) Pawlak, A.; Pluta, M.; Morawiec, J.; Galeski, A.; Pracella, M. *European Polymer Journal* **2000**, *36*, 1875-1884.

(21) Toda, T.; Yoshida, H.; Fukunishi, K. *Polymer* **1997**, *38*, 5463-5469.

(22) Radhakrishnan, J.; Kaito, A. *Polymer* **2001**, *42*, 3859-3866.

(23) Lin, S.-B.; Koenig, J. L. *Journal of Polymer Science: Polymer Physics Edition* **1982**, *20*, 2277-2295.

(24) Wang, Y.; Shen, D.; Qian, R. *Journal of Polymer Science: Part B: Polymer Physics* **1998**, *36*, 783-788.

(25) Lin, S.-B.; Koenig, J. L. *Journal of Polymer Science: Polymer Physics Edition* **1983**, *21*, 2365-2378.

(26) D'Esposito, L.; Koenig, J. L. *Journal of Polymer Science: Polymer Physics Edition* **1976**, *14*, 1731-1741.

(27) Everall, N. J.; Chalmers, J. M.; Local, A.; Allen, S. *Vibrational Spectroscopy* **1996**, *10*, 253-259.

(28) Sammon, C. In *Ph.D. Thesis*; Sheffield Hallam University, 1997.

(29) Sammon, C.; Yarwood, J.; Everall, N. *Polymer Degradation and Stability* **2000**, *67*, 149-158.

(30) Banwell, C. N.; McCash, E. M. *Fundamentals of Molecular Spectroscopy*, Fourth ed.; McGraw-Hill, 1994.

(31) Dadsetan, M.; Mirzadeh, H.; Sharifi, N. *Radiation Physics and Chemistry* **1999**, *56*, 597-604.

(32) Kazarian, S. G.; Brantley, N. H.; Eckert, C. A. *Vibrational Spectroscopy* **1999**, *19*, 277-283.

(33) Sammon, C.; Yarwood, J.; Everall, N. *Polymer* **2000**, *41*, 2521-2534.

(34) Belali, R.; Vigoureux, J. M. *Applied Spectroscopy* **1994**, *48*, 465-471.

(35) Walls, D. J. *Applied Spectroscopy* **1991**, *45*, 1193-1198.

(36) Hobbs, J. P.; Sung, C. S. P. *Macromolecules* **1983**, *16*, 193-199.

(37) Everall, N. J.; Bibby, A. *Applied Spectroscopy* **1997**, *51*, 1083-1091.

(38) Walls, D. J.; Coburn, J. C. *Journal of Polymer Science: Part B: Polymer Physics* **1992**, *30*, 887-897.

(39) Sung, C. S. P. *Macromolecules* **1981**, *14*, 591-594.

(40) Everall, N.; MacKerron, D.; Winter, D. *Polymer* **2002**, *43*, 4217-4223.

(41) Flournoy, P. A.; Schaffers, W. J. *Spectrochimica Acta* **1966**, *22*, 5-13.

(42) Hind, A. R.; Bhargava, S. K.; McKinnon, A. *Advances in Colloid and Interface Science* **2001**, *93*, 91-114.

(43) Fahrenfort, J.; Visser, W. M. *Spectrochimica Acta* **1962**, *18*, 1103-1116.

(44) Matthews, R. G.; Ajji, A.; Dumoulin, M. M.; Prud'homme, R. E. *Polymer* **2000**, *41*, 7139-7145.

(45) Ajji, A.; Cole, K. C.; Dumoulin, M. M.; Brisson, J. *Polymer* **1995**, *36*, 4023-4030.

(46) Schmidt-Rohr, K.; Hu, W.; Zumbulyadis, N. *Science* **1998**, *280(5364)*, 714-717.

(47) Huang, J.-M.; Chu, P. P.; Chang, F.-C. *Polymer* **2000**, *41*, 1741-1748.

(48) Liu, C.; Jin, Y.; Zhu, Z.; Sun, Y.; Hou, M.; Wang, Z.; Wang, Y.; Zhang, C.; Chen, X.; Liu, J.; Li, B. *Nuclear Instruments and Methods in Physics Research B* **2000**, *169*, 72-77.

(49) Ajji, A.; Guèvremont, J.; Cole, K. C.; Dumoulin, M. M. *Polymer* **1996**, *37*, 3707-3714.

(50) Zajicek, T. *Thèse 3ème Cycle, Besançon* **1987**.

(51) Göschel, U. *Polymer* **1996**, *37*, 4049-4059.

(52) Göschel, U.; Deutscher, K.; Abetz, V. *Polymer* **1996**, *37*, 1-6.

(53) Daubeny, R. D. P.; Bunn, C. W.; Brown, C. J. *Proc. Roy. Soc. Lon.* **1954**, *A226*, 531-542.

(54) Asano, T.; Calleja, F. J. B.; Flores, A.; Tanigaki, M.; Mina, M. F.; Sawatari, C.; Itagaki, H.; Takahashi, H.; Hatta, I. *Polymer* **1999**, *40*, 6475-6484.

(55) Mahendrasingam, A.; Martin, C.; Fuller, W.; Blundell, D. J.; Oldman, R. J.; Harvie, J. L.; MacKerron, D. H.; Riekel, C.; Engström, P. *Polymer* **1999**, *40*, 5553-5565.

(56) Mahendrasingam, A.; Martin, C.; Fuller, W.; Blundell, D. J.; Oldman, R. J.; MacKerron, D. H.; Harvie, J. L.; Riekel, C. *Polymer* **2000**, *41*, 1217-1221.

(57) Mahendrasingam, A.; Blundell, D. J.; Wright, A. K.; Urban, V.; Narayanan, T.; Fuller, W. *Polymer* **2003**, *44*, 5915-5925.

(58) Hughes, D. J.; Mahendrasingam, A.; Martin, C.; Oatway, W. B.; Heeley, E. L.; Bingham, S. J.; Fuller, W. *Review of Scientific Instruments* **1999**, *70*, 4051-4054.

(59) Mahendrasingam, A.; Fuller, W.; Forsyth, V. T.; Oldman, R. J.; MacKerron, D.; Blundell, D. J. *Review of Scientific Instruments* **1992**, *63*, 1087-1090.

(60) Marco, Y.; Chevalier, L.; Chaouche, M. *Polymer* **2002**, *43*, 6569-6574.

(61) Chaari, F.; Chaouche, M.; Doucet, J. *Polymer* **2003**, *44*, 473-479.

3 Materials

3.1 General introduction to polymers and PET

Polymers are everywhere and are increasingly relied upon in everyday life. The polymer under investigation in this study is poly(ethylene terephthalate). PET is renowned for its superb optical clarity, dimensional stability and high chemical resistance[1,2]. It possesses a high melting temperature, which enables it to find uses in more thermally demanding applications. It is also one of the most valuable of the recyclable polymers[3,4]. In 1998, 104000 tons of PET were recycled in Europe[5]. This figure is rapidly increasing compared to 1995 when only 36000 tons were recycled and just 23000 tons in 1993. The properties exhibited by any given polymer can vary significantly depending on its processing conditions, thermal history and exact chemical composition. Since the first polymers were used in industry, scientists from both industry and academia have made a continued effort to explore the nature of polymers at every stage of manufacture from resin production to conversion into products such as films and bottles.

This chapter gives a detailed summary of PET, from its chemical structure and synthesis to its physical properties and end uses. It includes a summary of some common chemical modifications presently used in the polyester industry.

3.1.1 Commercial uses

PET has many commercial uses. Perhaps most obvious are the contributions to the food packaging markets in the form of bottles and films. PET films are found in a huge array

of other applications, which DuPont Teijin Films sell under the brand names of Mylar®, Melinex®, Teijin® and Tetoron® to name but a few. The high dielectric strength and excellent thermal properties of PET give uses in the electrical industry such as cable coatings and components in electrical motors. It can also be used as the insulating layer in electrical capacitors, which allows for miniaturisation and higher service temperatures. The dimensional stability of PET and its ability to be treated for anti-static and slip finishes lends it for the industrial imaging market. Here the films can be tailored for use as microfilm, printed overlays, posters and book covers. Three different PET film layers can be found in some laminated security labels that contain printed circuits. For all these reasons, PET has an estimated worldwide production of 16 million tons a year[6].

The polyester film industry is ferociously competitive and continually evolving and thus it is important that new markets be exploited quickly. A potentially massive new market of PET film has been identified by DuPont Teijin Films, who discovered that incorporating a layer of PET into credit-card laminates considerably improves the thermal resistance, durability and lifetime of the card. This is a considerable improvement over existing cards, which are conventionally made from a 100 % PVC laminate construction. Any application involving the lamination of PET with other polymer types, adds extra importance to this study of PET surface characterisation. The permanence of the lamination or coating will be largely determined by the nature of the surface of the PET film.

3.2 The chemical properties of PET

3.2.1 Chemical structure

Poly(ethylene terephthalate) is a semi-crystalline polymer that belongs to the polyester family. The polymer chains are linear and consist of many connected repeat units, which each contain a terephthalate group and an ethylene group as shown in Figure 3-1.

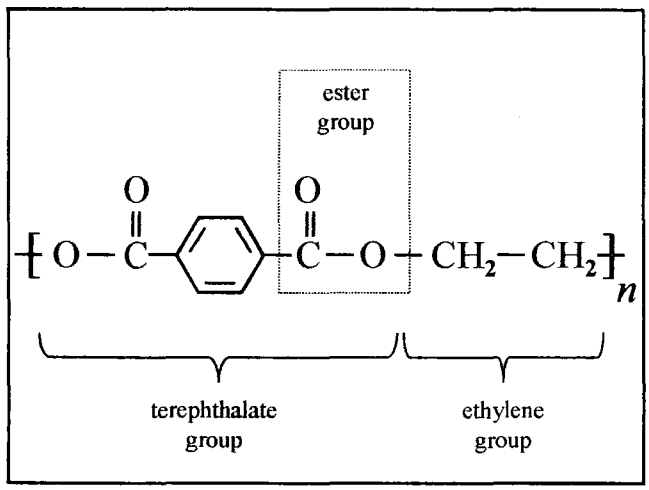

Figure 3-1: The terephthalate, ethylene and ester groups in the PET repeat unit

The esters within the terephthalate group are *polar*: the carbonyl oxygen atom has a partial negative charge while the carbonyl carbon atom is partially positive. This charge imbalance leads to attractive dipole-dipole forces between the ester groups of neighbouring chains, which allows them to line up and lock into position. It is this property that gives rise to the semi-crystalline nature of PET. The carbonyl groups and benzene ring are co-planar[7].

3.2.2 Synthesis of PET

There are two common routes available for the production of PET on the industrial scale[8], both of which require the production of *bis*-(2-hydroxyethyl)terephthalate (BHET) as the intermediate, but differ in the method of producing BHET. These are i)

the transesterification of dimethyl terephthalate (DMT) with ethylene glycol (EG) and ii) the direct esterification of terephthalic acid (TA) with EG. These routes are shown in Figure 3-2.

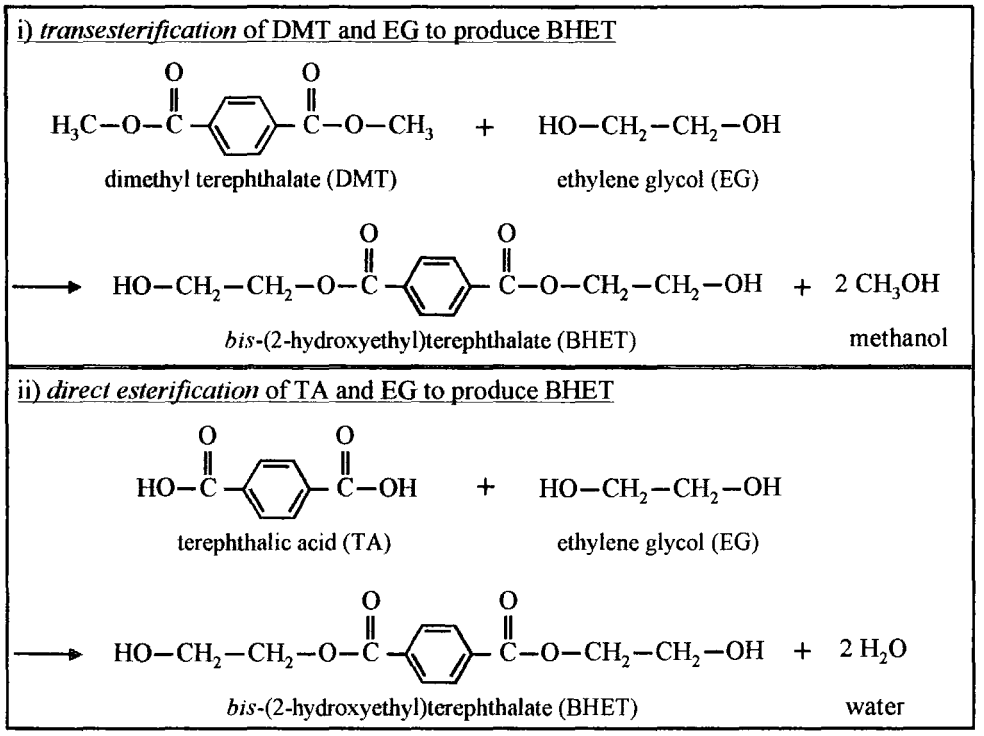

Figure 3-2: Two common routes to the production of BHET needed for PET synthesis

Each route has advantages and disadvantages and the adopted method is usually governed by factors including the raw material availability and regional health and safety regulations. The *transesterification* route used to be exclusively used in industry until TA became more affordable in bulk quantities. At the present time, the *direct esterification* approach is generally considered to be the industry favourite[9], due to its faster reaction rate and more favourable by-product of water. Once the BHET has been formed, the polymerisation of PET progresses as described in Figure 3-3.

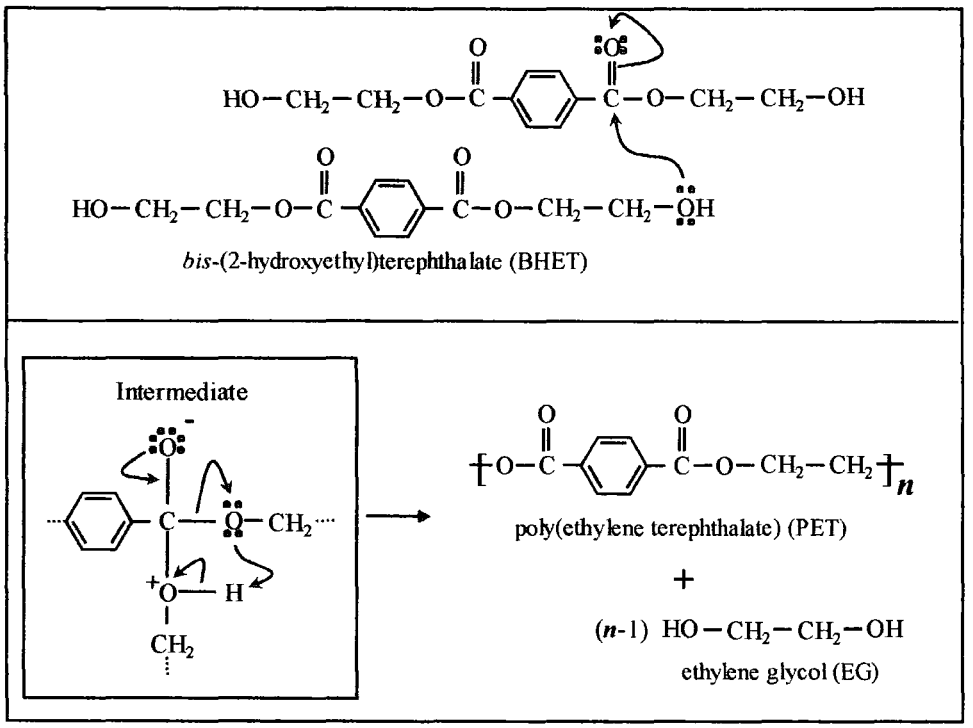

Figure 3-3: The polymerisation of PET from BHET

3.2.3 Typical molecular weights

During the synthesis of PET, the polymerisation continues until a desired molecular weight is reached. As the molecular weight increases, so does the intrinsic viscosity (IV) of the melt, thus the IV of the melt is often used to estimate the molecular weight of polymers[10]. On large-scale production rigs, the IV is estimated by the torque exerted by the melt stirrer. Thus, when the torque reaches a pre-defined value the material is dropped into the chipper. For PET films, the desired IV is 0.62 and for bottles the IV is 0.82. The IV can be pushed even higher for fibres, which require higher molecular weight values to promote additional strength in the fibre direction. DuPont's in-house data suggest that the molecular weights for the two most common polymer IVs used in industry are these given in Table 3-1.

Table 3-1: The typical molecular weights of the PET resins used in this study

IV	M_w /g mol^{-1}	M_n /g mol^{-1}
0.62	50700	22700
0.82	98000	44000

Throughout the rest of this document, it should be assumed that the bottle samples are made from the IV 0.82 resin and the films are IV 0.62 unless otherwise stated.

3.2.4 Chemical modifications and variations

Despite the excellent properties of pure PET, it is often desirable to modify the chemical structure of the polymer in order to reduce processing time and/or costs or to adjust the physical properties of the final product. Finding new applications and ways of improving the polymer film is particularly important in an industry that has had problems with oversupply in recent years[11]. One of the most effective ways of changing the properties is to add compounds during the polymerisation stage that are incorporated into the chains as a co-polymer. The most industrially important and most extensively used modifications are described below.

3.2.4.1 Isophthalic acid (IPA)

Replacing a small amount of terephthalic acid with IPA during synthesis (from 2 to 20 %) is by far the most commonly used modification made to commercial PET resins. PET bottles are almost exclusively blown from resin containing 2% IPA, which DuPont sells under the commercial name of *laser+*. The two benzenedicarboxylic acids (IPA and TA) used in PET manufacture are shown in Figure 3-4. Notice how the IPA unit results in the formation of a kink in the usually straight PET chain.

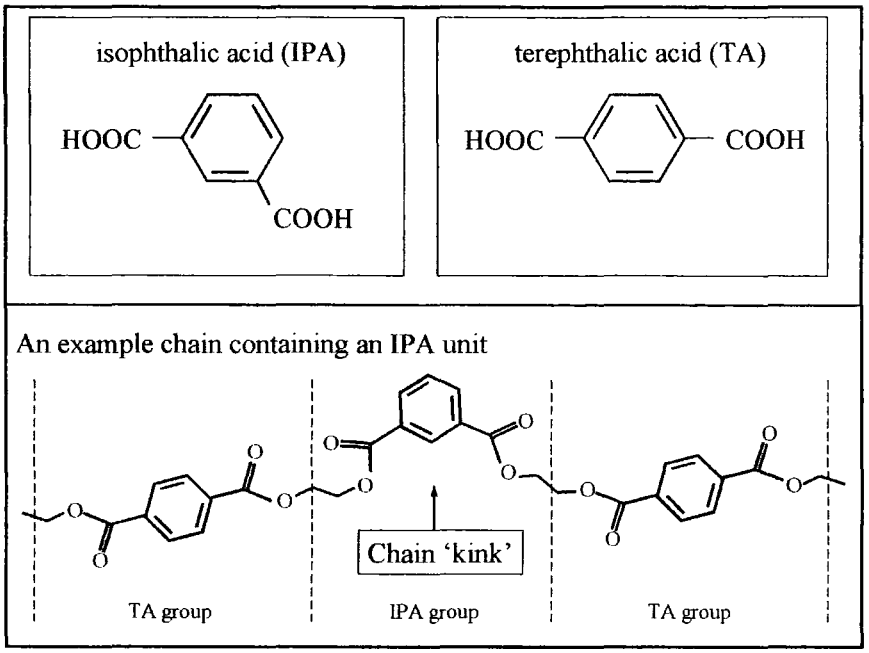

Figure 3-4: Diagram of an IPA group incorporated into a PET chain

When an IPA unit gets incorporated into a crystal, it disrupts the repeating structure and prevents another TA unit from joining the crystal at that point. It is known that the inclusion of a few percent IPA into PET limits the final crystallinity and reduces the crystallisation rate. Li[12] shows that PET resins containing 20 % or more IPA are non-crystallisable. This is useful for applications where extended heating periods are unavoidable and optical clarity may be compromised by excess crystallinity. Crystals in polymers that are in a state of little or no orientation (such as the neck and base of a PET bottle) typically grow to larger sizes that are in the order of the wavelength of visible light (400 – 700 nm). These large crystals then scatter light that can make the resin look cloudy and reduce the optical clarity of the finished product.

The inclusion of IPA is also known to lower the glass transition temperature, T_g, of the resin (see section 3.3.1 for the definition of T_g). This can be desirable in some applications, as the processing may go ahead at slightly lower temperatures, which reduces production costs. However, when filling bottles with orange juice, elevated

temperatures are required to pasteurise the juice to eliminate bacterial fouling. If the temperature of the hot-fill beverage is close to or above the T_g of the bottle resin, the bottle will deform in shape and so this reduces the amount of IPA that can be used in the resin. If the crystallinity could be limited while maintaining a high T_g, we would have a polymer better suited to hot-filling applications.

3.2.4.2 tertiary-butyl isophthalic acid (t-BIPA)

Tertiary-butyl isophthalic acid (t-BIPA) can hinder the growth of crystallinity during processing while keeping the T_g close to that of pure PET. At present, there is a lot of interest in characterising the properties of this new material, as the reasons for the beneficial properties it demonstrates are little understood. A schematic diagram of a chain section containing an IPA unit and a t-BIPA unit are compared in Figure 3-5.

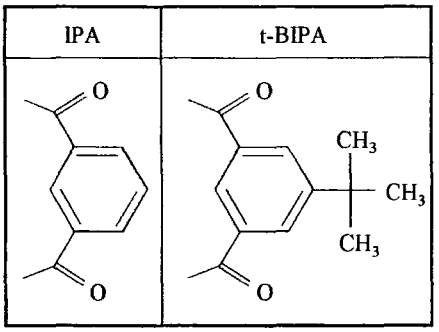

Figure 3-5: A comparison between an IPA chain section to a t-BIPA section

The preliminary research into this modification has been conducted by Kint *et al.*[13]. Kint synthesised PET-co-tBIPA polymers from 5 to 40 mol% *tert*-butyl isophthalic units and quantified properties including thermal transition temperatures (glass transition, crystallisation and melting temperatures), crystallisation properties, tensile properties and gas transport properties. In general, it was noted that increasing amounts of t-BIPA slows the crystallisation rate, except for the surprising case of 5 mol% which showed a quickening of the crystallisation. This observation was attributed to a

nucleation effect of the bulky alkyl side groups. The tensile properties were not affected for resins containing less than 15% t-BIPA. Kint's data also shows that the inclusion of 5 mol% t-BIPA increases the glass transition temperature from 78°C to 82°C. Analysis of X-ray diffraction data of these co-polymers reveals that the crystals adopt the same triclinic unit cell as pure PET, which suggests the t-BIPA units are excluded from the crystalline phase. One aim of this research is to address whether the inclusion of t-BIPA has any effect on the near-surface orientation of preliminary PET-co-tBIPA bottles.

3.2.4.3 Benzenetricarboxylic acid

It is possible to produce a cross-linked chain architecture by including 1,2,4-benzenetricarboxylic acid during the polymerisation stage. This introduces a branching point into the chain such that the chain is no longer completely linear. The architecture is not controllable and so when this compound is introduced, the chains can form various H and Y branching types. The effect of this is to add a high molecular weight tail to the distribution, which in turn affects the melt flow properties. The structure of 1,2,4-benzenetricarboxylic acid is shown in Figure 3-6.

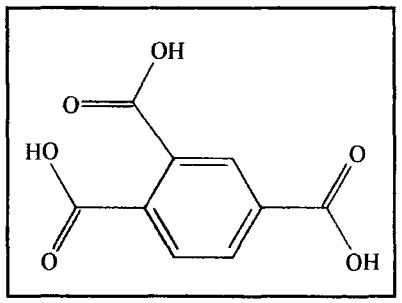

Figure 3-6: 1,2,4-benzenetricarboxylic acid

Many of the infra-red spectroscopy experiments on PET requires the use of a 1410 cm^{-1} normalisation band, which corresponds to the vibrational frequency of the benzene ring

of the terephthalic acid group. Modifying the ring, by adding an extra branching point for example, will inevitably change its characteristic vibrational modes. This would need to be taken into consideration when analysing the data for resins containing 1,2,4-benzenetricarboxylic acid.

3.3 The physical properties and processing of PET

3.3.1 The semi-crystalline nature of PET

Commercial polymers are generally categorised as amorphous or semi-crystalline. Amorphous polymers, which include poly(styrene) and poly(methyl methacrylate), are unable to crystallize, as the chains cannot order effectively due to steric hindrance of the bulky side groups or randomised chain configurations. PET falls into the category of semi-crystalline polymers along side nylons, poly(propylene), poly(ethylene) and many others.

The properties of amorphous polymers are largely affected by the glass transition temperature, T_g, of the polymer. The T_g is the lowest temperature at which molecular motion of the polymer chains can occur. Hence, an amorphous polymer below T_g is classed as glassy and is hard, rigid and brittle. On raising to temperatures above T_g, the polymer becomes increasingly soft and malleable and as such is classified as rubbery.

Semi-crystalline polymers contain both crystalline and amorphous regions. The crystalline regions grow from a supercooled polymer melt or a supersaturated solution via a chain-folding mechanism to form crystalline lamellae. The amorphous regions comprise of the lamellae folds and all other non-crystalline polymer materials between the crystalline lamellae. The amount of crystalline material present, i.e. the crystallinity of the polymer, is determined by the amount of time the supercooled melt or

supersaturated solution remains at crystallising temperatures (i.e. between T_g and T_m, the melting temperature of the polymer lamellae, or T_g and T_s, the saturation temperature of the polymer for polymer melts and solutions, respectively). Hence, this time can be varied to produce the required crystallinity range. Semi-crystalline polymers exhibit improved properties compared to their amorphous counterparts, because the amorphous regions impart a degree of flexibility, whilst the crystalline regions remain hard and rigid below T_m, imparting increased toughness and heat, chemical and abrasion resistance to the polymer. For PET, the T_g of the un-oriented amorphous regions is ~78°C, while the crystalline regions melt at a T_m ~260°C.

Semi-crystalline polymers have the advantage that the tensile properties can be altered after the bulk of the processing has occurred by increasing the levels of crystallinity in the resin. For PET films, this can be achieved by exposing the stretched films to elevated temperatures of around 200°C at which further crystallisation can occur, while mechanically holding the film taut to prevent shrinkage. This 'heat-setting' is typically incorporated into the film stenter technique used to manufacture PET films and dramatically improves the film's tensile strength and creep-resistance.

3.3.2 Processing techniques used in PET film and bottle manufacture

3.3.2.1 Bottle formation via the stretch-blow process

PET beverage bottles of various shapes and sizes including the standard 2 litre and 500 ml varieties are produced using the stretch-blown process, as shown schematically in Figure 3-7.

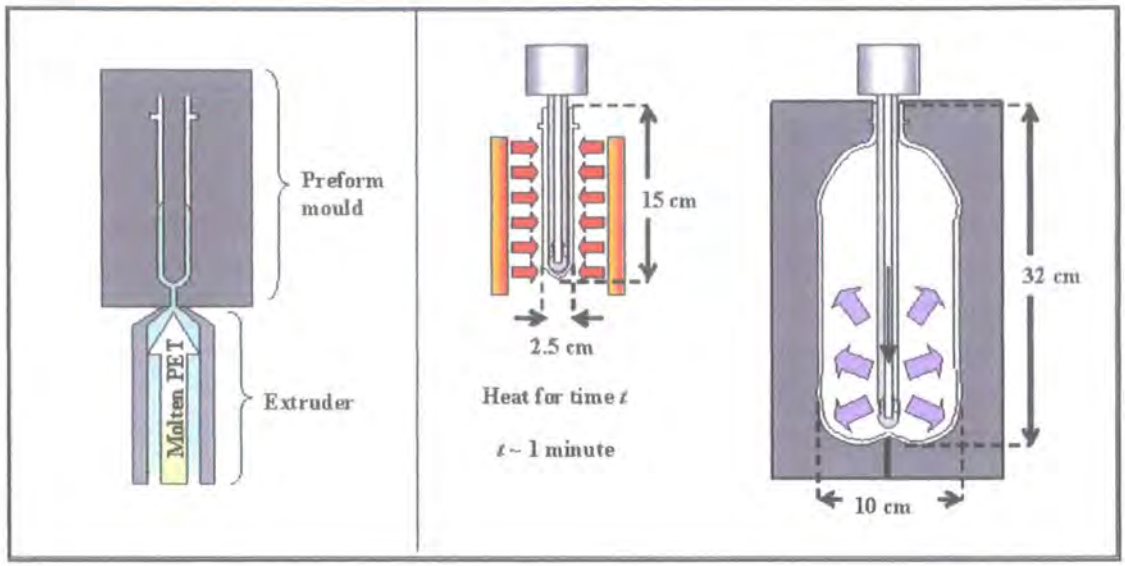

Figure 3-7: A schematic diagram of the stretch-blow process used in PET bottle manufacture

A 'preform' is produced by filling a preform mould with molten PET using the injection moulding process. When the resin has solidified, the preform is ejected and transferred to the stretch-blow station. The preform is then held close to heating elements and rotated for around one minute to ensure an even heat distribution in the radial direction. The heating element itself consists of several individually controlled heating units that exert a heating gradient down the length of the preform side that can be changed for different bottle designs and sizes. After the heating time has elapsed, the mechanical arm holding the preform swings to the blow mould, where a hollow metal rod thrusts downwards while compressed air is blown through the rod such that the preform expands to the size of the blow mould. The finished bottle is then ejected from the blow-mould and awaits filling.

3.3.2.2 The bottles analysed in this study

Table 3-2 summarises the bottles analysed in this study. Further details and photographs of some bottles are provided in the results sections of chapter 4.

Table 3-2: The PET bottles analysed in this study

Series name	Bottle name	Resin	Preform heat time	Notes
Bottle heating time	Bht-20	PET + 2% IPA	ideal time - 20 s	very poor optical clarity
"	Bht-15	PET + 2% IPA	ideal time - 15 s	very poor optical clarity
"	Bht-10	PET + 2% IPA	ideal time - 10 s	poor optical clarity
"	Bht-5	PET + 2% IPA	ideal time - 5 s	
"	Bht-i	PET + 2% IPA	ideal time	
"	Bht+5	PET + 2% IPA	ideal time + 5 s	
"	Bht+10	PET + 2% IPA	ideal time + 10 s	poor optical clarity
"	Bht+15	PET + 2% IPA	ideal time + 15 s	very poor optical clarity
BtBIPA	BtBIPA-2A	PET + 2% t-BIPA	ideal time	
"	BtBIPA-8A	PET + 8% t-BIPA	ideal time	
"	BtBIPA-I+	PET + 2% IPA	ideal time	Standard 2% IPA
Low Mol. weight	B5	PET + 2% IPA	ideal time	IV 0.62 resin
Small bottles	BSBhf-0A	Pure PET	ideal time	Heated blow-mould
"	BSB01	PET + 2% IPA	ideal time	Blown by DuPont customer
"	BSB02	PET + 2% IPA	ideal time	Blown by DuPont customer
"	BSB03	PET + 2% IPA	ideal time	Blown by DuPont customer

3.3.2.3 PET film manufacture

Industrial-scale PET film manufacture is typically carried out using the film *stenter* process[14] as shown in Figure 3-8 (diagram adapted from the Ph.D. thesis of Hodgson[8]). The process starts by drying the PET chips and feeding them into the hopper. The drying process is important, otherwise, hydrolysis is known to occur even at the low moisture levels that the resin readily absorbs from the atmosphere. The dried chip is then fed into the extruder, which melts the chip and forces the melt through a slit die. The melt 'curtain' then encounters a chill roll that quenches the polymer to a temperature below its crystallisation temperature range to prevent excess crystallinity forming, which could make subsequent drawing of the film more difficult. The cast film then gets heated to above its glass transition temperature and navigates a series of rollers. These are set at different speeds to introduce a forward draw, up to a maximum draw ratio of around 4. Two lines of grips take hold of the film edges and introduce a transverse draw into the films such that the film is bi-axially oriented. The film is then subjected to a heat-setting region where it is heated to temperatures above 200°C for a

few seconds to increase the levels of crystallinity in the film. The edges are trimmed, as the regions held by the grips are uneven and thicker than the central regions. These edges are fed back into the extruder as 'reclaim' to minimise waste.

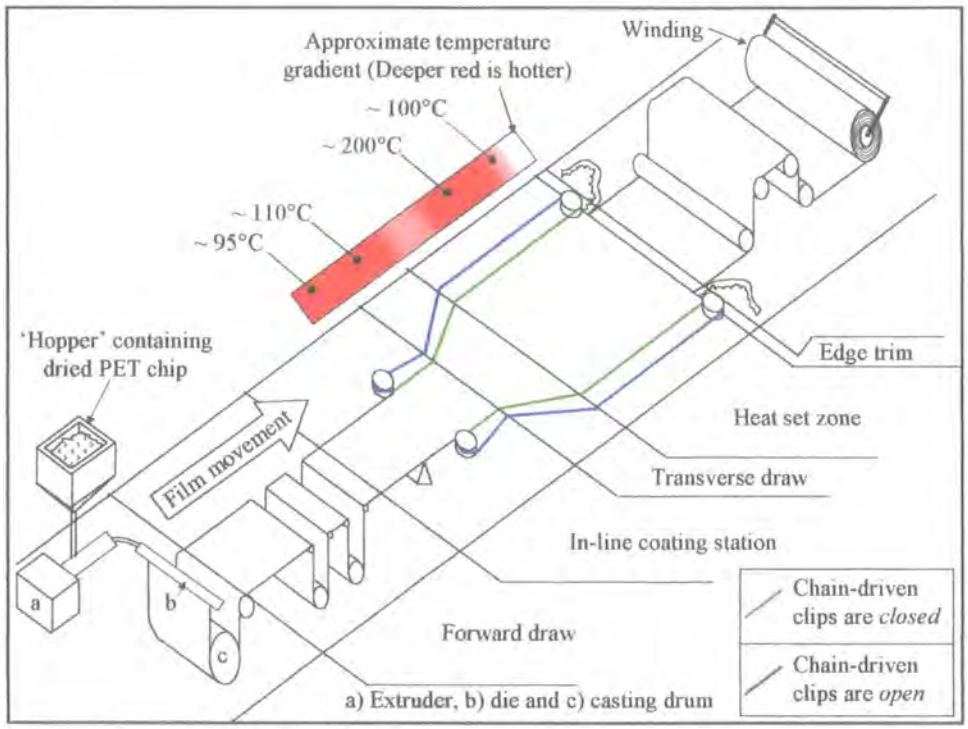

Figure 3-8: The film stenter process used to manufacture PET film

PET films drawn using the full-scale extrusion fed, sequential-draw stenter process finish as large rolls, which are cut into smaller sheets at a later time. The molecular orientation across the width of these drawn films is known to vary as a function of distance from the film centre. Characterising the properties of a PET sheet from the original roll is complicated by the fact that its original position in relation to the original roll is not known. For this reason, lab-based film stretching methods are typically employed in order to relate drawing conditions to the properties of the final film artefact, as it is possible to have more control over the drawing parameters.

3.3.2.4 Films produced using the Long stretcher

The drawn film samples analysed in this work were produced at DuPont Teijin Films, Wilton UK, on a 'Long stretcher'. Named after the inventor T. M. Long, the device is designed to mimic the standard biaxial stenter process on the laboratory scale. It offers the facility to heat the samples and stretch them uni- or biaxially with stretch magnitudes up to a draw ratio (DR) of four, using the standard configuration.

The initial samples were sections from an amorphous-cast roll that were cut into 112 by 112 mm squares. A 20 by 20 mm reference grid was drawn onto the samples that allowed localised draw ratios of the stretched sample to be measured. This is important as the sample may occasionally stretch unevenly depending on minor fluctuations in the heating profile or slight gradients in the initial sample thickness. The square sample sections were attached to a sample-positioning arm, which employs a vacuum to hold the sample flat while it is lowered into the sample grips. Once the sample is held in the correct position by the arm, an array of 13 small gas-powered clips clamp tightly along all four edges of the sample and the stretcher lid is lowered to allow for more even heat distribution. The sample is then held in this position for a pre-determined temperature and time to bring the resin to a temperature close to its T_g. Typically, this would be 90°C or 100°C for around one minute. A sketch of films uniaxially drawn to three and four draw-ratio is shown in Figure 3-9i. These films have a more even draw than films clamped only along two edges as shown in Figure 3-9ii. The operator then has manual control over the order of the biaxial stretch, the draw speed and draw ratio. Biaxial samples produced on a Long stretcher deviate from films produced on the stenter process by one important way: the transverse draw in the stenter process is carried out at

a higher temperature to the forward draw, but the temperature remains constant in the Long stretcher.

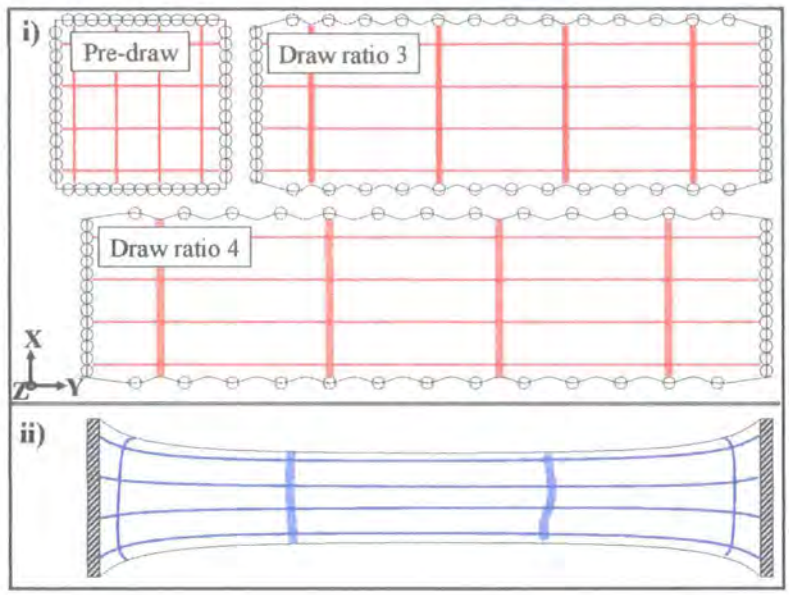

Figure 3-9: A sketch of films stretched on i) a Long stretcher, and ii) an Instron-style stretcher

Biaxial drawing on the Long stretcher it carried out at the same temperature for two reasons. 1) The temperature cannot be swiftly changed between the initial stretch and the transverse stretch and 2) re-clamping a uniaxially drawn sample after allowing the stretcher to stabilise at the second temperature is difficult, as the pre-stretched films often do not lie flat and the vacuum arm is designed to hold squares of 112 x 112 mm. Furthermore, the uniaxially stretched film would be likely to distort and curl as they approach the clamping position due to the elevated temperatures.

3.3.2.5 The heat-setting of PET films

The film stenter process typically includes a heating phase just after the biaxial draw. The film passes through an oven set at around 200°C for a few seconds while the film is being held by the clamps. This restraint is required for the film to maintain its shape

and resist shrinkage. To heat-set the films produced on the Long stretcher in this study, it was necessary to design and fabricate a device to restrain the film at elevated temperatures in the vacuum oven. The anti-shrinkage frames designed for this study transpired to be very effective and robust, so the designs are included for completeness. The specifications are shown below. Each half was machined in the chemistry department workshop from sheet aluminium of dimensions 80 x 80 x 6 mm. A sketch of the frame is shown in Figure 3-10.

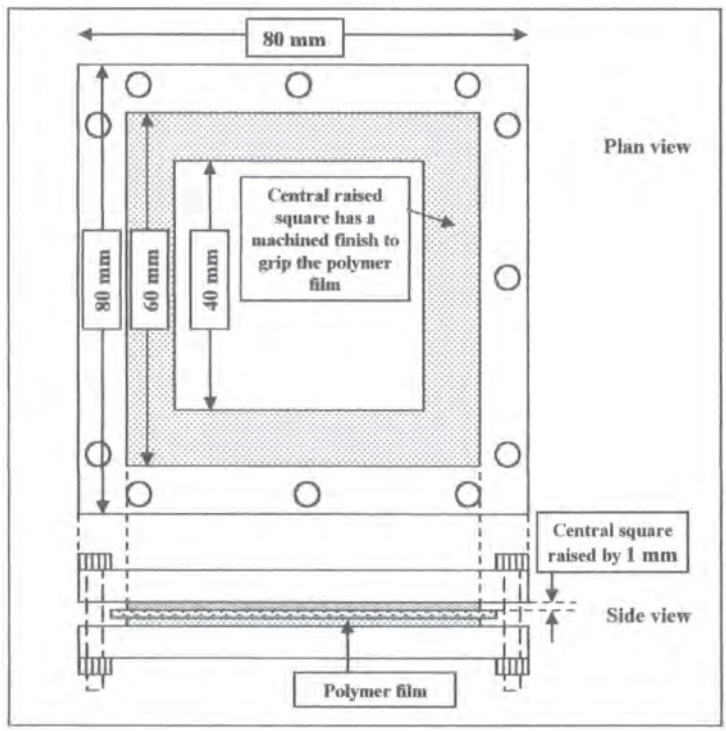

Figure 3-10: The author's original design for the anti-shrinkage frames used to heat PET films

The raised lip increases the pressure onto the edge of the film and so this frame can be used for any thickness of film. A photograph of the finished frame is shown in Figure 3-11. This frame design will be used to produce all the heat-set films described in this work.

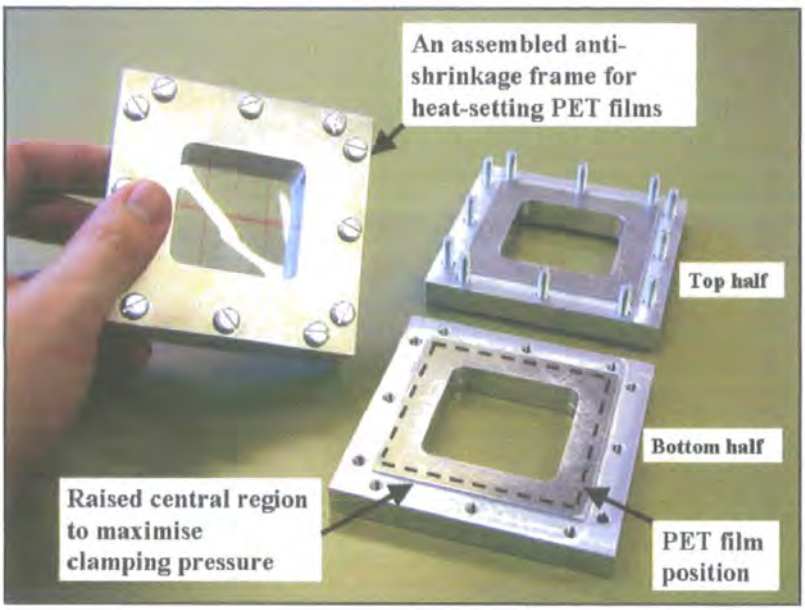

Figure 3-11: A photograph of the finished anti-shrinkage frames

3.3.3 The PET films used in this study

All the films examined here are made from E47 PET (0% IPA, IV 0.62) and stretched on a Long stretcher. A description of the films is presented in Table 3-3.

Table 3-3: The PET films used in the IR and X-ray chapters

Film	Full name	Draw ratio	Uni-/Biaxial	Heating regime	Thickness (μm)
1	E4U_75a200cool	3.75	Uni	75 minutes at 200°C	150 (+/- 1)
2	E3U_75a200cool	3	Uni	75 minutes at 200°C	190 (+/- 1)
3	E4U_unheat	3.75	Uni	pre-stretch only	160 (+/- 1)
4	E4U_200cool	3.75	Uni	0 minutes at 200°C	150 (+/- 1)
5	E4U_1h200	3.75	Uni	60 minutes at 200°C	150 (+/- 1)
6	E3B_unheat	2.75 x 2.75	Bi	pre-stretch only	60 (+/- 1)
7	E3B_75a200cool	2.75 x 2.75	Bi	75 minutes at 200°C	48 (+/- 1)
8	E47_30a161_600	No draw	-	30 minutes at 161°C	620 (+/- 10)

The local draw ratios were measured from the lines drawn onto the film prior to the draw. The heating regimes took place in a vacuum oven. Following each regime, the samples were left under vacuum while the oven was turned off, until ambient temperature was achieved. The thickness measurements were recorded using a

Mitutoyo micrometer and averaged from three measurements at different points on the film. Thickness measurements of the thicker samples may be over-estimates as they are inherently less flexible and less ready to lie flat in the polished clamp surfaces.

The films presented in Table 3-3 are analysed using both FTIR spectroscopy and X-ray diffraction, as detailed in chapter 6.

3.4 References for chapter 3

(1) Chiu, S. J.; Cheng, W. H. *Polymer Degradation and Stability* **1999**, *63*, 407-412.

(2) Zhao, J.; Wang, J.; Li, C.; Fan, Q. *American Chemical Society* **2002**, *Published on Web.*

(3) Smith, D. N.; Harrison, L. M.; Simmons, A. J. *Resources, Conservation and Recycling* **1999**, *25*, 17-34.

(4) Kurokawa, H.; Ohshima, M.-a.; Sugiyama, K.; Miura, H. *Polymer Degradation and Stability* **2003**, *79*, 529-533.

(5) Güçlü, G.; Yalçinyuva, T.; Özgümüs, S.; Orbay, M. *Thermochimica Acta* **2003**, *In Press.*

(6) Zhang, G.; Shichi, T.; Takagi, K. *Materials Letters* **2003**, *57*, 1858-1862.

(7) Daubeny, R. D. P.; Bunn, C. W.; Brown, C. J. *Proc. Roy. Soc. Lon.* **1954**, *A226*, 531-542.

(8) Hodgson, M. R. In *Chemistry - Ph.D. Thesis*; University of Durham, 2000.

(9) Rieckmann, T.; Völker, S. *Chemical Engineering Science* **2001**, *56*, 945-953.

(10) Al-AbdulRazzak, S.; Jabarin, S. A. *Polym. Int.* **2002**, *51*, 164-173.

(11) Website. *http://www.icraindia.com/rtaction/20030325vpfl.htm* **2003**, Venlon Polyester Film Limited.

(12) Li, B.; Yu, J.; Lee, S.; Ree, M. *European Polymer Journal* **1999**, *35*, 1607-1610.

(13) Kint, D. P. R.; Rudé, E.; Llorens, J.; Muñoz-Guerra, S. *Polymer* **2002**, *43*, 7529-7537.

(14) Ashford, E.; Bachmann, M. A.; Jones, D. P.; MacKerron, D. H. *Trans IChemE* **2000**, *78*, 33-38.

4 FTIR spectroscopy

4.1 A brief introduction to IR spectroscopy

Molecular spectroscopy may be defined as the study of the interaction of electro-magnetic (EM) waves and matter[1]. The energies encountered in the infrared region of the EM spectrum (λ = 100 μm to 1 μm) correspond to those of molecular vibrations and/or rotations. The IR beam consists of a whole range of IR frequencies. As the beam encounters the sample, the frequencies corresponding to the vibrational energies of molecular bonds get absorbed. Any given chemical group, such as the CH_2 group in the PET chain, are known to vibrate in one of a few vibrational modes (wagging, twisting, scissoring etc.), each of which has a set frequency as determined by the quantum mechanical nature of the chemical system. FTIR spectroscopy can thus be used to monitor proportions of different chemical species within the sample and changes that occur on the molecular scale.

4.1.1 Attenuated Total Reflection (ATR)

The ATR technique provides a way of collecting IR spectra from thick or highly absorbent materials[2]. The name 'ATR' refers to the physical principle of Attenuated Total Reflection[1] as shown in Figure 4-1. The solid sample is placed onto a highly refractive, transparent ATR crystal (or *internal reflection element (IRE)*) and for solid samples, a pressure-applicator is screwed down onto the reverse side. This is necessary in order for the contact between the sample and the IRE to be as intimate as possible. IR radiation is then directed through the crystal at an angle θ from the normal to the

interface. The sudden lowering of refractive index between the ATR crystal and the sample forms a reflective interface. The incident IR beam is directed through the crystal, where it reflects from the crystal/sample interface, exits the crystal and is directed towards the detector via a series of mirrors.

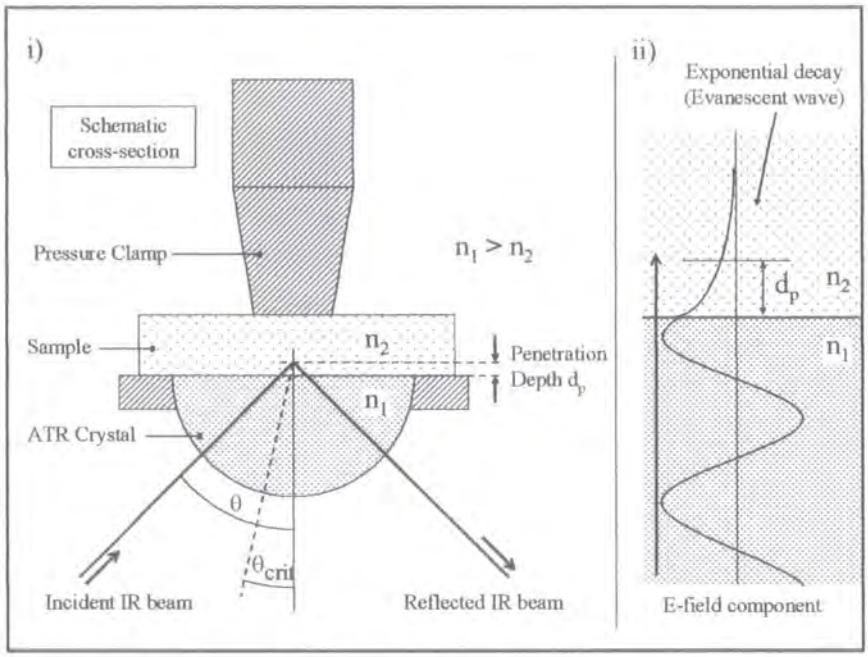

Figure 4-1: The principle of the ATR technique

Under conditions of total internal reflection at the interface which occurs when the IR incident angle is at of above a critical angle (θ_{crit}), the magnitude of the electric field due to the totally reflected rays suffers an exponential decay with distance into the rarer material. This is termed an evanescent wave (see Figure 4-1 part ii). The reflected beam then contains the IR absorption information from the sample's surface region probed by this evanescent wave. A quantity known as the penetration depth d_p is used to quantify the depth probed at the sample's surface[3,4], as shown in Equation 4-1.

$$d_p = \frac{\lambda}{2\pi . n_1 \left(\sin^2 \theta - \left(\frac{n_2}{n_1} \right)^2 \right)^{1/2}}$$

Equation 4-1

where λ is the wavelength of the incident radiation, n_1 and n_2 are the refractive indices of crystal and the sample, respectively, and θ is the angle of incidence. The penetration depth corresponds to the distance travelled into the sample when the electric field has decreased to 1/e of its original value at the sample surface. Typical d_p values for a polymer such as PET are in the order of microns (approximately 0.5 -2.5 μm depending on λ, n_1 and the n_2 values of the system).

For Equation 4-1 to hold, the expression within the square root must be non-negative. This gives rise to the experimental condition that measurements must be taken at angles of incidence at or above the *critical angle* shown in Equation 4-2, where

$$\theta_{crit} = \sin^{-1}\left(\frac{n_2}{n_1}\right)$$

Equation 4-2

By using a combination of different crystal and angle combinations, different d_p values can be obtained and different depths probed. The design of the ATR accessory determines whether this is possible or not.

The standard accessories contain a fixed, tailor-made IRE and mirrors set to give a fixed angle of incidence at the sample/crystal interface. This set-up is often desirable as it requires minimal maintenance and adjustment and thus offers the easiest data collection and the most reproducible results. Other accessories incorporate a combination of concave and moving mirrors that can be used to focus the beam and direct it through a hemispherical crystal onto the interface, which allows for a range of incident angles. This accessory type is known as a *variable angle, single bounce accessory.* Alternatively, a long, slender ATR crystal can be sandwiched between two uniform film samples, which enables the beam to reflect many times (usually between 10 and 25)

from the opposing interfaces, before exiting the crystal. The motivation behind these *multi-reflection* geometries is that the signal to noise ratio is improved as the beam has many more opportunities to retrieve its absorption information from the sample. The information retrieved from the multi-reflection geometry is also an average of the total sample surface in contact with the crystal. This can be advantageous if the averaged properties are desired, but render it useless if one was interested in mapping variations across the surface. Another disadvantage of this technique is that the samples have to be of a uniform thickness and display a smooth surface for the crystal/sample contact to be satisfactory. The majority of samples cannot be prepared to these exacting specifications. Everall[5] states that the biggest drawback of the ATR technique is the need to obtain an intimate contact between the crystal and the specimen. For solid polymer samples, especially hard or inflexible artefacts, is impossible to achieve the same contact once the original contact is broken.

4.1.2 The choice of ATR crystal

Generally, the most important property of an ATR material is its inherent refractive index (n). A highly refractive germanium crystal ($n_1 = 4$) makes the measurement more surface-specific. The RI of the crystal is known to affect more than just the depth of measurement. When the RI of the sample approaches that of the ATR crystal, spectral distortions can arise[5]. This phenomenon is known to occur when a diamond crystal ($n_1 = 2.4$) is used to collect ATR spectra from oriented PET, as these specimens exhibit perturbed refractive indices. Another important property of the ATR crystal is its useable wavelength range. Each material has its own absorbing properties. Germanium for example, has its low energy cut-off point at ~830 cm^{-1}. The useful wavelength

ranges and refractive indices of common ATR element materials are summarised in Table 4-1.

Table 4-1: The properties of some common ATR crystal materials. Wavenumbers are in cm^{-1}.

IRE Material	RI	Wavenumber range
KRS-5	2.4	4000-400
ZnSe	2.4	4000-650
Silicon	3.4	4000-1500 & 360-70
Ge	4	4000-830
Diamond	2.35	2500-200

KRS-5 and ZnSe are the two most commonly used materials. KRS-5 is the material favoured by the ATR pioneers of early 1960s, and is made from a thallium-based compound. This makes KRS-5 highly poisonous, which is why ZnSe, with its comparable optical properties and reduced toxicity, is commonly used as a replacement for KRS-5 in modern accessories.

4.2 The FTIR apparatus used

This section describes the apparatus used in these studies. The specification and design will be described along with some general experimental procedures that will be used throughout the experimental section.

4.2.1 FTIR spectrometer and collection parameters

IR spectra were collected via a Nicolet NEXUS FTIR spectrometer connected to a personal computer running Omnic spectral manipulation software. The detector in this spectrometer was based on mercury cadmium telluride (MCT-A) which requires cooling from liquid N_2. Throughout this study, IR spectra were collected at a resolution of 2 cm^{-1} and averaged over 64 scans. Dry purge gasses were not available and so longer collection times would allow fluctuations of atmospheric water vapour levels to show in the spectra.

4.2.2 The Nicolet Spectra-Tech Thunderdome ATR accessory

The ATR accessory used throughout this study is a single reflection unit that contains a fixed germanium crystal. It is similar in layout to the 'Golden Gate' (Graseby Specac) unit, favoured by various FTIR-ATR authors[5,6]. The main section of the Thunderdome contains the germanium crystal. A pressure tower is situated vertically, normal to the upper crystal surface. The maximum available clamping force available to the anvil is limited by an inbuilt torque-ratchet mechanism. This is necessary, as although germanium is hard, it is very brittle and could chip easily under the application of high pressure. The angle of incidence at the crystal/sample interface is fixed at 45°. Extending from both sides of the central unit are funnels that have been designed to carry purge gases through the accessory.

4.2.2.1 Modifications made to the commercial Thunderdome ATR accessory

The determination of molecular orientation requires the use of an IR polariser in conjunction with the Thunderdome ATR accessory. The purge funnels occupied the length of the sample chamber, so a section had to be removed for the polariser to be positioned in the beam path. The exit funnel was slightly longer than the entrance and so the last 15mm was removed from this side in the mechanical workshop. A simple polariser-holder was fabricated from sheet aluminium (1 mm gauge) and bolted to the base plate. A schematic cross-section of the modified Thunderdome and polariser assembly is shown in Figure 4-2, where the dashed section of the exit funnel indicates the portion removed. Another simple modification was the inclusion of an angle reference guide, which was affixed to the flat plane that contains the useable crystal surface, shown in Figure 4-3. This is required, as the draw direction of the sample will

need to be placed at certain angles with respect to the polarised IR beam. From now on, the angles on this dial will be referred to as the X-Y sample angle.

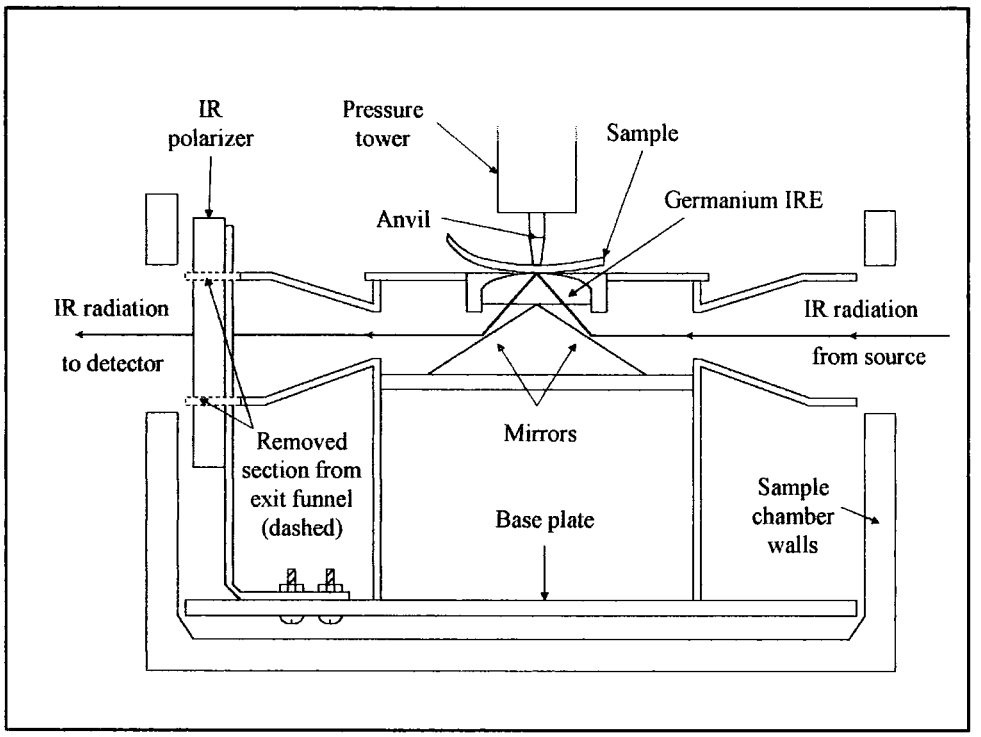

Figure 4-2: The modified Thunderdome accessory and IR polariser apparatus

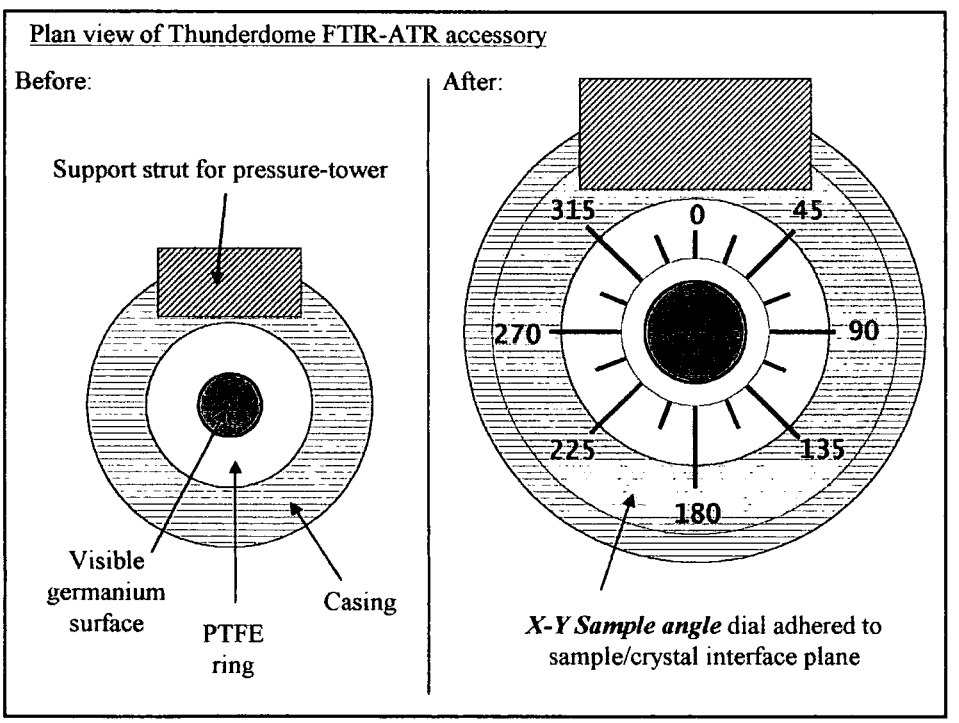

Figure 4-3: A modification allowing the sample to be accurately positioned on the crystal

4.3 Mapping the surface orientation of PET bottles

4.3.1 General introduction and aims

Everall and Bibby[5] have published a complete method of measuring the orientation properties of polymer surfaces using polarised FTIR-ATR spectroscopy. The IR polariser is used to limit the electric field component of the incident radiation to specific directions so that only vibrating groups with transition dipole moments lying in the same direction of the electric field direction absorb the IR radiation. To date, his work has been concerned with quantifying the molecular orientation within PET films, uniaxially drawn to different draw ratios and comparing these results to the values predicted by theory. They have also measured the orientation from the inside and outside of the panel and shoulder sections of different sizes of PET bottles. To the best of my knowledge, the chain orientation of a PET bottle has not been fully mapped by taking measurements at equally spaced positions from the top of the bottle down to the base.

The aim of the experimental section is to examine the near-surface orientation of various other bottles including:

1) Bottles blown after different preform heating times
2) PET resins containing t-BIPA comonomer, which is a possible replacement for PET resins containing IPA.
3) A low-molecular weight resin. This material is similar the resin fed into film extrusion lines[7].

In addition, a series of small bottles in a variety of different shapes were investigated including one made from homopolymer PET (0% IPA), which was blown into a heated blow mould to increase crystallinity.

The extraction of the orientation parameters from the IR spectra in Everall's theory is relatively complicated and the degree of orientation cannot be seen directly from the collected spectra. As will be described, this is mainly because the bands used to derive the orientation parameters are based on ring vibrations that have their transition dipole moments at angles of 20° and 85° to the chain axis. It would therefore be advantageous if an alternative and simpler orientation quantifier were available, especially for PET resins containing high levels of ring substituents, which would inevitably result in perturbations of the ring vibrations.

4.3.2 Surface orientation theory

The derivation of the orientation parameters shown here is taken from the work of Everall and Bibby[5] which itself was built on the previous works of Fluornoy[8], Jarvis[9] and Walls[10]. This describes how orientation information can be extracted form polarised FTIR-ATR spectra of PET. The derivation is included here for completeness as a considerable amount of work presented here is based on this method. Some of the theoretical assumptions will also be addressed.

The theory begins by setting up two independent co-ordinate systems. Adhering to the notation used by Everall[5], we consider the macroscopic sample system (X, Y, Z) and the local co-ordinate system for a specific unit in the polymer chain (x, y, z). For a sample having a uniaxial geometry, we nominate Y to be the primary draw direction (the machine direction, MD), X to be perpendicular to Y and along the surface of the film

(the transverse direction, TD) and Z to be normal to the film's surface. For an arbitrary chain, we nominate the y-axis to be along the chain direction and we will simply say that x and z are mutually perpendicular to y. We can relate these two systems to one another by using the Euler angles[9], Θ and Φ, as depicted in Figure 4-4.

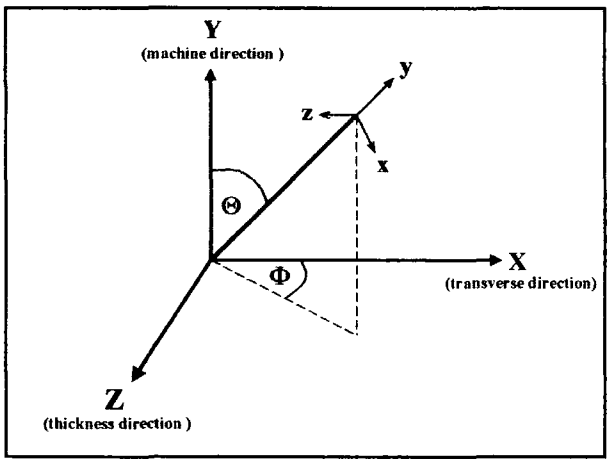

Figure 4-4: Definitions of the chain and sample axes

The other Euler angle Ψ (not shown) describes the rotation of the x and z axes in relation to the long chain director, y. The chain orientation is evaluated by describing the distribution of x, y, z structural unit orientations with respect to the X, Y, Z sample axes. Jarvis *et al.*[9] detail how this distribution is best described by a series of generalized spherical harmonics. However, the equations needed for this particular analysis are a small sub-group of the general forms described by Jarvis and so we will neglect his more extensive analysis. The spherical harmonic P_{lmn} coefficients that will be most useful for calculating chain orientation are provided in Equations 4-3 to 4-6:

$$P_{200} = \frac{1}{2}\left\langle 3\cos^2\Theta - 1 \right\rangle \qquad \textbf{Equation 4-3}$$

$$P_{220} = \frac{1}{4}\left\langle (1-\cos^2\Theta)\cos 2\Phi \right\rangle \qquad \textbf{Equation 4-4}$$

$$P_{202} = \frac{1}{4}\left\langle (1-\cos^2\Theta)\cos 2\Psi \right\rangle \qquad \textbf{Equation 4-5}$$

$$P_{222} = \frac{1}{4}\left\langle (1+\cos^2\Theta)\cos 2\Phi\cos 2\Psi - 2\cos\Theta\sin 2\Phi\sin 2\Psi \right\rangle \qquad \textbf{Equation 4-6}$$

The aim of the experiment is to calculate these P_{lmn} coefficients, which will quantify the extent of orientation. The chain orientation can also be considered in terms of the average squared direction cosine (ASDC) between the long chain axis, y, and each of the sample axes, X, Y and Z. For any particular sample axis, the ASDC will have a value in the range of 1 (perfectly orientated in that direction) to 0 (no chains lying in the specified sample axis). There also exists a general condition that $\langle\cos^2(yX)\rangle + \langle\cos^2(yY)\rangle + \langle\cos^2(yZ)\rangle = 1$. Jarvis[9] showed that the ASDC relate to the experimentally determinable P_{lmn} coefficients as shown in Equations 4-7 to 4-9.

$$\left\langle \cos^2(yY) \right\rangle = \frac{1}{3} + \frac{2}{3}P_{200} \qquad \textbf{Equation 4-7}$$

$$\left\langle \cos^2(yX) \right\rangle = \frac{1}{3} - \frac{1}{3}P_{200} + 2P_{220} \qquad \textbf{Equation 4-8}$$

$$\left\langle \cos^2(yZ) \right\rangle = \frac{1}{3} - \frac{1}{3}P_{200} - 2P_{220} \qquad \textbf{Equation 4-9}$$

Converting the calculated P_{lmn} coefficients into ASDC values provides us with an easy to follow scale for measuring orientation. Note that for a randomly orientated amorphous sample, we would expect each of the three ASDC to equal 1/3, as there would be an equal proportion of chains in each of the three sample axis directions.

The aim of the experiment is to measure the absorbance of an IR band when the radiation is selectively polarised along the X, Y and Z-axes. The ratio of these spectra then gives us k_x/k_y, k_x/k_z and k_y/k_z, dichroic ratios. Practically, it turns out that probing

vibrational bands solely in the primary draw direction or solely in the transverse direction, X, is straightforward. One simply polarises the radiation such that the electric field component oscillates perpendicularly to the plane of reflection (called the transverse electric [TE] configuration). The radiation then only probes vibrations with their transition dipole moments lying in whichever sample axis happens to be perpendicular to the reflection plane. A selective sample positioning, followed by a rotation of 90° thus allows the X and Y-axes to be accessed independently. However, it is impossible to select a single sample-polariser geometry, which can probe the Z-direction independently. Instead, we have to introduce two more geometries in order to access the Z information. The four geometries are shown schematically in Figure 4-5. Note that the ATR crystal has been omitted from the diagram for ease of visualisation.

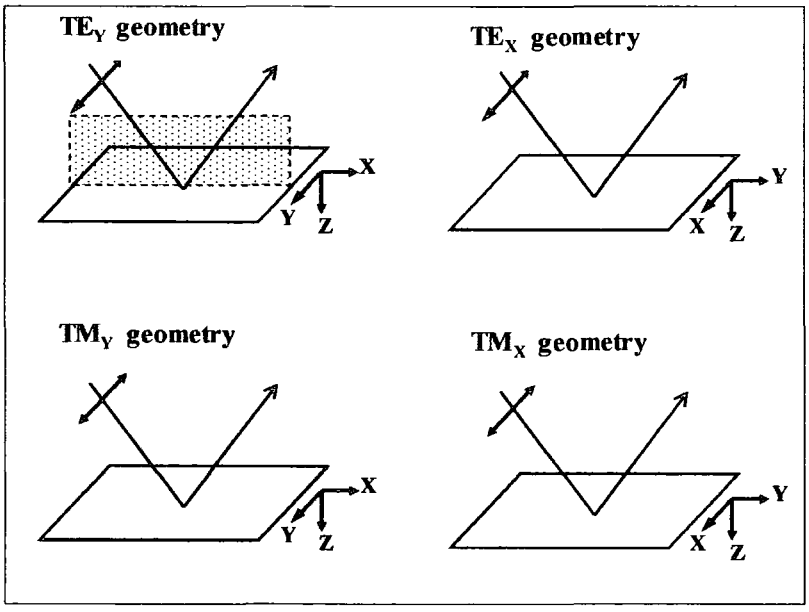

Figure 4-5: The four geometries obtainable, using an IR polariser

In Figure 4-5, the shaded box depicts the plane of incidence. When the incident radiation is polarised such that its electric vector lies in the plane of incidence (Transverse Magnetic [TM]), the sample's surface will be probed in both the direction

of propagation *and* in the thickness direction. The sample direction(s) probed by each of the geometries is given in Table 4-2.

Table 4-2: The direction(s) probed using the different sample/polariser geometries

Geometry	Direction Probed
TEY	Y only
TEX	X only
TMY	X and Z
TMX	Y and Z

Thus by considering both the TM_Y and TM_X geometries, it is possible to extrapolate the information relating to the Z direction only. The absorbance of any particular band can be expressed more formally by Equations 4-10 to 4-13.

$$A(TE_X) = \alpha_X k_X \qquad \textbf{Equation 4-10}$$

$$A(TE_Y) = \alpha_Y k_Y \qquad \textbf{Equation 4-11}$$

$$A(TM_X) = \beta_X k_Y + \gamma_X k_Z \qquad \textbf{Equation 4-12}$$

$$A(TM_Y) = \beta_Y k_Y + \gamma_Y k_Z \qquad \textbf{Equation 4-13}$$

where α, β and γ are constants that depend on the refractive indices of the polymer in the three sample directions X, Y and Z as well as quantities such as the refractive index of the ATR element and the angle of incidence used. Since polymers such as PET can have different refractive index values in different sample directions, (i.e. orientated PET is *birefringent*) the refractive index experienced by the IR radiation will depend on its polarisation direction. Hence, the subscripts added to each of the α, β and γ constants. The exact dependence of the α_X, β_X and γ_X constants on the refractive indices and the angle of incidence were derived by Flournoy and Schaffers[8] and are expressed in Equations 4-14 to 4-16.

$$\alpha_X = \frac{-4n_X^{\,2}}{n_1^{\,2}\tan\theta\left(1-\frac{n_X^{\,2}}{n_1^{\,2}\sin^2\theta}\right)^{1/2}\left(1-\frac{n_X^{\,2}}{n_1^{\,2}}\right)} \qquad \textbf{Equation 4-14}$$

$$\beta_X = \frac{-4n_Y n_Z\left[1-\frac{n_Z^{\,2}}{n_1^{\,2}\sin^2\theta}\right]}{n_1^{\,2}\tan\theta\left(1-\frac{n_Z^{\,2}}{n_1^{\,2}\sin^2\theta}\right)^{1/2}\left(1-\frac{n_Z^{\,2}}{n_1^{\,2}\sin^2\theta}+n_Y^{\,2}n_Z^{\,2}\frac{\cot^2\theta}{n_1^{\,4}}\right)} \qquad \textbf{Equation 4-15}$$

$$\gamma_X = \frac{-4n_Y n_Z}{n_1^{\,2}\tan\theta\left(1-\frac{n_Z^{\,2}}{n_1^{\,2}\sin^2\theta}\right)^{1/2}\left(1-\frac{n_Z^{\,2}}{n_1^{\,2}\sin^2\theta}+n_Y^{\,2}n_Z^{\,2}\frac{\cot^2\theta}{n_1^{\,4}}\right)} \qquad \textbf{Equation 4-16}$$

where n_i is the refractive index value of the sample in the i direction, n_1 is the refractive index of the ATR crystal and θ is the angle of incidence at the crystal-sample interface. These subscript-X expressions can be converted into subscript-Y by swapping n_Y for n_X wherever they occur in the relations above. Normalising the band of interest by the 1410 cm^{-1} band gives Equations 4-17 to 4-20

$$\frac{A(TE_X)}{A(TE_X)_{1410}} = \frac{k_X}{k} \qquad \textbf{Equation 4-17}$$

$$\frac{A(TE_Y)}{A(TE_Y)_{1410}} = \frac{k_Y}{k} \qquad \textbf{Equation 4-18}$$

$$\frac{A(TM_X)}{A(TM_X)_{1410}} = \frac{(\beta_X k_Y + \gamma_X k_Z)}{k(\beta_X + \gamma_X)} \qquad \textbf{Equation 4-19}$$

$$\frac{A(TM_Y)}{A(TM_Y)_{1410}} = \frac{(\beta_Y k_X + \gamma_Y k_Z)}{k(\beta_Y + \gamma_Y)} \qquad \textbf{Equation 4-20}$$

Here it is assumed that the attenuation index k of the 1410 cm^{-1} band is perfectly independent of the direction of measurement, and that α, β and γ are identical for the

1410 cm^{-1} and the bands to be measured. For the next stage of the theory, we need to find ways of retrieving the dichroic ratios k_X/k_Y, k_X/k_Z and k_Y/k_Z from the measured IR spectra. The first two normalised absorbance ratios, *R1* and *R2*, are given by Equations 4-21 and 4-22

$$R1 = \frac{\left[\dfrac{A(TE_Y)}{A(TE_Y)_{1410}}\right]}{\left[\dfrac{A(TE_X)}{A(TE_X)_{1410}}\right]} = \frac{k_Y}{k_X} \qquad \textbf{Equation 4-21}$$

$$R2 = \frac{\left[\dfrac{A(TM_Y)}{A(TM_Y)_{1410}}\right]}{\left[\dfrac{A(TM_X)}{A(TM_X)_{1410}}\right]} = \kappa\frac{(\beta_Y k_X + \gamma_Y k_Z)}{(\beta_X k_Y + \gamma_X k_Z)} \qquad \textbf{Equation 4-22}$$

where κ is defined in Equation 4-23.

$$\kappa = \frac{(\beta_X + \gamma_X)}{(\beta_Y + \gamma_Y)} \qquad \textbf{Equation 4-23}$$

The normalised ratio, R1, shows that we can calculate the first of the dichroic ratios k_Y/k_X straight from the raw spectra. For a biaxially orientated sample such as a PET bottle, we also need to measure k_Y/k_Z or k_X/k_Z. Manipulation of the expressions above reveals Equations 4-24 and 4-25.

$$\frac{k_X}{k_Z} = \frac{\gamma_X}{\beta_X}\cdot\frac{(R2 - \kappa C2)}{(\kappa C1 - R1\cdot R2)} \qquad \textbf{Equation 4-24}$$

$$\frac{k_Y}{k_Z} = \frac{\gamma_X}{\beta_X}\cdot\frac{R1(R2 - \kappa C2)}{(\kappa C1 - R1\cdot R2)} \qquad \textbf{Equation 4-25}$$

where Everall introduced the parameters $C1 = \beta_Y/\beta_X$ and $C2 = \gamma_Y/\gamma_X$.

However, the expressions for k_X/k_Z and k_Y/k_Z are found to be highly sensitive to spectral absorbance measurement errors, so instead, a new ratio R3 is defined in Equation 4-26.

$$R3 = \left[\frac{\dfrac{A(TM_Y)}{A(TM_Y)_{1410}}}{\dfrac{A(TE_Y)}{A(TE_Y)_{1410}}} \right] = \frac{(\beta_Y k_X + \gamma_Y k_Z)}{k_Y(\beta_Y + \gamma_Y)} \qquad \textbf{Equation 4-26}$$

$$= \frac{C3 \cdot k_X + C4 \cdot k_Z}{k_Y}$$

where $C3 = \beta_Y/(\beta_Y + \gamma_Y)$ and $C4 = \gamma_Y/(\beta_Y + \gamma_Y)$. This leads to a new expression for k_Y/k_Z that is found to be a lot less sensitive to experimental measurement uncertainties, as shown in Equation 4-27.

$$\frac{k_Y}{k_Z} = \frac{C4}{\left[R3 - \dfrac{C3}{R1} \right]} \qquad \textbf{Equation 4-27}$$

Finally, the P_{lmn} values can be calculated from the measured dichroic ratios by using the expressions formulated by Jarvis *et al.* shown as Equations 4-28 and 4-29.

$$\frac{\dfrac{2k_Y}{k_Z} - \dfrac{k_X}{k_Z} - 1}{\dfrac{k_Y}{k_Z} + \dfrac{k_X}{k_Z} + 1} = 2p_{200}(\beta)P_{200} + 4\{p_{200}(\beta) - 1\}P_{202} \qquad \textbf{Equation 4-28}$$

$$\frac{\dfrac{k_X}{k_Z} - 1}{\dfrac{k_Y}{k_Z} + \dfrac{k_X}{k_Z} + 1} = 4p_{200}(\beta)P_{220} + \frac{4}{3}\{p_{200}(\beta) - 1\}P_{222} \qquad \textbf{Equation 4-29}$$

where $p_{200}(\beta) = 0.5(3\cos^2\beta - 1)$ and β is the angle between the direction of the dipole moment and the polymer axis which will depend on the particular band of interest. In

order to calculate all four P_{lmn} coefficients, we need to measure the dichroic ratios for at least two independent bands in the spectra for which the dipole angle, β, is known. This way, we can set up the previous two equations as simultaneous equations in four unknowns and solve simultaneously to obtain P_{200}, P_{220}, P_{202} and P_{222}. For PET, it is convenient to use bands at 1019 cm^{-1} ($\beta = 20°$) and 875 cm^{-1} ($\beta = 85°$) which are well-characterised ring vibrations. The approximate forms of these vibrations, according to Jarvis[9], are given in Figure 4-6 and Figure 4-7.

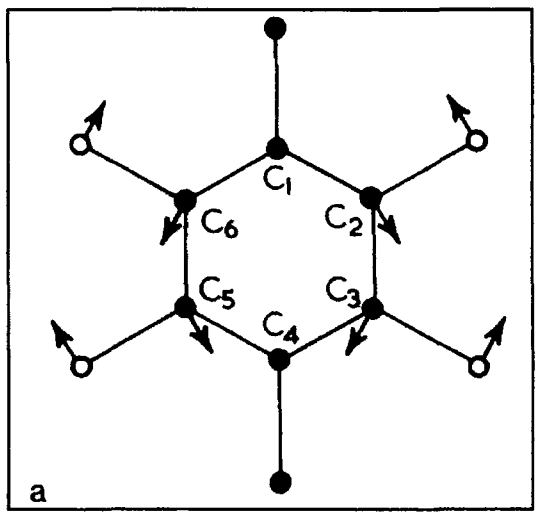

Figure 4-6: The approximate form of the IR band at 1019 cm^{-1}, where β=20°

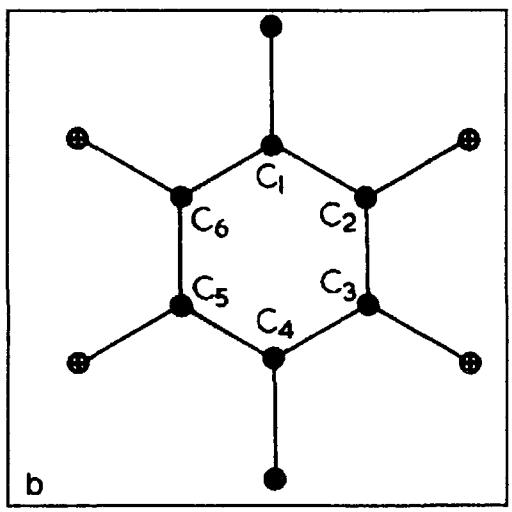

Figure 4-7: The approximate form of the IR band at 875 cm^{-1}, where β=85°

The four hydrogen atoms in Figure 4-7 simultaneously move in and out of the plane of the page.

Properties of refractive index anisotropy

After this derivation, Everall goes on to consider the suitability of this technique to birefringent samples for which the refractive index, n is calculated to vary between 1.5 and 1.7. The expressions for α, β and γ demonstrate the dependence of the final orientation values on the sample's refractive indices in each of the sample directions. However, Everall and Bibby evaluates the sensitivity of this dependency by varying the n_X, n_Y and n_Z parameters and seeing their effect on a sample set of spectra. He concluded that by altering the n_X and n_Y parameters from 1.5 to 1.7 the calculated dichroic ratios had a variation less than 1%. The refractive index in the direction perpendicular to the sample surface (Z-direction) was more sensitive and could change the ratios by 3% when using RI values between 1.5 and 1.6. However, RI measurements from drawn PET films show that n_Z yields values between 1.54 and 1.6. It was concluded that they could safely approximate $n_X = n_Y = n_Z = 1.57$ as slight variations on these values would have little effect on the computed dichroic ratios. The same approximation was used in our study.

4.3.3 Experimental procedure

4.3.3.1 Sample preparation

A permanent marker was used to mark out a strip approximately 1.5 cm wide on a line connecting the bottle top to its base, ensuring that this strip terminated at one of the bottle 'feet' as depicted in Figure 4-8. This section was carefully cut from the bottle.

The thicker region at the top of the bottle was ignored and in these discussions, the 'bottle top' refers to the thinner material from 2 cm downwards. The base of the bottle posed fewer problems on the standard bottles. Parallel guide lines were then drawn along the hoop direction of the strip at 2 cm intervals.

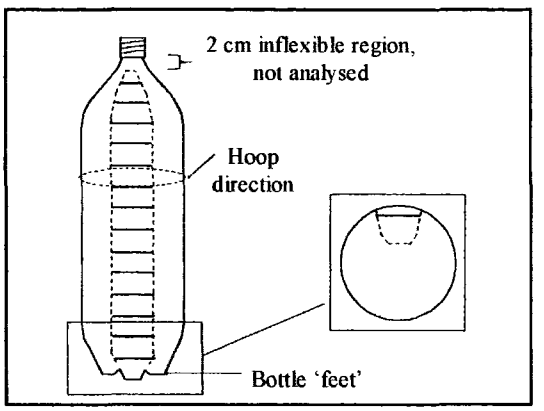

Figure 4-8: Sample strip preparation. One of the six 'feet' of the bottle was included in the strip

The modified Thunderdome ATR unit and IR polariser combination was placed in the sample chamber of the IR spectrometer and the detector was filled with liquid N_2 and left to cool for 30 to 40 minutes. After this time, the detector temperature had stabilised and two backgrounds were recorded: one with the polariser in the Transverse Electric (TE) direction, then a background after the polariser was rotated through 90° to access the Transverse Magnetic (TM) geometry. It was necessary to collect backgrounds for each of the polariser positions, as the beam was inherently polarised slightly by the spectrometer mirrors. The first area towards the neck of the bottle was clamped such that the outer wall was in contact with the crystal. The order of the collection was:

1. TE_X → Turn polariser by 90°, load TM background
2. TM_X → Unclamp sample, rotate by 90° and re-clamp
3. TM_Y → Turn polariser back 90°, load TE background
4. TE_Y → Select next sampling region and repeat steps 1, 2, 3 and 4.

This order was decided, as it requires the sample-crystal contact to be broken and re-clamped the minimal number of times, i.e. once, for each sample position. This process was repeated at every mapping point from the top to the bottom of the bottle, with fresh backgrounds recorded at the start of each group of four spectra. The whole process was repeated for the inner bottle wall of the same sample strip at the equivalent position as the outer wall.

4.3.4 Analysis techniques

The spectral analysis was performed using a Microsoft Excel spreadsheet, which enabled the calculations to be completed in a modular fashion. The three primary objectives of the spreadsheet were to:

a) Normalise the spectra by equating the absorbance values of the 1410 cm^{-1} normalisation band in each spectrum.

b) Extract the absorbencies of the 875 and 1019 cm^{-1} benzene ring vibrations.

c) Perform the calculations required to transform these absorbency values into the direction cosines that describe the chain orientation properties.

The spreadsheet format was advantageous as it allowed graphs to be easily plotted during the design stage. Not only did the graphs help calculation errors to be spotted during the development stage, but they also came in useful when considering the consequences of potential problematic scenarios such as spectral peak shifting and noisy data. In order for the FTIR data to be fed into the spreadsheet, each spectrum was saved in a text format such as a *comma-separated values* (csv) file.

The normalisation process involves measuring the magnitude of the 1410 cm^{-1} normalisation band and multiplying every point in that spectra by the factor required to

make the magnitude of the 1410 cm^{-1} peak equal to a pre-defined value. Throughout the spreadsheet, measuring the magnitude of an absorbance peak involves fitting a suitable baseline to the area of the spectrum under investigation and measuring the maximum height of the peak above the baseline. This *close-baseline* technique (also known as pseudo baseline[11]) is used not only for normalisation purposes but also for other peak measurements. For completeness, the derivation of the equation used to calculate the baseline in Excel is included, as it was a particularly useful tool in the analysis.

4.3.4.1 Baseline calculation

A model data set containing two peaks of interest is shown in Figure 4-9. The data points require a sloping baseline in order for reliable heights, H_1 and H_2, to be measured.

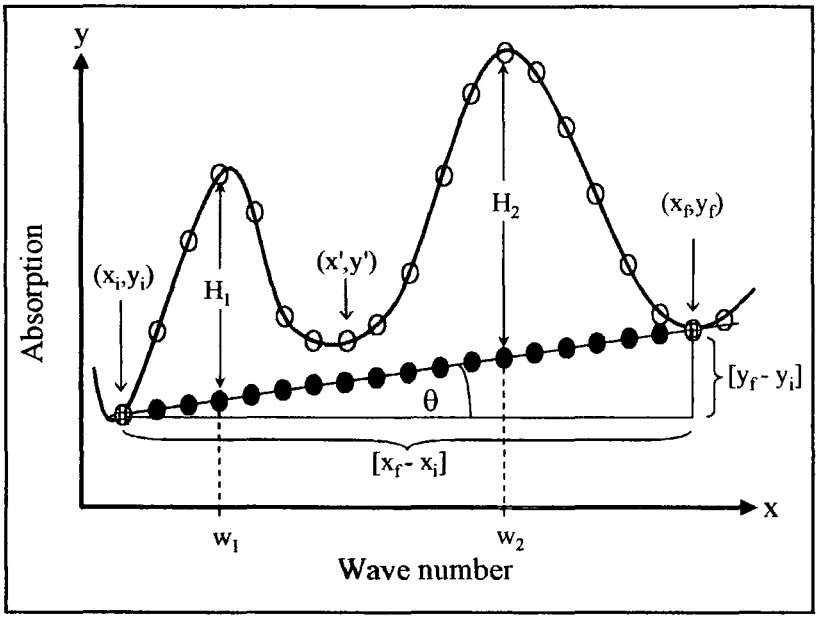

Figure 4-9: A model data-set containing two peaks and a close baseline

The aim of the spreadsheet baseline calculation is to produce a baseline point (black circle) for every data point (hollow circle) in the spectral range under investigation. The baseline points will effectively lie on a line connecting two localised minima either side

of the range. For an arbitrary data point in the range of interest (x', y'), the height, h, of the equivalent baseline point above the lowest baseline point, y_i, is given by Equation 4-30.

$$h = (x'\text{-}x_i)\tan\theta \qquad \textbf{Equation 4-30}$$

Using the known values at the peak troughs, trigonometry reveals Equation 4-31.

$$\tan\theta = \frac{y_f - y_i}{x_f - x_i} \qquad \textbf{Equation 4-31}$$

Therefore, the expression needed to generate the baseline B is Equation 4-32.

$$B = y_i + \left[\left(\frac{y_f - y_i}{x_f - x_i}\right)(x'\text{-}x_i)\right] \qquad \textbf{Equation 4-32}$$

Selecting the most suitable points for the initial and final baseline anchor positions needed some careful consideration. The only way to allow large numbers of spectra to be processed using the same spreadsheet is to nominate the same points in every spectrum of the series. Spectral examples taken from highly orientated, crystalline and largely amorphous PET samples were carefully observed to ensure the proposed trough positions did not change considerably as a function of variables such as the amount of orientation and crystallinity. The averaged squared direction cosine (ASDC) orientation parameters rely on peak-height measurements at 1019 cm^{-1} and 875 cm^{-1} that are assigned to different modes of benzene ring vibrations[9]. It was observed that the 875 cm^{-1} band required special treatment. Below 830 cm^{-1}, the germanium element becomes optically thick which manifests itself as the onset of noise in the IR spectra, affecting the low energy tail of the 875 cm^{-1} peak, as shown in Figure 4-10.

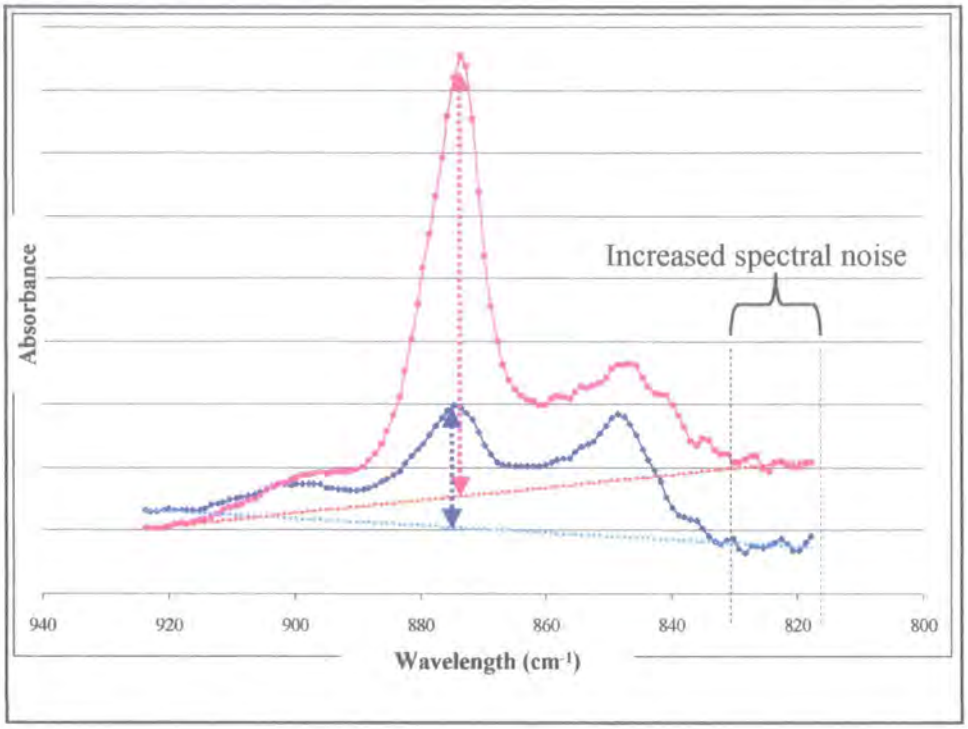

Figure 4-10: The increased spectral noise at the low energy end of the IR spectra

To overcome this problem, the baseline equation was modified such that it included an *averaged* low-energy tail anchor point. This is achieved by replacing the y_f parameter with an average absorbance value as expressed in Equation 4-33

$$y_f = \frac{y_1 + y_2 + y_3 + \ldots + y_n}{n} \qquad \textbf{Equation 4-33}$$

where y_1 to y_n are neighbouring points around the region of the ideal low-energy anchor position. The number of averaged points, n, found to give the most reliable results varied between 8 and 10.

It was observed that the exact position of the peak maximum could be slightly different in each spectrum of the series. To be sure of measuring the correct height, the absorbencies above the close baseline were measured for a few points either side of the literature peak positions, and the maximum of these values was used as the peak height.

4.3.4.2 A note on the errors associated with this FTIR-ATR technique

The normalisation procedure using the well-characterised 1410 cm^{-1} band has been claimed to remove the variability of absorbency associated with changes in the sample/IRE contact[10]. The intimacy of the contact will inevitably change as the sample is re-clamped to access all four experimental geometries. This assumption was tested by repeatedly re-clamping the same region of a stretched PET film (Homopolymer, 3.75 draw ratio) onto the ATR accessory (arbitrarily in the TE_Y geometry) and collecting a spectrum with each new sample/crystal contact. The results of ten different trials of clamping this film onto the ATR crystal are presented in Figure 4-11. The spectra are shown not to change significantly during this re-clamping procedure. Experimentally, the addition of the simple X-Y Sample angle dial on the modified ATR accessory (see Figure 4-3) also minimises the likelihood of misaligning the sample when clamping it onto the crystal. Any misalignment of drawn PET films would inevitably show up in the IR spectra as a change in the bands sensitive to changes in orientation.

The biggest source of error in the ASDC values is likely to be the assignment of the close base lines and the effect this has on the measured absorbance values. It was found that by measuring absorbance heights using a range of sensible baseline assignments, the calculated ASDC values changed by a maximum of 6 %. However, in the original work, Everall *et al.*[5] did not attempt to quantify the errors associated with this technique. Everall noted systematic differences (particularly at low draw ratios) for the orientation parameters computed using this FTIR-ATR method and those calculated using other techniques, concluding that;

"Further work is needed to identify the exact cause of the discrepancies. For this reason, at present the method should perhaps be utilized primarily for comparing orientation between samples rather than for computing absolute orientation parameters."

Therefore, the ASDC graphs should be read in terms of the relative orientation trends along the bottle walls, rather than considering the absolute ASDC values. However the excellent agreement to within 3 % that we have found between all our PET film ASDC values calculated from the FTIR-ATR and bulk X-ray diffraction techniques (presented in Chapter 6) make us confident that the bottle FTIR-ATR ASDC values have a similar high degree of accuracy.

Everall *et al.*[12] performed the same type of polarised FTIR-ATR measurements on PET films, and noted that the measurements were extremely reproducible. Five duplicate measurements on the same sample revealed ASDC measurements of 95 % confidence. Although the same *duplicate measurement* treatment was not employed in our study, the reproducibility of the IR spectra when the sample is re-clamped (see Figure 4-11) suggests that our system would reveal a similar degree of ASDC measurement reproducibility. No bottle was mapped more than once in this study, largely due time restrictions as each mapping requires the collection of 180 IR spectra and backgrounds.

The maximum measurement error for all the FTIR ASDC values presented in this thesis is 0.06, as suggested by the maximum 6 % variation in ASDC values resulting from different baselines assignments, as mentioned above. From the re-clamping trials, the height of the 1340 cm^{-1} band was found to vary by a maximum of 1.8 % (0.002

absorbance units as presented in the '1340 cm^{-1} height' curves of this thesis, where the 1410 cm^{-1} band height in each spectrum has been scaled to 0.05 absorbance units).

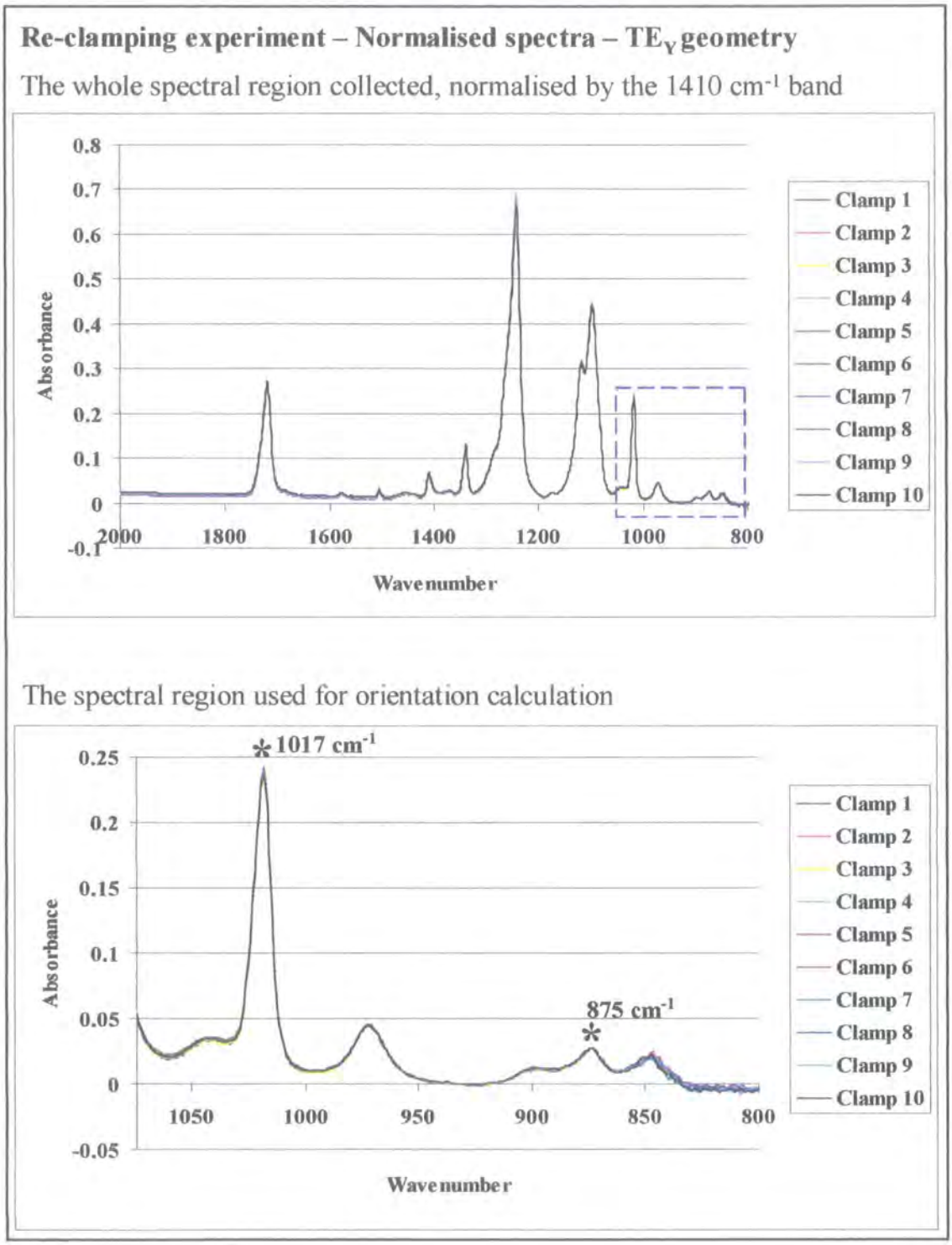

Figure 4-11: Trials showing how the same sample region can be repeatedly clamped onto the ATR accessory to reveal consistent spectra, after normalisation by the 1410 cm^{-1} band.

4.3.4.3 Testing the spreadsheet using samples with predictable morphologies

Before the finished spreadsheet was used to calculate the orientation of industrially produced films and bottles, it was first tested by applying it to calibration samples with predictable morphologies.

Calibration case 1: Drawn PET fibres

Rudimentary PET fibres were made by dipping a spatula into the melt and lifting it out at a uniform speed. Further orientation was achieved by drawing the fibres at ambient temperature. A bundle of the drawn PET fibres had to be used, as single fibres were too thin for useful spectra to be obtained using the ATR crystal. The sample coordinates were easy to assign as there was a clear primary draw direction Y along the fibre axis. The transverse draw direction X thus lies around the circumference of the bundle and Z is the direction into the centre of the bundle. For fibres, it is expected that the majority of the chains will be oriented along the Y (fibre) direction. The distribution of the remaining chains between the X and Z directions is more difficult to predict.

The experimental results show that for these PET fibres,

- $\langle \cos^2(yX) \rangle = 0.17$
- $\langle \cos^2(yY) \rangle = 0.73$
- $\langle \cos^2(yZ) \rangle = 0.10$

These results are consistent with those predicted. The spreadsheet reports that the majority of the chains are in the fibre axis direction, Y. For these fibres, it appears that there are more chains directed around the circumference of the fibres than normal to the fibre surface. This result alone is not enough to give confidence that the spreadsheet is

giving correct orientation values for the X and Z directions. Another sample had to be made, which had predictable orientation properties in a different direction.

Calibration case 2: Lamellae mats

The synthesis of the mats involves preparing dilute solutions of PET in solvent (in this case 5% w:w pure PET chip IV0.62 in dichloroacetic acid). Water, a non-solvent, is then added and the solution is heated for several hours on a hot plate. This treatment produces single chain-folded lamellae crystals. The crystal suspension is then filtered leaving the sedimented lamellae crystals on the filter paper. The paper is then left to dry under vacuum to reveal the lamellae crystals as a waxy residue on the filter paper. The resulting plate-like chain-folded lamellae crystals are expected to lie flat on the filter paper as shown in Figure 4-12, especially when clamped to the ATR crystal.

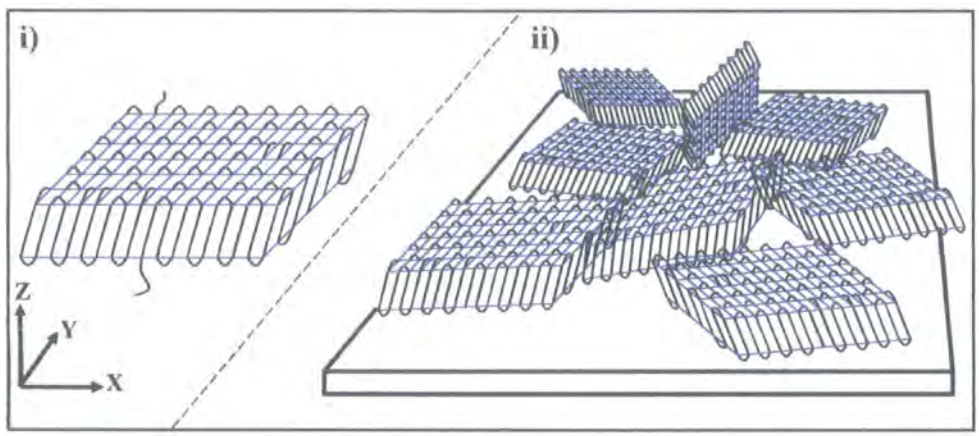

Figure 4-12: i) a singe chain folded lamellae PET crystal and ii) how collections of lamellae are expected to lie on a flat surface

When handling this sample, there is no way of nominating a 'primary draw direction', Y and a transverse direction X, as we expect there to be no preferential orientation between the two. Experimentally, the mat was just placed on the ATR crystal for the first two polarisations and then simply turned through 90° for the latter two. This would

show up any inconsistencies between the arbitrarily nominated X and Y directions. The nature of the chain folding dictate that we would expect to see the majority of the chains to be pointing into the Z-direction and the numbers of chains in the X and Y directions to be lower and similar to each other. The lamellae mats ASDCs are:

- $\langle\cos^2(yX)\rangle = 0.18$
- $\langle\cos^2(yY)\rangle = 0.18$
- $\langle\cos^2(yZ)\rangle = 0.64$

The direction cosines in the X and Y directions have identical values, which is a very pleasing result. The angle between the chain axes in the lamellae and the vertical Z-axis is 35.81° (see Appendix 1). So for perfectly aligned lamellae, the expected Z-ASDC is $\cos^2(35.81)$ which results in a value of ~0.657. This value is in close agreement with the measured value of 0.64. Hence, I was confident that there were no errors in the spreadsheet, which was then used to map the orientation along PET bottles.

4.3.5 Detailed analysis and results for a standard 2l PET bottle

This section covers the orientation results for *Bht-i*: a standard laser+ bottle (containing 2% IPA), blown after heating the preform for the standard heating time. The analysis here will be in more detail than for the other bottles and each stage of the automated analysis will be demonstrated. The following examples are for the first position towards the bottle top on the outer bottle surface. Exactly the same procedure occurs for all 30 sampling positions (15 for both the inner and outer walls) on each bottle.

The four raw spectra corresponding to the different polariser and sample orientations are shown in Figure 4-13. Towards the centre of these spectra is the 1410 cm^{-1} band needed for normalisation, this spectral region is magnified in Figure 4-14. The height of this 1410 cm^{-1} band in each spectrum is made equal by first fitting the baseline as

demonstrated in Figure 4-15 for the TE_X and TM_X examples only. Multiplication of each point in the spectra so that the 1410 cm^{-1} peak height equals the arbitrary value of 0.05 absorbance units reveals the normalised spectra shown in Figure 4-16. Figure 4-17 shows the normalised spectra when the foot of the 1410 cm^{-1} peak is adjusted to a value of zero so that the magnitude of the 1340 cm^{-1} band can be compared in each spectrum. To find the absorbance of the 875 cm^{-1} band, a baseline is then fitted to the 875 cm^{-1} region as shown for the TE_X and TM_X geometries in Figure 4-18. The height above the baseline for this spectral region gives the required absorbance value, as shown for all four experimental geometries in Figure 4-19. The same treatment is applied to the 1017 cm^{-1} region, as shown in Figure 4-20 and Figure 4-21. The heights of these two bands above the baseline from the normalised spectra are then fed into the equations at the end of the sheet to determine the orientation parameters, i.e. the average squared direction cosine (ASDC) values.

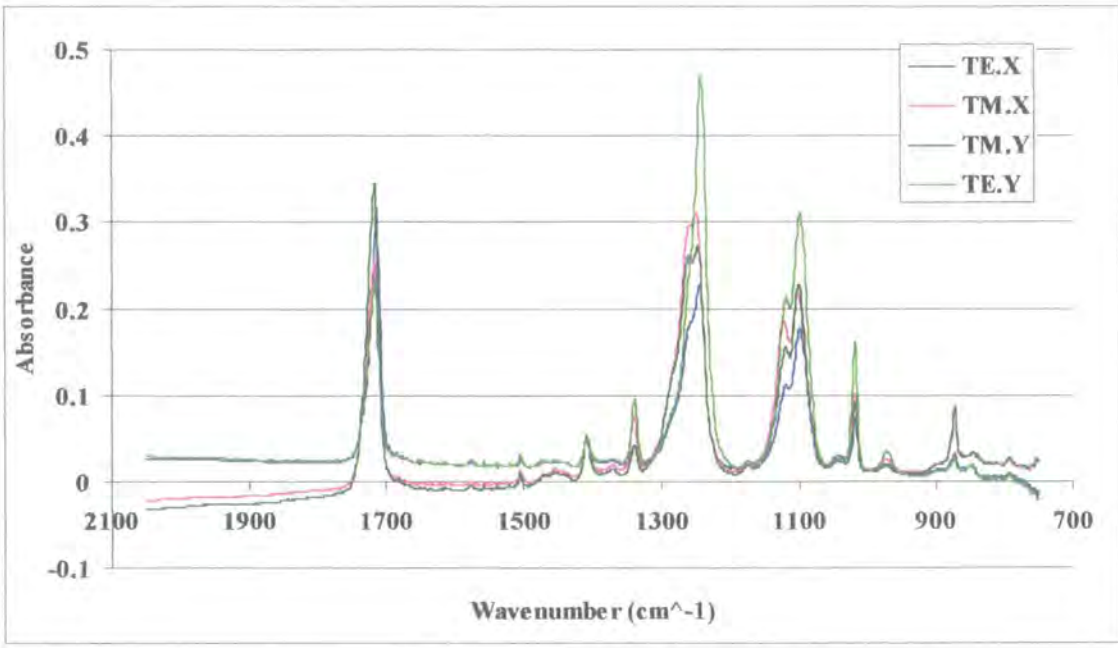

Figure 4-13: The four FTIR-ATR spectra needed to calculate the orientation parameters where TE.X denotes TE_X, TM.X denotes TM_X etc.

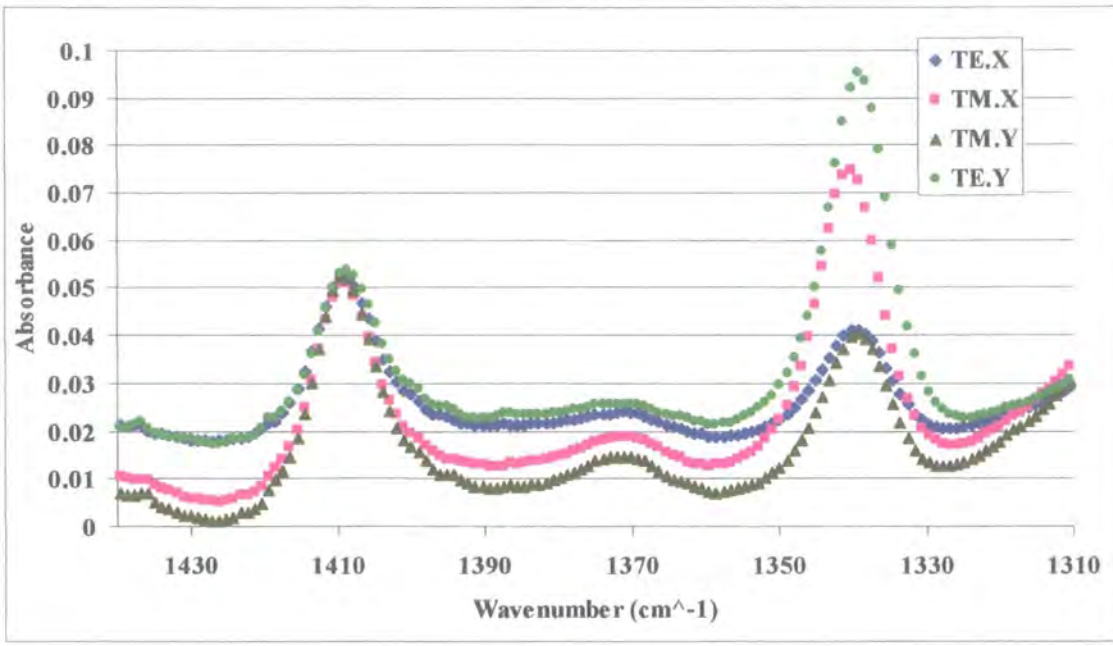

Figure 4-14: A close-up on the un-normalised 1410 cm^{-1} and 1370 cm^{-1} bands

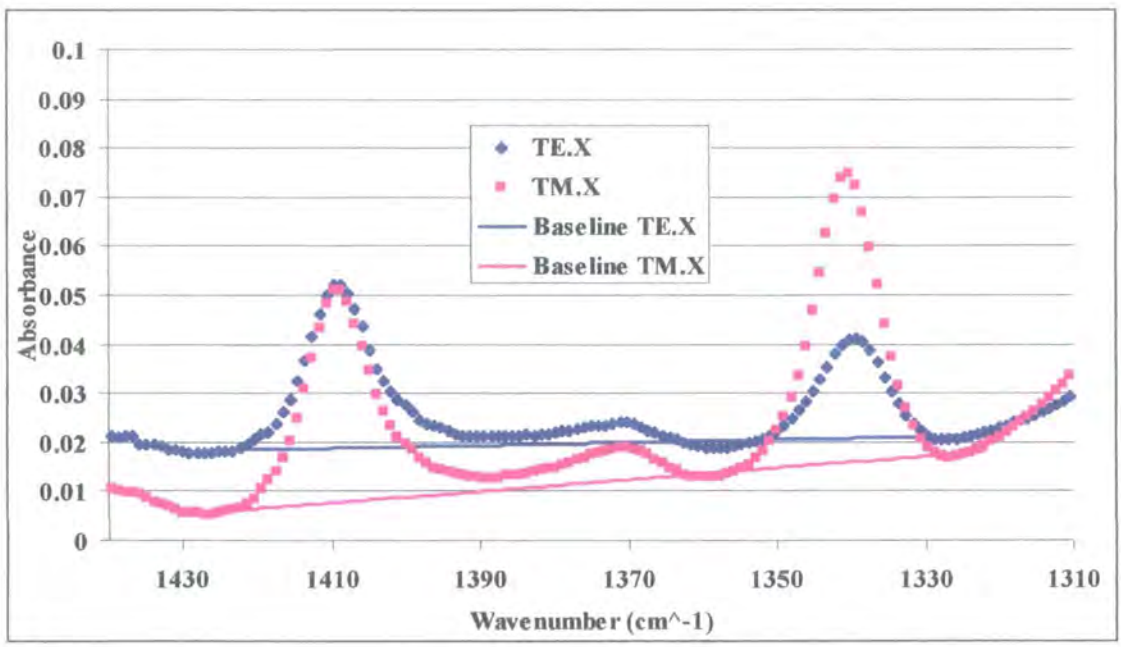

Figure 4-15: Close baselines fitted to the 1410 cm^{-1} and 1370 cm^{-1} region (only TE_X and TM_X shown).

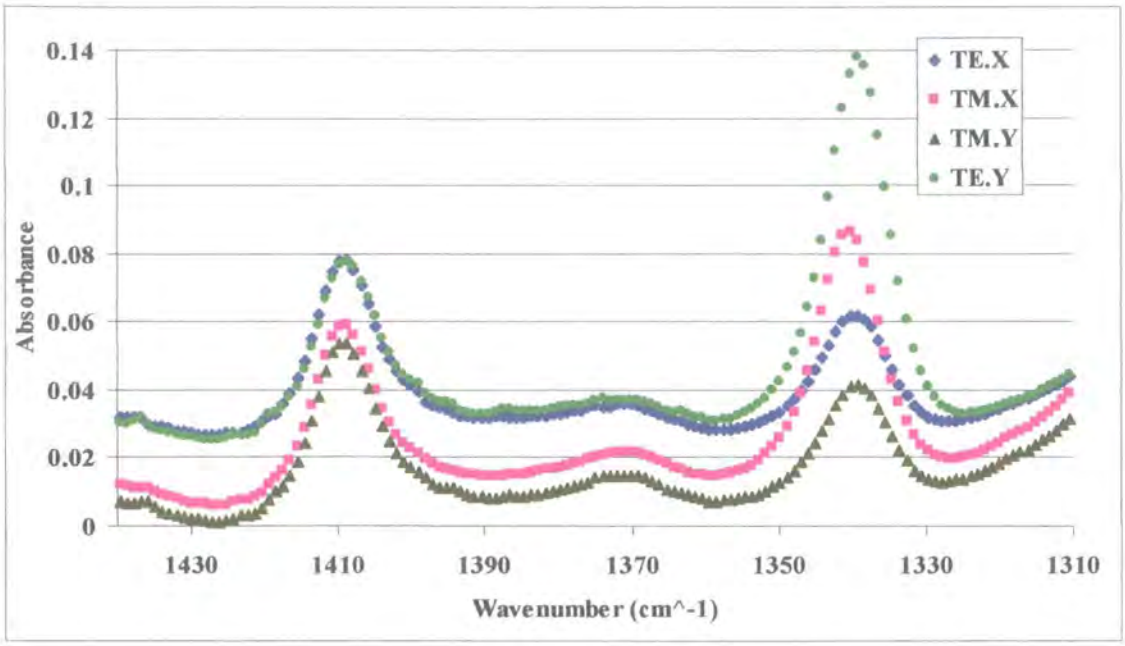

Figure 4-16: The normalised spectra for all four sampling geometries. The height of the 1410 cm^{-1} band measured above the close baseline is 0.05 arbitrary units in each case.

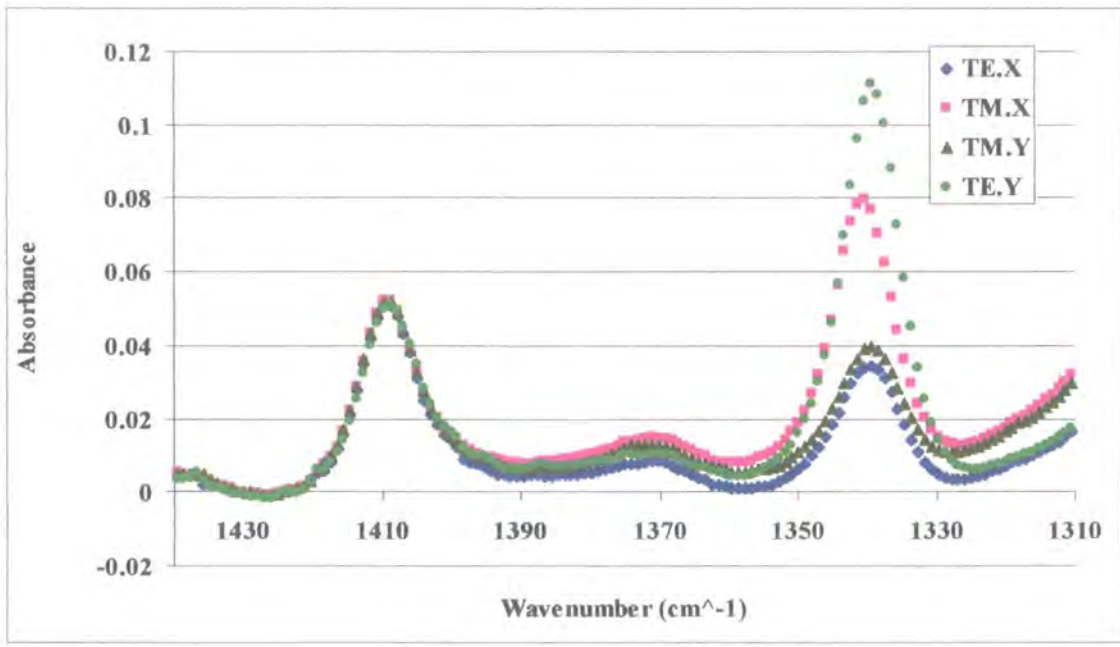

Figure 4-17: The same spectra shown in Figure 4-16 shifted such that the 1410 cm^{-1} tail is at zero absorbance. The heights of the neighbouring 1340 cm^{-1} band can now be compared.

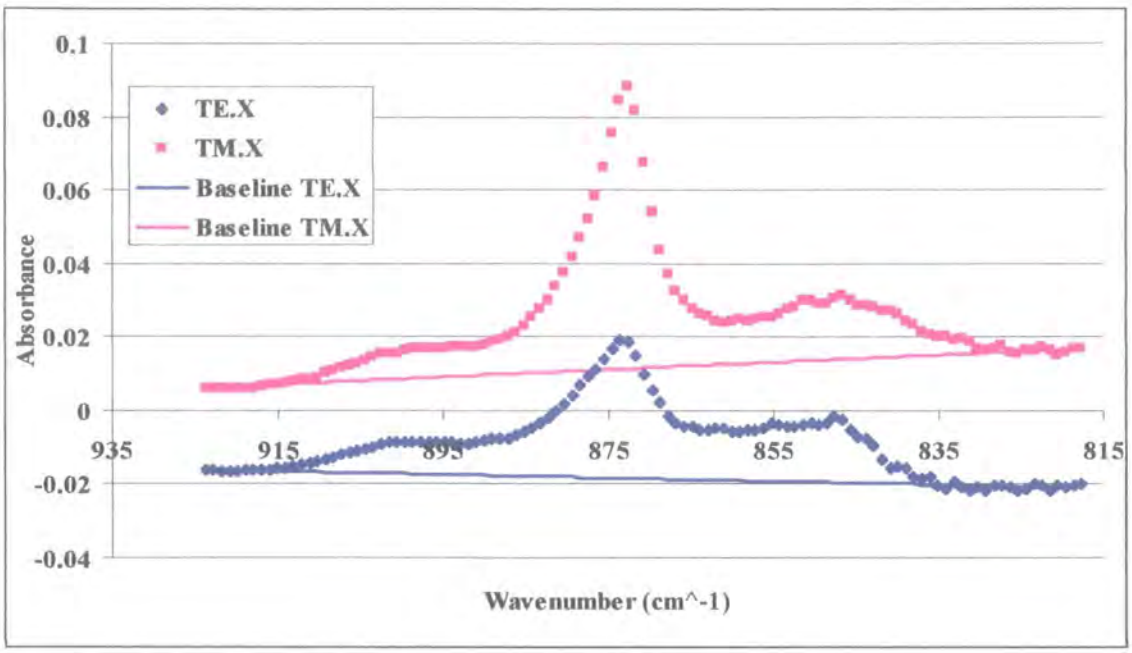

Figure 4-18: Baselines fitted to the 875 cm^{-1} band needed for orientation calculations

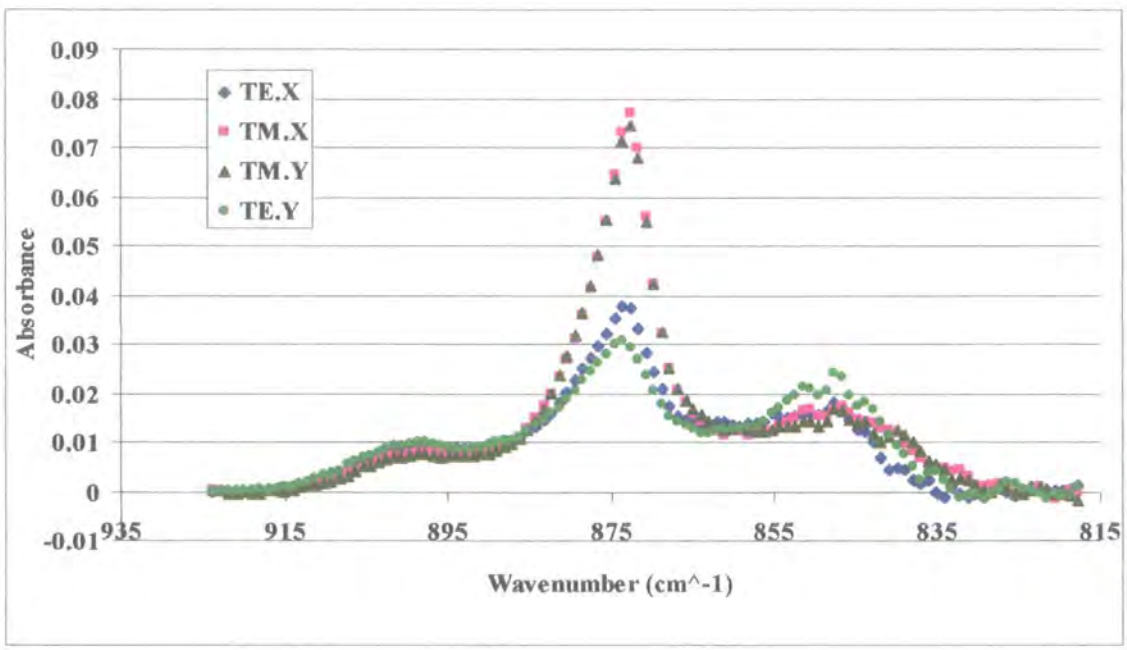

Figure 4-19: The height above the baseline for the 875 cm^{-1} region for all four experimental geometries. Note the increased spectral noise at the low energy wavenumbers.

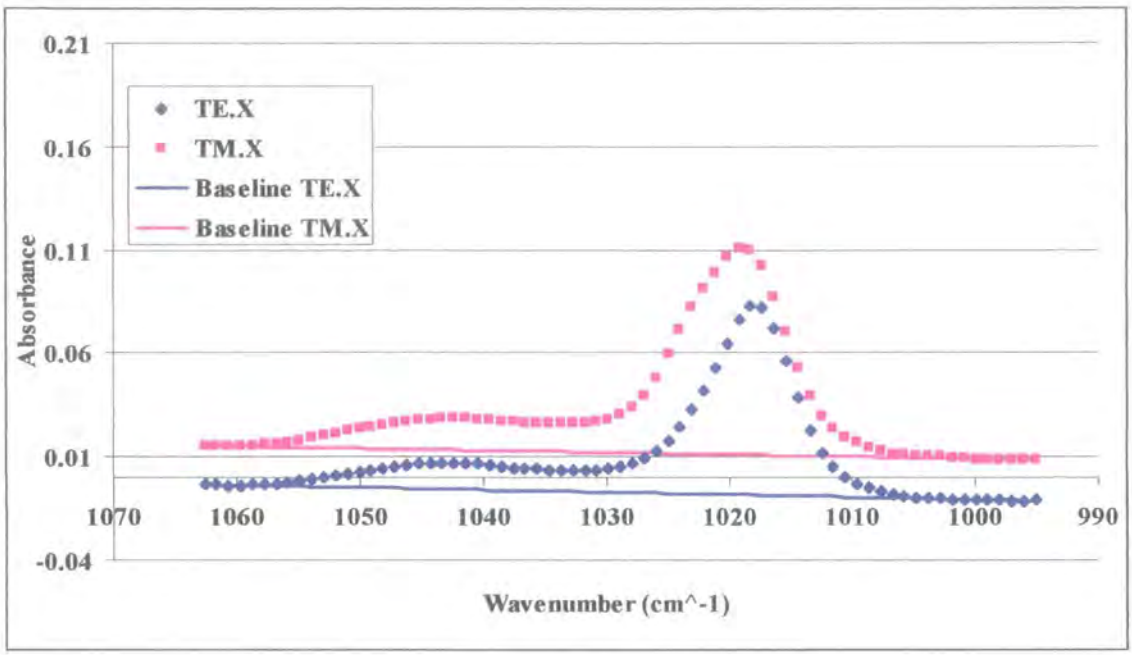

Figure 4-20: Baselines fitted to the 1017 cm^{-1} band needed for orientation calculations

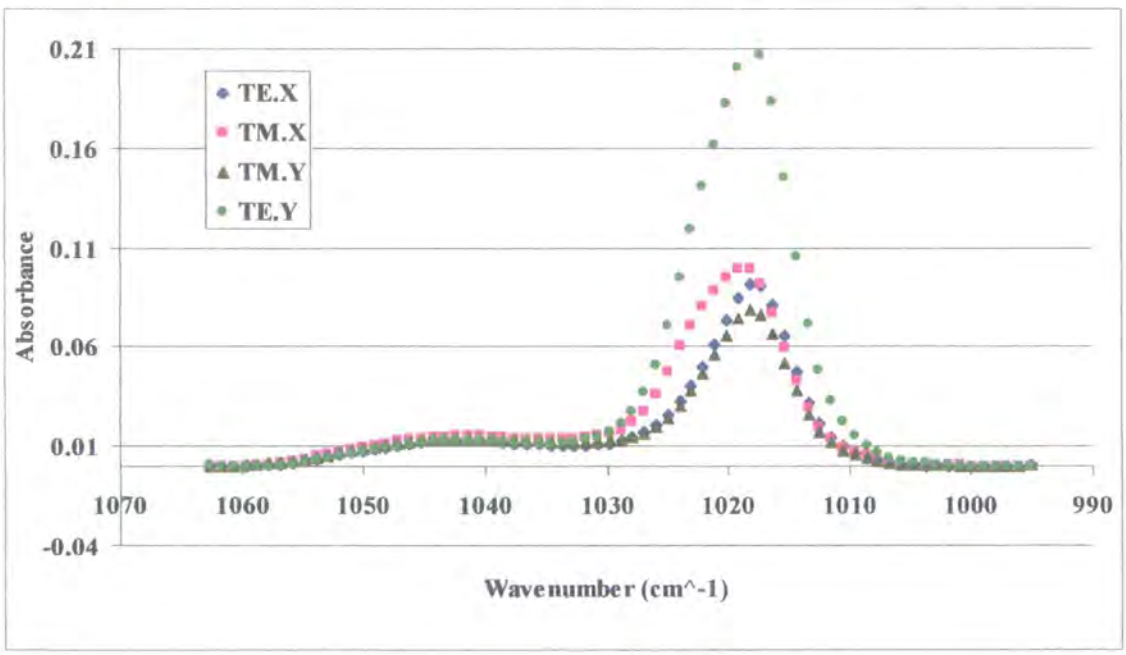

Figure 4-21: The height above the baseline for the 1017 cm^{-1} region for all four experimental geometries

Using these absorbance measurements, the orientation was mapped at 2 cm intervals as indicated in Figure 4-22, which also shows the X Y Z sample directions for different

positions probed along the bottle, and the thicknesses of the bottle wall, measured using a micrometer.

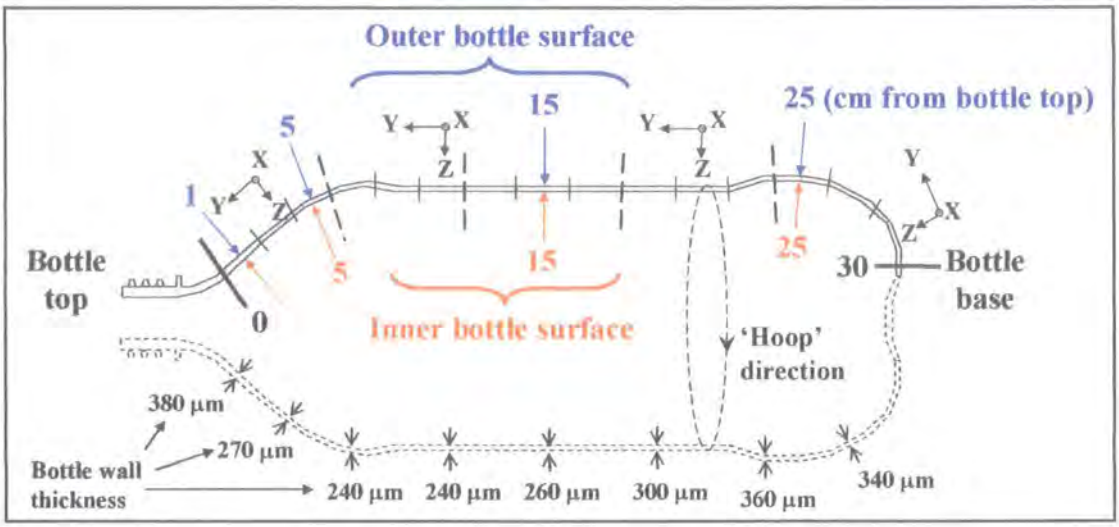

Figure 4-22: Relating the X, Y, Z sample directions to the positions probed on the bottle. Note that the bottle wall thickness (240 μm) is much greater than the ATR sampling depth (0.5 μm), which allows the orientation along the inner and outer bottle surfaces to mapped independently.

In displaying the orientation results for each bottle, two figures are presented, which correspond to the outer and inner bottle surfaces. Each figure contains two graphs. The upper graph in each case shows the calculated average squared direction cosines (ASDCs), which describe the proportion of chains lying in the X, Y and Z sample directions (see Figure 4-22). The lower graphs show a simple height measurement of the 1340 cm^{-1} CH_2 wagging mode of the *trans* ethylene glycol conformer. For these measurements, the *X-* and *Y-ONLY* 1340 cm^{-1} heights were taken from the spectra, corresponding to the TE_X and TE_Y geometries, respectively. Hence, the peak height relates to the number of *trans* chains pointing in the direction indicated by the subscript. For each figure, the 1340 cm^{-1} heights can be compared to the X and Y-ASDCs to see if there is any correlation between the two.

4.3.5.1 Orientation results for a standard 2l PET bottle

The FTIR-ATR surface orientation results for a standard bottle are presented in Figure 4-23 and Figure 4-24.

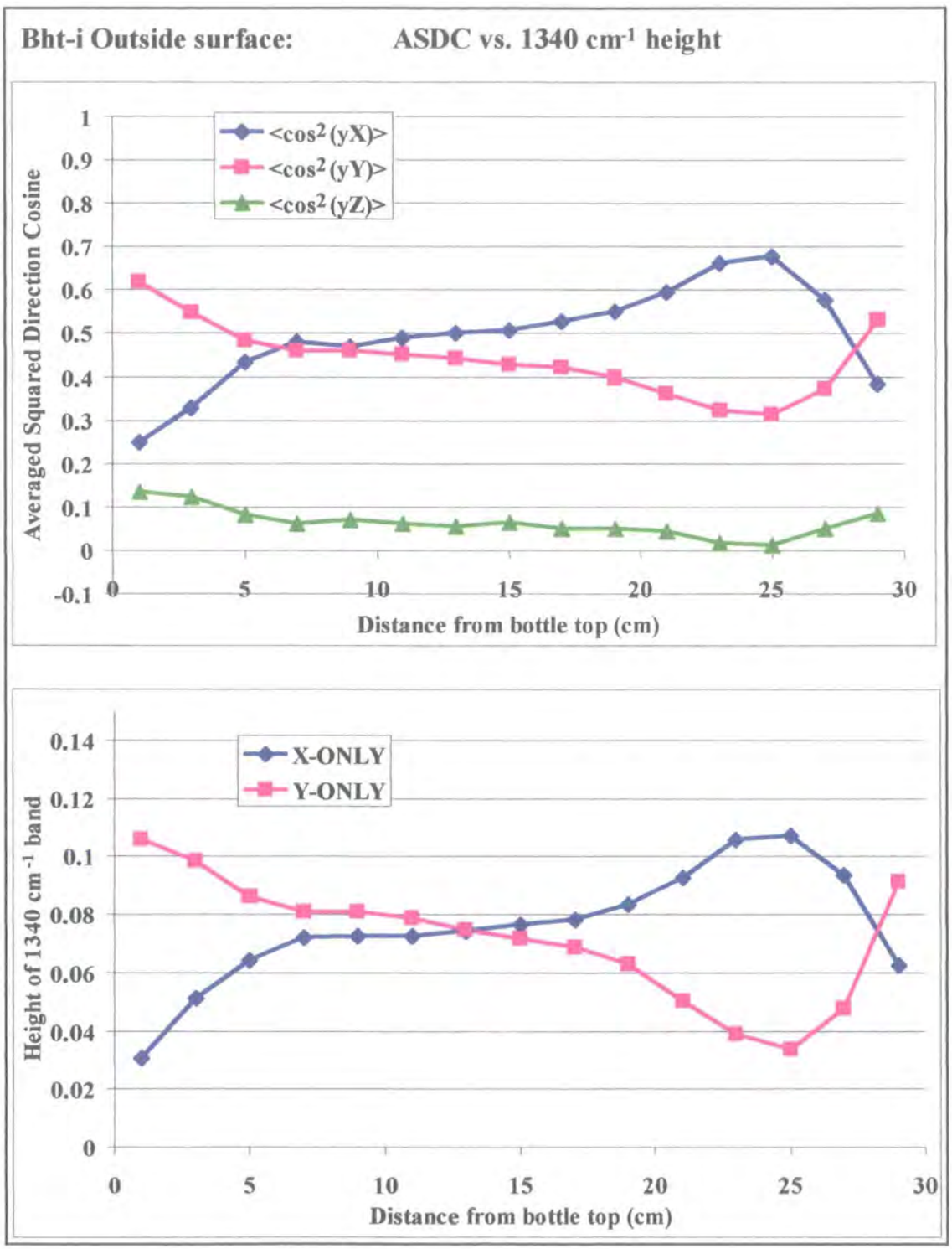

Figure 4-23: Orientation results for a standard PET bottle - outer wall

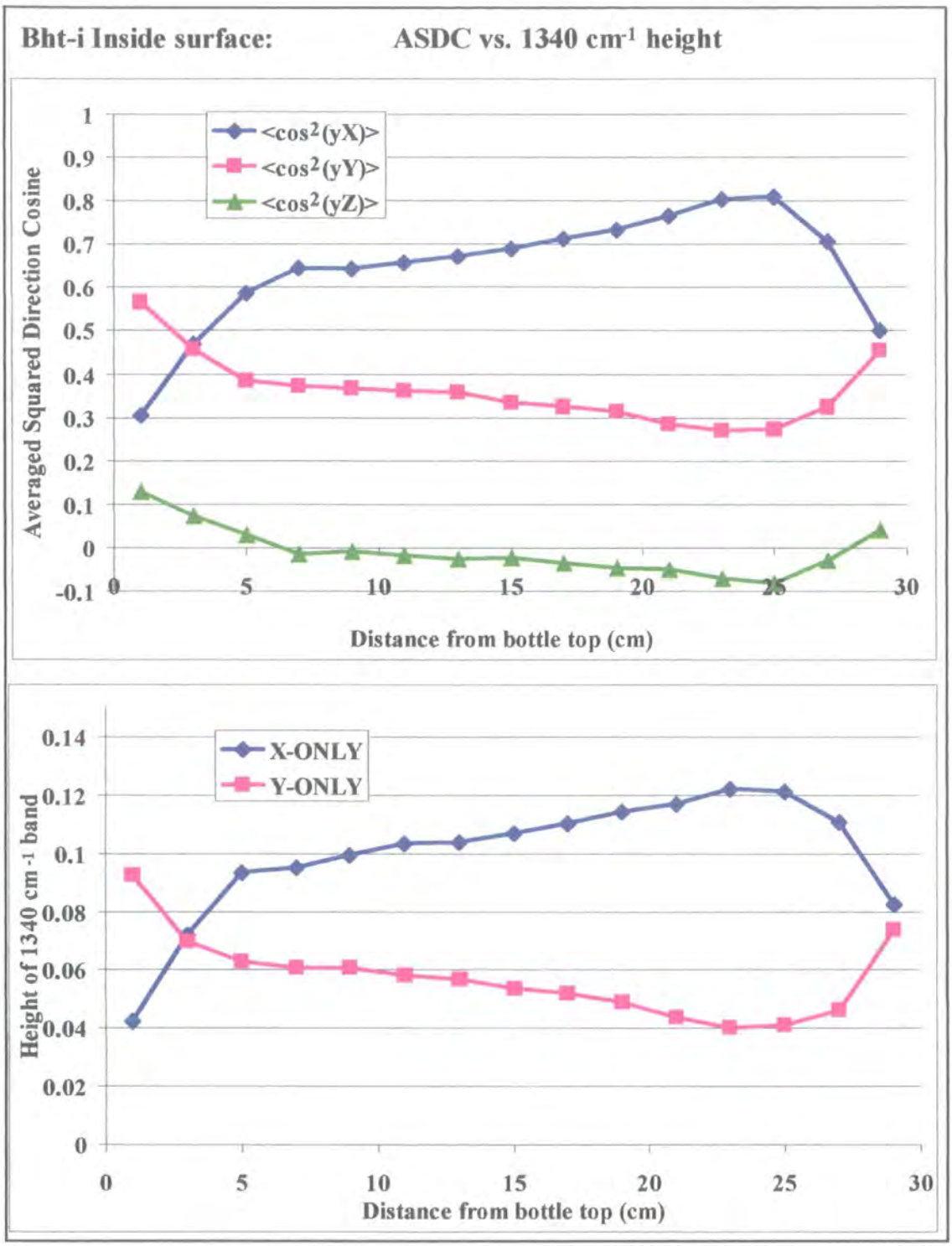

Figure 4-24: Orientation results for a standard PET bottle - inner wall

Looking at the outside wall (Figure 4-23) at the first position probed near the neck of the bottle, the Y-ASDC dominates. As we move over the shoulder of the bottle, the

proportion of chains lying in the Y, bottle length, direction decrease at the same rate that the X-ASDC, hoop orientation, begins to increase. Although the Z-ASDC decreases slightly, it undergoes less of a change than the other directions. As we might expect from biaxially oriented polymer, the chains preferentially lie in the two primary draw directions, X and Y. So to the first order, any loss of chains from the Y direction is counteracted by an equal growth of chains in the X direction and vice-versa. At a distance of 7 cm from the bottle top, the X and Y ASDC values are similar, which suggests that equal proportions of chains lie in these directions. Probing further down the bottle wall reveals that the number of chains in the X direction begins to dominate, resulting in an outer-wall orientation maximum in the hoop direction at 25 cm from the bottle top. The base region shows a downturn in the X-ASDC to the last sampling region under the foot of the bottle, where the number of chains in the X and Y directions are roughly equal.

The inner wall of the bottle (Figure 4-24) shows somewhat different orientation trends. At 1 cm from the bottle top, the number of chains in the Y direction dominates in a similar fashion to the outside wall. However, the switch between predominantly Y-direction chains to predominantly X-direction chains occurs much higher up the bottle at 3 cm from the bottle top. The number of chains in the X, hoop direction, then dominates for the rest of the bottle except for the base of the bottle, where the Y and X-ASDCs become approximately equal.

The simple height measurements of the 1340 cm^{-1} band mimics the more thorough ASDC approach of Everall[5] surprisingly closely. This band will be followed for the subsequent bottles in order to establish how robust the use of this band is to map orientation trends.

The orientation results for a standard PET bottle are summarised in Figure 4-25.

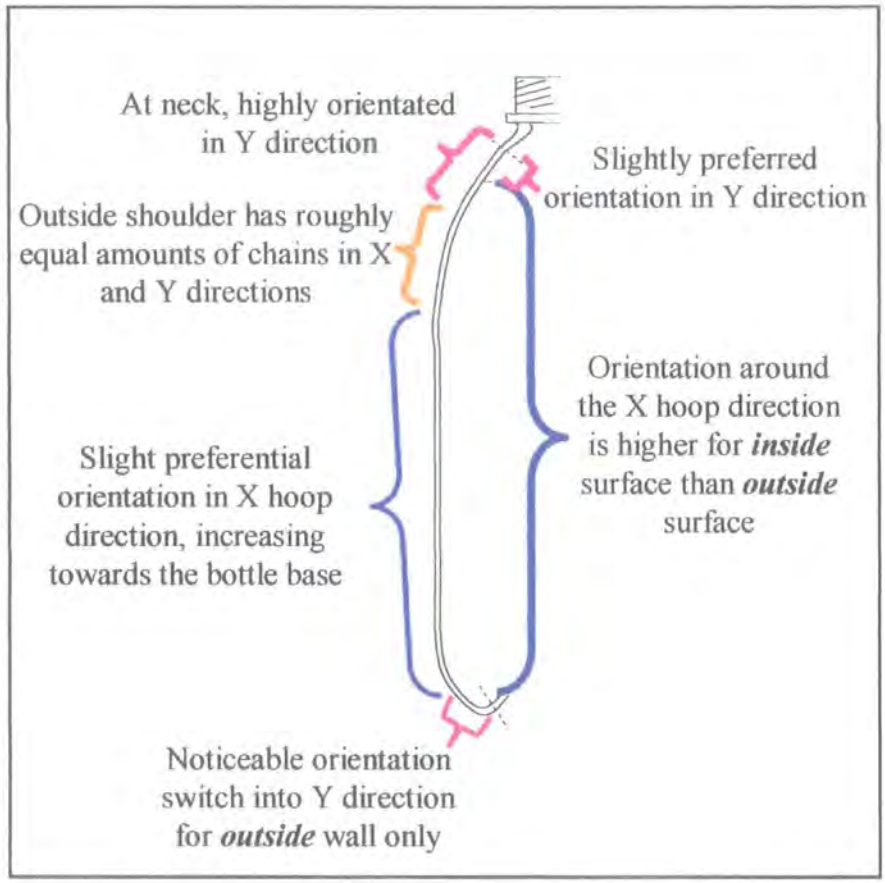

Figure 4-25: A simple graphic showing the general orientation trend of the outer and inner surface of stretch-blown PET bottles as determined by this work

The observation that the inner surface possesses higher levels of orientation can be accounted for by the fact that the inner wall suffers a larger hoop extension than the outer wall. It has previously been calculated that typical hoop extensions for a 2l bottle are around 5 and 4 draw ratio for the inner and outer walls respectively[12]. This can be seen by considering the dimensions of the preform and final bottle, indicated in Figure 3-7 in the materials chapter. There is a relatively good correlation between the extension of the preform in the length and hoop directions and this explains why the outline of the X and Y-ASDC curves roughly mimics the 2l bottle shape.

For the most highly oriented regions of the inner wall, the Z-ASDC values become very slightly negative. This is non-physical and could be due to the following reasons. In the initial work, this technique was applied to PET films drawn to a maximum of 3.5 draw ratio[5]. The inner wall hoop extension is thought to be at least 5 draw ratio, which is a 43 % increase above the maximum draw previously analysed. The 1410 cm^{-1} normalisation band has only been tested on films up to draw ratio 4. Normalisation failures at higher draw ratios would inevitably influence the orientation calculation. Another possible explanation of the slight negative Z-ASDC values is that slightly inaccurate baselines on the normalisation and absorbance measurements could give rise to perturbed orientation values, as could the measurement of band heights instead of areas to give the required absorbance values. Whatever the reason for the perturbed ASDC values at the highest draw ratios, the technique can still be used to compare the *relative* orientation values for each region of the bottle while being cautious of the absolute ASDC values. Once the surface orientation of a standard bottle had been mapped, the same spreadsheet was applied to the other bottles listed at the start of section 4.3.

4.3.6 Results for the Bht (bottle heating times) series

This section describes the orientation results for a series of eight bottles, which have been stretch-blown after various preform heating times. The times range from the ideal preform heating time (t) minus 20 seconds (Bht-20), to t plus 15 seconds (Bht+15) in 5 second increments. A photograph of the bottles is provided in Figure 4-26. The orientation results are presented in Figure 4-27 to Figure 4-42.

It was not possible to blow adequate bottles outside of this heating time range. Please note that the preforms in this series were taken from the same batch. This eliminates the

problem of anomalies due to slight variations in resin molecular weights and IPA contents. The actual preform heating time is omitted from this thesis, but it is close to 1 minute.

Figure 4-26: A photograph of the Bht series of 2l PET bottles

4.3.6.1 Observations of the optical clarity in the Bht series

The photograph of the Bht bottles (Figure 4-26) reveals two types of optical clarity deterioration that will be briefly discussed. The Bht+15 bottle shows excess crystallinity, which formed in the preform prior to the stretch, with the crystalline regions remaining at the neck, and base regions that have undergone less of a stretch. The pearl-like clouding observed in the Bht-20 to Bht-10 bottles is more difficult to account for. This effect was reproduced by cold drawing PET strips on an Instron stretching machine. Drawing at slow rates (10-20 mm/min) produced a transparent film of draw ratio 4. However, when the draw speed was increased, the films would become highly opaque in the drawn regions in a way that matched the walls of the Bht-20 bottle. When clamping the opaque Bht-20 specimens to the ATR element, the clamped regions became transparent once more. This suggests this opaqueness could be attributed to the formation of tiny air bubbles of the dimensions that promote light scattering, introduced

due to the cooler preform being unable to stretch quickly enough under high draw ratios. This hypothesis could be tested in a subsequent study.

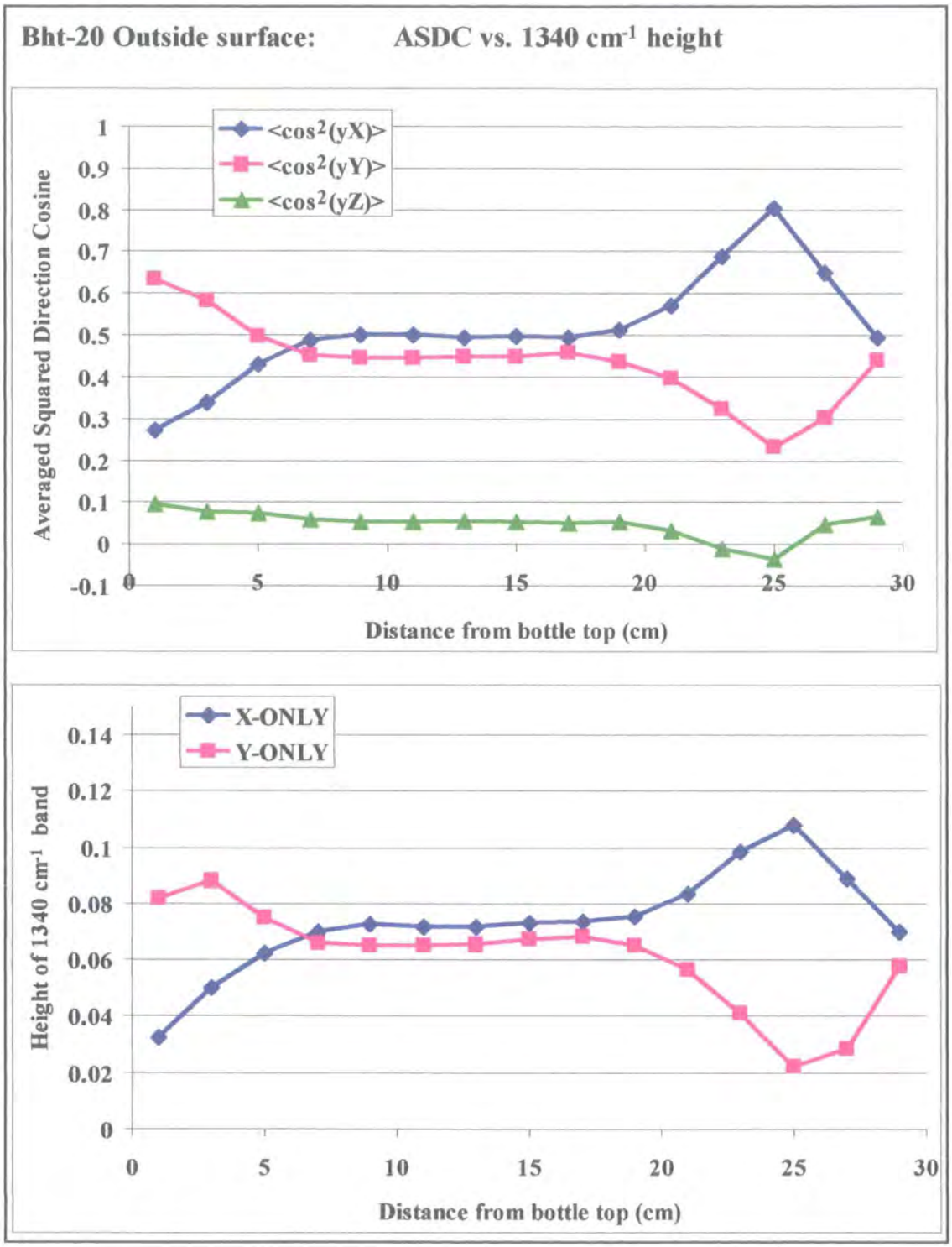

Figure 4-27: Ideal preform heating time minus 20 seconds - Outside surface

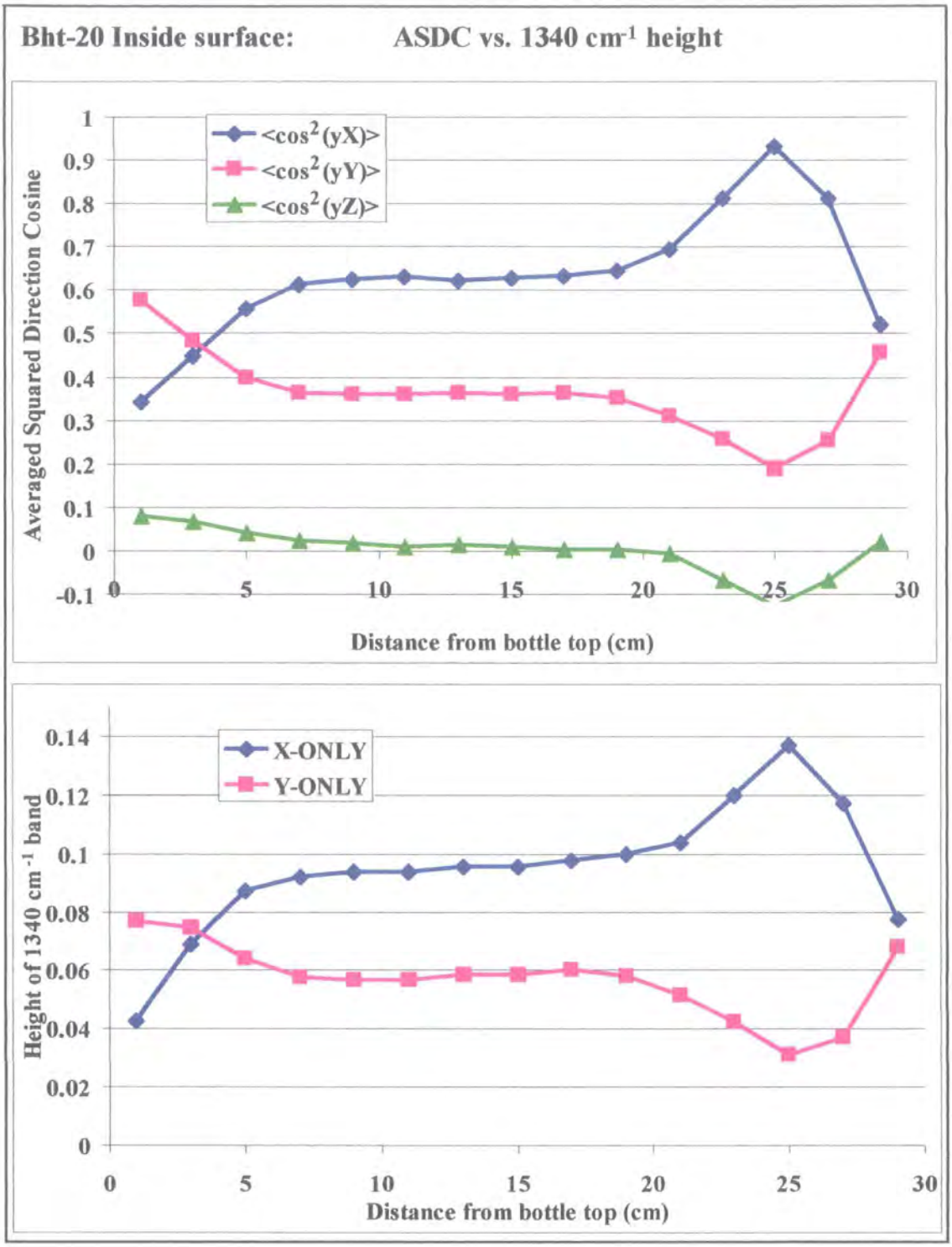

Figure 4-28: Ideal preform heating time minus 20 seconds - Inside surface

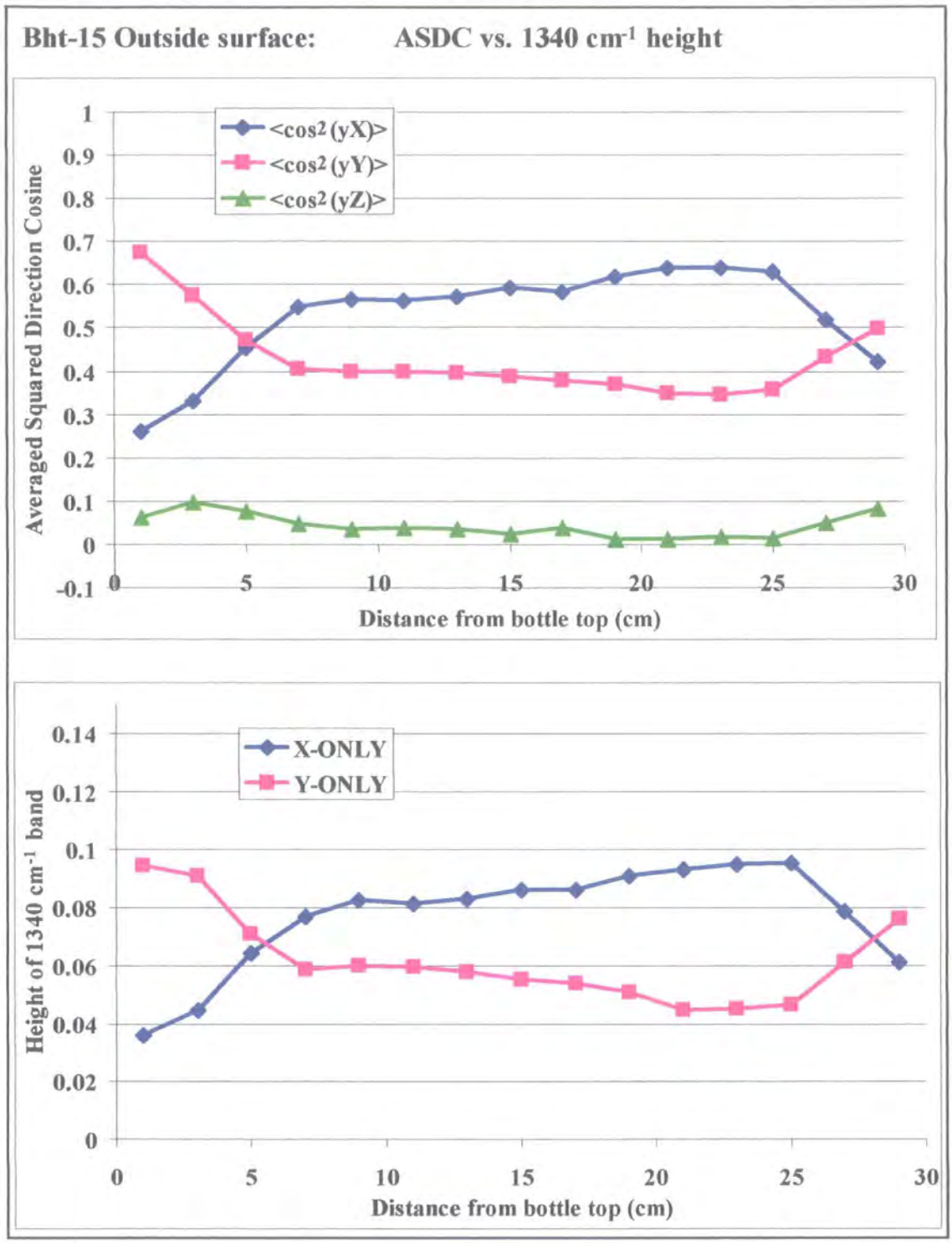

Figure 4-29: Ideal preform heating time minus 15 seconds - Outside surface

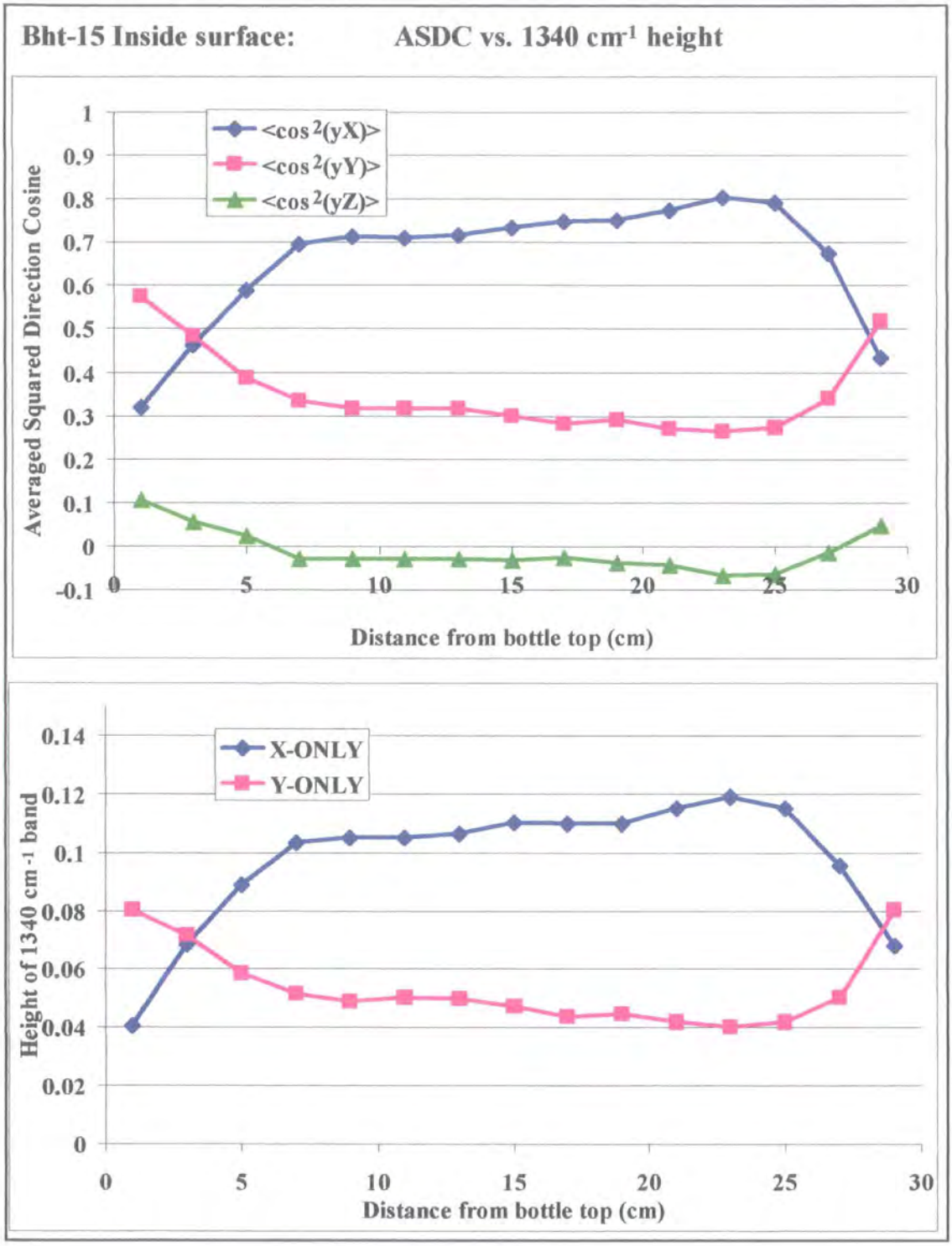

Figure 4-30: Ideal preform heating time minus 15 seconds - Inside surface

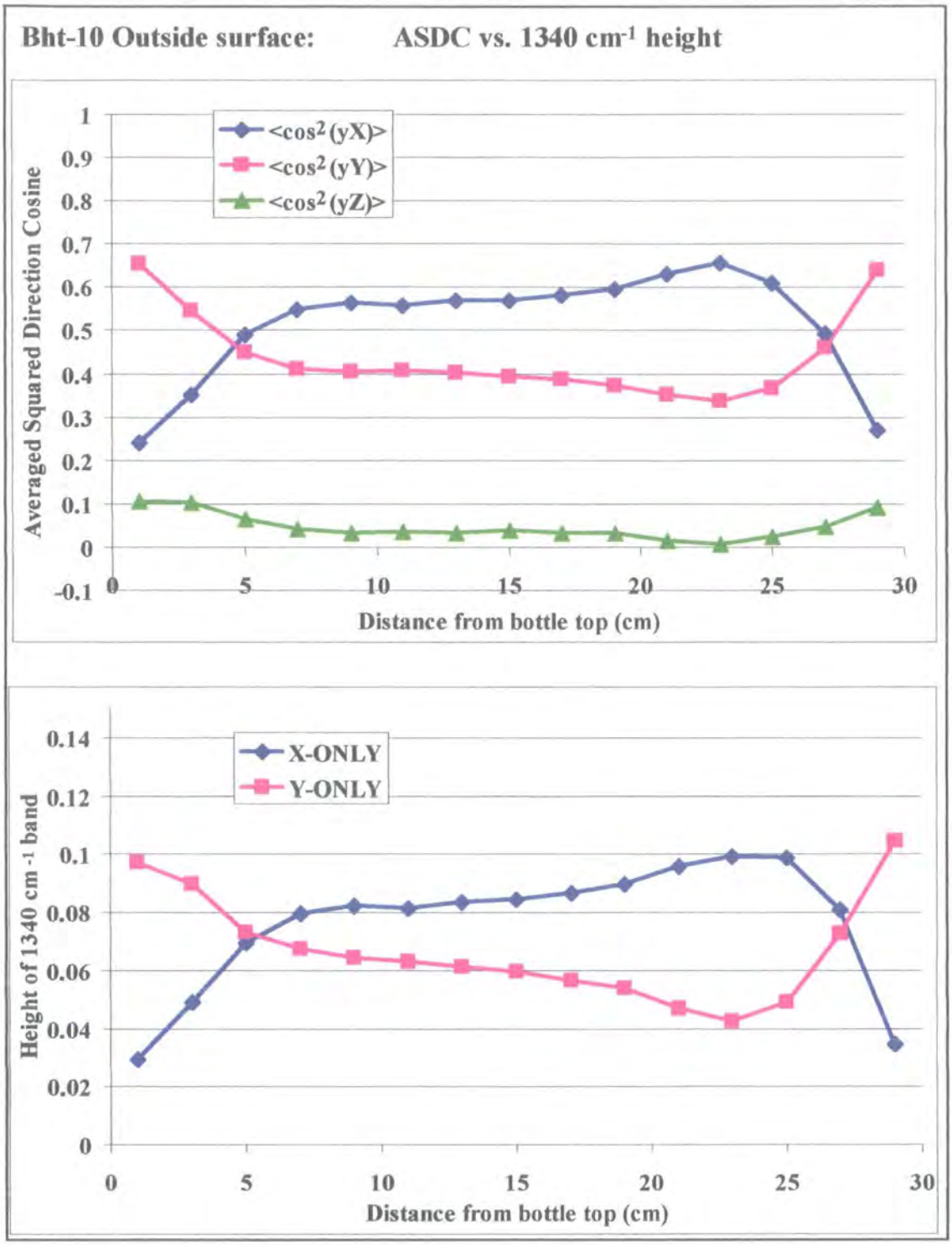

Figure 4-31: Ideal preform heating time minus 10 seconds - Outside surface

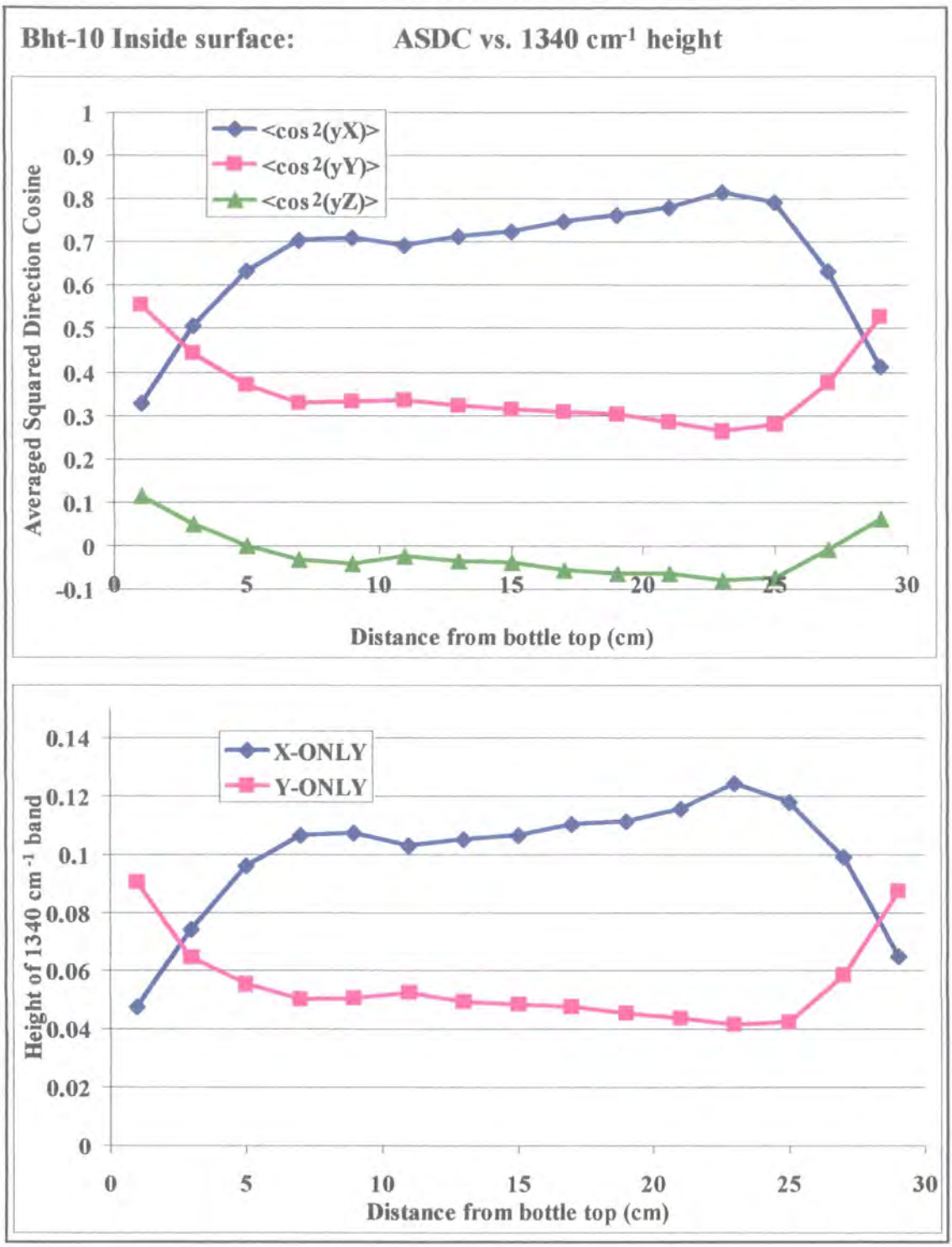

Figure 4-32: Ideal preform heating time minus 10 seconds - Inside surface

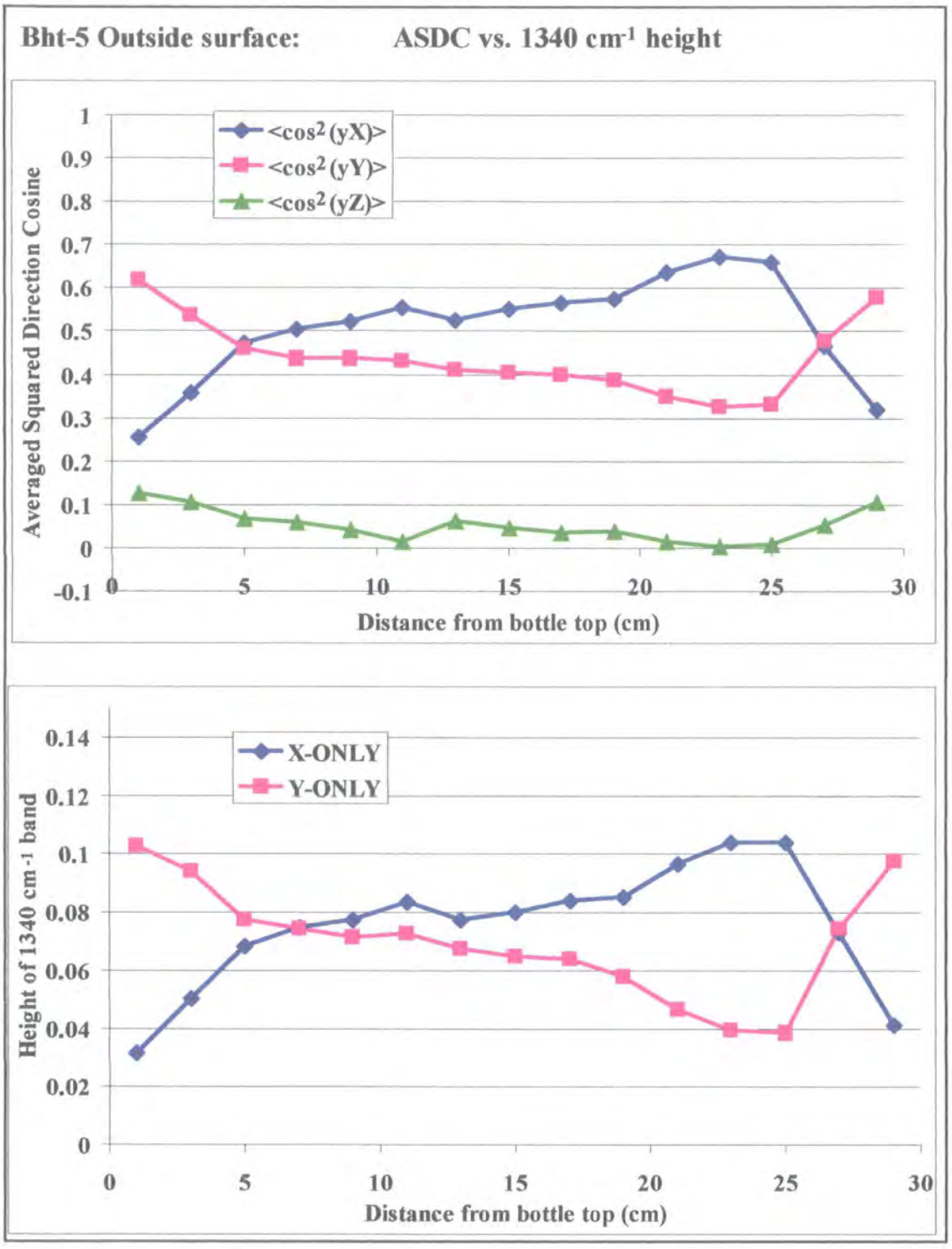

Figure 4-33: Ideal preform heating time minus 5 seconds - Outside surface

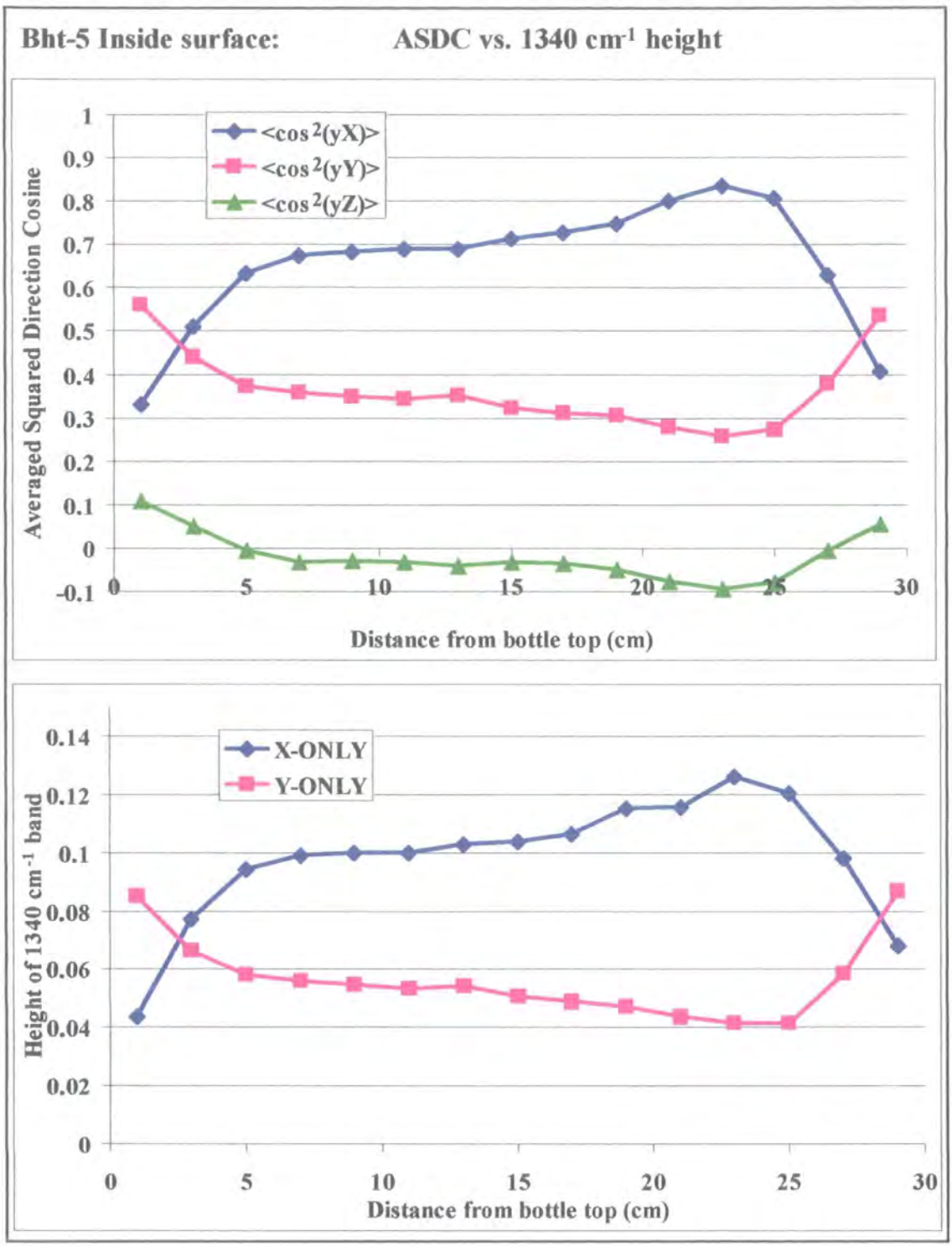

Figure 4-34: Ideal preform heating time minus 5 seconds - Inside surface

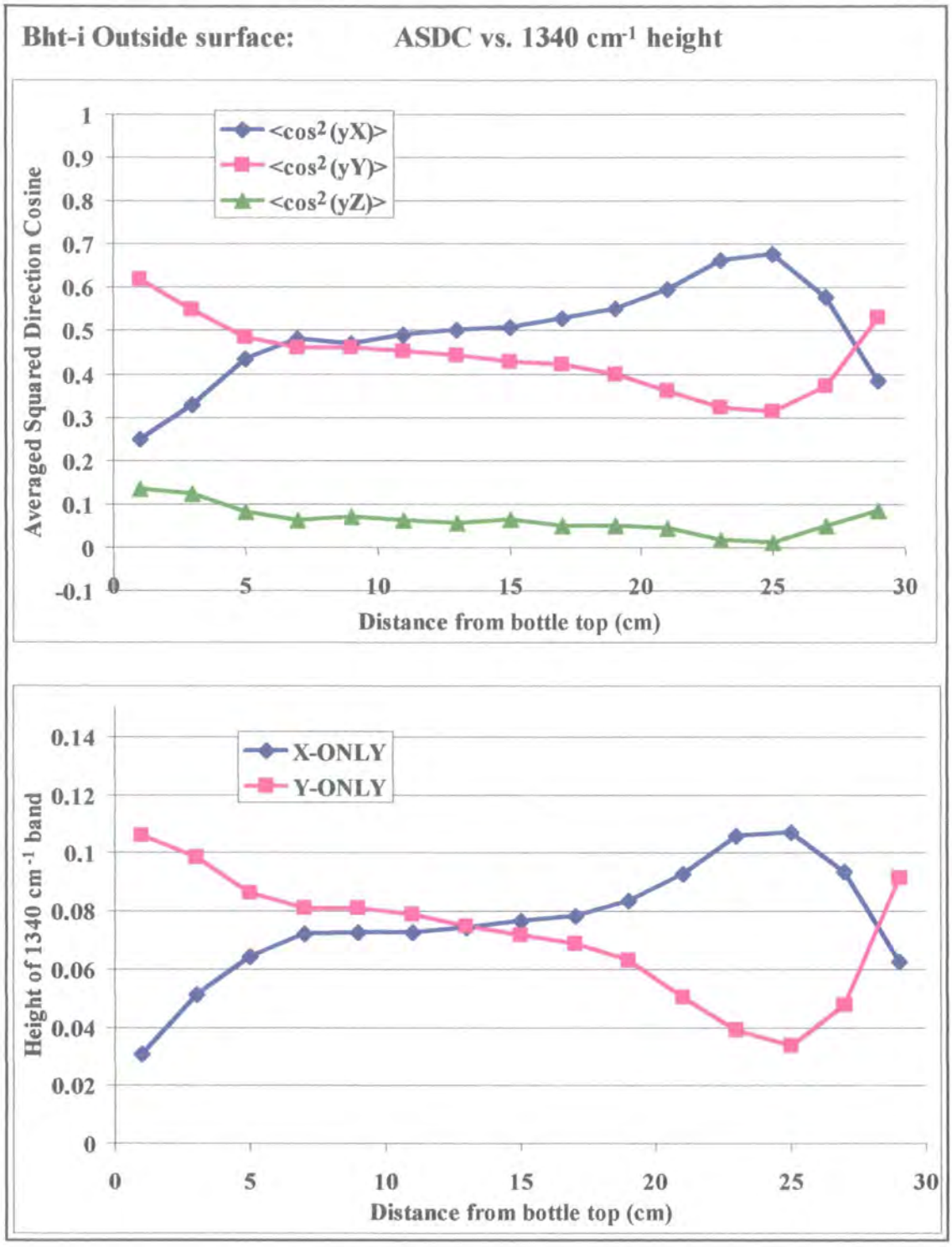

Figure 4-35: Ideal preform heating time - Outside surface - reproduced from Figure 4-23 for completeness of the series

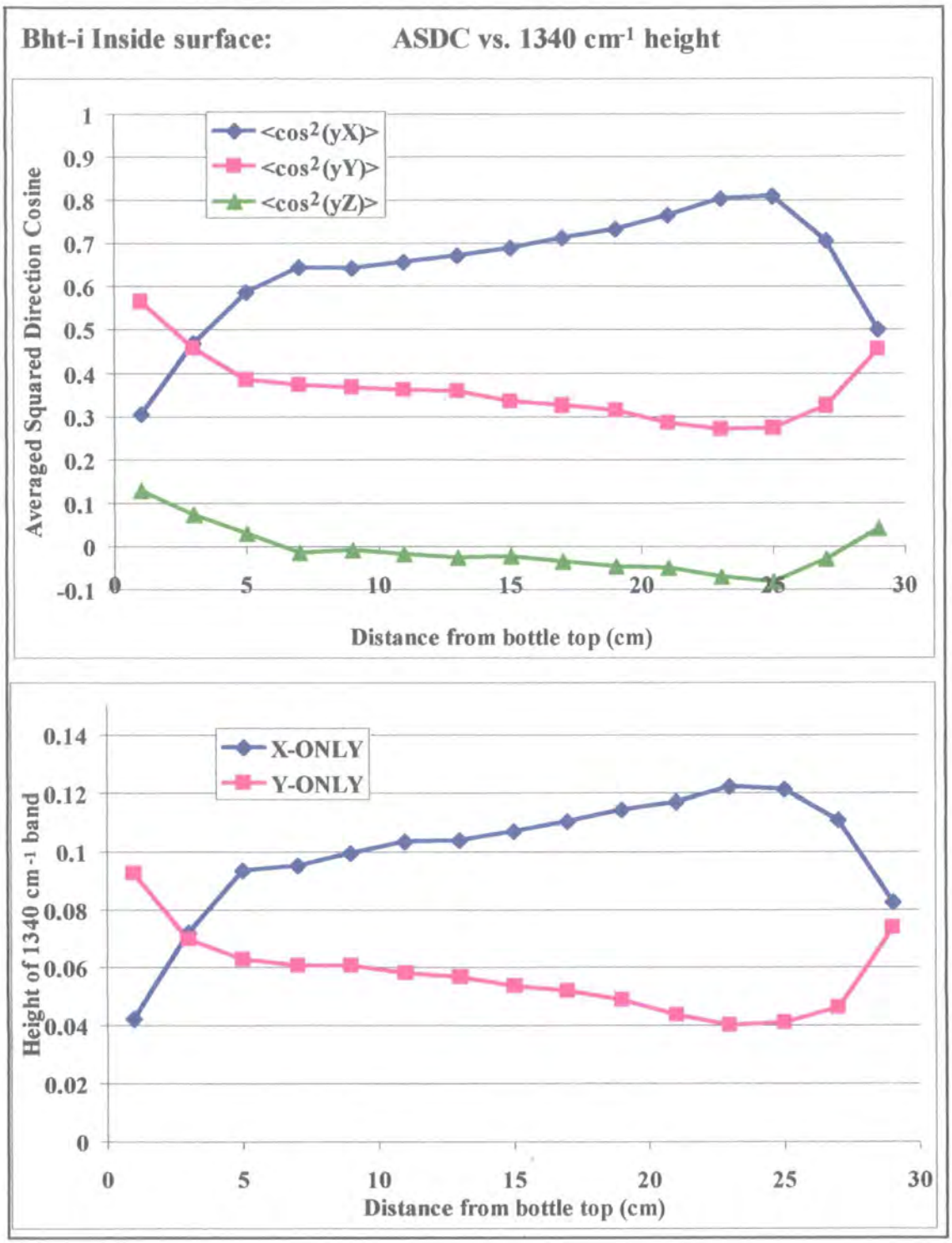

Figure 4-36: Ideal preform heating time - Inside surface - reproduced from Figure 4-24 for completeness of the series

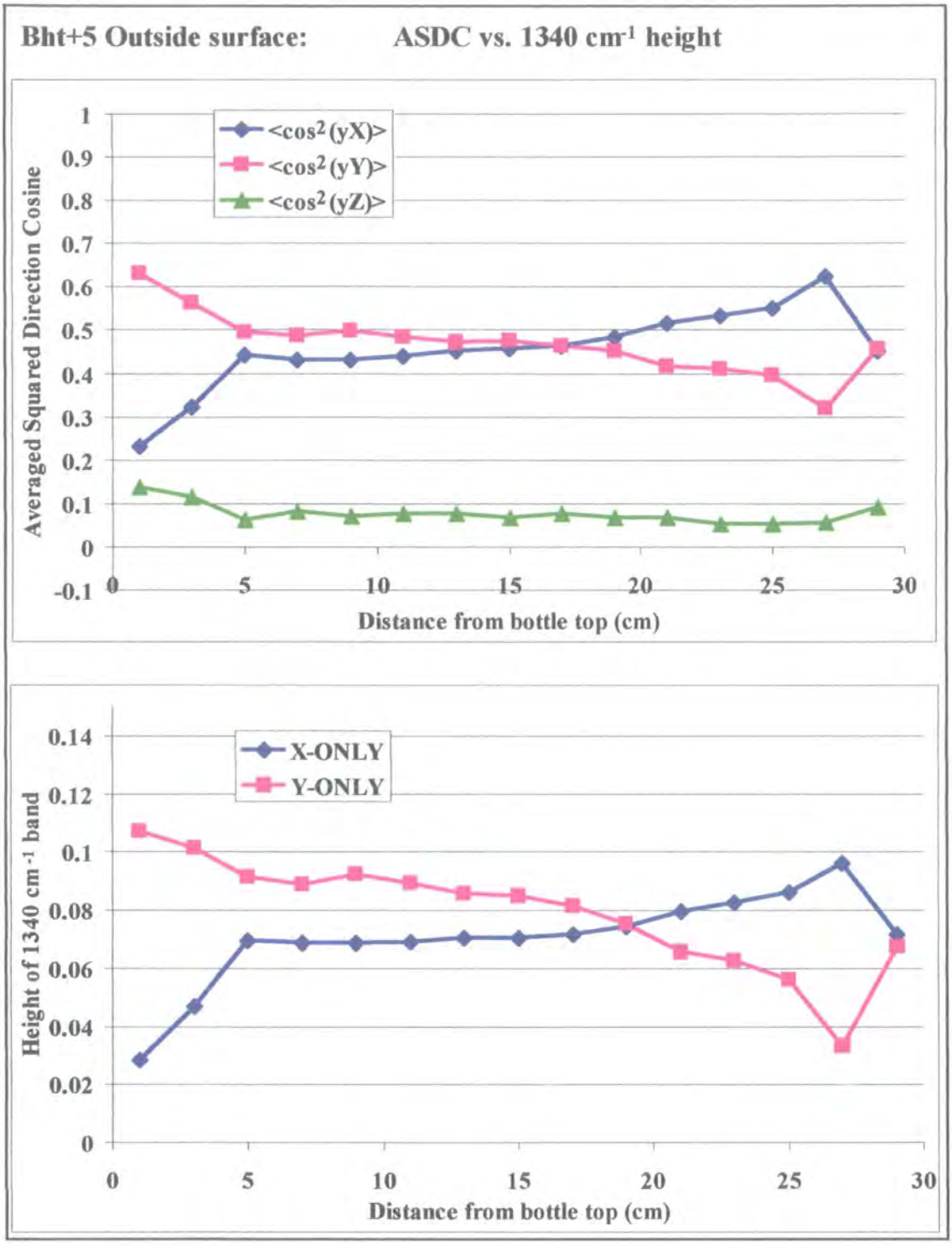

Figure 4-37: Ideal preform heating time plus 5 seconds - Outside surface

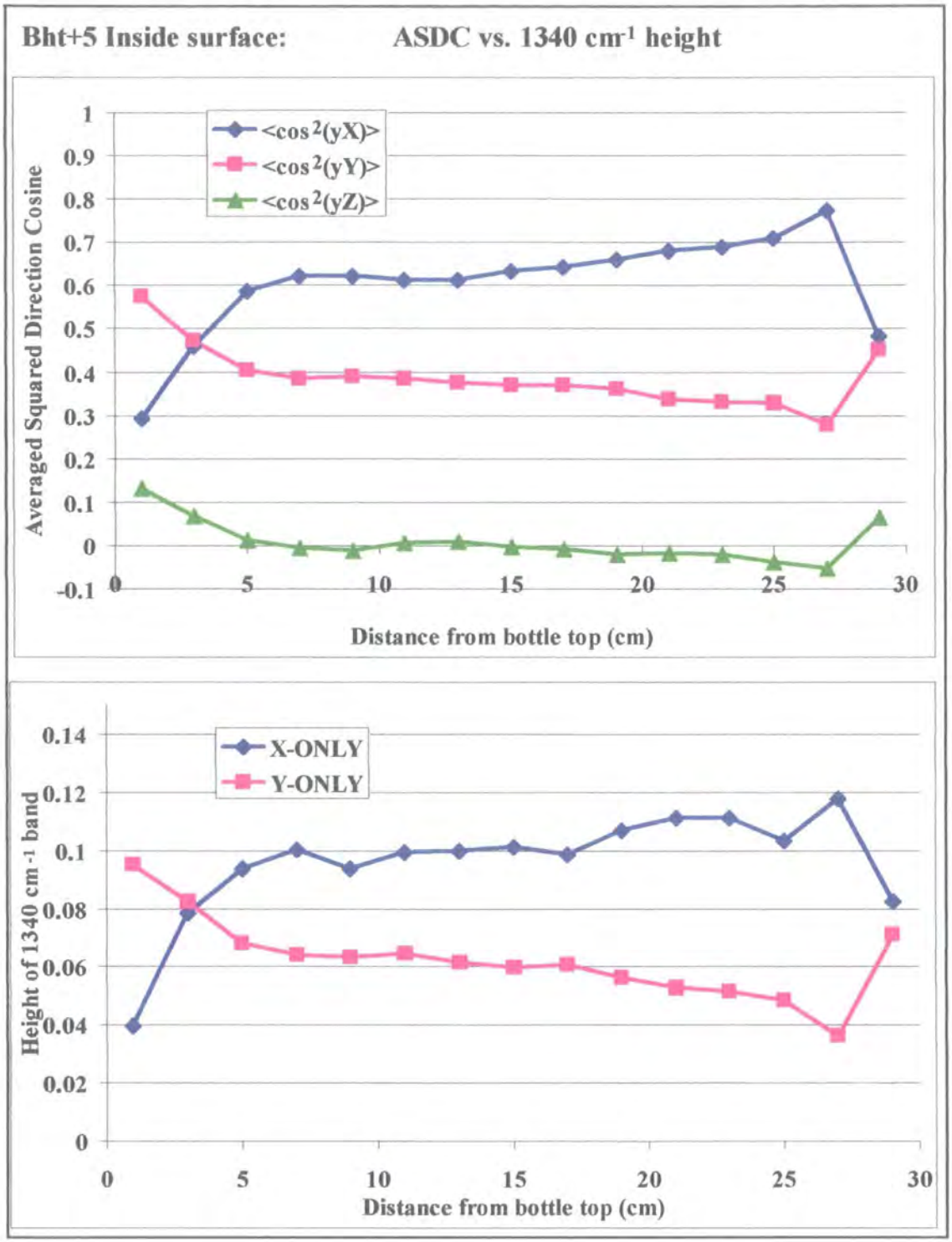

Figure 4-38: Ideal preform heating time plus 5 seconds - Inside surface

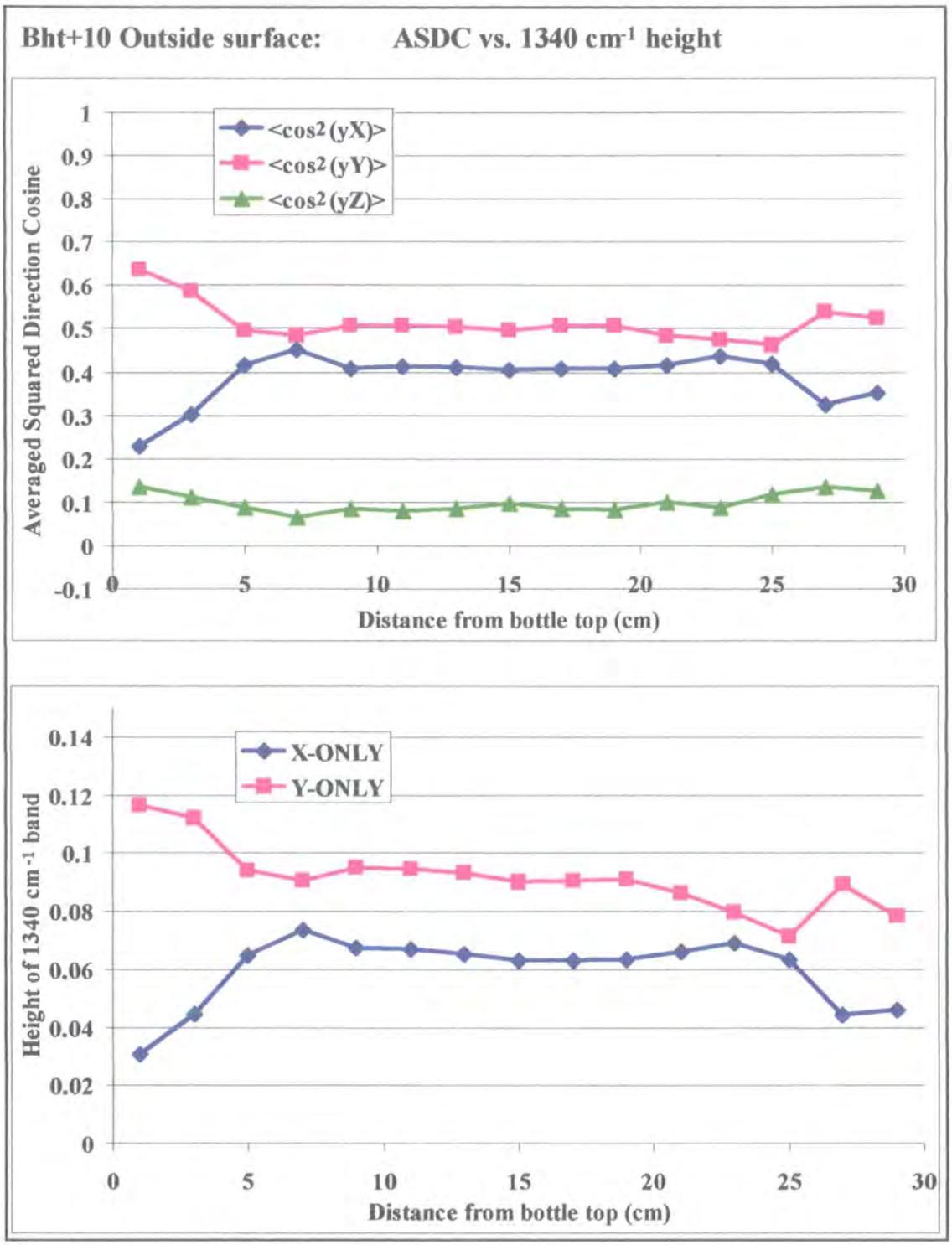

Figure 4-39: Ideal preform heating time plus 10 seconds - Outside surface

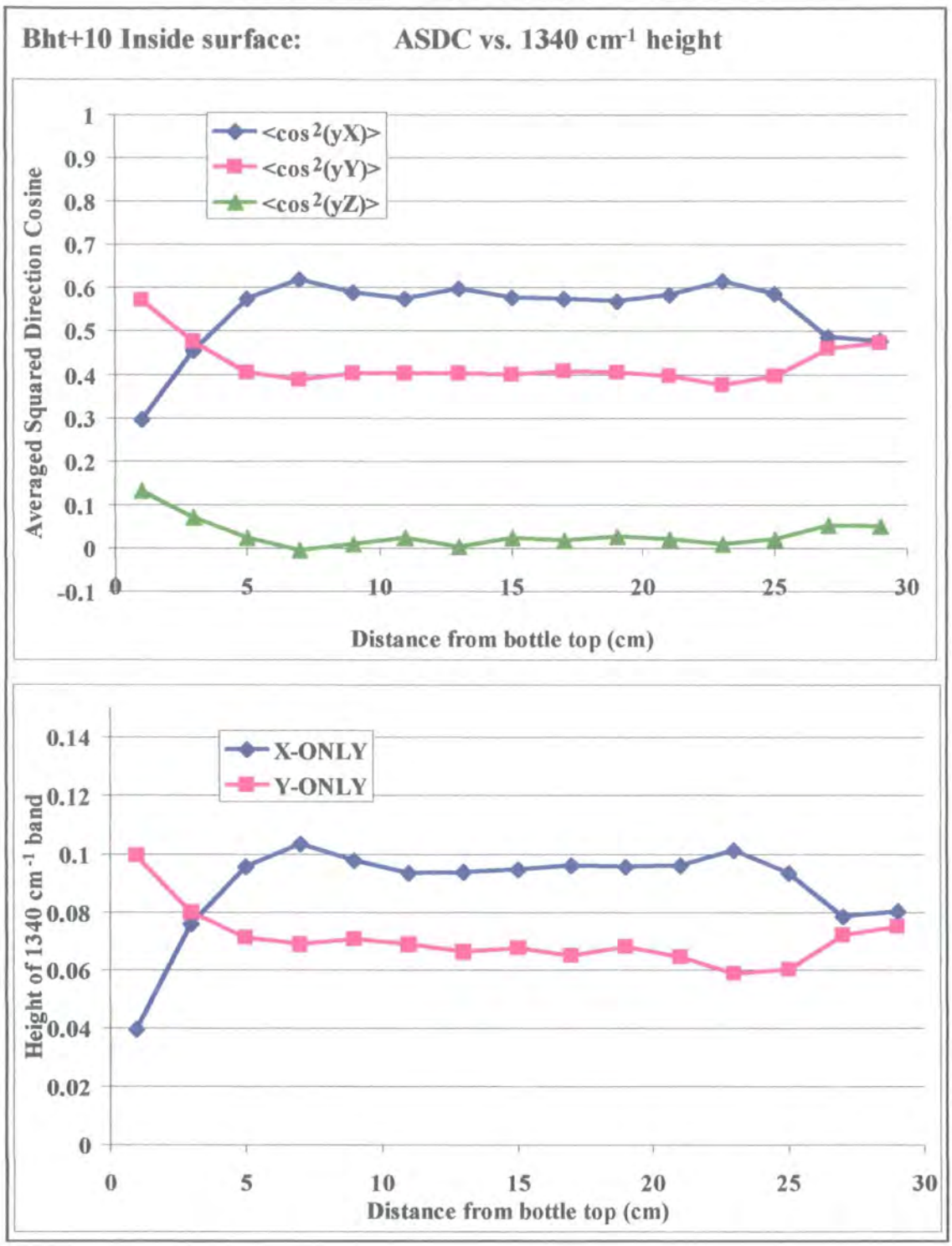

Figure 4-40: Ideal preform heating time plus 10 seconds - Inside surface

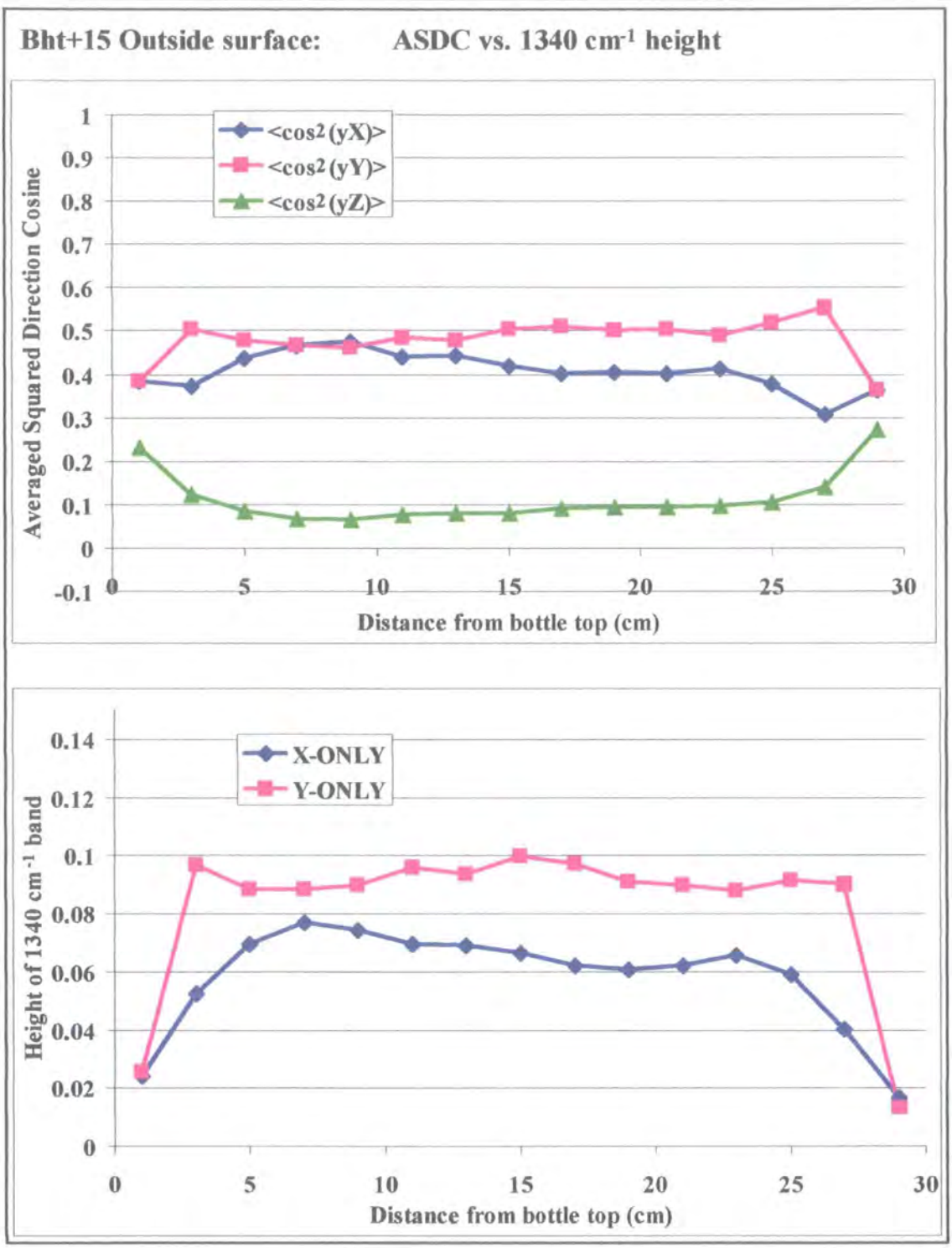

Figure 4-41: Ideal preform heating time plus 15 seconds - Outside surface

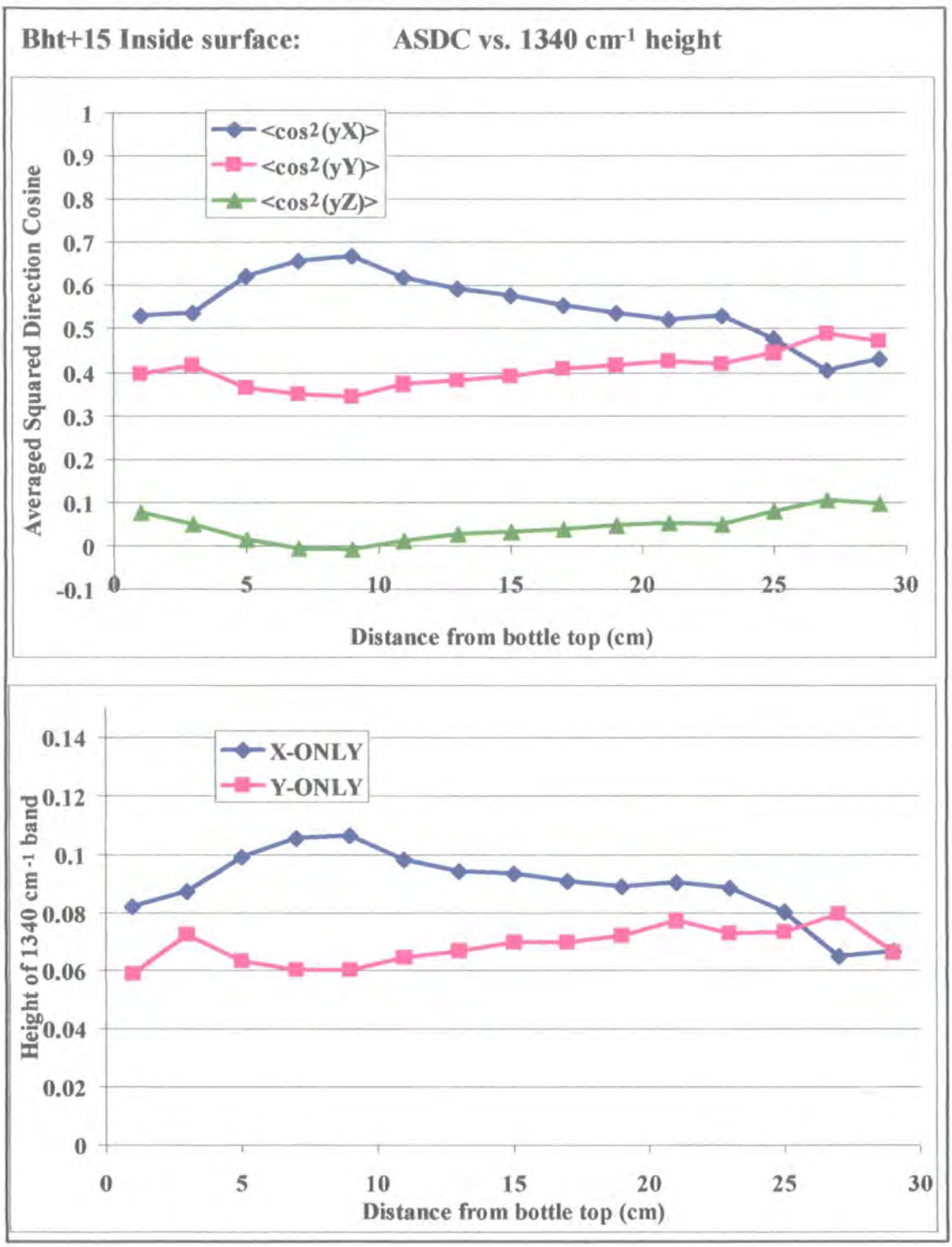

Figure 4-42: Ideal preform heating time plus 15 seconds - Inside surface

4.3.6.2 Bht series analysis

The ASDC of the bottle blown after t-20 seconds (see Figure 4-27 and Figure 4-28) display a sharp increase of orientation in the X-direction towards the base region, which peaks at 25 cm from the bottle top. This is true for both the inner and outer wall.

The CH_2 band mimics this trend very closely, which is an excellent result for the supposition that this band height can be used to map orientation trends. As we shall see for the remaining comparisons, the CH_2 height almost exactly matches the equivalent ASDC curve, which is derived from the two benzene ring vibrations at 875 and 1019 cm^{-1}. The most noticeable difference between the computed ASDC and the measured 1340 cm^{-1} band occurs for the first point in the $\langle\cos^2(yY)\rangle$ curve. These data suggest that there are chains lying in the Y direction, but the dip in the CH_2 curve suggest that they are not *trans* conformers. This makes sense, as the material directly under the cap is a lot thicker and thus has not undergone as much deformation. Remember that the ASDC curve shows the orientation of both *trans* and *gauche* transformers but the CH_2 curve shows the *trans*-only conformers.

For Bht-15 (see Figure 4-29 and Figure 4-30), some aspects of the standard bottle orientation are observed. The Z-ASDC remains consistently low. These orientation trends are beginning to resemble the Bht_i bottle more closely (see Figure 4-23 and Figure 4-24). Although the optical properties degenerate for bottles blown after shorter preform heating times, the orientation tends to resemble a standard bottle. A similar trend exists for Bht-10 and Bht-5, as shown in Figure 4-31 to Figure 4-34.

As the heating time increases above the time of a standard bottle, the orientation variation along the bottle reduces markedly. Bht+5 shows a sudden decrease in orientation and the switch from predominantly Y to predominantly X occurs much further down the side of the bottle for the outer wall, at around 17 cm from the bottle top (see Figure 4-37 and Figure 4-38). There is no sharp increase in orientation towards the base of the bottle as we have seen with the other bottles so far.

Increasing the preform heating time to i+10 seconds results in even less orientation in the final product (shown in Figure 4-39 and Figure 4-40). In this case, the Y-ASDC dominates throughout the entire length of the bottle. Even on the inside wall here, there is not a great deal of difference in the orientations in the X and Y sample directions.

The longest preform heating time that was supplied was t+15 seconds. In this case, the orientation appears to be consistent throughout the outside and inside walls, independent of the amount the bottle has been stretched (see Figure 4-41 and Figure 4-42). The X and Y-ASDC values are seen to be similar for the entire length of the bottle. The polymer temperature was too high above its T_g during this draw and thus flowed much more easily during deformation. It is known that PET films at relatively high temperatures (above T_g, e.g. 90°C) can, during low strain rates, stretch without resultant orientation or crystallinity occurring; this is called flow drawing[13].

The 1340 cm^{-1} measurement, which probes the CH_2 *trans*-only conformer, on the Bht+10 and Bht+15 specimens were less indicative of the orientation results provided by the ASDCs. The deterioration of optical clarity in these bottles, especially at the neck and base regions, is likely to be due to large un-oriented spherulites composed of

lamellae crystals forming, in which the crystalline regions are known to contain only *trans* conformers. Thus, the 1340 cm^{-1} band height method is better suited to standard bottles that have limited or evenly-distributed crystallinity levels.

This study reveals that it is particularly important not to heat the preforms for too long before the stretch-blow procedure if high levels of orientation are to be preserved. The optical clarity for both Bht-i and Bht+5 is very similar and thus bottles that have been over heated would be difficult to spot during production.

4.3.7 Results for BtBIPA bottles

The FTIR-ATR surface orientation results for the bottles containing 2% and 8% t-BIPA are shown in Figure 4-43 to Figure 4-46. The BtBIPA series also contains a standard laser+ (2 % IPA) bottle blown at the same time as the t-BIPA bottles (see Figure 4-47 and Figure 4-48). Inconsistencies between this bottle and the earlier bottles might also be due to slight differences in resin properties that are known to vary slightly from batch to batch.

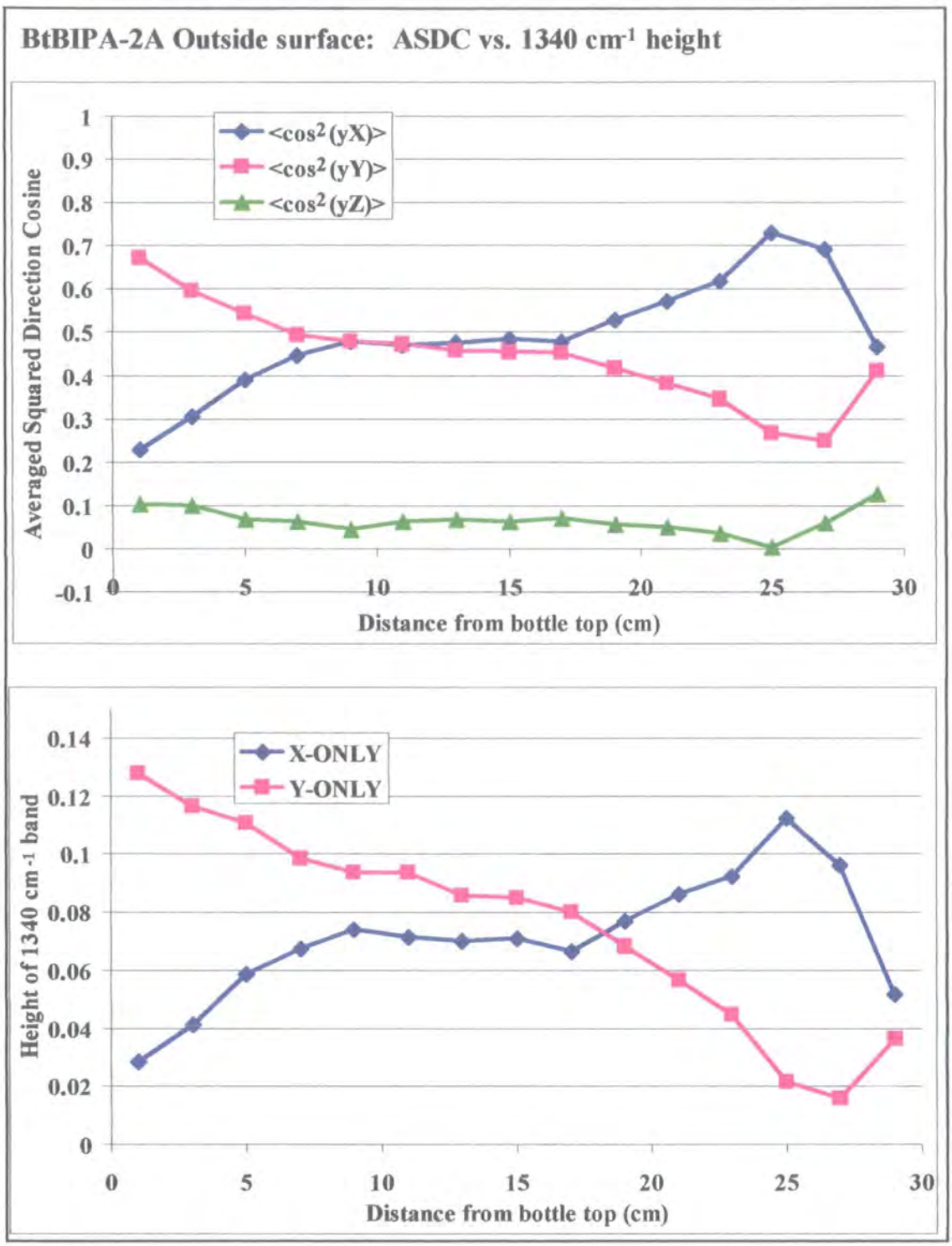

Figure 4-43: A 2l bottle containing 2 % t-BIPA - Outside surface

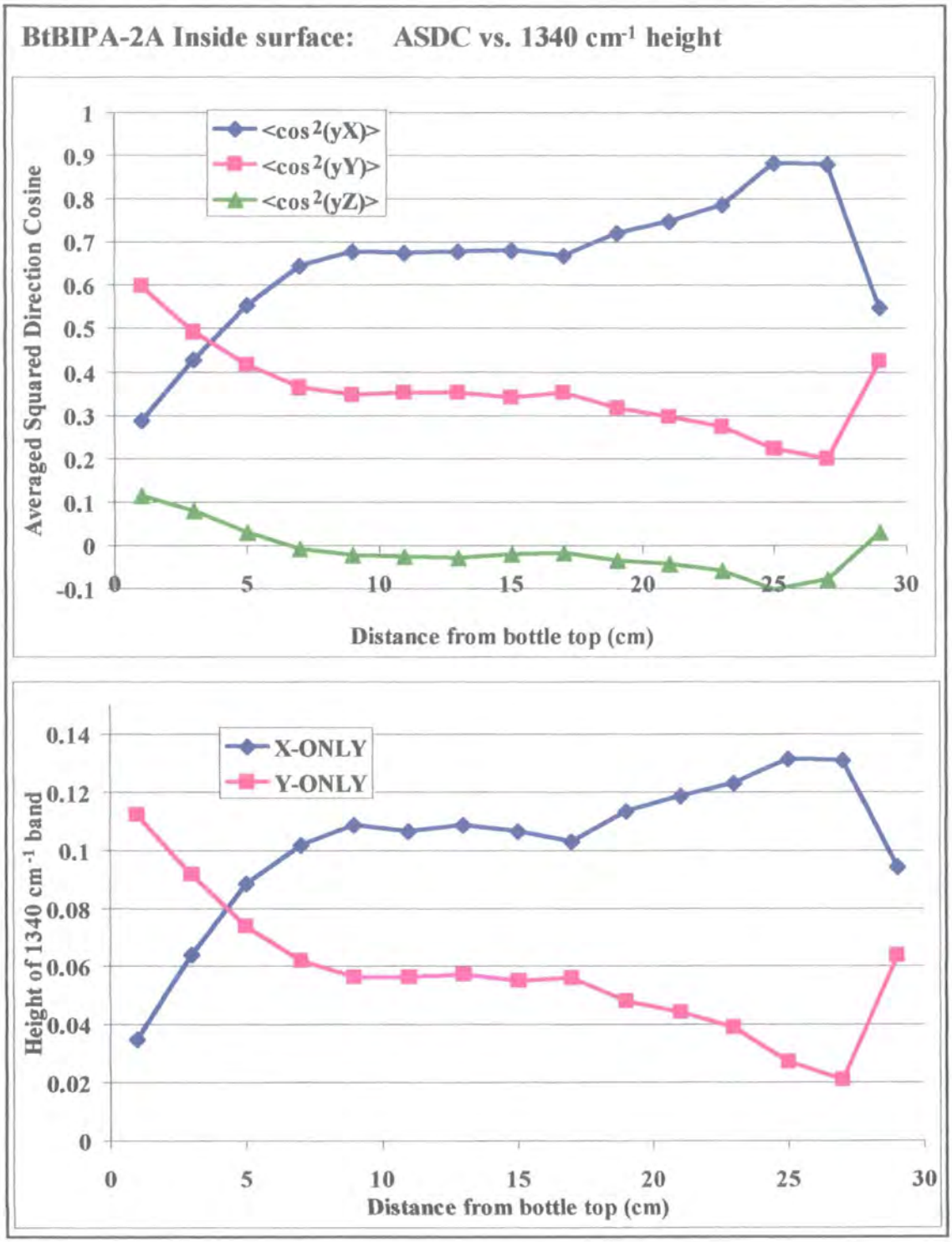

Figure 4-44: A 2l bottle containing 2 % t-BIPA - Inside surface

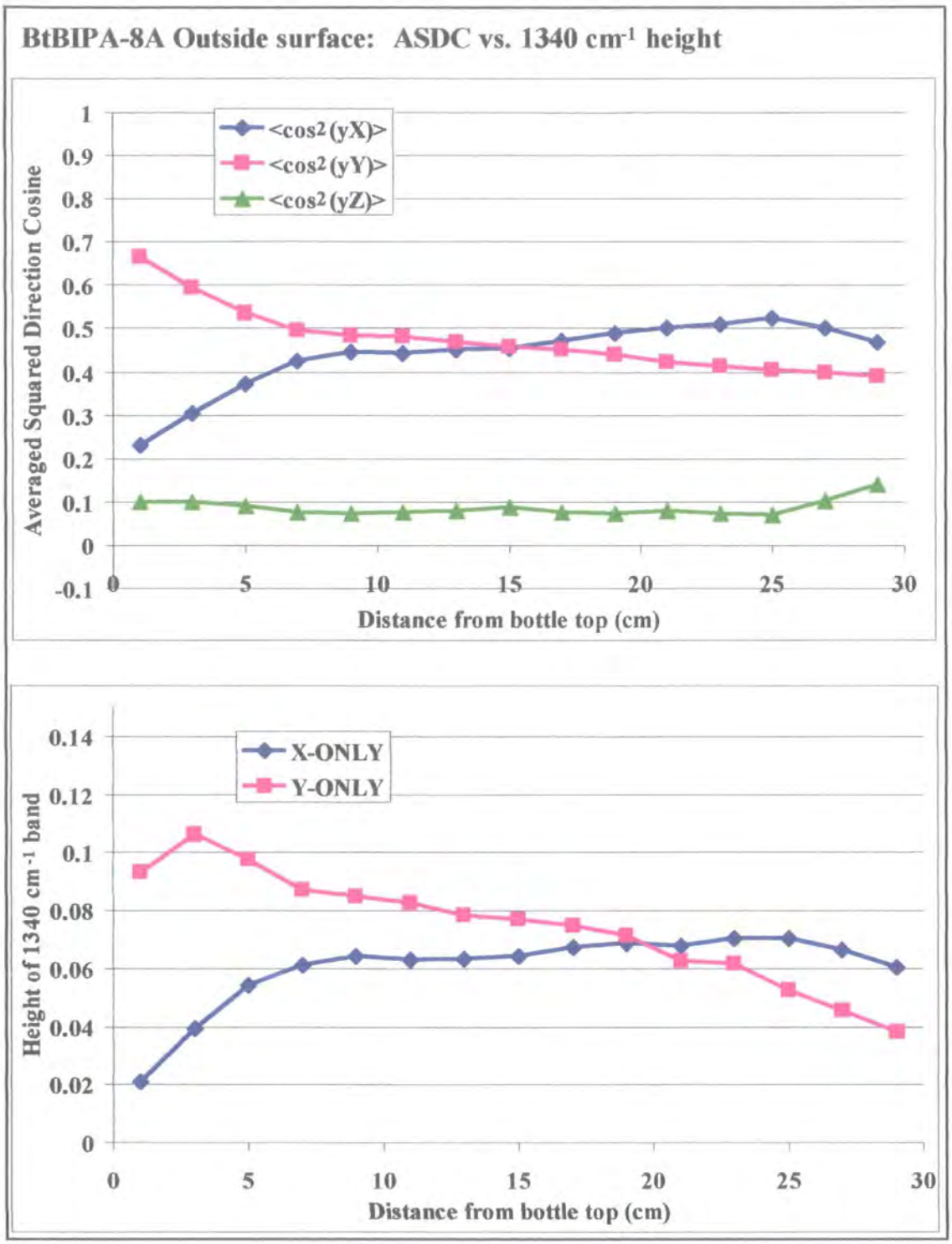

Figure 4-45: A 2l bottle containing 8 % t-BIPA - Outside surface

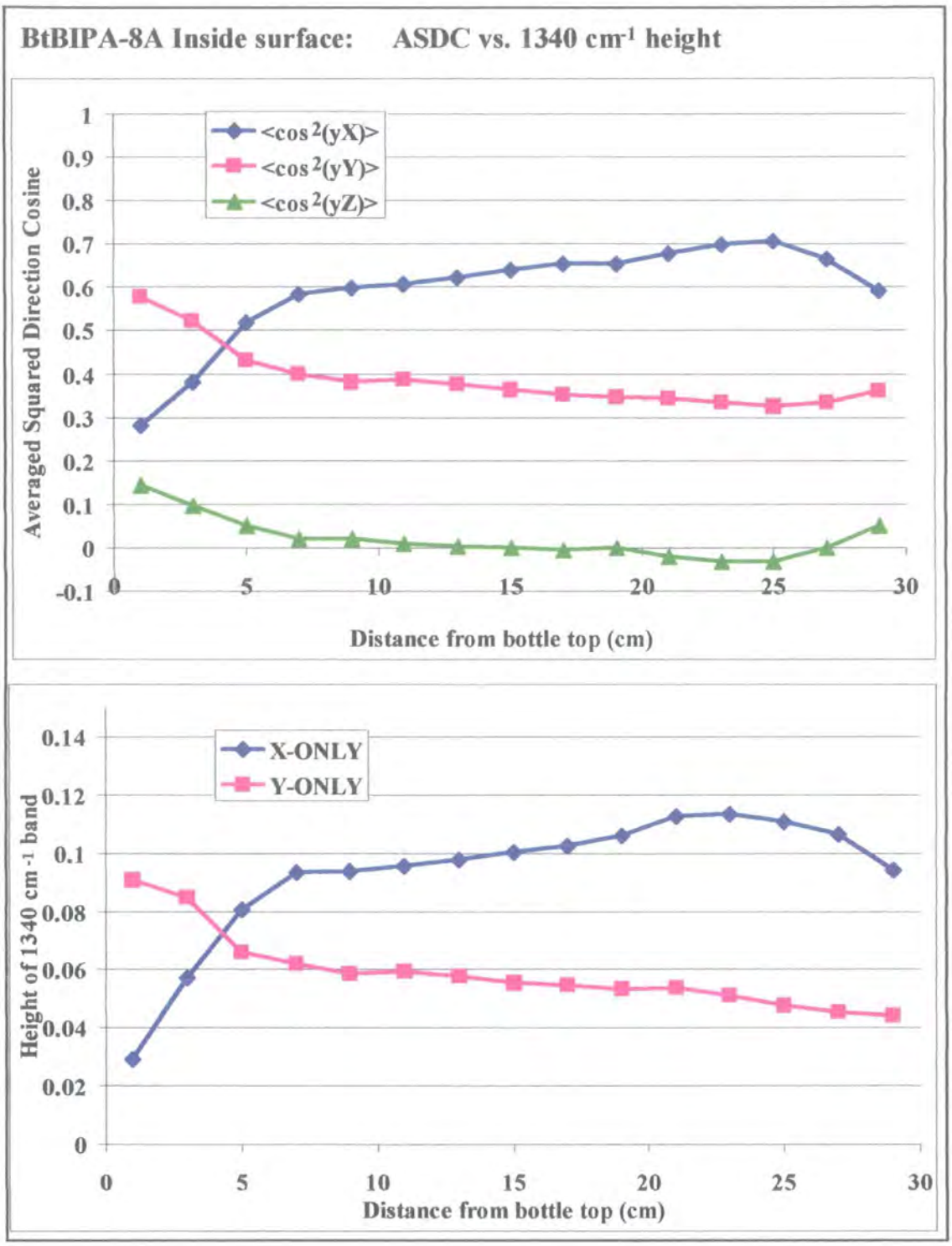

Figure 4-46: A 2l bottle containing 8 % t-BIPA - Inside surface

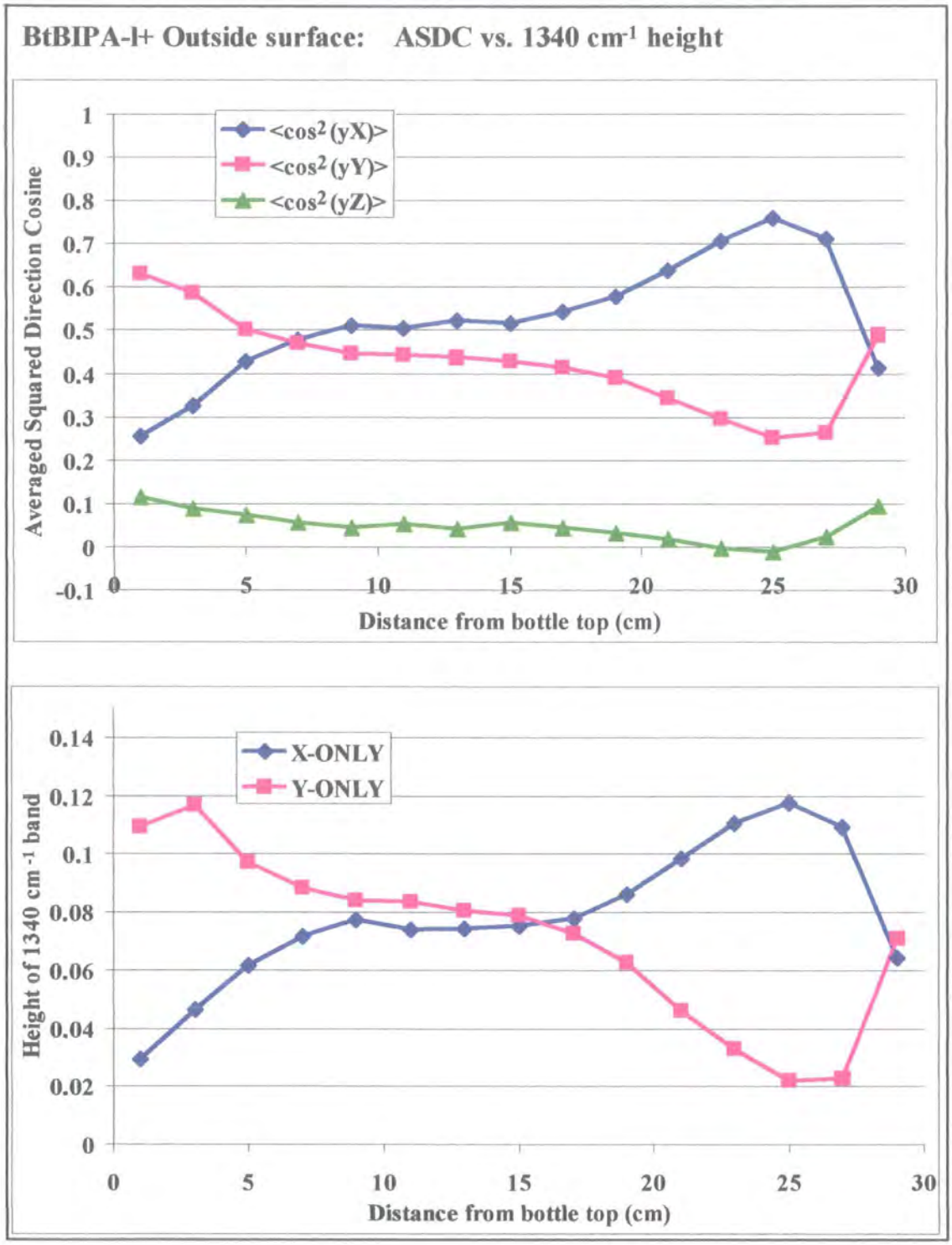

Figure 4-47: A standard Laser+ bottle blown at same time as t-BIPA bottles - Outside surface

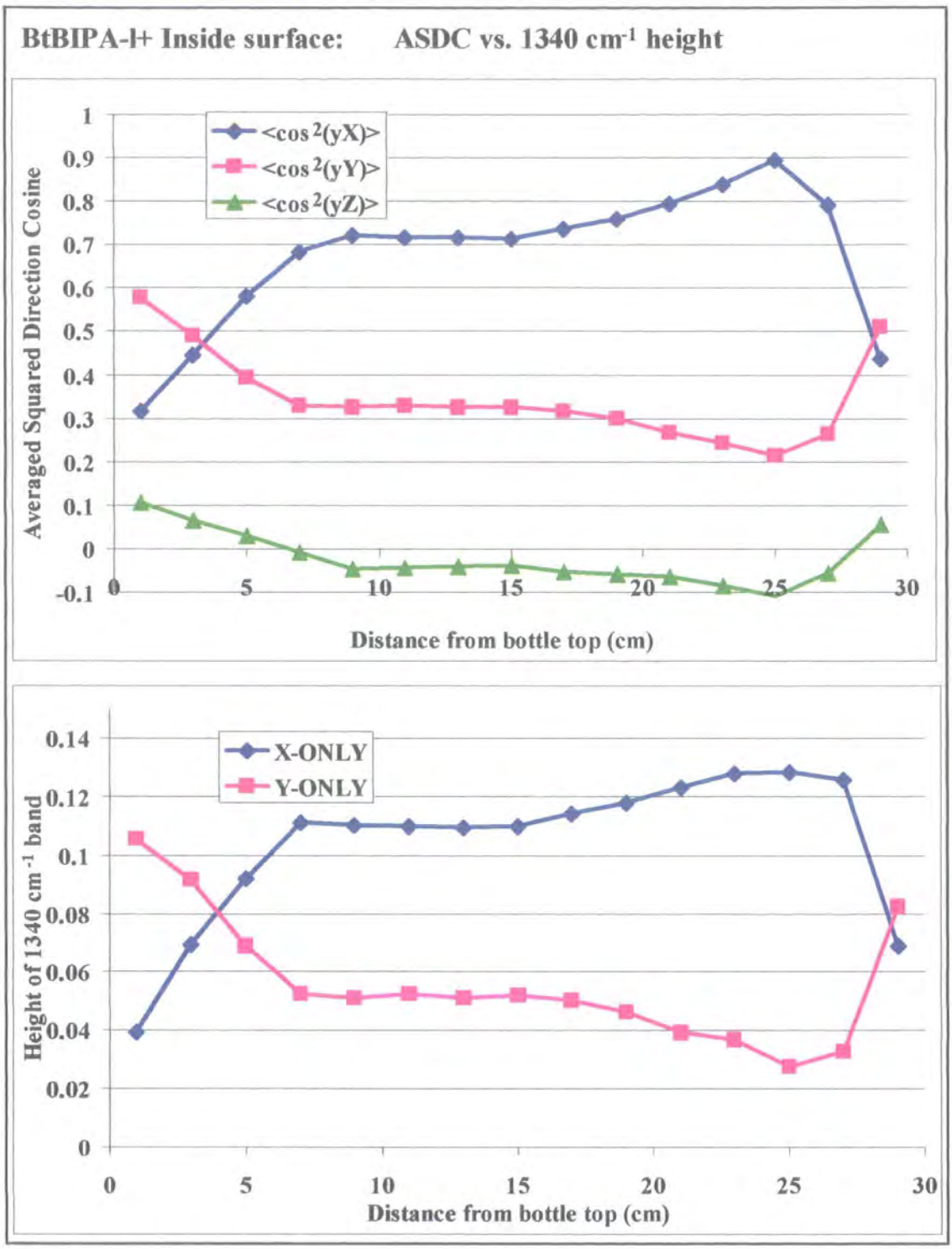

Figure 4-48: A standard Laser+ bottle blown at same time as t-BIPA bottles - Inside surface

4.3.7.1 Analysis for BtBIPA bottles

The outside ASDC curves for the 2 % t-BIPA bottles (Figure 4-43), bear a close relation to a standard laser+ bottle (see Figure 4-47). The inclusion of 2 % t-BIPA appears not to hinder or promote any different orientation properties in the material during the stretch blow process. This is a good result as it suggests that bottles made with a 2 % t-BIPA content are likely to have tensile properties comparable with their IPA equivalents.

The outside CH_2 curves deviate from the ASDC more than usual in this case. The switch from majority Y, to majority X-direction chains occurs much further down the bottle wall. There is a better correlation between the inside wall ASDC and the equivalent CH_2 curves, as shown in Figure 4-44 compared to the outside wall.

The outer-wall orientation results for 8% t-BIPA bottle (Figure 4-45), are quite different to those we have seen so far. The curves indicate no sudden switches in orientation but rather, low amounts of preferential orientation in the X and Y directions throughout the length of the bottle. The subtle change from predominantly-Y to predominantly-X occurs exactly half way down the bottle, rather than the usual trend of it switching at the shoulder. The outside CH_2 curves report the switch slightly further down the wall at 20 cm from the bottle top. The orientation at the inner wall (Figure 4-46) resembles a standard bottle more closely than the outer wall, although the magnitude of the orientation is a lot less.

The CH_2 curves match the ASDCs almost perfectly for the inner wall, in Figure 4-46.

4.3.8 Low molecular weight bottle results

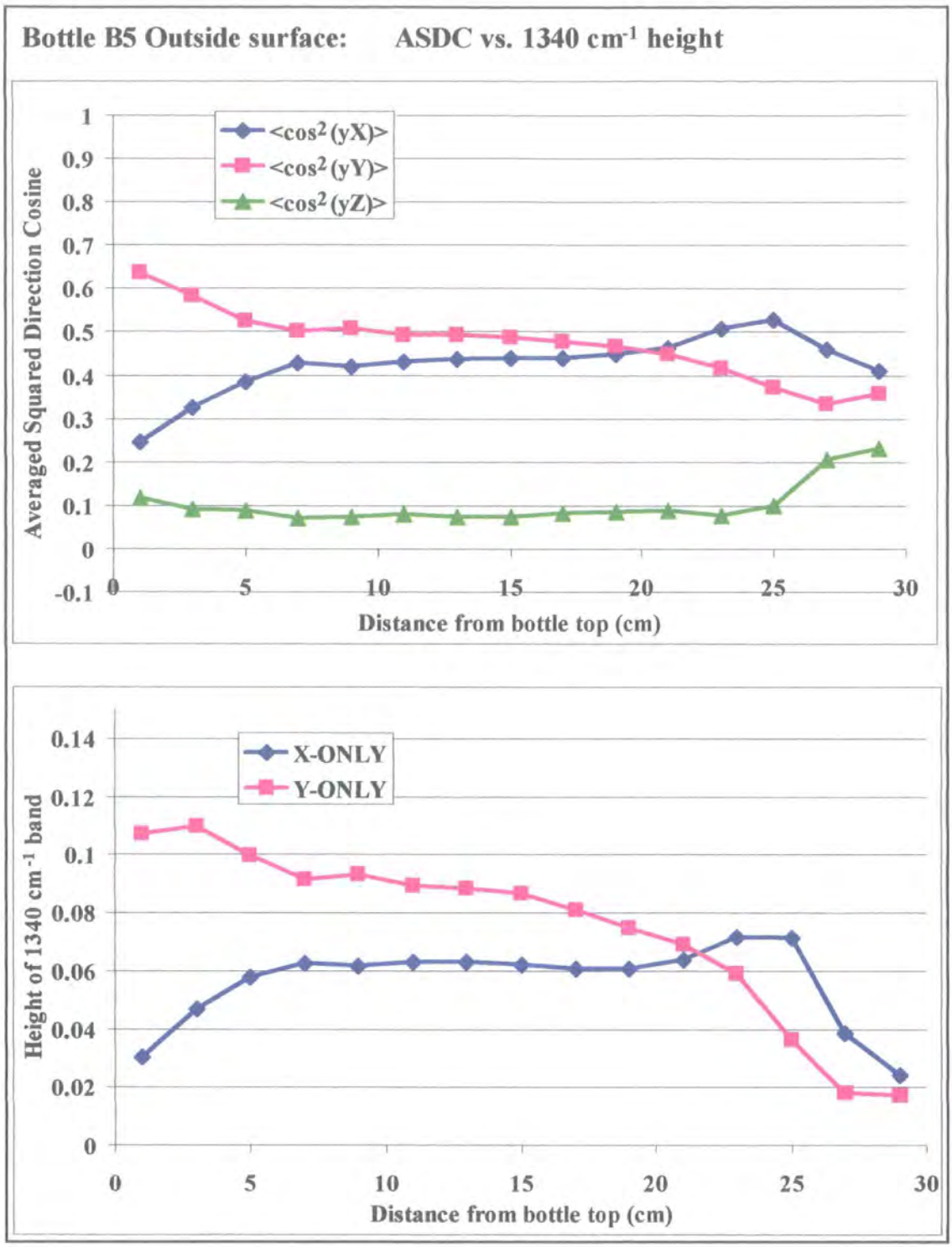

Figure 4-49: A low molecular weight (IV = 0.62) bottle - Outside surface

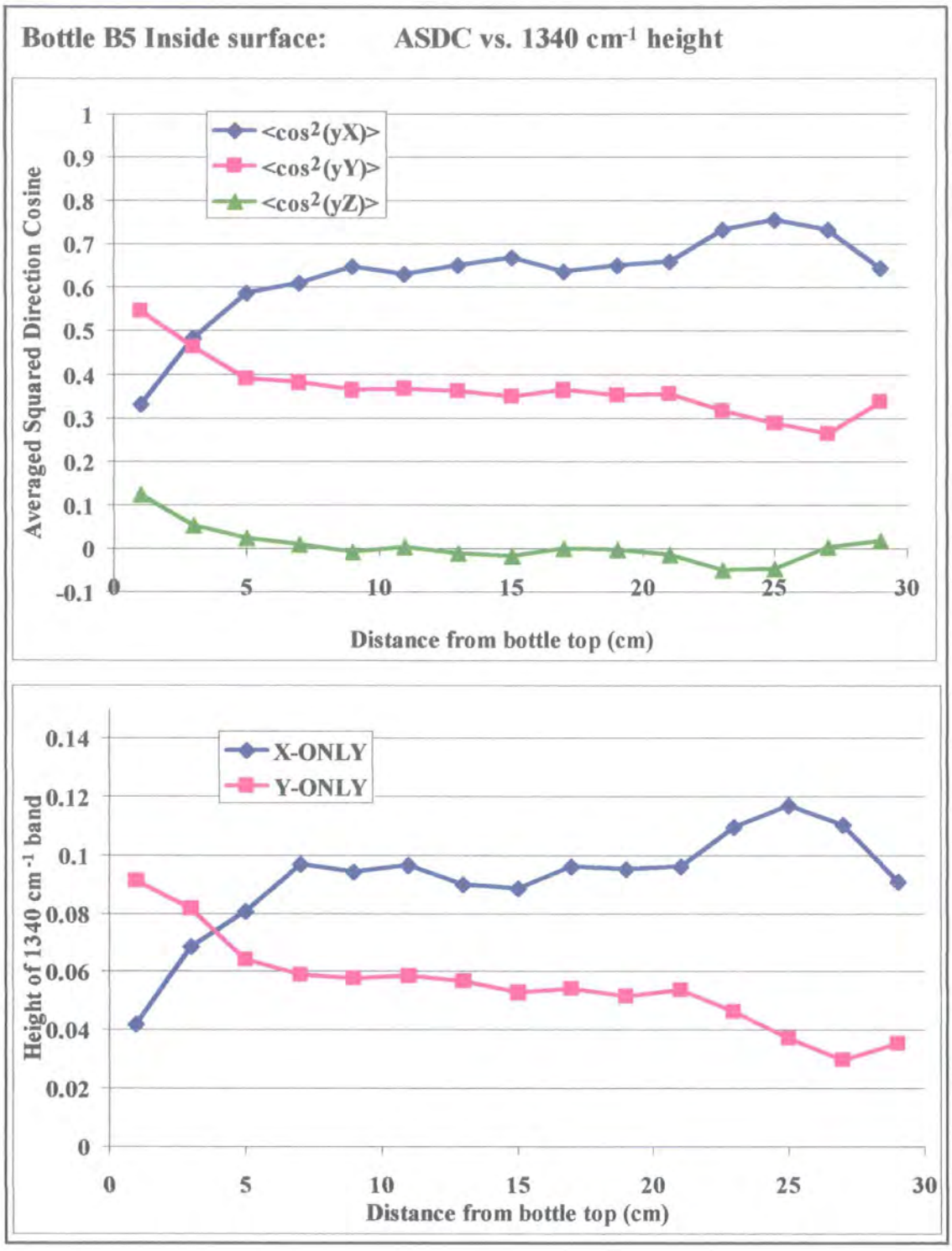

Figure 4-50: A low molecular weight (IV = 0.62) bottle - Inside surface

4.3.8.1 Analysis of bottle B5

The bottle in this study was made from a film grade resin (IV of 0.62), which has a lower molecular weight than the standard bottle grade (IV of 0.82). The material distribution in this case was not as good as a standard bottle, which results in more material towards the base of the bottle.

It appears that decreasing the IV also results in a decrease of overall orientation, particularly for the outer wall (see Figure 4-49 and Figure 4-50). Initial impressions suggest that the orientation of this bottle is very similar to the bottle blown from 8% t-BIPA. Interestingly, it appears that the chains in the Y direction dominate until the base region for the outside of the bottle, yet the X direction is prominent for the inner wall except for the very top of the bottle. The orientation within the walls of this bottle could be reduced because the reduced molecular weight would result in less chain entanglement, enabling the chains to move past one another more easily to even out locally high stresses and strains that would promote chain orientation.

For bottle B5, the CH_2 curves match the ASDCs more closely for the inner wall than the outer wall. This could be due to excess crystallinity forming on the outer wall during the preform heating stage.

4.3.9 The small bottle (SB) series results

This data, presented in Figure 4-52 to Figure 4-57, aims to address whether the polarised FTIR-ATR technique can be used to measure the orientation of smaller bottles (shown in Figure 4-51) to see how the shape of these bottles effect the orientation.

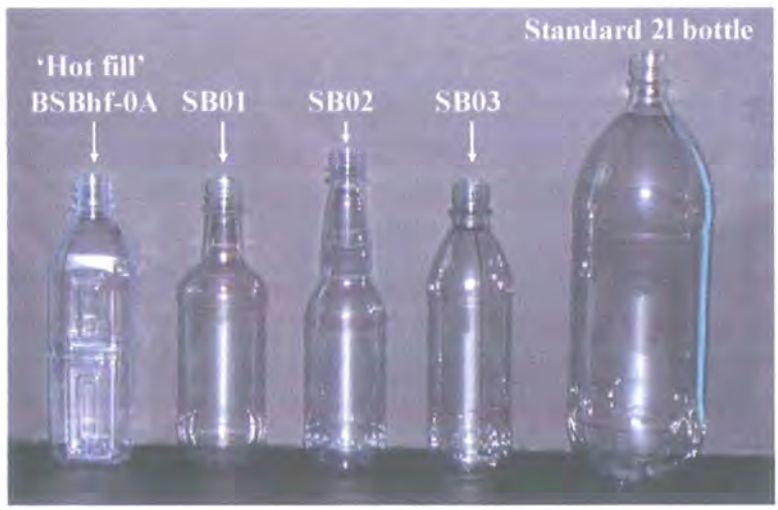

Figure 4-51: A photograph of the small bottles and a large bottle for size comparison

Any difficulty collecting ATR measurements from this type of bottle are due to small bottles having a thicker, less flexible wall. This is a problem when using the ATR technique as the overall absorbance is a sensitive function of the intimacy of contact between the sample and the ATR crystal. This problem was worsened by the Thunderdome accessory used in this study, which only allows relatively low pressures to be exerted on the inherently brittle germanium IRE. This series also contains a homopolymer bottle, which was blown into a heated blow-mould and held at temperatures to increase its final crystallinity. This is an experimental bottle production technique, designed to identify a means of making bottles that can withstand higher temperatures during the bottle filling technique.

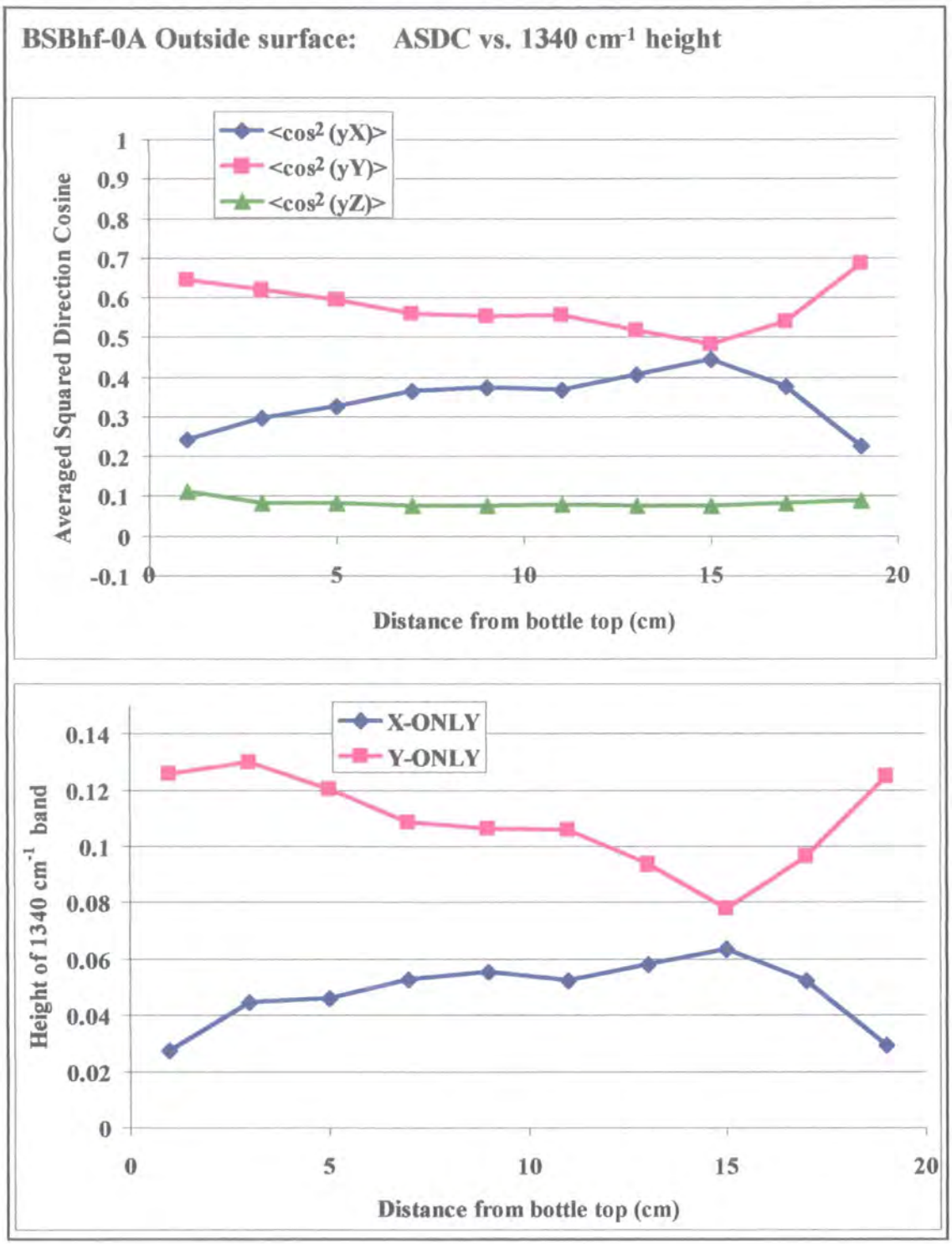

Figure 4-52: Orientation results from a small 'hot fill' 0 % IPA PET bottle - Outside surface

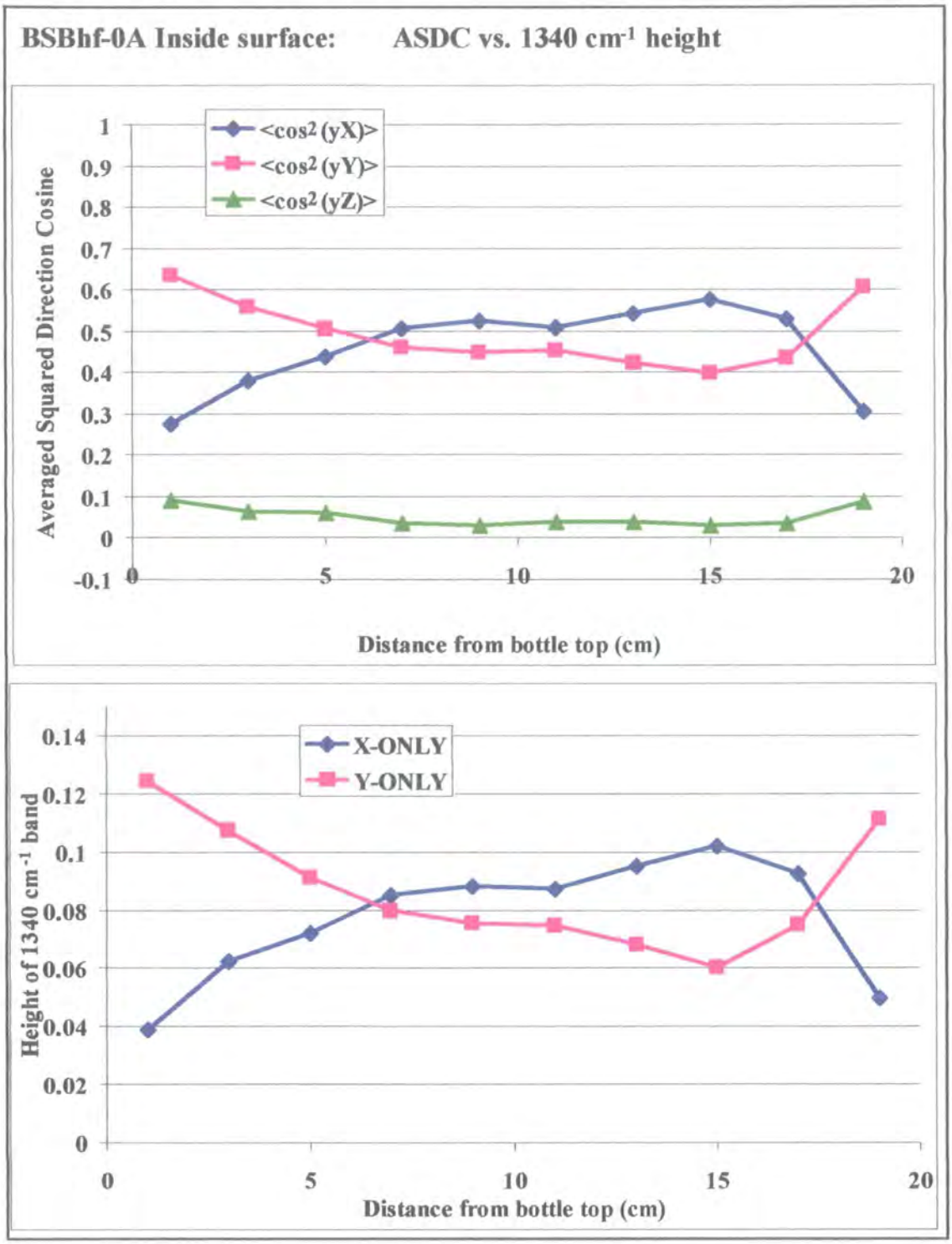

Figure 4-53: Orientation results from a small 'hot fill' 0 % IPA PET bottle - Inside surface

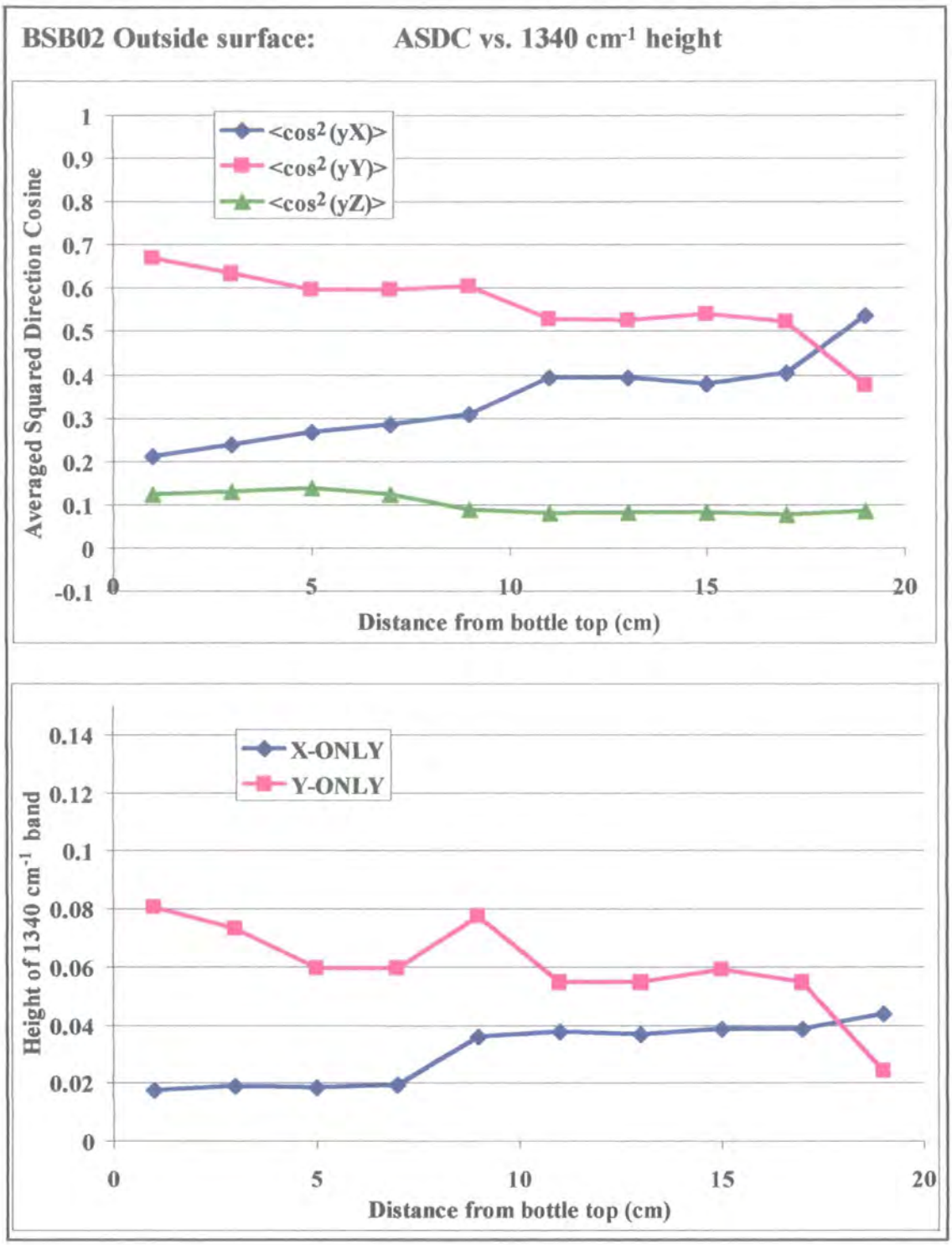

Figure 4-54: Orientation results for the small PET bottle 'BSB02' - Outside surface

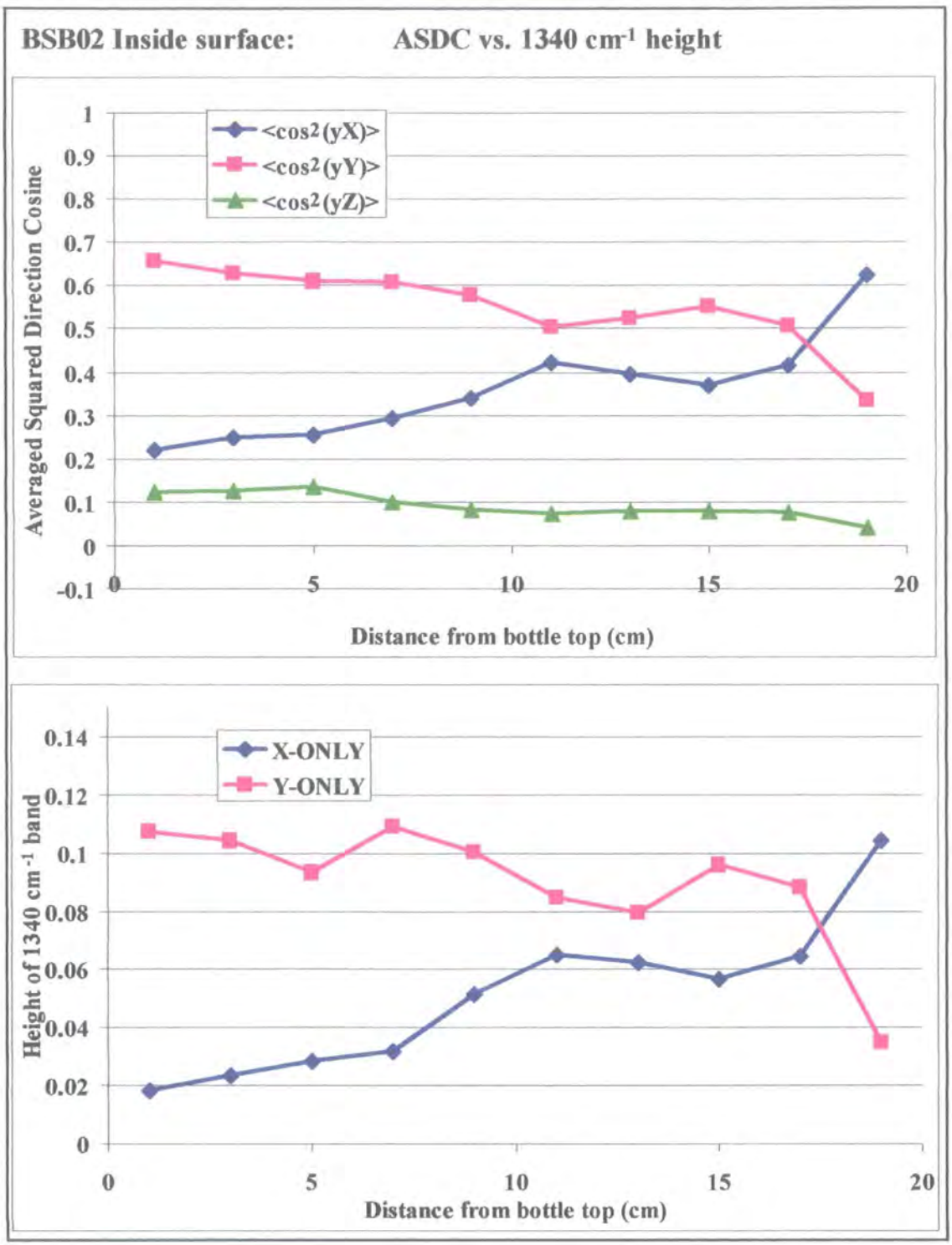

Figure 4-55: Orientation results for the small PET bottle 'BSB02' - Inside surface

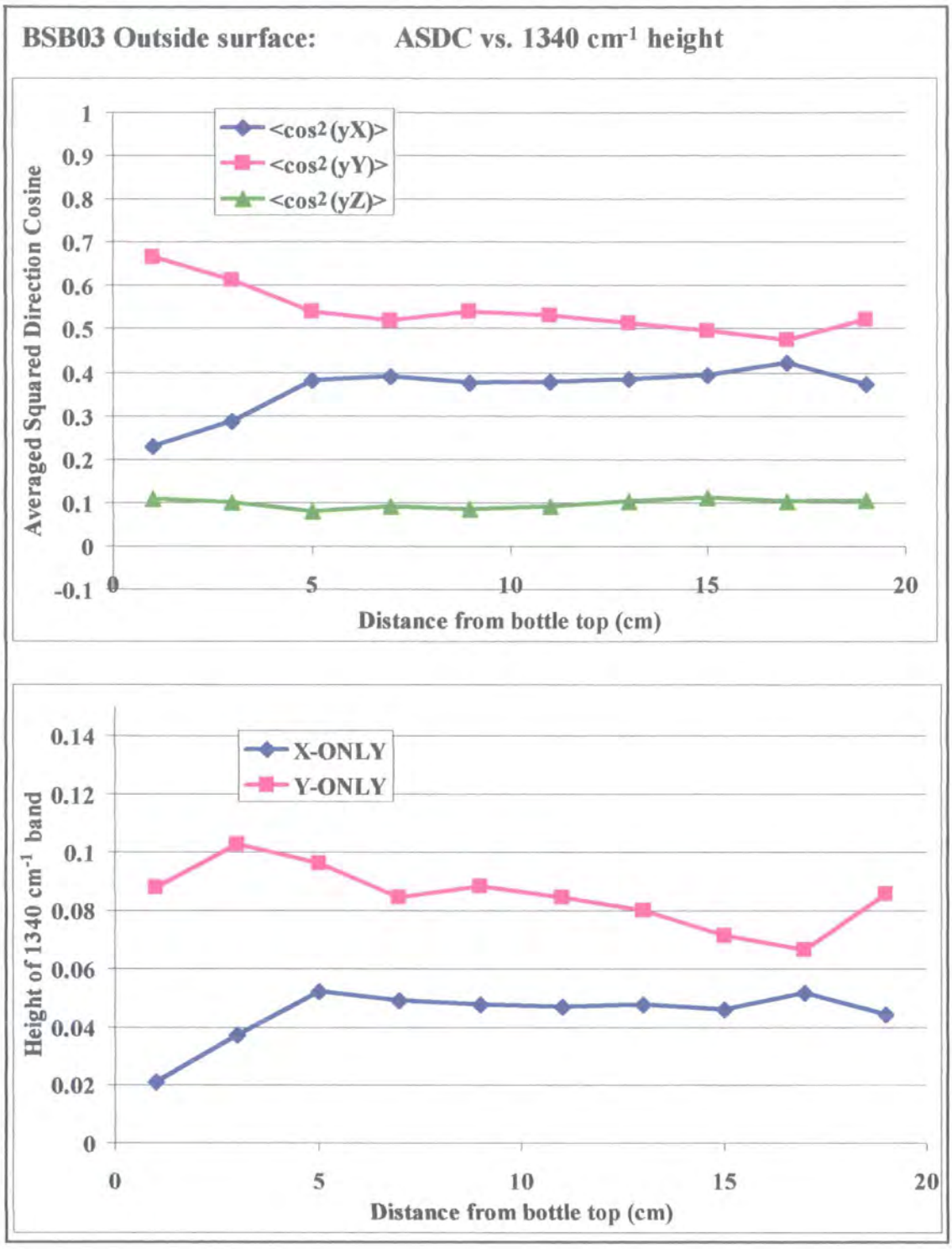

Figure 4-56: Orientation results for the small PET bottle 'BSB03' - Outside surface

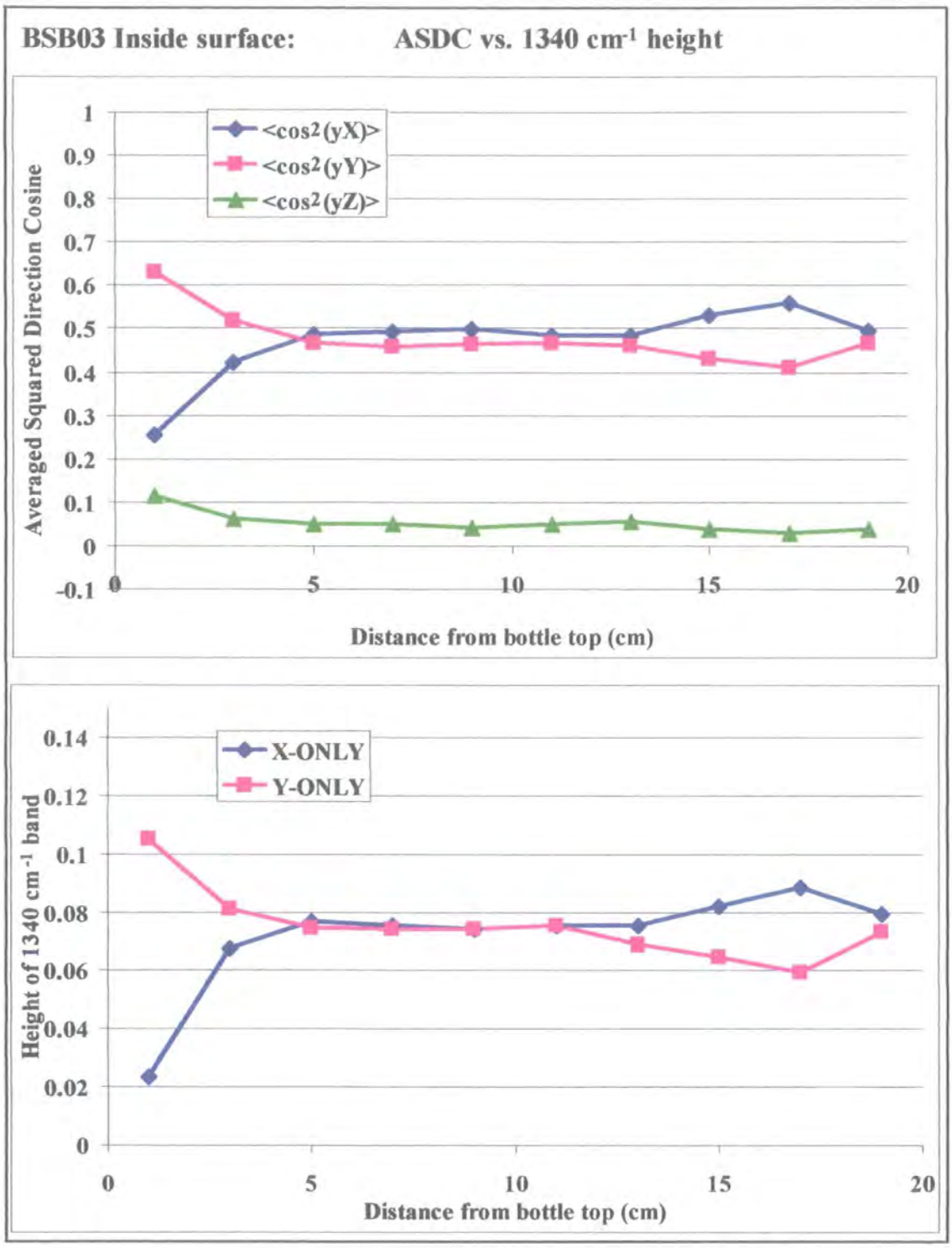

Figure 4-57: Orientation results for the small PET bottle 'BSB03' - Inside surface

4.3.9.1 Small bottle (SB) series analysis

The first thing to note is the exclusion of the small bottle, SB01, from the analysis. The small neck diameter and sharp curves at the shoulder region made this design impossible to flatten onto the ATR crystal in these areas. This shows one of the limitations of this mapping technique. Although the accessory can be used to extract excellent IR spectra from most samples, it fails when rigid, *concave* surfaces are under investigation. Fortunately, the other bottles in the SB series were suitably flexible along the length of the bottle for measurements to be made at all positions along the inner and outer walls.

Instantly it can be seen that for the outside of the Bhf-0A homopolymer bottle (Figure 4-52), the number of chains in the Y-direction dominates, at all positions probed. This is because the preform size is similar for both small and large bottles, so the larger bottles have undergone a comparatively larger radial extension (Unfortunately, the dimensions of the small bottle preforms were not available, but they are typically only slightly smaller than the 2 l preform equivalents). Again, the X-ASDC gradually increases towards the base region until it tails off for the last 3 sample positions. The inverse is true for the Y-ASDC but at a lower ASDC range. This is further evidence that the numbers of chains in the hoop and bottle length directions are traded off against one another. The Z-ASDC remains consistently low, which gives us confidence that neglecting the CH_2 absorption in the Z direction still gives us a good description for the main orientation features.

The inside wall shows the same orientation shape with the ASDCs (see Figure 4-53), with the overall X orientation shifted up by the same amount that the overall Y

orientation has shifted down. The Z-ASDC in this case, remains positive. This is important proof that the negative direction cosines occur at the samples with maximum orientation indicating that the assumption of constant refractive indices in the X, Y and Z sample directions becomes increasingly inaccurate for higher orientations. This may result in the negative Z-ASDC values as larger n_2 values from increased orientation will result in the IR evanescent wave extending to greater depths, and hence leading to greater recorded absorbencies than regions with lower n_2 values.

The CH_2 curves seem to be a little noisier in this case. This might be due to micro-structuring from surface crystallites forming; especially on the outside wall, which has been subjected to elevated temperatures. Despite this noise, the same general characteristics are observed. There is a better correlation between the ASDCs and CH_2 orientation indicators for the inside of the bottle, which has fewer surface crystallites.

The narrow neck diameter of bottle BSB02 proved to be rather difficult to flatten onto the ATR crystal. By making the sample strip sufficiently narrow, the concave curvature at the inner neck surface could be minimised, allowing the measurements to take place. The shape of the bottle is reflected in the orientation trends (see Figure 4-54 and Figure 4-55). It is quite easy to point out the distinctive long neck and shoulder regions in this case. As with the hot-fill bottle, the Y-ASDC dominates for most of the bottle, except for the last point sampled at its base. Unusually, for this bottle series, this is true for the outer and inner walls. The CH_2 equivalents here are slightly disappointing in terms of their correlation with the ASDCs, especially along the inside wall. Remember that we have undergone less of a stretch in these smaller bottles and the CH_2 wag mode at 1340 cm^{-1} relates only to the straight *trans* conformers of the ethylene glycol moiety.

There is a better correlation between the ASDCs and CH_2 curves for bottle BSB03 (see Figure 4-56 and Figure 4-57). This bottle exhibits gentle orientation curves, suggesting similar X and Y orientation at all points along the bottle wall. For the inside wall, both the ASDCs and CH_2 equivalents describe a similar orientation in the X and Y directions along the straight side. As with all the small bottles, all of the direction cosines remain positive. This is likely to be due to the material in the bottle wall being subjected to less deformation, which limits the material to smaller draw ratios, for which our chosen 1410 cm^{-1} normalisation band has proven not to be dependant on orientation.

4.3.10 Summary of the effects of bottle processing conditions, resin composition and bottle size on orientation

The first variable examined was the preform heating time. It was found that for the bottles drawn too cold (i.e. heated for the least number of seconds), the characteristic orientation patterns exhibited by a standard bottle were observed except for a large orientation peak in the hoop direction towards the base of the bottle. As the heating time increased, this peak became progressively smaller until we came to the bottle drawn under the standard conditions. This observation could be accounted for by a slight preference in the heating gradient towards the base of the preform, bringing it to the T_g before the other regions. As the heating times began to surpass the ideal time, the degree of orientation began to fall off. This was a major effect even for the bottle blown after only 5 seconds additional heating time. The bottle blown after 15 extra seconds showed the least amounts of preferential orientation in the X and Y directions. These observations were accounted for by the hotter polymer flowing more easily and hence reducing local stress and strain gradients more readily, so that less orientation occurred.

Bottles blown after too much preform heating would lack tensile strength, as the orientation appears compromised in these studies. A similar conclusion can be reached for the lower IV, lower molecular weight bottle, which showed reduced orientation, presumably due to the effects of decreased chain entanglements.

This work showed that the inclusion of 2 % t-BIPA in the bottle resin produces a stretch-blown PET bottle with an orientation profile that closely matches that of the common 2 % IPA resin. This shows that there is not a detrimental effect on the molecular orientation when t-BIPA is added in small quantities. It is envisaged that the tensile strength of 2 % t-BIPA bottles would be similar to a standard bottle because of the similar orientation levels, but mechanical tests should be performed to verify this. However, the bottle containing 8 % t-BIPA showed reduced orientation levels that could compromise bottle strength. Further work needs to be done on PET resins containing t-BIPA to ensure it could be used in PET bottle manufacture, without compromising bottle performance.

The smaller bottles analysed in this study have different orientation trends to the bigger 2 l equivalents. The proportion of chains lying in the X hoop direction was reduced in these bottles, as the smaller size required less of a hoop extension during the stretch-blow process. The only homopolymer bottle analysed (BSBhf-0A) showed no adverse orientation effects from the experimental heated blow-mould processing route. However, more hot-fill bottles should be analysed to ensure this type of processing has no detrimental effects on the surface orientation.

All these orientation trends for the different bottles can be conveniently visualised by plotting the single parameter of the difference between the X-ASDC and Y-ASDC

values, $\Delta ASDC_{XY}$, as a function of distance from the bottle top for each of the bottles, as the Z-ASDCs are low throughout. Figure 4-58 and Figure 4-59 show these plots for a selection of the 2 l bottles, and the small bottles respectively.

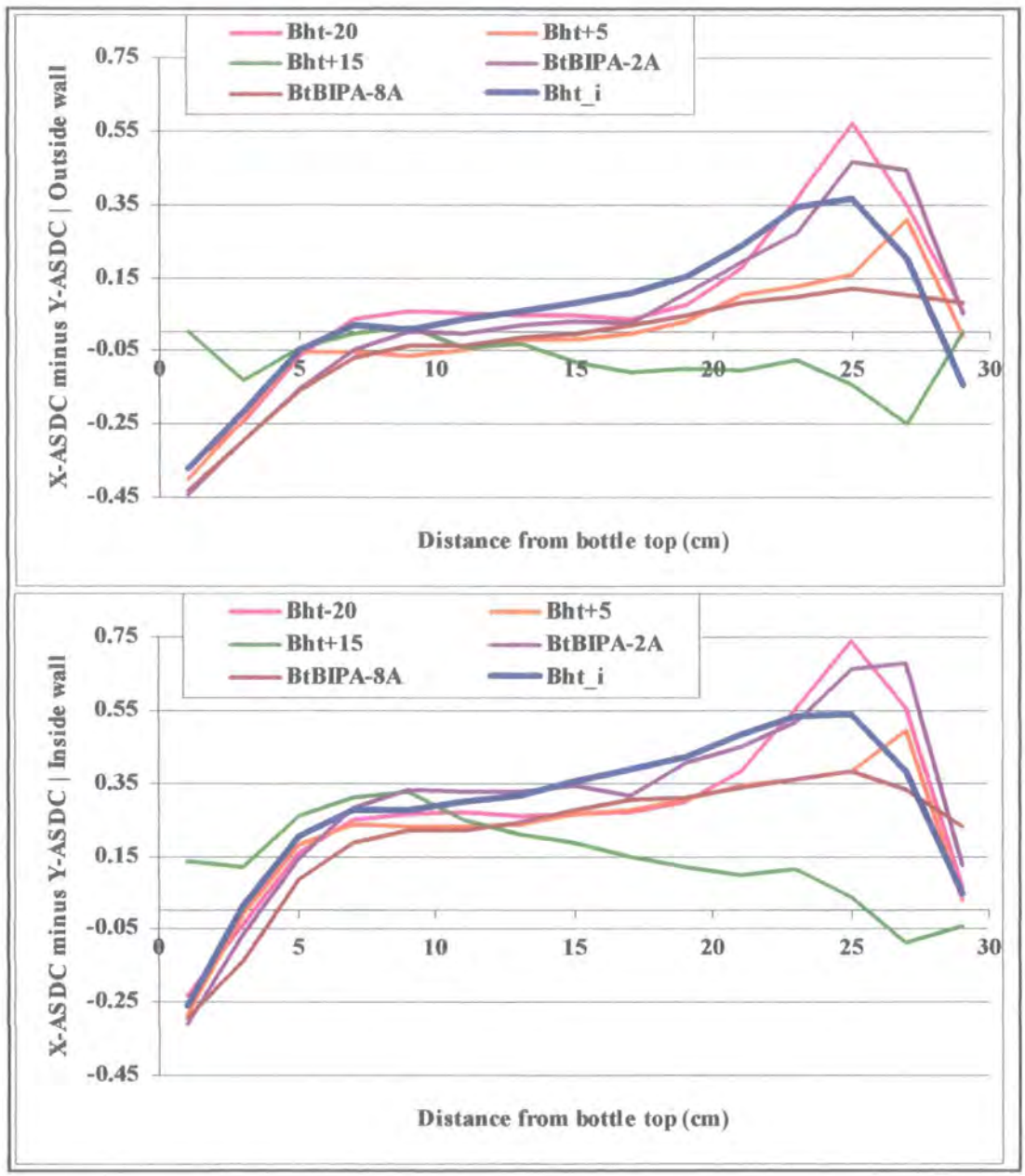

Figure 4-58: Two plots that summarise the orientation trends along the outside wall (upper graph) and inside wall (lower graph) for a selection of the 2 l bottles analysed in this study. The thicker blue line represents the orientation trends in a standard 2 l PET bottle.

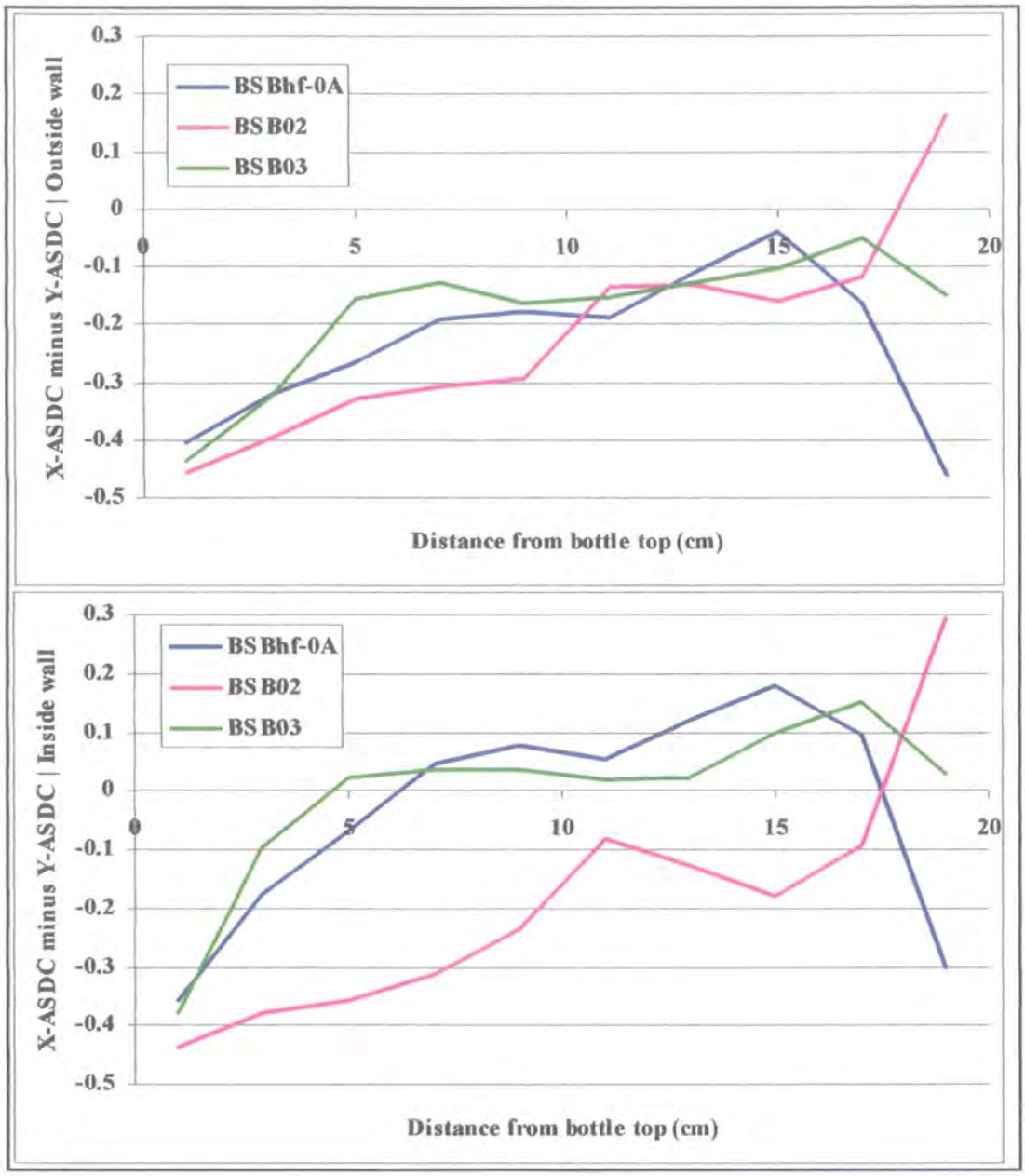

Figure 4-59: Two plots that summarise the orientation trends along the outside wall (upper graph) and inside wall (lower graph) for the small bottles analysed in this study.

4.3.11 Summary of the technique for mapping bottle orientation

The polarised FTIR-ATR orientation theory developed by Everall[5] has been used to map the near surface molecular orientation of PET bottles. The surface probing nature of the ATR technique means it was possible to probe the inner and outer walls

independently to a depth of ~0.5 μm. Measurements were thus taken at 20 mm intervals along the outside wall and again at the equivalent points along the inside wall.

The FTIR data collection was simple and only required minimal sample preparation. The lack of spectrometer purging facilities meant that two new backgrounds had to be collected for each set of four spectra. This was necessary to minimise troublesome water vapour peaks that were found to become a problem with backgrounds more than 20 minutes old. This large number of spectra required to map a bottle meant that the collection of this data was a time-consuming task.

The heights of the CH_2 wag mode of the *trans* ethylene glycol conformation gave excellent results, which appears to match the ASDC results almost exactly. This suggests that the majority of the chains in highly orientated polymers exhibit *trans* conformations. This trend was discovered because the heights of the 1340 cm^{-1} band match the distinctive orientation trends of the ASDC curves. Single measurements of this band would have been impossible to relate to the equivalent value of the ASDC in that sample direction. This CH_2 measurement offers a simple way of measuring the orientation in the two primary sample directions (X & Y) without the need for excessive calculation. It also offers a visual indication of orientation on the spectra when the sample and polariser geometries are either TE_X or TE_Y, which was unavailable before. Only when the crystallinity levels change dramatically throughout the bottle (which is disadvantageous anyway, and easily spotted by uneven cloudiness), or the crystallinity is particularly low, does the CH_2 trace begin to differ more wildly from the actual ASDC curves.

One limitation of this FTIR-ATR mapping technique was the inability to collect FTIR-ATR information from the less flexible regions of the bottles. This particularly affected the smaller bottles and the thicker base and neck regions of the larger bottles. This might be remedied by using a diamond ATR crystal, which allows for much higher pressured to be applied to the reverse of the sample to gain a better contact. However, the less refractive diamond ATR element can give problems with spectral distortions[5]. The application of high pressures could also change the morphology of the sample.

4.4 Measurements of the Benzene ring orientation in PET bottles

The ASDC graphs presented so far have reported the average distribution properties of the chain director, y, into each of the three primary sample directors, X, Y and Z, as depicted in Figure 4-4. These quantities are important, as it is known that the degree and direction of chain orientation can dictate many properties of the polymer including the tensile strength and refractive indices of the drawn film. However, Jarvis *et al.*[9] published the general forms that describe the orientation of all three chain co-ordinates, x, y and z into the three primary sample directions, X, Y and Z.

This section will build on the analysis presented so far, by considering the orientation of the benzene rings relative to the films surface. This type of analysis was mentioned in the original work of Everall *et al.*[5,12], who neglected it in favour of the characterisation of the orientation of the long chain director, y. Again, we shall use the co-ordinate notation adopted by Everall *et al.*[5]. Since Everall didn't specify the x and z chain directors (by simply stating that x and z were mutually perpendicular to y), we were free to assign their directions relative to the benzene ring. In our work, the chain co-

ordinates relate to the benzene ring directions of the PET chains, in the manner shown in Figure 4-60. Our system can thus be transformed in to that of Jarvis *et al.* by replacing x, y, z, X, Y and Z with x^r_1, x^r_3, x^r_2, X_1, X_3 and X_2 respectively.

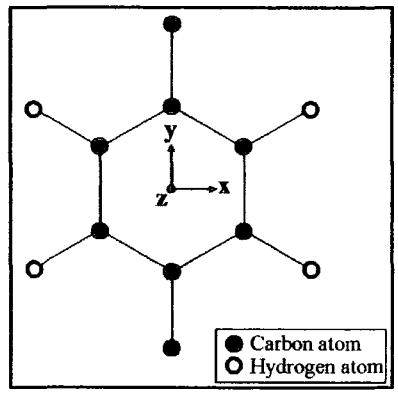

Figure 4-60: Definitions of the x, y and z chain directors, where only the long chain director, y, was considered in the work of Everall et al.[5,12]. Note that the z chain director lies perpendicularly to the plane of the benzene ring.

According to Jarvis *et al.*[9], the ASDC expressions describing the orientation of the x and z directors relative to the primary sample directors are given in Equations 4-34 to 4-39.

$$\left\langle \cos^2(xX) \right\rangle = \frac{1}{3} + \frac{1}{6}P_{200} - P_{220} - P_{202} + P_{222} \qquad \textbf{Equation 4-34}$$

$$\left\langle \cos^2(xY) \right\rangle = \frac{1}{3} - \frac{1}{3}P_{200} + 2P_{202} \qquad \textbf{Equation 4-35}$$

$$\left\langle \cos^2(xZ) \right\rangle = \frac{1}{3} + \frac{1}{6}P_{200} + P_{220} - P_{202} - P_{222} \qquad \textbf{Equation 4-36}$$

$$\left\langle \cos^2(zX) \right\rangle = \frac{1}{3} + \frac{1}{6}P_{200} - P_{220} + P_{202} - P_{222} \qquad \textbf{Equation 4-37}$$

$$\left\langle \cos^2(zY) \right\rangle = \frac{1}{3} - \frac{1}{3}P_{200} - 2P_{202} \qquad \textbf{Equation 4-38}$$

$$\left\langle \cos^2(zZ) \right\rangle = \frac{1}{3} + \frac{1}{6}P_{200} + P_{220} + P_{202} + P_{222} \qquad \textbf{Equation 4-39}$$

where the P_{lmn} values have previously been described in Equations 4-3 to 4-6 in section 4.3.2 of this chapter. The equivalent ASDC expressions for the long chain director, y, are presented as Equations 4-7 to 4-9 of the same section.

A previous study on spin-coated PET films have suggested that the rings orientate preferentially parallel to the film's surface[14], and so it will be interesting to see whether the draw and temperature conditions that the bottles are subjected to also lead to preferential alignment of the benzene rings with the bottles' surfaces. Since the P_{lmn} values required by Equations 4-34 to 4-39 have already been calculated from the dichroic FTIR-ATR spectra using the large spreadsheet (described in section 4.3.4), these new ASDC values could be calculated (from the original IR spectra) after a simple addition to the spreadsheet.

The ASDC between the z axis, which we have nominated to be perpendicular to the benzene ring plane, and the Z film thickness direction reveals the extent of the orientation of the benzene ring relative to the film surface. The higher the value of $\langle\cos^2(zZ)\rangle$ up to a maximum of unity, the higher the preference of the benzene rings to orientate parallel to the film's surface.

The ASDC graphs relating the z director to the X, Y and Z sample directors are presented in the next section. These graphs represent the inner and outer walls of three bottles. These are Bht_i (a standard bottle), BSBhf-0A (a small homopolymer PET bottle) and Bht+15 (a standard bottle blown after too much preform heating time). A photo of these bottles and further details are presented in sections 4.3.6 and 4.3.6.1. Table 3-2 of the Materials chapter details all the PET bottles studied.

4.4.1 Benzene ring orientation ASDC curves for selected PET bottles

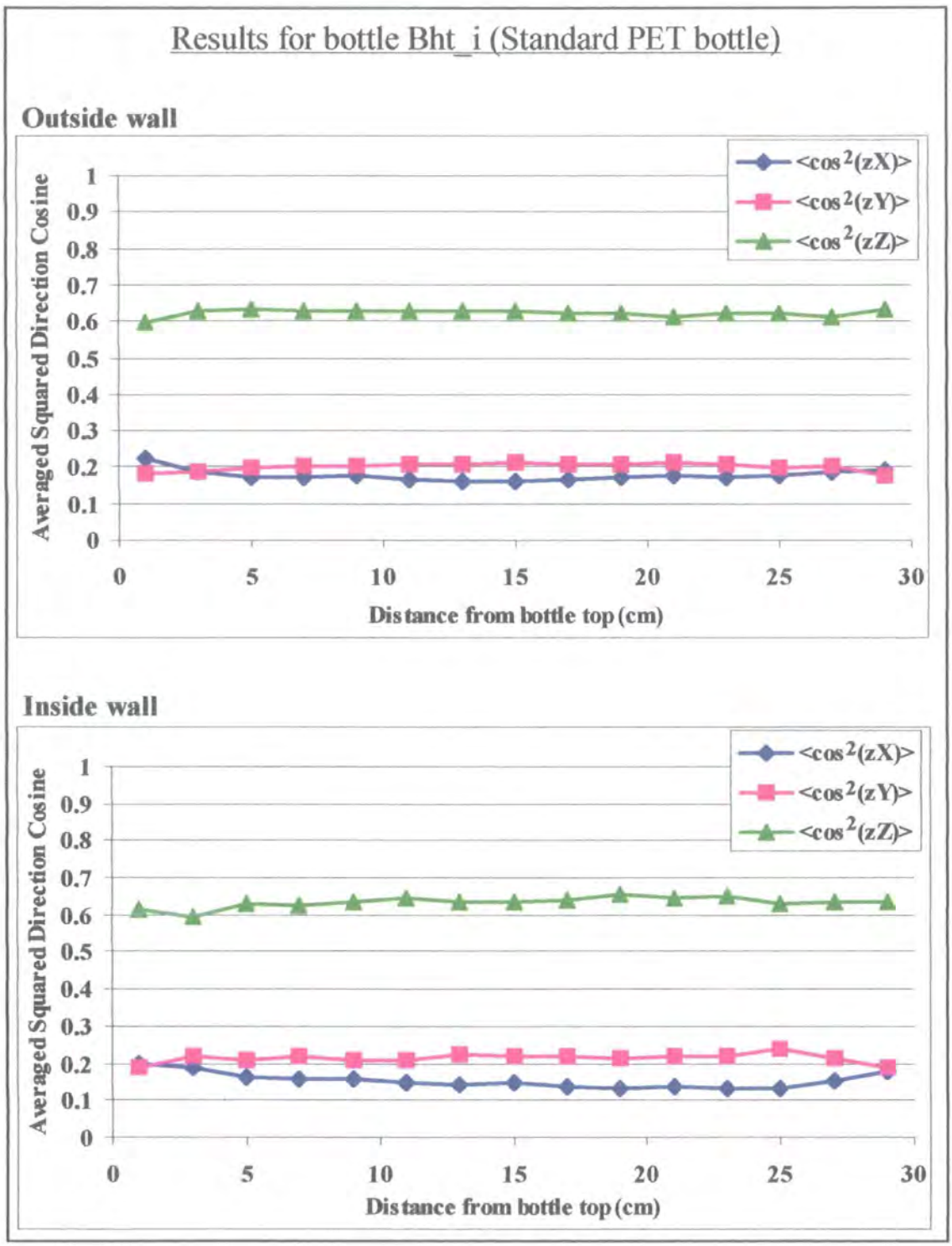

Figure 4-61: The ASDCs between the normal to the benzene ring, z, and the X, Y and Z sample directors for the standard 'Bht-i' bottle, blown after the ideal preform heating time.

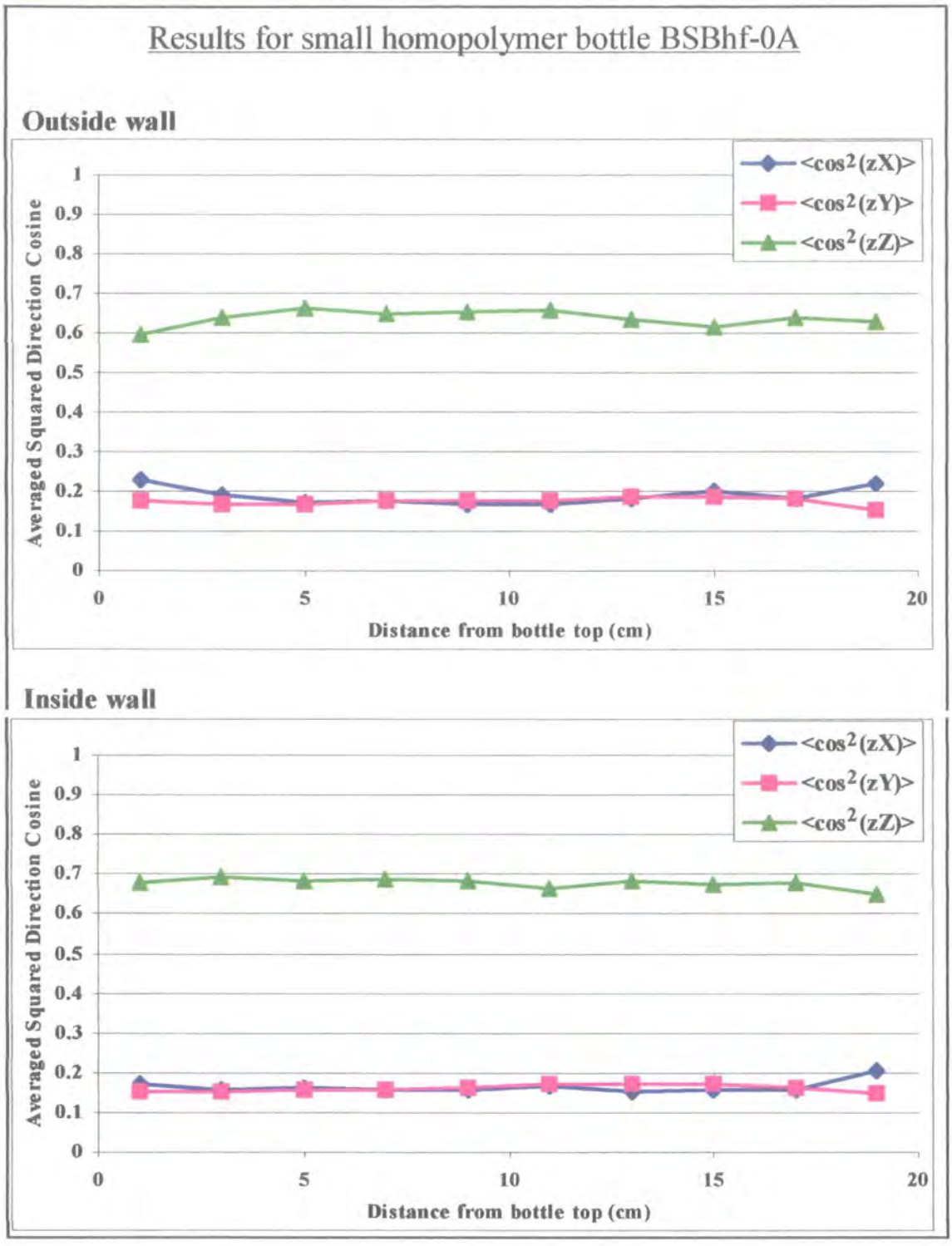

Figure 4-62: The ASDCs between the normal to the benzene ring, z, and the X, Y and Z sample directions for the small homopolymer PET bottle.

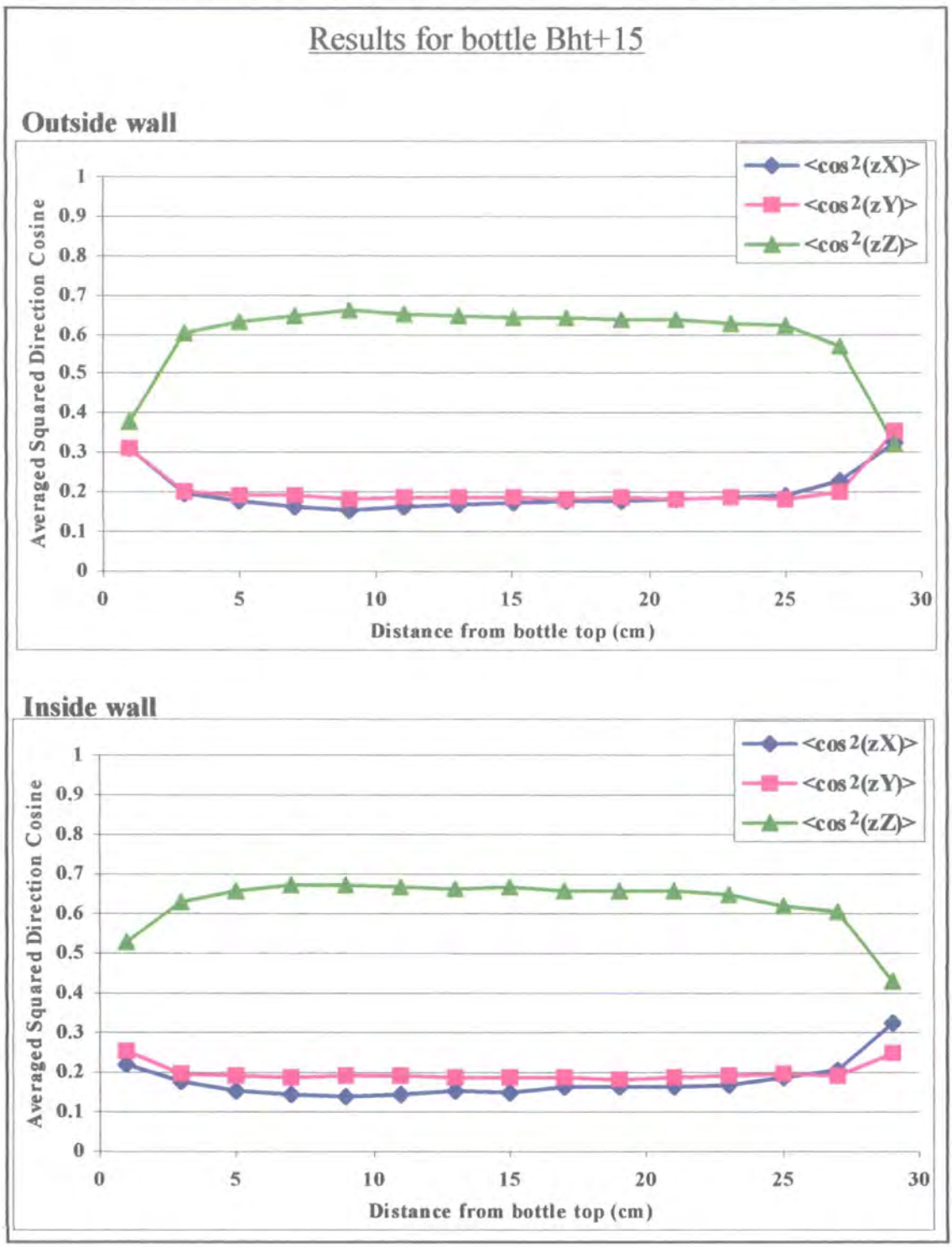

Figure 4-63: The ASDCs between the normal to the benzene ring, z, and the X, Y and Z sample directions for the bottle blown after 15 seconds too much preform heating time.

4.4.2 Discussion of the benzene ring orientation relative to the bottle surface

The dominance of $\langle\cos^2(zZ)\rangle$ throughout Figure 4-61 shows that the benzene rings within the PET chains do indeed preferentially align parallel to the plane of the bottle wall for both the inner and outer surfaces. This general trend was witnessed for all the PET bottles tested (even the small bottles such as BSBhf-0A shown in Figure 4-62), except for the case of the bottle blown after 15 seconds too much preform heating time (Bht+15) as shown in Figure 4-63. For this bottle, the number of benzene rings lying parallel to the film surface decreases at the neck and base regions. For the outer wall (top half of Figure 4-63), each ASDC becomes approximately 1/3, which is the value expected for a random distribution of these units. This can be explained by the neck and base regions of bottle Bht+15 containing spherulitic type crystalline growths (see photograph in Figure 4-25), whose constituent chains and lamellae crystals are randomly positioned. This is in agreement with the explanation for the discrepancy between the y-ASDCs and the 1340 cm^{-1} height measurement on the same bottle (shown in Figure 4-40).

The approximately constant value of $\langle\cos^2(zZ)\rangle$ throughout the entire length of the PET bottles (except the Bht+15 bottle) suggests that the rings preferentially align parallel to the surface regardless of the degree of chain orientation into the machine-draw and transverse-draw film directions. This ring alignment is thus not a consequence of the exact amount of mechanical draw, as our y-ASDC curves have shown that the chain orientation changes considerably along the length of these bottles. This observation is consistent with the discovery that the benzene rings orientate parallel to the film surface in Durell's spin-coated PET specimens[14], which are generally take on a random orientation in the X-Y film plane.

Since the penetration depth associated with this FTIR-ATR technique is less than 1 μm (see Appendix 2), these results do not tell us if the benzene rings preferentially align parallel to the plane of the film in the core of the film. However, Chapter 6 will show that for uniaxially drawn PET films, the rings within the crystalline regions align parallel to the film plane for the film surface (penetration depth ~100 nm into surface) *and* towards the film's core (penetration depth ~90 μm into surface). Further work is needed to see if the same is true for PET bottles.

4.5 An approximate characterisation of β for the 1340 cm^{-1} band

From the bottle orientation results presented in section 4.3, the height of the 1340 cm^{-1} signal is seen to be closely related to the orientation in the sample. The 1340 cm^{-1} heights quoted were taken from the spectra collected using the transverse electric (TE) geometry of Figure 4-5, which probes the sample direction that lies perpendicular to the plane of incidence[5]. The orientation analysis in section 4.3 required just two sample positions, where the primary draw direction lies perpendicular and parallel to the plane of incidence. Further information regarding the near surface orientation could be extracted by setting the polariser to the TE position and positioning the sample draw directions at various angles in the X-Y plane as indicated in Figure 4-64.

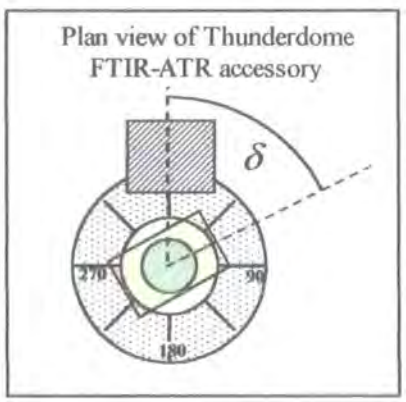

Figure 4-64: The technique used to characterise the 1340 cm^{-1}

Although not strictly a full characterisation of β (the angle between the transition moment and the chain axis), this type of measurement can reveal if the maximum absorbance occurs when the polarised light direction corresponds with the draw direction. This would suggest that the transition moment lies approximately in the chain direction, which was assumed before the analysis of section 4.3. It is therefore expected that an absorbance maximum will occur at $\delta = 90°$ and 270°.

4.5.1 Experimental procedure

The modified Thunderdome ATR accessory and IR polariser were placed into the sample chamber of the FTIR spectrometer. The polariser was adjusted to transmit IR radiation plane-polarised in the transverse electric orientation. A background spectrum was collected. A token was removed from the stretched PET film and clamped in the $\delta = 0$ position on the X-Y plane. A spectrum was recorded using the collection parameters defined in section 4.2.1, page 53. The sample was then unclamped, rotated by 22.5° clockwise on the ATR crystal and re-clamped onto the crystal. A new spectrum was recorded. This process was repeated until the sample had undergone a full 360° rotation on the crystal. The measurements at $\delta = 0°$, 180° and 360° were equivalent and should reveal the same absorbance measurements.

The analysis was performed on a spreadsheet that uses the normalisation procedure described in 4.3.4. Absorbance measurements were taken of the 1340 cm^{-1} and 1714 cm^{-1} bands from the normalised spectra by fitting close baselines and finding the maximum height above these baselines. It was envisaged that the 1340 cm^{-1} band would have a maximum absorbance when the draw direction coincided with the IR excitation (i.e. when $\delta = 0°$). The highly absorbing region at ~1714 cm^{-1} is thought to

contain several components, but is generally associated with stretching modes of the carbonyl C=O double bond[15,16]. The transition moment of this species lies approximately perpendicular to the chain and is included here for comparison with the 1340 cm^{-1} band. This experiment was performed on PET films drawn on a Long stretcher but not subjected to any heat-setting procedures. The localised draw ratios were measured from the distances between ink marks that were drawn onto the films prior to the stretch. These draw ratios are 3.75, 3, 2 and 1 (not drawn). Each of the experiments shown in Figure 4-65 to Figure 4-69 were executed just once, but the similar values at $\delta = 0°$, 180° and 360° (i.e. equivalent sample orientations) demonstrate the excellent reproducibility of these measurements. Note that '0 = BTup' means $\delta = 0$ when the machine draw direction lies perpendicularly to the plane of incidence.

4.5.2 Results for β characterisation

The results for this experiment are provided in Figure 4-65 to Figure 4-69.

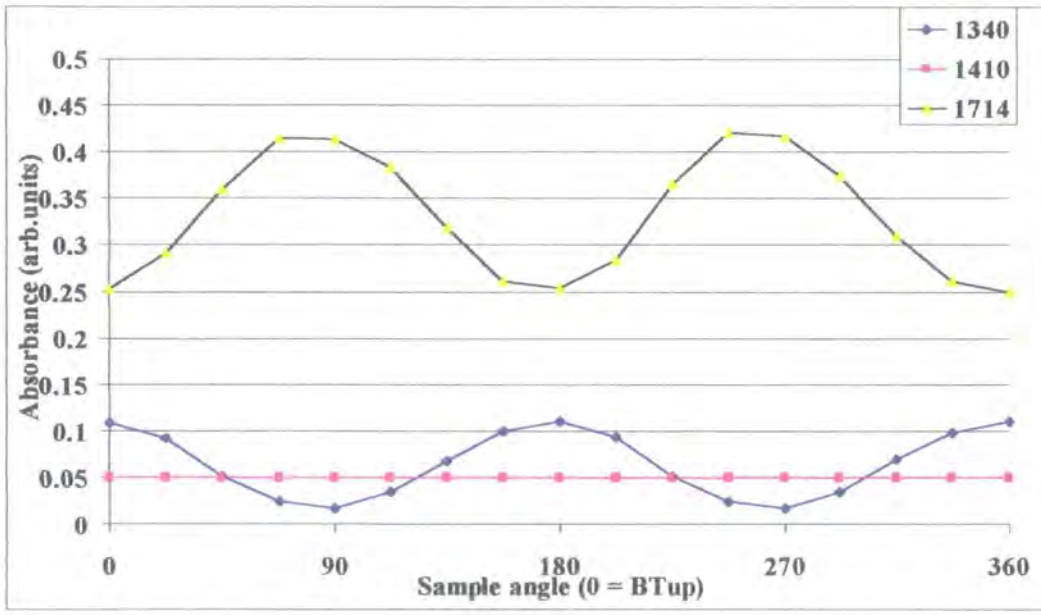

Figure 4-65: E47 Draw ratio 3.75 (no heat set treatment) film. Absorbance of the 1340 cm^{-1}, 1410 cm^{-1} and 1714 cm^{-1} bands relative to the draw direction

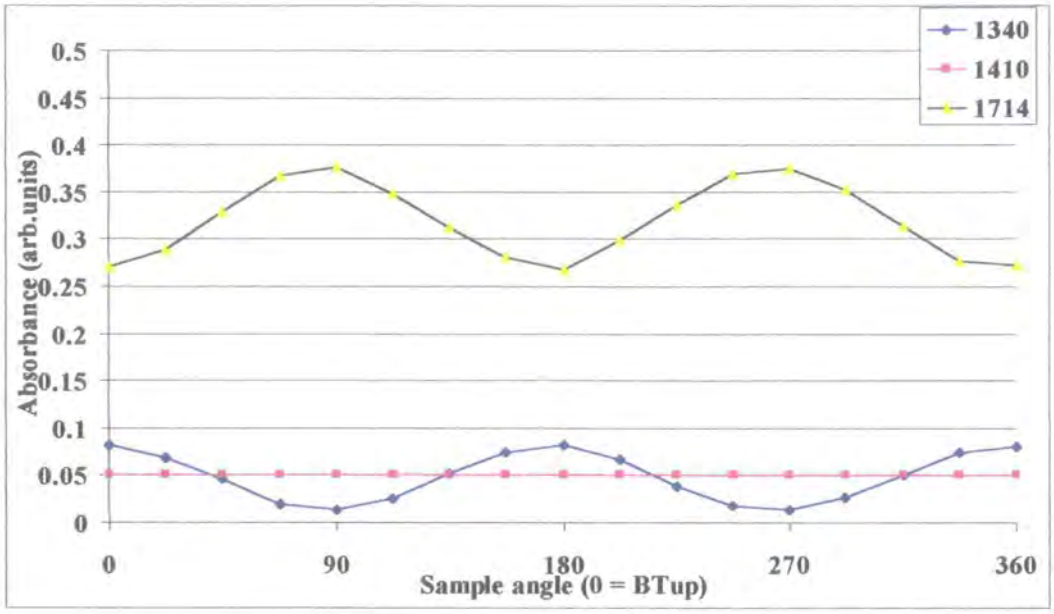

Figure 4-66: E47 Draw ratio 3 (no heat set treatment) film. Absorbance of the 1340 cm^{-1}, 1410 cm^{-1} and 1714 cm^{-1} bands relative to the draw direction

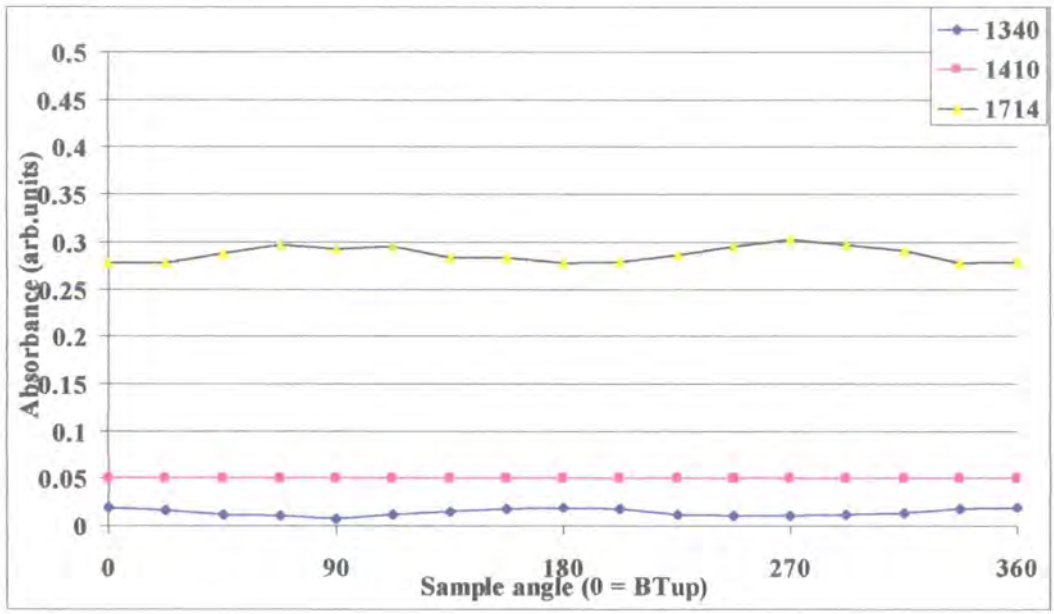

Figure 4-67: E47 Draw ratio 2 (no heat set treatment) film. Absorbance of the 1340 cm^{-1}, 1410 cm^{-1} and 1714 cm^{-1} bands relative to the draw direction

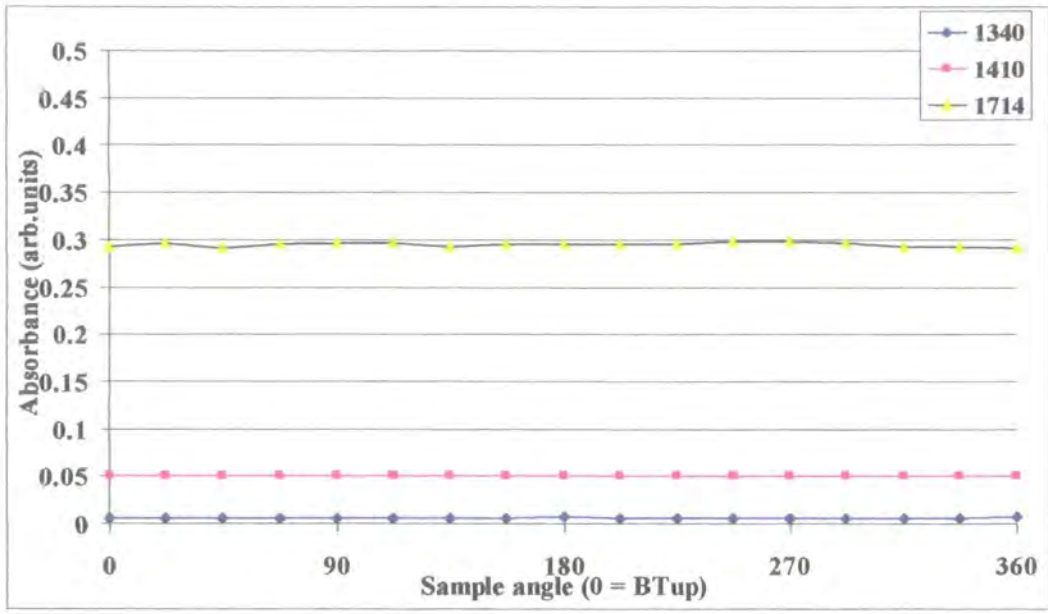

Figure 4-68: E47 no draw (Held in pre-stretch heat for one minute in long stretcher) film. Absorbance of the 1340 cm^{-1}, 1410 cm^{-1} and 1714 cm^{-1} bands relative to the draw direction

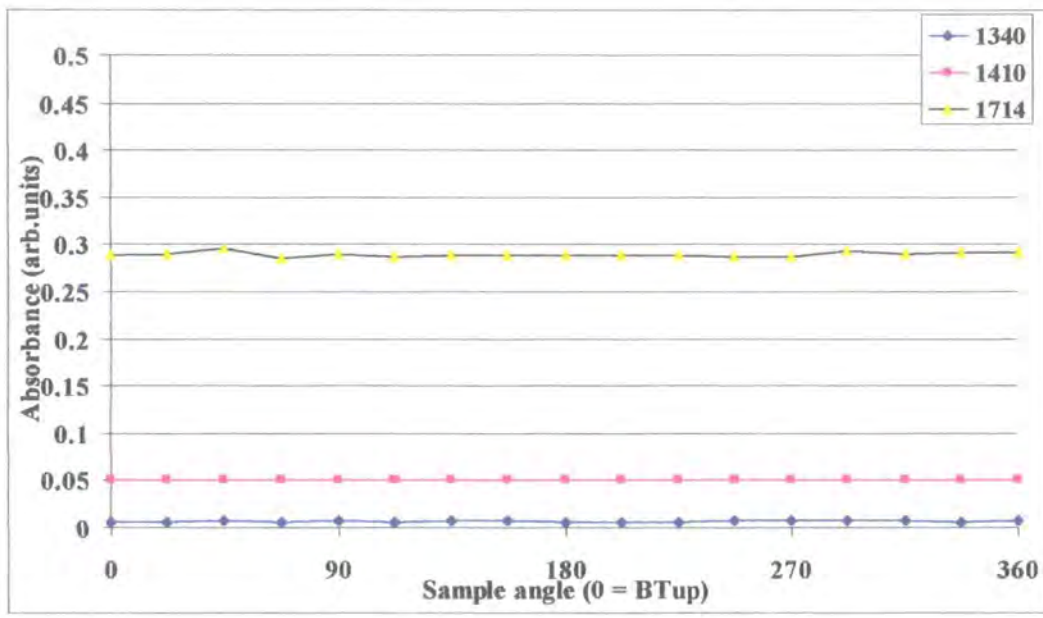

Figure 4-69: E47 no draw (virgin) film. Absorbance of the 1340 cm^{-1}, 1410 cm^{-1} and 1714 cm^{-1} bands relative to the draw direction

4.5.2.1 Analysis of β characterisation

For each spectrum, the height of the 1410 cm^{-1} normalisation band was forced to a value of 0.05 arbitrary absorbance units. Figure 4-65 contains the results for the film drawn to 3.75 draw ratio. The height of the 1340 cm^{-1} band is maximum at $\theta = 0°$, 180° and 360°, as expected. This is consistent with the idea that the transition moment of the CH_2 wagging mode of the *trans* ethylene glycol conformer lies approximately along the chain direction. The band at around 1714 cm^{-1} shows absorbance maxima at 90° and 270°, which is consistent with the idea of the responsible transition moment lying perpendicular to the chain axis.

The phenomenon of the 1340 cm^{-1} band having absorbance maxima in the draw direction is clearly visible for the highly drawn film shown in Figure 4-65 and the film drawn to 3-draw ratio in Figure 4-66. However, this observation is a lot more subtle for the film drawn to 2-draw ratio (Figure 4-67). This shows that measuring orientation from the 1340 cm^{-1} band may prove more difficult from less oriented PET specimens. The un-stretched films shown as Figure 4-68 and Figure 4-69 showed no change in these bands at different δ values. This confirms that the cast film has no orientation as is comes from the chill roll of the stenter process.

It is important here to consider the relation between the dipole transition direction, the chain axis and the sample draw direction, as shown in Figure 4-70. The transition moment subtends an angle β to the chain axis. By considering the axis of rotation around the chain axis, it is clear that the dipole moment can exist in any direction around the chain that forms a hollow cone, as depicted in Figure 4-70. As long as the

average angle,Θ, between the chains and the draw direction is small, the majority of the dipoles will point approximately in the draw direction, for β ~ 0°.

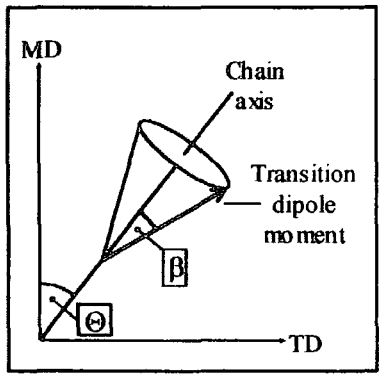

Figure 4-70: A diagram relating the transition dipole moment, chain axis , machine draw (MD) and transverse draw (TD) directions

It has been quoted in the literature[17,18] that the β value for the 1340 cm^{-1} band is 21°. As long as the orientation is high enough for Θ to be small, a large proportion of dipole moments are expected to be aligned approximately in the draw direction. This would explain the observations of Figure 4-65 and Figure 4-66. In contrast, the 1410 cm^{-1} band is expected to have a β value of ~ 54.74° (i.e. $\cos^{-1}[\sqrt{(1/3)}]$), and hence for a highly drawn sample, with Θ ~ 0°, the absorbance of this band would still have equal values in all 3 directions. This, together with the lack of absorbance dependence on crystallinity values, explains why it is such an effective normalisation band for PET. However, any deviation from β = 54.74° for the 1410 cm^{-1} would result in normalisation inaccuracies, especially for sample with very high molecular orientations.

4.6 Conclusions on using the 1340 cm^{-1} band in the IR analysis of PET

To date, the absorbance of the 1340 cm^{-1} band has been almost exclusively associated with the crystallinity within the sample[6,19-21]. The work presented in this thesis has

highlighted the fact that the absorbance of the 1340 cm^{-1} band in pure PET is heavily influenced by three primary factors:

- The crystallinity within the sample
- The direction and amount of chain orientation within the sample
- The polarisation of the incident IR beam

To be confident of retrieving reliable crystallinity measurements using the approach of Belali and Vigourex[22] (Equations 2-1 and 2-2 in literature review), it is highly recommended that the crystallinity measurements are performed after orientation measurements prove that there is no net orientation within the sample. Simply measuring the height of the 1340 cm^{-1} band and attributing an increase in absorbency to an increase in crystallinity is likely to prove particularly erroneous.

To illustrate this point, the normalised IR spectra recorded from a highly oriented region of a standard PET bottle will be considered. All four spectra in Figure 4-71 were recorded from the same sample at the same region, and will therefore have the same degree of crystallinity. Changing the incident polarisation from TE_X to TM_X results in a dramatic change in the 1340 cm^{-1} height. Similarly, a change in the sample orientation from TE_X to TE_Y also has a drastic effect on the band height.

Despite the dependence of the 1340 cm^{-1} on both orientation and crystallinity, section 4.3 demonstrated that the 1340 cm^{-1} orientation mimics the more thorough ASDC methods of Everall[5] for many bottles, including the standard 2 % IPA bottles blown under normal conditions. The 1340 cm^{-1} height measurements became inaccurate when

excess crystallinity formed in the bottle walls (Bht+5 to Bht+15). This was attributed to the measurements recording the extra *trans* conformers packed into these crystals, as it is well known that only *trans* conformers of the ethylene glycol linkages allow for close packing into crystal domains.

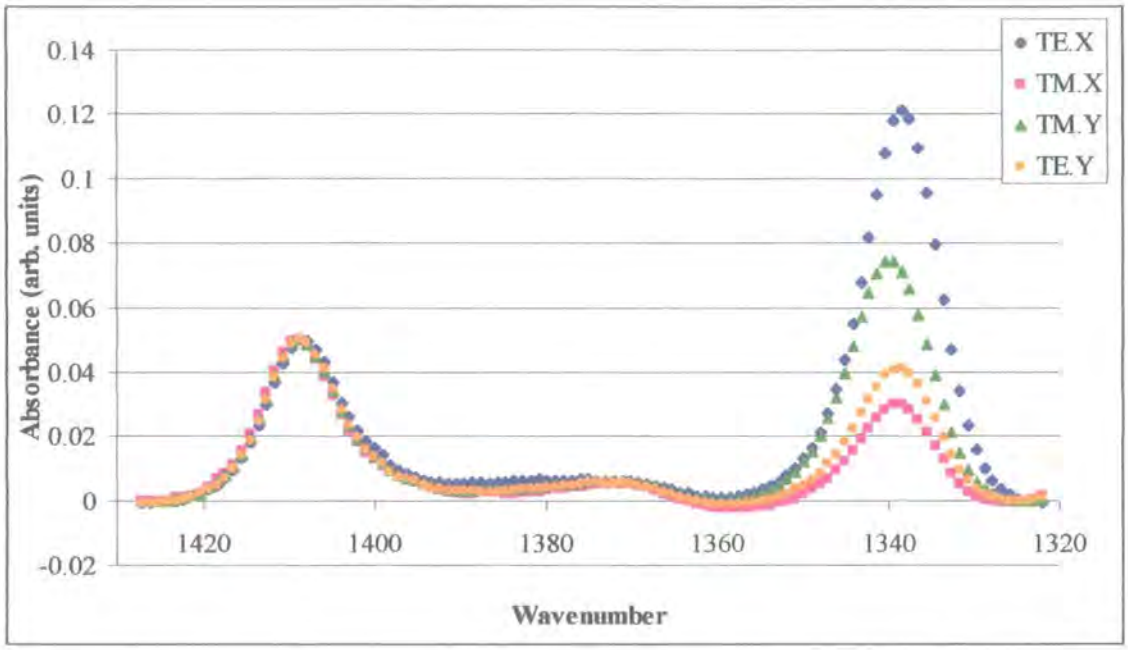

Figure 4-71: The height above a close baseline for the normalised TE_X, TM_X, TM_Y and TE_Y spectra taken from Bht-i, 25 cm from the bottle top of the inner surface

Practically, PET bottles are not industrially blown under such extreme conditions that high levels of uneven crystallinity can form, as the resulting opacity is undesirable. Therefore, 1340 cm^{-1} measurements using the TE_X and TE_Y geometries could offer a quicker way of characterising surface orientation, than the more meticulous approach of Everall and Bibby[5]. This may be useful for quality control tests on standard PET bottles, especially as heating the preform for slightly too long can diminish the orientation while the optical clarity looks fine to the stretch-blow operator.

4.7 Summary for the FTIR studies

In this chapter, we have shown the following:

1. The polarised FTIR-ATR technique is a reliable and reproducible method of determining orientation trends in PET bottles.
2. The use of the 1340 cm^{-1} band absorbencies on the TE_X and TE_Y geometries is particularly simple and yet accurate method of determining orientation trends in PET for all bottles except those showing very uneven crystallinity, or particularly low orientation / crystallinity levels.
3. Increased preform heating times for standard 2 l PET bottles have a detrimental effect on the bottle orientation trends, whereas decreased preform heating times has a less dramatic effect on bottle orientation, but can result in bottle clouding.
4. Using a lower molecular weight PET resin in the 2l bottles also has a detrimental effect on bottle orientation.
5. The inclusion of 2% t-BIPA instead of the usual 2% IPA in the bottle resin had little effect on the orientation properties of the standard 2 l bottle, but the inclusion of 8% t-BIPA seriously compromised the usual orientation trends.
6. The smaller PET bottles show different orientation trends to the larger bottles, with reduced orientation in the hoop direction. The small homopolymer bottle, processed via an experimental heated-blow mould route, displayed no adverse orientation trends.

4.8 References for chapter 4

(1) Banwell, C. N.; McCash, E. M. *Fundamentals of Molecular Spectroscopy*, Fourth ed.; McGraw-Hill, 1994.

(2) Fahrenfort, J.; Visser, W. M. *Spectrochimica Acta* **1962**, *18*, 1103-1116.

(3) Walls, D. J.; Coburn, J. C. *Journal of Polymer Science: Part B: Polymer Physics* **1992**, *30*, 887-897.

(4) Hind, A. R.; Bhargava, S. K.; McKinnon, A. *Advances in Colloid and Interface Science* **2001**, *93*, 91-114.

(5) Everall, N. J.; Bibby, A. *Applied Spectroscopy* **1997**, *51*, 1083-1091.

(6) Kazarian, S. G.; Brantley, N. H.; Eckert, C. A. *Vibrational Spectroscopy* **1999**, *19*, 277-283.

(7) Hodgson, M. R. In *Chemistry - Ph.D. Thesis*; University of Durham, 2000.

(8) Flournoy, P. A.; Schaffers, W. J. *Spectrochimica Acta* **1966**, *22*, 5-13.

(9) Jarvis, D. A.; Hutchinson, I. J.; Bower, D. I.; Ward, I. M. *Polymer* **1980**, *21*, 41-54.

(10) Walls, D. J. *Applied Spectroscopy* **1991**, *45*, 1193-1198.

(11) Cunningham, A.; Ward, I. M. *Polymer* **1974**, *15*, 749-756.

(12) Everall, N.; MacKerron, D.; Winter, D. *Polymer* **2002**, *43*, 4217-4223.

(13) Ajji, A.; Guèvremont, J.; Cole, K. C.; Dumoulin, M. M. *Polymer* **1996**, *37*, 3707-3714.

(14) Durell, M.; MacDonald, J. E.; Trolley, D.; Wehrum, A.; Jukes, P. C.; Jones, R. A. L.; Walker, C. J.; Brown, S. *Europhysics Letters* **2002**, *58*, 844-850.

(15) Daniels, W. W.; Kitson, R. E. *Journal of Polymer Science* **1958**, *XXXIII*, 161-170.

(16) Holland, B. J.; Hay, J. N. *Polymer* **2002**, *43*, 1835-1847.

(17) Matthews, R. G.; Ajji, A.; Dumoulin, M. M.; Prud'homme, R. E. *Polymer* **2000**, *41*, 7139-7145.

(18) Guèvremont, J.; Ajji, A.; Cole, K. C.; Dumoulin, M. M. *Polymer* **1995**, *36*, 3385-3392.

(19) Liu, C.; Jin, Y.; Zhu, Z.; Sun, Y.; Hou, M.; Wang, Z.; Wang, Y.; Zhang, C.; Chen, X.; Liu, J.; Li, B. *Nuclear Instruments and Methods in Physics Research B* **2000**, *169*, 72-77.

(20) Dadsetan, M.; Mirzadeh, H.; Sharifi, N. *Radiation Physics and Chemistry* **1999**, *56*, 597-604.

(21) Freure, C.; Chen, G.; Horton, J. H. *Surface Science* **1999**, *437*, 231-238.

(22) Belali, R.; Vigoureux, J. M. *Applied Spectroscopy* **1994**, *48*, 465-471.

5 Molecular modelling

5.1 Introduction to molecular modelling

Modern computers have the processing and graphical capability to deal with the often complex and processor-intensive modelling of chemical systems[1,2]. For this study it is useful to build a model PET crystal from the generally accepted atomic co-ordinates established by Daubeny *et al.*[3]. The Cerius2 software can then simulate the resulting diffraction from this ideal crystal and the 2θ locations of the peaks can be established. This information can thus be used to index the diffraction signals in the real XRD experiments in chapter 6. One advantage that the simulated pattern has over real semi-crystalline PET data is that the amorphous halo is absent, which enables the weaker peaks to be located. The virtual crystal can be rotated and viewed from a range of angles and perspectives. Another useful tool is the Miller plane visualisation which can be drawn onto the crystal structure to help envisage the diffraction planes which give rise to the most intense diffraction peaks.

The molecular modelling and simulations were performed at Durham University's Department of Chemistry on a Silicon Graphics workstation running Cerius2 molecular simulations software.

5.2 Visualisations of the model PET crystals

The generally accepted unit cell parameters for PET were determined in 1954 by Daubeny *et al.*[3] In this work, the atomic co-ordinates of the electron-rich carbon and

oxygen atoms (compared to hydrogen) were deduced from the positions and relative intensities of measured X-ray reflections. Although authors have since repeated this work with more advanced technology[4], the unit cell parameters reported by Daubeny are considered the most generally accepted by the vast majority of authors who use XRD to study PET[5-7]. The unit cell parameters are listed in Figure 5-1.

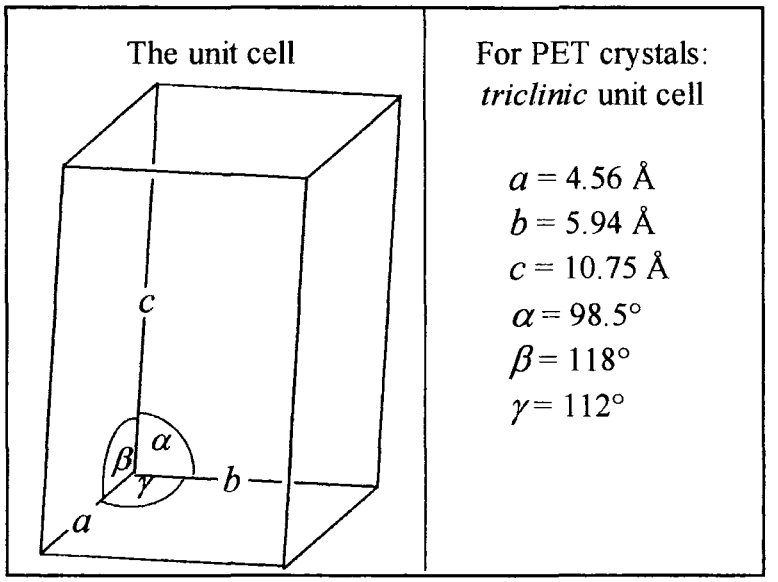

Figure 5-1: The unit cell parameters deduced by Daubeny[3]

The unit is classed as triclinic as $a \neq b \neq c$ and $\alpha \neq \beta \neq \gamma$. The unit cell parameters shown in Figure 5-1 were inputted into the Cerius2 software, along with the atomic coordinates of the carbon and oxygen atoms listed in Table 2-3, in the literature review. The locations of the hydrogen atoms cannot be determined from XRD experiments, as these atoms do not posses a high enough electron density to contribute to the observed diffraction signals. Chapter 6 will describe how XRD studies the interaction between X-rays and the electron density surrounding atoms and molecules.

A crystal section containing one triclinic unit cell is shown in Figure 5-2, along with a repeat unit lying across each of the c-axes to show the nature of the chain packing. Note

that a single isolated unit cell would only contain one repeat unit – $CO.C_6H_4.CO.O.(CH_2)_2O$-.

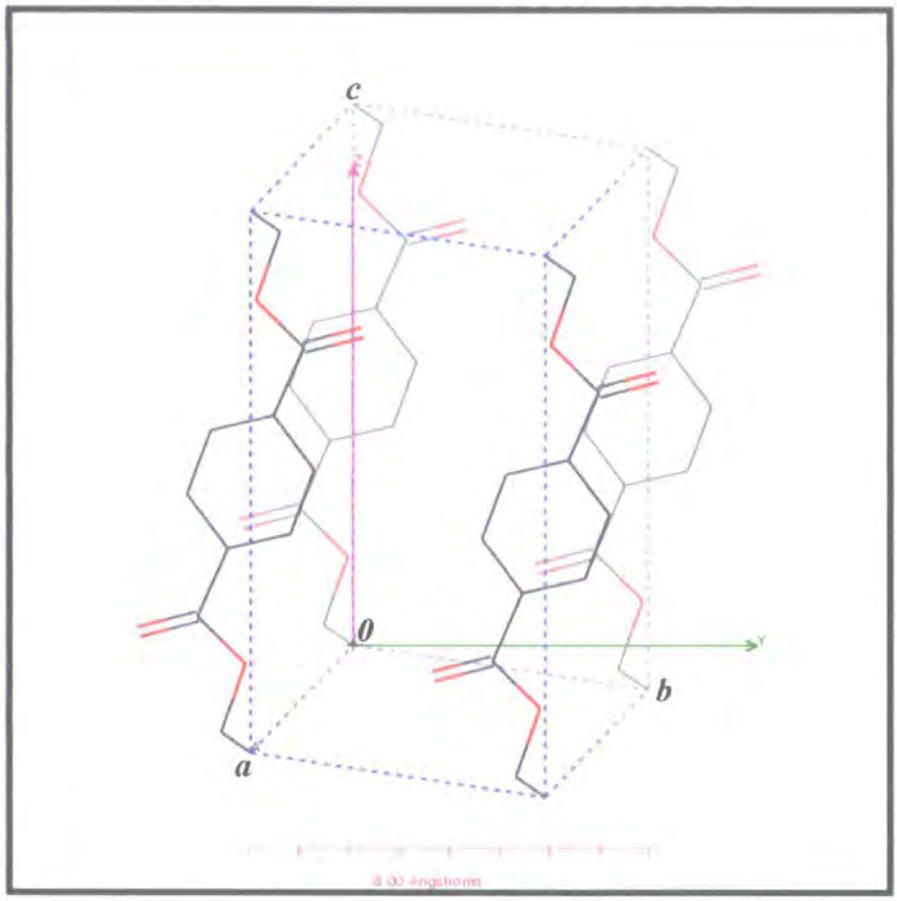

Figure 5-2: A visualisation of a PET unit cell using the atomic parameters of Daubeny *et al.*

In Figure 5-2, the grey sections represent bonds to carbon atoms, the red sections represent bonds to oxygen atoms and the dashed blue lines show the outline of the unit cell.

5.2.1 Calculated wide-angle X-ray diffraction from a simulated PET crystal

Once the idealised virtual crystal has been constructed, the resulting diffraction pattern can be calculated for a given incident X-ray wavelength. For these simulations, the wavelength of 1.5418 Å was selected, which corresponds to the intense Copper K_α peak selected by most lab-based tube and rotating anode generators. These diffraction

patterns and signal 2θ positions should not be compared directly to data collected from PET at Synchrotron radiation facilities, which tend to use other wavelengths. For example, Mahendrasingam *et al.*[6] recently used λ = 0.95 Å at beamline ID2A at the ESRF in Grenoble, but has also used λ = 0.92 Å at beamline ID13 at the same synchrotron[8].

5.2.1.1 Simulated diffraction from a typical film system

The simulated diffraction pattern shown in Figure 5-3 depicts a collection of ideal PET crystals of dimension a = 300, b = 300 and c = 30 Å, with the crystal *c*-axes preferentially oriented along the vertical draw direction but random orientation of the *a* and *b* axes about the *c*-axis.

Figure 5-3: A simulated X-ray 'fibre' diffraction from oriented PET crystals

An orientation half-width of 15° between the crystal c-axes and the draw direction was artificially imposed to mimic a more realistic film system, as perfect orientation in drawn polymer films is never achieved. This manifests itself as the arcing nature of the reflections. This simulation doesn't take into account the amorphous chains which would add a broad 'halo' between 2θ angles of around 15° and 25°, due to the approximately Gaussian distribution of interchain spacings. The fibre diffraction image shown in Figure 5-3 best describes the diffraction from a uniaxially drawn PET film, but two other classes of diffraction image will be briefly described.

5.2.1.2 Powder diffraction and highly oriented fibre diffraction simulations

A collection of randomly orientated crystals (i.e. a *powder*) gives rise to a diffraction pattern showing a series of concentric rings. Alternatively, perfectly oriented *fibre* diffraction would give rise to discrete intense peaks, as shown in Figure 5-4.

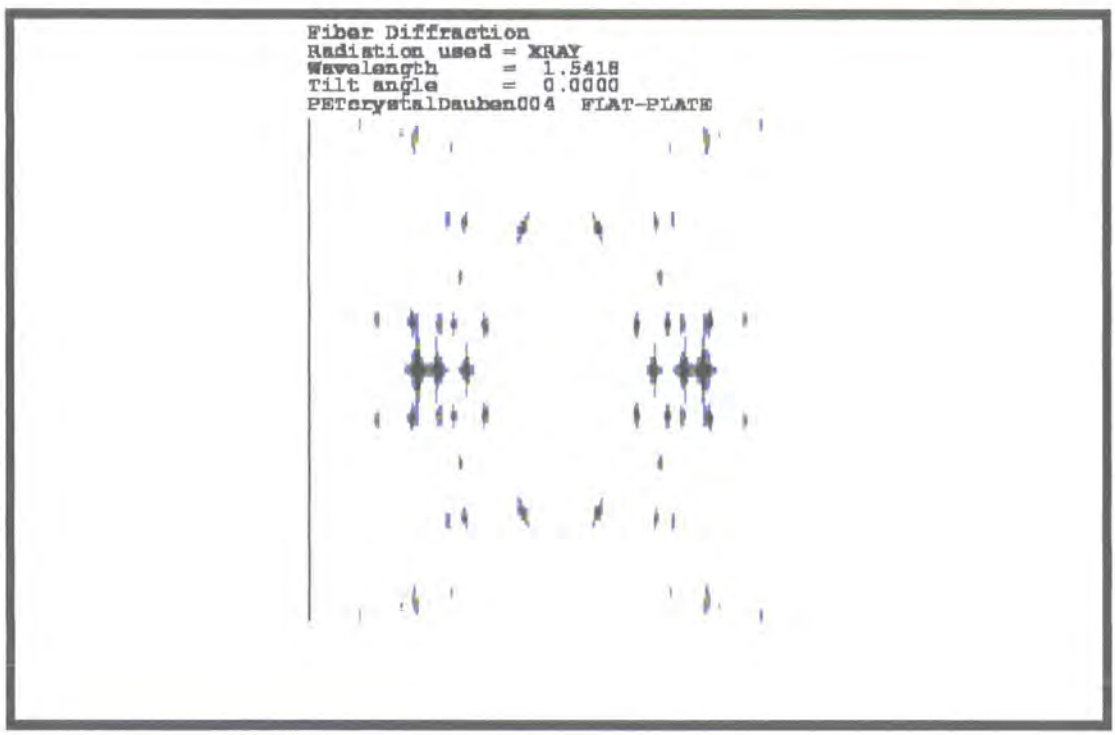

Figure 5-4: A highly oriented fibre simulation showing intense discrete peaks

For authors such as Daubeny[3] who set out to calculate the unit cell parameters for PET crystals, the aim is to achieve a pattern as close to the highly oriented fibre pattern as possible. This is usually achieved by collecting diffraction patterns from highly drawn, highly annealed fibres. A high sample crystallinity and crystallite orientation are required to provide accuracy in intensity measurements and well-defined reflections for accurate indexing, respectively[4]. It is important to note that attempts to calculate unit cell parameters from patterns such as Figure 5-3 would typically result in a less accurate unit cell determination than a similar attempt from Figure 5-4, since the spreading of the diffraction signals over wider arcs leads to a lower intensity above background.

5.2.2 Determining 2θ locations from simulated diffraction data

For any given crystal unit cell and incident X-ray wavelength, the signal from any particular (hkl) planes will appear at a set 2θ angle. This is true regardless of whether the diffraction pattern was that of a powder or fibre geometry. It is useful to monitor the 2θ positions of X-ray diffraction signals by taking a digital 'slice' through the image. This involves recording the intensity at every point along a line that cuts through the centre of a particular diffraction signal. Every point along the line is attributed to a 2θ angle by knowing the sample to detector distance and applying elementary trigonometry. This is similar to the 'Chi scan' that will be used in the XRD experiments of chapter 6. The output of a slice operation is thus an intensity versus 2θ curve, where the centre of the peak maxima corresponds to the measured 2θ position.

A radial scan through the equatorial reflections of Figure 5-3 is provided in Figure 5-5.

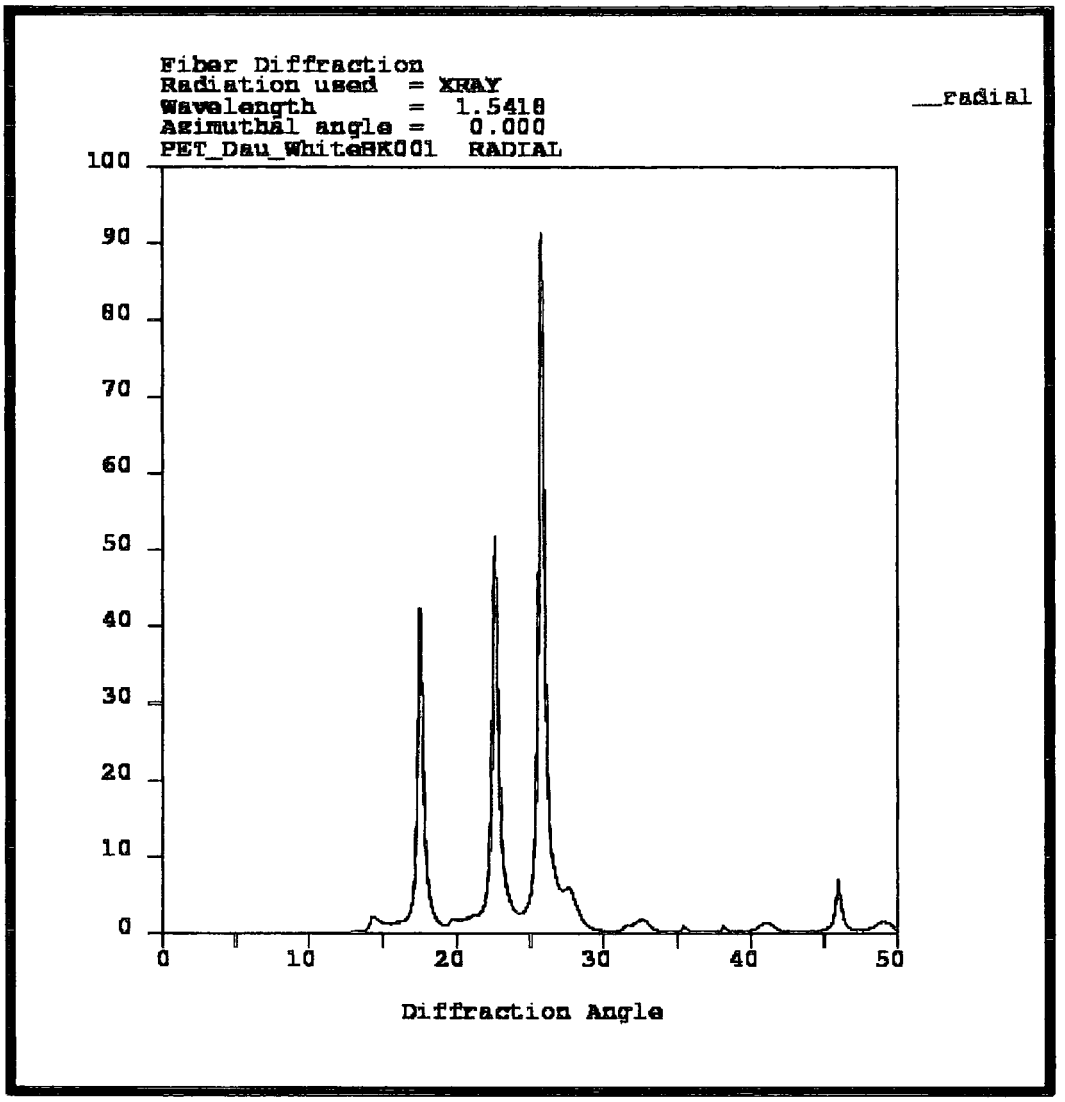

Figure 5-5: An intensity versus 2θ slice through the equator of Figure 5-3

The 2θ locations of the most intense diffraction peaks according to this simulation are listed in Table 5-1, where the d-spacing between the specified *(hkl)* miller planes is quoted in Angstroms, the 2θ locations are in degrees and the intensities are relative to the most intense (100) signal. The 2θ locations from the same simulation are also ordered from small to large 2θ angles in Table 5-2.

Table 5-1: The 30 most intense X-ray peaks from PET crystals in a fibre orientation according to the Cerius2 simulation

h	k	l	d-spacing	2-theta	Intensity (%)
1	0	0	3.467	25.694	100
1	-1	0	3.9439	22.544	48.11
0	1	0	5.0587	17.531	31.98
1	0	-5	2.1188	42.671	29.79
1	-1	1	3.2044	27.841	15.07
0	1	-1	5.3992	16.417	12.32
2	-1	0	1.9768	45.905	11.47
1	0	-3	3.3712	26.438	9.56
0	2	-4	2.1158	42.734	8.03
1	-1	-1	4.1701	21.306	7.32
0	0	3	2.9061	30.766	6.85
1	-1	-2	3.603	24.709	5.69
1	2	-4	1.9208	47.324	5.3
0	1	1	3.7753	23.565	5.12
2	0	-5	1.8798	48.42	4.93
1	1	-3	2.7602	32.436	4.15
0	2	-1	2.7358	32.732	3.44
2	-1	-4	2.0622	43.903	3.41
1	-1	-4	2.2644	39.807	2.68
1	-3	2	1.884	48.306	2.47
1	-3	-1	1.8569	49.058	2.38
2	-1	-1	2.1758	41.502	1.97
2	-1	-2	2.2769	39.58	1.97
0	2	1	2.2069	40.89	1.88
2	-1	-5	1.8388	49.572	1.77
1	2	-1	1.8415	49.495	1.58
1	-2	-1	2.7248	32.868	1.41
1	-1	-5	1.8459	49.37	1.39
0	1	-3	3.1054	28.747	1.37
1	1	0	2.3554	38.209	1.32

In Table 5-1 and Table 5-2, the '1 -1 0' (hkl) notation refers to the $(1\bar{1}0)$ Miller planes and the '1 -1 -2' refers to the $(1\bar{1}\bar{2})$ Miller planes, etc.

Table 5-2: The simulated fibre diffraction signals ordered from low to high 2θ values

h	k	l	d-spacing	2-theta	Intensity (%)
0	0	1	8.7183	10.146	0.88
0	1	-1	5.3992	16.417	32.7
0	1	0	5.0587	17.531	46.03
0	0	2	4.3591	20.372	0.64
0	1	-2	4.2317	20.992	0
1	-1	-1	4.1701	21.306	16.11
1	0	-1	4.1352	21.488	0.15
1	0	-2	4.0798	21.783	1.5
1	-1	0	3.9439	22.544	54.4
0	1	1	3.7753	23.565	10.4
1	-1	-2	3.603	24.709	8.76
1	0	0	3.467	25.694	100
1	0	-3	3.3712	26.438	6.31
1	-1	1	3.2044	27.841	26.72
0	1	-3	3.1054	28.747	1.24
0	0	3	2.9061	30.766	6.8
1	1	-2	2.8715	31.145	0.12
1	-1	-3	2.8528	31.355	0.04
1	-2	0	2.8451	31.442	0.47
0	1	2	2.7999	31.963	0.72
1	1	-3	2.7602	32.436	4.28
0	2	-1	2.7358	32.732	5.34
1	0	1	2.7295	32.81	0.22
1	-2	-1	2.7248	32.868	2.18
0	2	-2	2.6996	33.184	0.25
1	1	-1	2.6957	33.233	0.12
1	-2	1	2.685	33.37	0.18
1	0	-4	2.6517	33.801	0
0	2	0	2.5294	35.489	0.93
1	-1	2	2.5254	35.547	0.32
-	-	-	-	-	-
1	0	-5	2.1188	42.671	6.47

5.2.3 Miller plane visualisations

Bragg's law (Equation 6-1) and the conditions required for X-ray diffraction to occur will be described fully in chapter 6. For now, it is sufficient to know that the incident X-ray beam interacts with diffraction planes within the crystal. The diffraction planes are typically described by their Miller indices (hkl). A visualisation of the (100), $(1\bar{1}0)$ and (010) Miller planes superimposed on a group of four unit cells are shown in Figure 5-6.

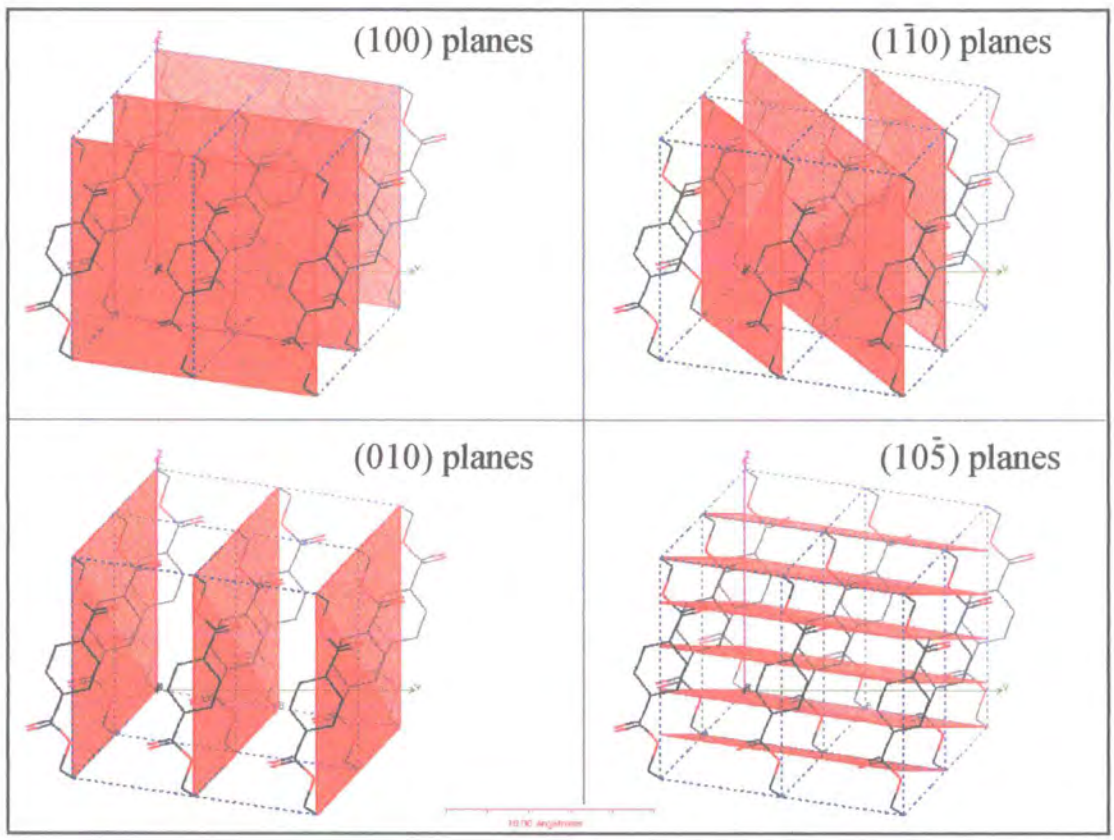

Figure 5-6: Miller planes that give rise to the four most intense diffraction signals in PET crystals

5.2.3.1 The $(10\bar{5})$ Miller planes

Crystallite orientation determination is commonly achieved by observing the reflection due to the $(10\bar{5})$ planes. The visualisation presented in Figure 5-7 illustrate why the $(10\bar{5})$ peak is such a useful orientation indicator in semi-crystalline PET. Figure 5-7 part a) shows the $(10\bar{5})$ miller planes oriented perpendicularly to the page and Figure 5-7 part b) shows the same plane oriented parallel to the page. These visualisations clearly show that the $(10\bar{5})$ planes are perpendicular to the chains within the PET crystal and thus a determination of the orientation of the $(10\bar{5})$ planes leads to a direct determination of crystallite orientation. Bhatt *et al.*[4] states that the $(10\bar{5})$ diffraction signal, corresponding to the interplanar $(10\bar{5})$ direction, is within just 10° of the fibre direction.

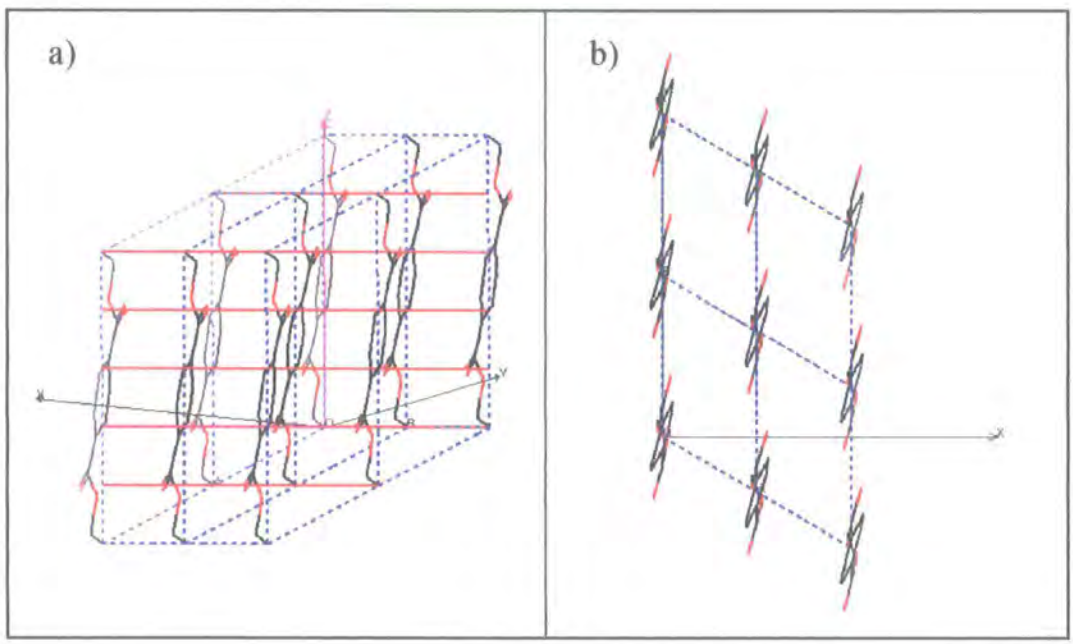

Figure 5-7: Visualisations that illustrate why the $(10\bar{5})$ planes are suited to orientation studies

The $(10\bar{5})$ planes are separated by a relatively small d-spacing (2.1188 Å), which means that its associated diffraction peak occurs at a large 2θ value of 42.671°. Unfortunately, this convenient peak lies on the edge of the detectable range of our detector and so the alternative approach of using the (100), $(1\bar{1}0)$ and (010) peaks was adopted for the X-ray crystallite orientation analysis. Not only is the extraction of crystallite orientation information more complicated from these three planes compared to the $(10\bar{5})$, but also peak measurements are complicated by the broad amorphous halo that spans the 2θ range of these three signals. A full description of how crystallite orientation can be determined from the three intense (hk0) signals will be described in chapter 6.

5.3 Summary for the molecular modelling studies

In this chapter, the following have been performed:

1. A model PET crystal has been built by inputting the generally excepted atomic co-ordinates of Daubeny et al. into the Cerius2 molecular simulations software.

2. A simulated diffraction pattern has been calculated by considering a collection of idealised PET crystals and an incident X-ray wavelength of λ = 1.5418 Å, which corresponds to the X-ray frequency commonly selected for use with most lab-based XRD systems.

3. The thirty most intense signals of the simulated diffraction have been tabulated, which can be used to aid the indexing of signals produced during real X-ray diffraction experiments.

4. The Miller planes, which give rise to the four most intense diffraction signals of PET, have been projected onto crystal visualisations.

5. The visualisations demonstrate that the $(10\bar{5})$ planes are suited to crystallite orientation determination in PET, as the normal to these planes lie approximately in the chain direction. Unfortunately, the $(10\overline{5})$ diffraction signals occur at large diffraction angles (42.6°), which is why several authors have thus sought alternative methods, as discussed in the literature review.

5.4 References for chapter 5

(1) Haire, K. R.; Windle, A. H. *Computational and Theoretical Polymer Science* **2001**, *11*, 227-240.

(2) Okada, O.; Oka, K.; Kuwajima, S.; Toyoda, S.; Tanabe, K. *Computational and Theoretical Polymer Science* **2000**, *10*, 371-381.

(3) Daubeny, R. D. P.; Bunn, C. W.; Brown, C. J. *Proc. Roy. Soc. Lon.* **1954**, *A226*, 531-542.

(4) Bhatt, G. M.; Bell, J. P.; Knox, J. R. *Journal of Polymer Science: Polymer Physics Edition* **1976**, *14*, 373-376.

(5) Göschel, U. *Polymer* **1996**, *37*, 4049-4059.

(6) Mahendrasingam, A.; Blundell, D. J.; Wright, A. K.; Urban, V.; Narayanan, T.; Fuller, W. *Polymer* **2003**, *44*, 5915-5925.

(7) Asano, T.; Calleja, F. J. B.; Flores, A.; Tanigaki, M.; Mina, M. F.; Sawatari, C.; Itagaki, H.; Takahashi, H.; Hatta, I. *Polymer* **1999**, *40*, 6475-6484.

(8) Mahendrasingam, A.; Martin, C.; Fuller, W.; Blundell, D. J.; Oldman, R. J.; Harvie, J. L.; MacKerron, D. H.; Riekel, C.; Engström, P. *Polymer* **1999**, *40*, 5553-5565.

6 X-ray diffraction

6.1 An introduction to X-ray diffraction techniques

X-ray diffraction (XRD) studies the interaction between X-rays and the electron density that surrounds atoms and molecules. Sharp diffraction signals occur when the molecules or atoms are arranged in a regularly repeating lattice, such as the chains within a polymer crystal. Example diffraction planes within a PET crystal are shown in the *Molecular modelling* chapter. The most fundamental relation that encapsulates the phenomenon of diffraction is Bragg's law, depicted in Figure 6-1 and Equation 6-1.

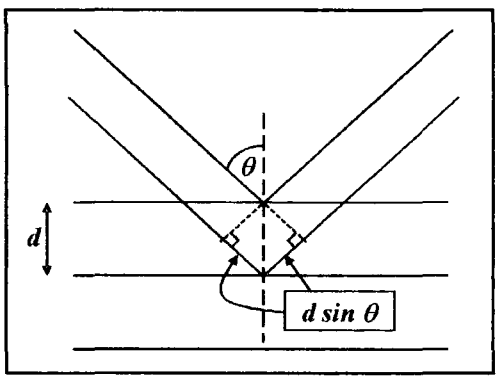

Figure 6-1: A graphical representation of Bragg's law

$$n\lambda = 2d\sin\theta \qquad \textbf{Equation 6-1}$$

where n is the order number (integer values 1, 2, 3..), λ is the wavelength of the X-ray radiation, d is the distance between diffraction planes and θ is the Bragg angle.

6.1.1 Grazing incidence X-ray diffraction

X-ray experiments on polymers are typically carried out in transmission mode[1-6]. A new technique named grazing incidence X-ray scattering (GIXD) has emerged which

enables X-ray diffraction information to be retrieved from the surface material only[7-11]. The name describes the very shallow angles of incidence used to probe the surface layer of the specimen. GIXD is based on the fact that the refractive index of a polymer, *n*, is seen to be *less than unity* where X-rays are involved[7,12] as described in Equation 6-2.

$$n = 1 - \delta - i\beta \qquad \textbf{Equation 6-2}$$

where

$$\delta = N_A \rho_{el} \lambda^2 r_0 / 2\pi \qquad \textbf{Equation 6-3}$$

and

$$\beta = \lambda\mu / 4\pi \qquad \textbf{Equation 6-4}$$

where N_A is Avogadro's number, ρ_{el} is the molar electron density, r_0 is the classical electron radius, μ is the linear attenuation coefficient (2.82×10^{-15}), and λ is the X-ray wavelength. It is possible to satisfy the condition of total external reflection (TER) at the interface between the air and the sample, which has a lower refractive index. When TER is achieved, a component of the X-ray beam penetrates into the sample, in the form of an evanescent wave. This process is analogous to that of total internal reflection described in the ATR-FTIR section. The critical angle at which X-ray total external reflection occurs in GIXD is given by Equation 6-5.

$$\alpha_c = \sqrt{2\delta} \qquad \textbf{Equation 6-5}$$

For grazing incidence studies on PET, Durell *et al.*[11] calculated that the critical angle was 0.20°. Durell used three angles of incidence: 0.60°, which probes the bulk material, the critical angle 0.20° that reportedly probes 340 Å and 0.18° which has a penetration depth of 80 Å. However, all previous GIXD work on polymers has involved spin-coating thin layers onto silicon wafers to ensure that the samples are exceptionally

smooth and flat and the application of the technique to drawn and annealed polymer films, which have a greater surface roughness, has been neglected in the literature.

6.2 The X-ray apparatus used

The X-ray experiments were performed on a Brüker D8 Discover diffractometer in the Materials Chemistry building in the University of Durham. The D8 is fitted with a multi-wire area detector, which makes it an excellent tool for the characterization of crystallite orientation in semi-crystalline polymers such as PET, as differences between the meridonal and equatorial reflections can be easily observed. The detector is offset in the horizontal plane such that a quadrant of the diffraction pattern is observed. The layout of the D8 is shown in Figure 6-2.

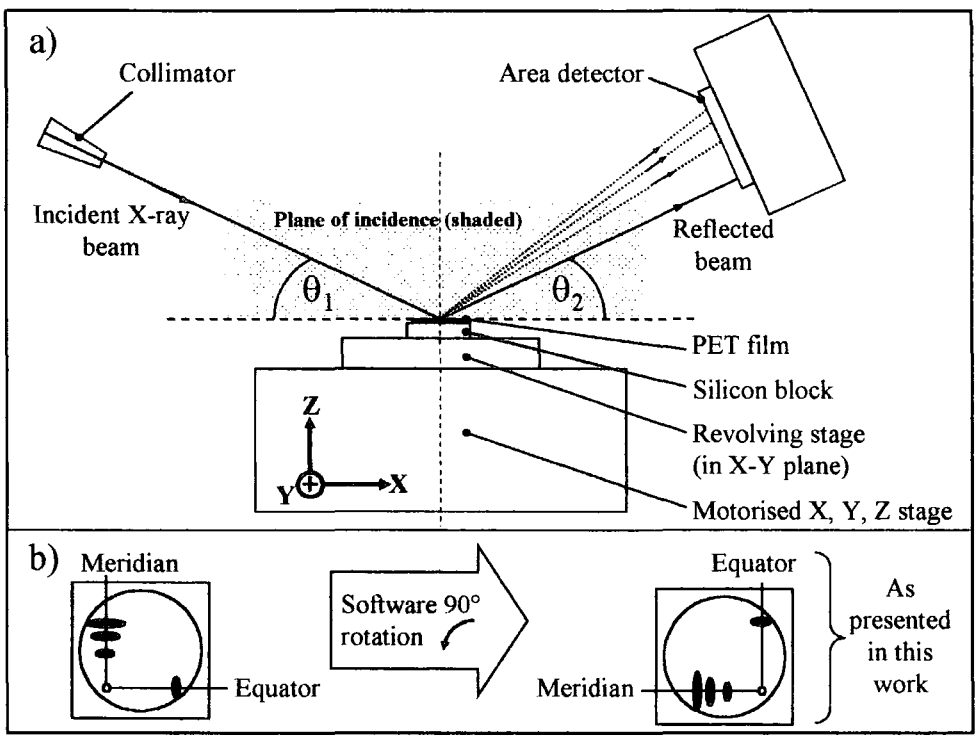

Figure 6-2: A schematic diagram of the D8 diffractometer

The angle of incidence (θ_1), detector arm angle (θ_2) and sample stage (X, Y and Z) are moved by independent stepper motors, controlled via a PC. There is no stage tilt

function on the D8, primarily because the tube X-ray generator on the θ_1 arm is mobile. This is in contrast to the equivalent stages based at Synchrotron radiation facilities (e.g. station 16.2 at Daresbury Laboratory, UK) where the highly collimated incident beam is immovable and thus changes in 2θ values are achieved via a coupled movement of the stage tilt and detector arm. On the D8, the X-rays are produced via a tube-generator typically operating at 40mA - 40kV, but the power can be reduced to 20 mA and 5 kV, which produces a greatly reduced X-ray flux. This has proven to be useful when there is a potential danger of hitting the sensitive detector with the main beam, when setting up an experiment or positioning the beam-stop. The detector face has been modified to allow the inclusion of a small brass attenuator sheet (~15 x 20 x 1 mm) in the beam path. This reduces the beam intensity considerably before it arrives at the detector, which allows for direct observations of the X-ray beam when the tube is operating at full power.

6.2.1 Experimental sample orientation

For these investigations, two film sample orientations will be considered. Both orientations are shown in Figure 6-3.

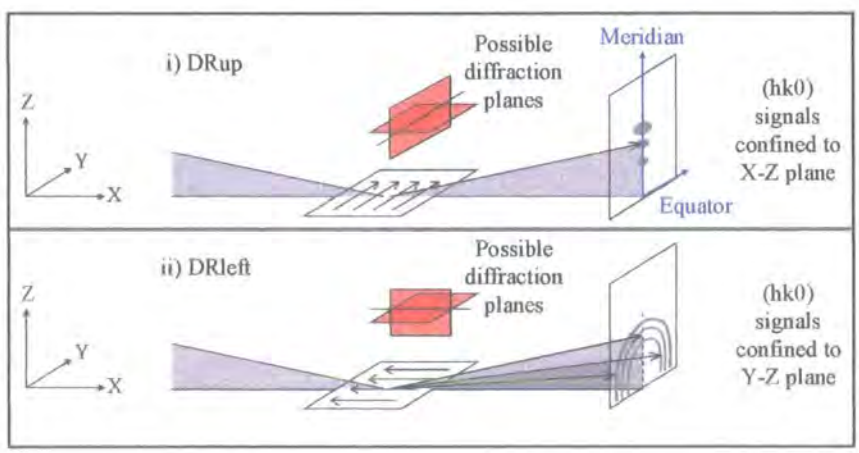

Figure 6-3: The two sample orientations being considered in this study

The first is when the draw direction of the film is perpendicular to the plane of incidence (DRup) and the second is when the sample is positioned such that its draw direction is parallel to the plane of incidence (DRleft). For the DRup geometry, the draw direction lies in the Y-stage direction. The (hk0) signals must have the normal to the diffraction planes in the X-Z plane. Therefore, the diffracted (hk0) signals using the DRup geometry will appear on the meridian of the detector, and arise from diffraction of (hk0) planes close to parallel to the film surface, in order for Bragg's law to be obeyed. This results in a diffraction image similar to a fibre diffraction pattern where the fibre lies along the Y direction. The 90° rotation of the image by the Brüker software (see Figure 6-2) means that the DRup images presented here look like typical fibre patterns where the fibre is positioned vertically.

However, for the DRleft geometry, the normal to the (hk0) planes must be in the Y-Z plane and the diffracted beam can be contained anywhere in the Y-Z plane. If a signal is found close to the equator, the corresponding diffraction planes are preferentially oriented perpendicular to the surface. Alternatively, the planes lie nearly parallel to the sample surface if the signals occur towards the meridian.

6.2.2 Investigation of the X-ray beam optics

The methodologies presented here to determine the X-ray beam optics were first formulated by the author's Ph.D. supervisor, Dr. Sharon Cooper. The beam properties may differ slightly for other D8 systems.

6.2.2.1 Beam intensity profile

It would be convenient to consider an X-ray beam to be cylindrical, with a uniform intensity at every point of its cross-section. Unfortunately, this is not the case. It is

therefore important to understand the nature of the beam on any given system, especially when the beam cross-section and sample target area become of a comparable size at small GIXD incident angles. It is possible to determine the beam dimensions and intensity profile across the beam by setting $\theta_1 = \theta_2 = 0$, lowering the sample away from the beam path so that the beam is fired straight at the detector. This straight through beam is passed through a brass attenuator immediately before it hits the detector, to avoid detector damage. This type of measurement reveals that the beam has an intensity profile that can be approximated by a Gaussian curve as shown in Figure 6-4.

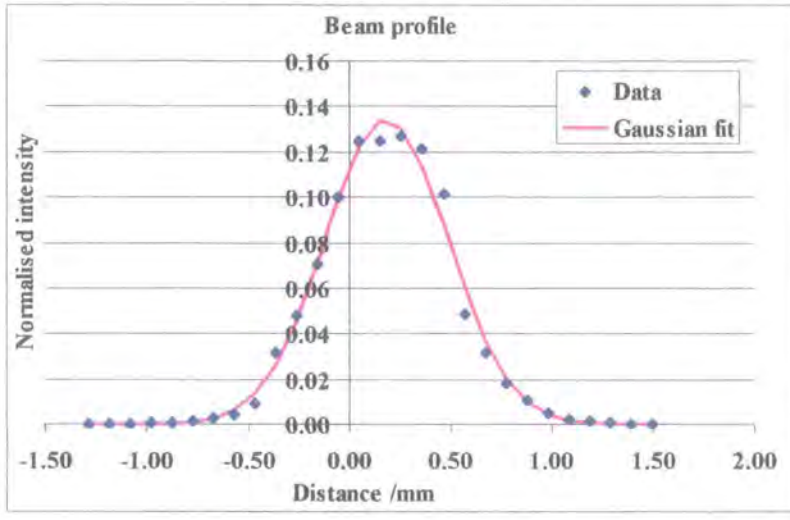

Figure 6-4: The beam intensity profile fitted with a Gaussian peak

where the x-axis denotes the distance from the detector centre and the y-axis shows the normalised intensity of the beam. The Gaussian fit in this example was performed on a spreadsheet, using Equation 6-6.

$$y = \left(A/\left\{sd\left[\sqrt{2\pi}\right]\right\}\right)\exp\left[-\frac{1}{2}.\left\{(x - x_c)/sd\right\}^2\right]$$

Equation 6-6

where A is the area under the curve, *sd* denoted the standard deviation and x_c is the beam centre. This measurement reveals that the central region of the beam is far more

intense than the outer regions. By measuring the distance between the Gaussian tails, it is possible to deduce that the *total* beam diameter at the detector is approximately 2 mm.

6.2.2.2 Beam divergence

The X-ray beams produced by tube and rotating anode generators tend to possess a measurable level of beam divergence. In other words, the cross-sectional area of the beam tends to increase with distance from the source. For these GIXD studies, the beam size at the sample will have a great effect on the proportion of the beam interacting with the sample. By considering the Brüker beam collimator specifications together with the size of the beam at the detector, it is possible to deduce an estimate of the beam divergence on this particular system. The collimator used throughout this work has a diameter of 0.3 mm, and the collimator to sample distance, and sample to detector distance were 187.5 mm and 150 mm, respectively. The beam divergence is shown schematically in Figure 6-5. From trigonometric considerations, the beam intensity profile at the sample position (shown as distance x) spans 0.8 mm. Knowing the size of the beam at the sample position is important as it allows calculations to be made regarding the proportion of the beam interacting with the sample as shown in section 6.2.2.3.

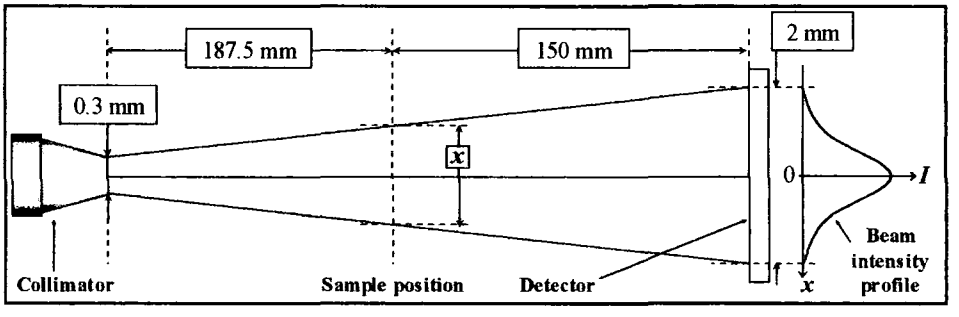

Figure 6-5: The estimated beam divergence

6.2.2.3 Proportion of beam hitting the sample

For both cases in Figure 6-6, the beam will have the same initial diameter of 0.8 mm, both intensity profiles can be assumed to be Gaussian and the total X-ray intensity given by the area under both functions is identical. The sizes of both the beam width and θ_I angles are exaggerated in this diagram for clarity, but the same principle applies for a smaller beam diameter when much smaller incident angles are used. Also, assume that the beam centre is directed towards the centre of the sample. Any deviation from this criterion would result in the whole Gaussian distribution shifting left or right relative to the sample.

In Figure 6-6, the beam component *A* hits the side of the sample and underlying stage and so never reaches the detector, component *B* has the opportunity to reflect and diffract off the sample and component *C* passes over the sample and heads towards the detector undeflected. At large incident angles, the majority/all of the beam interacts with the sample as indicated by the area of component *B*. As the angle of incidence decreases, the area illuminated by the beam far exceeds the sample length and a much smaller portion of the beam interacts with the specimen. Under the conditions shown in Figure 6-6, if θ_I was reduced to zero degrees, exactly half the beam would be lost and the other half would head towards the detector.

From this analysis, fitting the beam to a Gaussian profile, it is possible to determine the proportion of the total X-ray flux that hits the sample, the proportion hitting the sample side and hence never reaching the detector, and the proportion passing undeflected over the sample and reaching the detector, as detailed later in section 6.3.1.2.

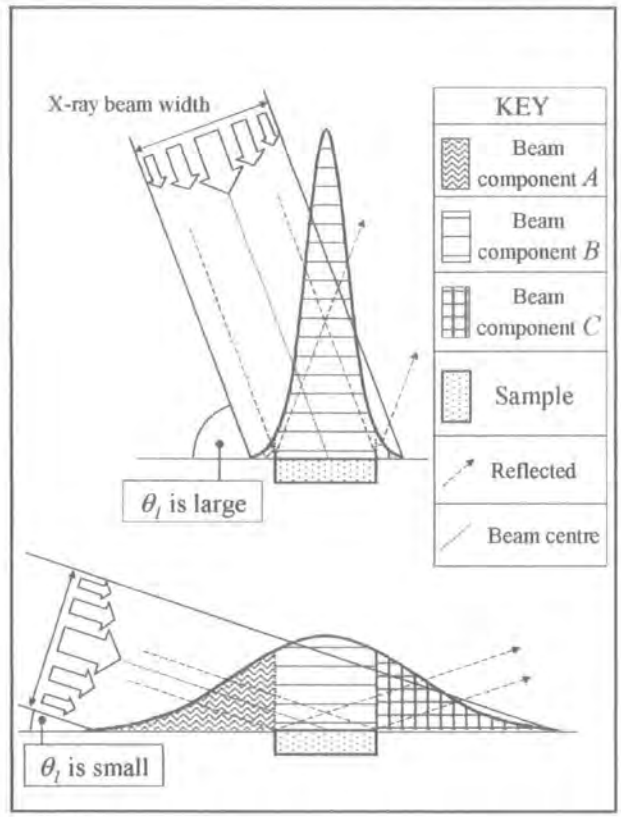

Figure 6-6: The portions of the X-ray beam hitting and missing the sample

6.2.3 Methods employed for accurate sample positioning

For standard transmission X-ray experiments on polymer films, it is easy to position the sample in the beam, as the target area is large in comparison to the beam cross-section. However, when the incident angles are reduced to less than 0.2°, an accurate sample position becomes crucial. Although the sample position in the X, Y plane defined in Figure 6-2 can be achieved by eye, the correct position of the stage height direction Z requires more consideration. Two techniques used to align the sample in the Z direction will now be described.

6.2.3.1 The Brüker D8 laser and camera method

Above the X, Y, Z sample stage is a CCD camera and a laser as shown in Figure 6-7. The camera contains fixed cross hairs that appear on-screen, superimposed on the image

of the sample's surface. The laser projects a red dot onto the sample, which is relayed onto the screen.

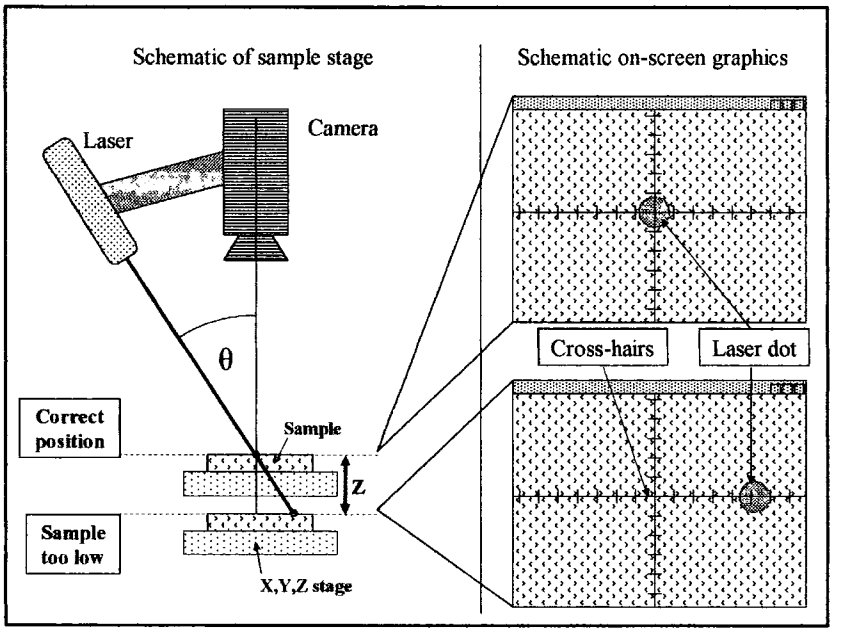

Figure 6-7: The Brüker laser and camera method of sample positioning

The laser direction subtends an angle θ to the camera axis, which ensures that the laser dot is centrally located in the cross hairs when the sample surface is at the correct height. Due to slight inaccuracies in the camera positioning away from the true centre of the goniometer stage, this technique is best suited for angles of incidence above ~5° where the precise position of the stage in the Z direction is not so critical.

6.2.3.2 The half-cut beam method

The camera and laser method cannot be used to position a sample accurately enough for grazing incidence experiments. Confidence in the correct sample position in this study was achieved using a half-cut beam method, which was achieved as follows. The θ_1 and θ_2 motors are both moved to the 0° position and an attenuator sheet affixed to the detector. The sample stage was lowered such that the sample is clearly out of the beam path. The X-ray shutter is then opened for a count of 10 seconds allowing the

attenuated beam to hit the detector and produce an intense central dot corresponding to the reduced main beam intensity. A box is then drawn around the dot and the total intensity within the box counted using the GADDS software. The intensity of the reduced primary beam (total number of counts over the 10 seconds) I_{full}, is measured and the target half beam value of $I_{full}/2$ is noted. The sample was positioned approximately in the beam path using the D8 camera-laser method. The height of the stage is then altered incrementally and 10-second intensity measurements taken at each height. This procedure is shown schematically in Figure 6-8, where the same principle occurs for a divergent beam as for the perfectly collimated beam in the sketch. When the intensity falls to the target value, the sample is cutting out exactly half the beam and the stage is in the correct 'half-cut' position, at the centre of the goniometer stage. GIXD experiments on that sample can thus be made by raising the beam rotation arm by a small angle α. This whole procedure needs to be repeated for every new sample and also if the sample is moved or rotated in a way to achieve the experimental geometries described in 6.2.1.

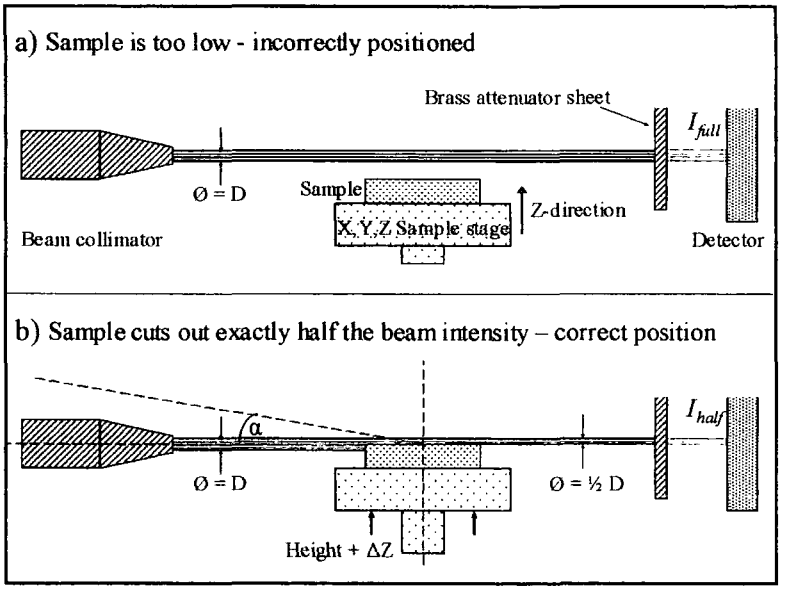

Figure 6-8: The beam half-cutting method for accurate sample positioning

6.3 Preliminary GIXD measurements

6.3.1 Direct observations of total external reflection (TER)

On assessing the suitability of GIXD on stretched film specimens, the first issue that needed to be addressed was whether drawn PET films were sufficiently flat for TER to be observed to any degree. High levels of TER would prove that the diffraction measurements taken at grazing angles are representative of the surface material only. The penetration depths associated with GIXD will be discussed in section 6.3.1.2. Film curvature and surface roughness are factors that would certainly reduce the amount of TER achievable.

6.3.1.1 Experimental procedure

A small silicon wafer (25 mm diameter) was smeared with silicone grease and a similarly sized section of the heat-set PET film was pressed onto it. The film-silicon assembly was then placed on the sample stage and positioned in the beam using the half-cut beam method. Direct observations of the primary beam were then made by setting $\theta_1 + \theta_2 = 0$ and collecting 10 second exposures for incident angles $\theta_1 = 0.1°$ to 0.3° with 0.02° increments. Under conditions of TER, two beam components can be observed within the detector region shielded by the brass attenuator; one due to the proportion of the beam passing undeflected over the sample, and the other due to TER of the beam hitting the sample surface, as shown schematically in Figure 6-11. The images shown in Figure 6-9 were recorded from a 150 μm thick homopolymer PET film, drawn to 3.75 draw-ratio (sample name E4U_200cool_DRup).

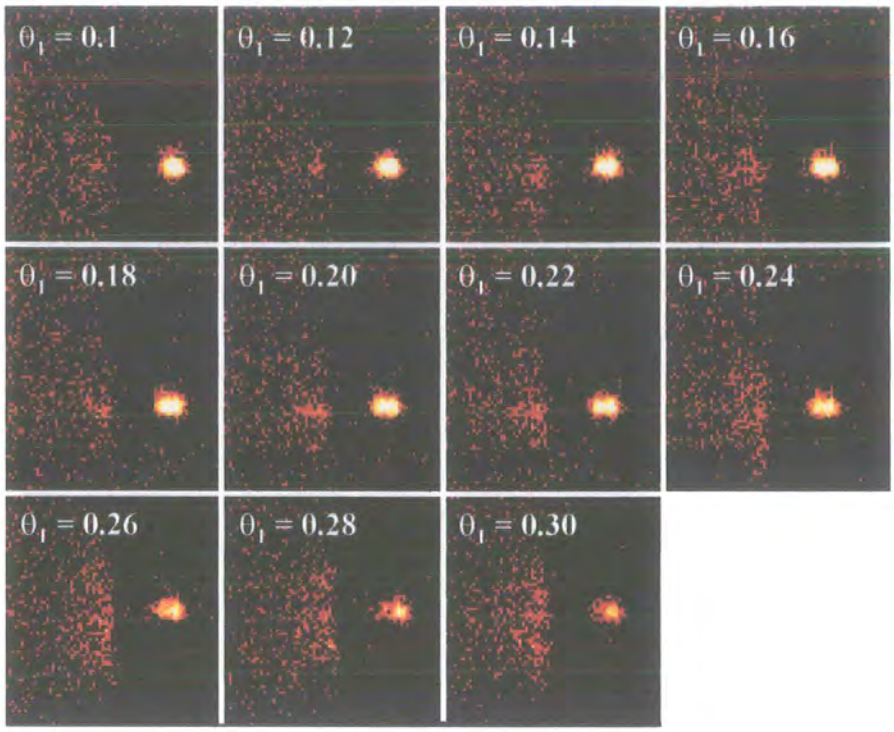

Figure 6-9: Images showing total external reflection

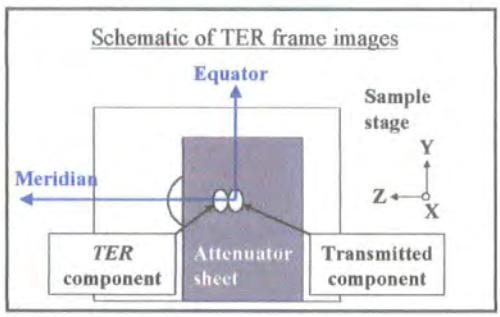

Figure 6-10: A representation of the frames shown in Figure 6-9

The frames presented in Figure 6-9 are typical of many of the PET films that demonstrated high levels of TER. The intense 'central spot' is seen to broaden with increasing incident angle and at 0.2°, it is apparent that this spot actually comprises of the overlapping main beam and TER components. Above 0.2°, the reflected intensity reduces markedly, due to the incident angle being above the critical angle required for TER. The two components due to the reflected beam component and the portion of primary beam that misses the sample as depicted in Figure 6-11.

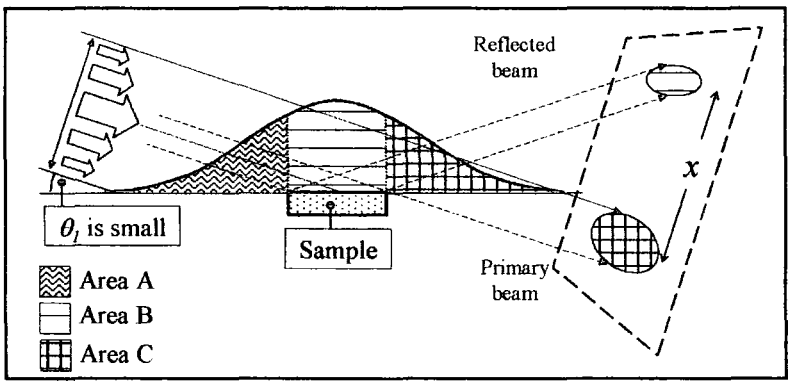

Figure 6-11: An explanation of the two dots observed in the frames of Figure 6-9

This experiment demonstrates that a measurable amount of reflection occurs from the film's surface below the critical angle for TER. It is important to quantify how much TER is being achieved, as this will dictate the depth at which the sample is being probed.

6.3.1.2 Estimating the degree of total external reflection

By knowing the beam intensity profile at the sample, the intensity of the full primary beam and the total intensity of the partly reflected / partly transmitted beam at the detector, is it possible to extrapolate what portion of the measured intensity is due to TER. This was achieved by drawing a box around the primary and reflected beam components using the GADDS software. The total intensity within the box (I_{BOX}) was then noted. Using the Gaussian beam profile fit (see Figure 6-4) the expected intensity of the primary beam passing over the sample I_{PRIM}, and the expected intensity of the beam hitting the sample which could then be reflected, I_{SAMP}, were calculated. Thus, I_{SAMP} represents the X-ray intensity expected for 100% TER, from a perfectly flat surface with the X-ray incidence angle less than the critical angle. From Figure 6-11, I_{PRIM} and I_{SAMP} are the integrated intensities of area C and area B, respectively. The fraction of TER can then be calculated using Equation 6-7.

$$f_{TER} = (I_{BOX} - I_{PRIM})/I_{SAMP}$$ **Equation 6-7**

This technique relies on the total beam intensity to be constant for each of the data collection times. The beam intensity from tube generators is known to drift slightly over time, which could perturb the values. For the short data collection times considered here, this phenomenon is thought to have a negligible effect. By estimating the degree of TER achieved, it is then possible to estimate the X-ray penetration depth for each X-ray incidence angle used.

6.3.2 Estimates of the penetration depth

As X-rays enter a sample, they become progressively absorbed, according to the law

$$I = I_0 \exp\left(-\frac{d}{\tau}\right)$$ **Equation 6-8**

where I is the X-ray intensity at sample depth, d, I_0 is the incident X-ray intensity and τ can be defined as the penetration depth. τ represents the distance travelled into the surface at which the X-ray intensity has reduced to 1/e of the intensity prior to reflection. Therefore, τ is a similar measure to the penetration depth d_p, described in the FTIR-ATR discussion. For measurements taken below the critical angle for TER (α_c) the penetration depth[9] is shown in Equation 6-9.

$$\tau = \sqrt{2}\left(\frac{\lambda}{4\pi}\right)\left\{\left[\left(\alpha^2 - \alpha_c^2\right)^2 + (2\beta)^2\right]^{1/2} - \left(\alpha^2 - \alpha_c^2\right)\right\}^{-1/2}$$ **Equation 6-9**

where $\beta = \lambda\mu/4\pi$ (Equation 6-4), in which μ is the linear attenuation coefficient and λ is the X-ray wavelength and α_c are defined at the start of this chapter and α is the angle of incidence (which has also been called θ_I in this thesis). For incident angles $\alpha > \alpha_c$, Equation 6-10 takes effect.

$$\tau = \sin\alpha / \mu$$

Equation 6-10

The calculated penetration depths calculated using these relationships for various angles of incidence are shown in Table 6-1. These calculations suggest that for data collected below the critical angle, it is possible to extract structural information from the top few nanometres of the film's surface. However, this assumes a perfectly flat surface, so that 100% TER occurs.

Table 6-1: Estimates of the penetration depths for GIXD experiments on PET at various angles of incidence, assuming 0% and 100% TER

Incident angle (Degrees)	Assuming no TER (μm)	Assuming 100% TER (μm)
0.02	0.371	0.00403
0.04	0.741	0.00412
0.06	1.11	0.00427
0.08	1.48	0.0045
0.1	1.85	0.00488
0.12	2.22	0.0055
0.14	2.59	0.00665
0.16	2.96	0.00978
0.18 (~critical angle)	3.34	0.75
0.2 (~ critical angle)	3.71	1.78
0.22	4.08	N/A
0.24	4.45	N/A
0.26	4.82	N/A
0.28	5.19	N/A
0.3	5.56	N/A
0.4	7.41	N/A
0.5	9.26	N/A
1	18.2	N/A
5	92.6	N/A
10	185	N/A
80	1050	N/A

For further information on the sampling depths associated with these GIXD and FTIR-ATR experiments, please see Appendix 2.

6.4 GIXD and bulk sample X-ray diffraction measurements of drawn PET films

The aim of the following experiments was to see if grazing incidence XRD observations can be made on drawn, heat-set PET films by taking measurements at various angles of incidence above and below the theoretical critical angle of $\theta_1 = 0.2°$. To ensure that each diffraction pattern appeared at the same position on the multi-wire area detector, the $\theta_1 + \theta_2$ value has to be fixed at a constant value for every angle of incidence. For diffraction observations of PET on our system, the optimum value was found to be $\theta_1 + \theta_2 = 18°$ to ensure the maximum amount of meridonal and equatorial diffraction information fell onto the detecting area. Unless otherwise stated, the general experimental method employed for this series of films was as follows.

6.4.1 General GIXD experimental procedure

Drawn PET samples were prepared on a Long stretcher at DuPont Teijin Films, Wilton and heat-set using a specially designed heat clamp at the University of Durham, as described in chapter 3. After allowing the aluminium frames to slowly cool to ambient temperature, the heat-set film was removed from the film clamp and a 2.5 x 2.5 cm token was removed from the film centre. The token was laid flat onto a silicon vacuum greased 2.5 cm silicon wafer (to encourage the film to lie flat) while wearing powder-free latex gloves to minimise the risk of contaminating the PET film surface.

The specimen was then placed onto the X-Y stage in the D8 diffractometer in the DRup orientation. The positioning laser (see 6.2.3.1) was activated and the sample was moved such that the laser dot fell on to the centre of the specimen. This ensured the correct positioning in the X stage direction. The beam half-cut method was used for precise

positioning in the Z stage direction. If necessary, the position in the Y direction was altered using the stepper motor via the computer, ensuring that the half-cut method was repeated prior to the measurement. The attenuator sheets needed for the half-cut method were removed from the detector and the film was subjected to 5-minute exposures, taken at the angle progression shown in Table 6-2.

Table 6-2: The angles used in the GIXD and bulk sample experiments on PET films

Frame	Theta 1	Theta 2	2-Theta	Regime
001	0.06	17.94	18	A
002	0.08	17.92	18	(+0.02)
003	0.1	17.9	18	
004	0.12	17.88	18	
005	0.14	17.86	18	
006	0.16	17.84	18	
007	0.18	17.82	18	
008	0.2	17.8	18	
009	0.4	17.6	18	B
010	0.6	17.4	18	(+0.2)
011	0.8	17.2	18	
012	1	17	18	
013	5	13	18	C
014	10	8	18	(+5)
015	15	3	18	

The angle progression presented in Table 6-2 can be divided into three regimes (A, B and C) to help part-automate the data collection. After frame 015, direct observations of the proportion of total external reflection were made following the method shown in section 6.2.3.2.

Once all 15 frames were collected, the sample was rotated by 90° to achieve the DRleft sample orientation and the procedure was repeated, including the beam half-cut positioning. This whole process was repeated for each of the PET films.

6.4.2 Typical diffraction images above and below the critical angle

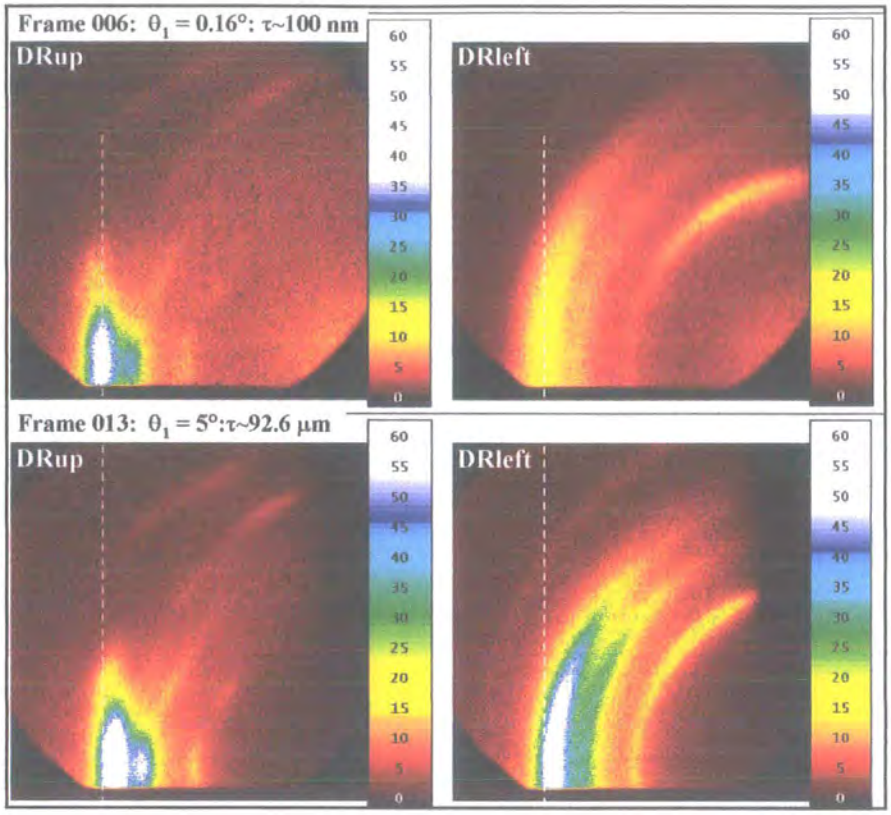

Figure 6-12: Typical 2D diffraction images collected below and above the critical angle. The white, blue, green, yellow, and red colours represent decreasing X-ray intensity at the detector, with black regions corresponding to zero X-ray intensity.

The 2D diffraction patterns shown in Figure 6-12 were collected from a 3 draw-ratio uniaxial PET film using the incident angles and the sample orientations shown on the figure. A similar layout of the diffraction patterns were observed for all of the uniaxially drawn films and so these patterns will be described in detail.

The overall diffraction intensity is much higher in frame 013 than 006. This is due to the higher angle of incidence allowing the beam to probe more material than in the grazing incidence geometry, and the greater proportion of the total X-ray flux hitting the sample at the higher incidence angle. In the DRup sample orientation, the (hk0) signals lie on the meridian as described in section 6.2.1. For the DRleft sample orientation,

where the (hk0) signals can occur at any location between the meridian and equator, the (010) signal can be seen to be more intense at the equator than at the meridian. The (010) Miller planes lie approximately perpendicular to the benzene rings of the PET crystal. Therefore, this indicates that the benzene rings preferentially orientate parallel to the films' surface in these uniaxially drawn films.

An unusual feature of these patterns is that the radial positions, and hence 2θ positions, of the intense (100), (010) and ($1\bar{1}0$) meridonal signals are slightly different in frames collected above and below the critical angle for TER. The dashed white lines are provided to show the nature of the shift in peak positions. The nature of the observed radial shift in diffraction signals was explored by taking Chi scans (described in detail in the next section) along the meridian at every angle of incidence and determining the radial positions of the (hk0) signals for each angle. This was repeated for films stretched to different draw ratios and subjected to different heat-setting regimes. A Chi scan was taken from each of the diffraction patterns to monitor the positions of the peaks. 2-Theta scans (also detailed in the next section) were performed on frames 006 and 013 for each of the three primary meridonal reflections (100), (010) and ($1\bar{1}0$). These frames correspond to measurements taken below and above the proposed critical angle of 0.2°.

6.4.3 Methods employed for extracting quantities from 2D diffraction images

The Brüker GADDS software interface

The GADDS software offers several useful software tools for extracting quantitative values from the 2D diffraction data. The two most frequently used procedures used in

this study will be described along with the chosen parameters, which were kept consistent throughout the study.

6.4.3.1 GADDS Chi scans

The radial position, and hence 2θ value, of the diffraction peaks was determined using the GADDS Chi scan facility (Figure 6-13). This scan retrieves an intensity value for every 2-Theta angle between the 2-Theta begin and 2-Theta end parameters. An example output of a typical Chi scan is shown in Figure 6-14. Throughout this work, the parameters for the Chi scan are shown in Table 6-3 unless otherwise stated.

Table 6-3: The GADDS Chi scan parameters used

Parameter	Value
2-Theta begin	10.0
2-Theta end	31.2
Chi begin	-92.0
Chi end	-88.0

The Chi scan is similar to an equatorial slice, which is favoured by several authors, but is more accurate as it takes into account the larger arc spread of peaks at larger 2-Theta values.

6.4.3.2 GADDS 2-Theta scans

The GADDS 2-Theta scan (or 'Azimuthal scan'[2]) operation involves obtaining an intensity value between the equatorial and meridonal directions over an arc of fixed 2θ angle, as shown in Figure 6-15, and hence this relays information about the preferred orientation of each diffraction plane that produces a diffraction signal at the detector. The raw output of this operation (Figure 6-16) gives Chi angles of -180° to -90°. To determine the orientation parameters, the integrals require that the Chi range be converted to 0° to 90°. This was achieved using a simple spreadsheet by adding 180°.

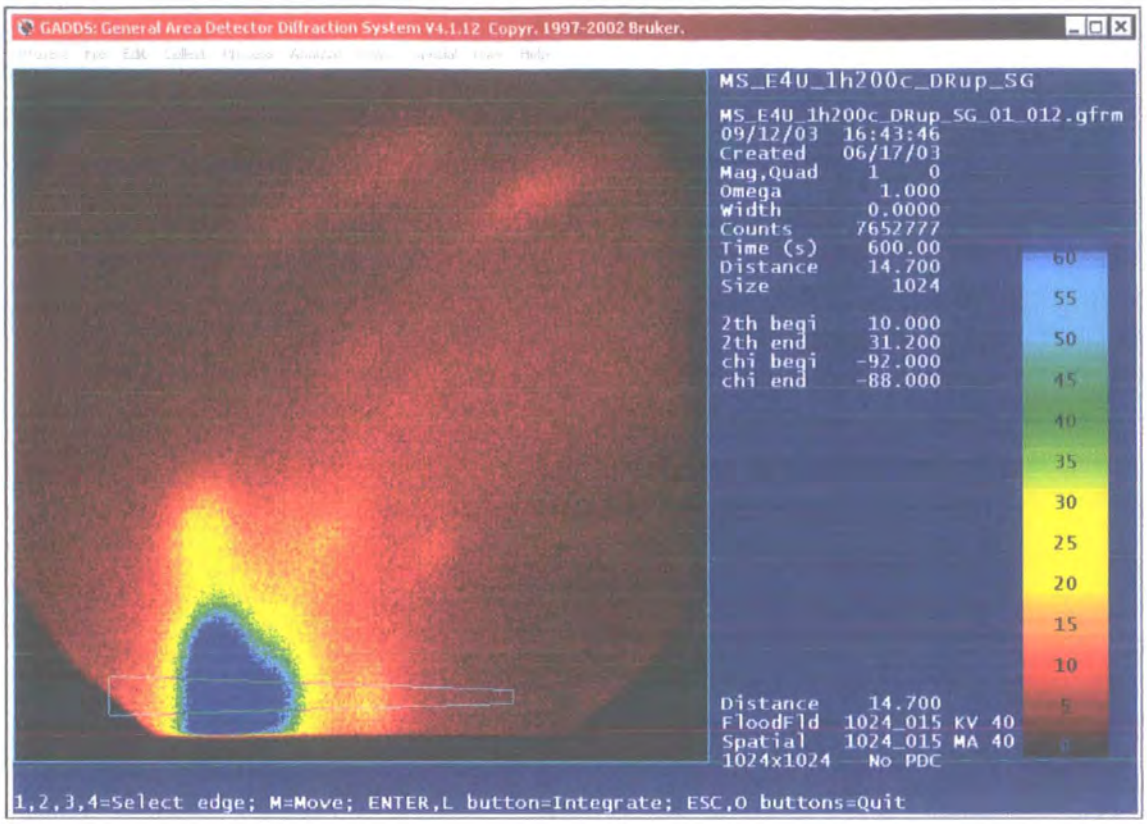

Figure 6-13: An example 'Chi-scan' using the GADDS software, where the box centred on the meridian indicates the region analysed. Within this box, an intensity value is calculated by adding the intensities of all the pixels lying along the 4° arc subtended at each 2θ location.

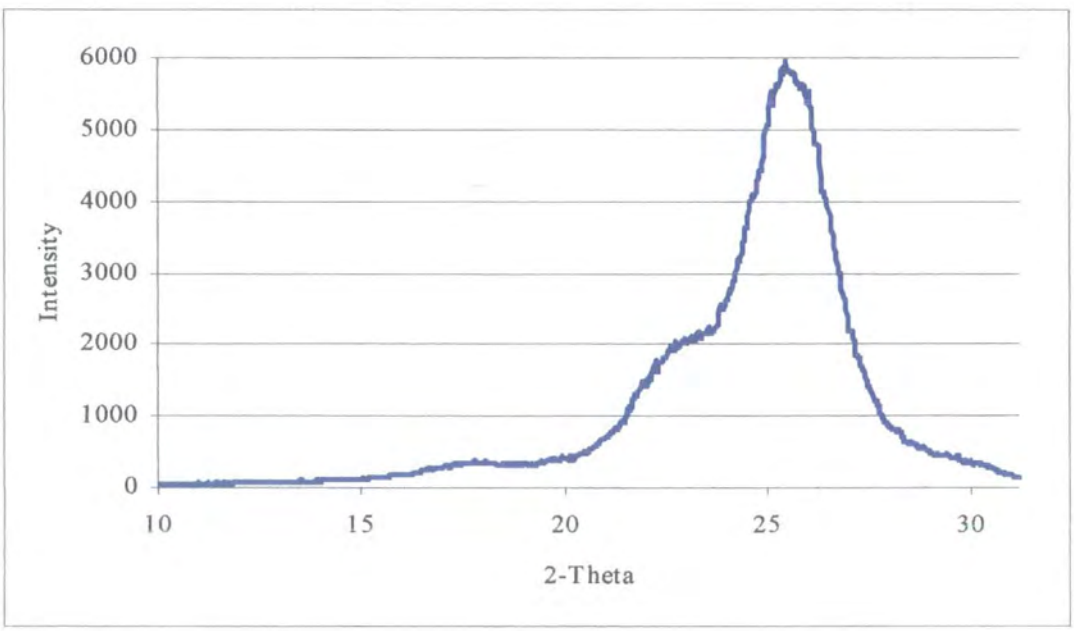

Figure 6-14: The output of the 'Chi-scan' operation shown in Figure 6-13

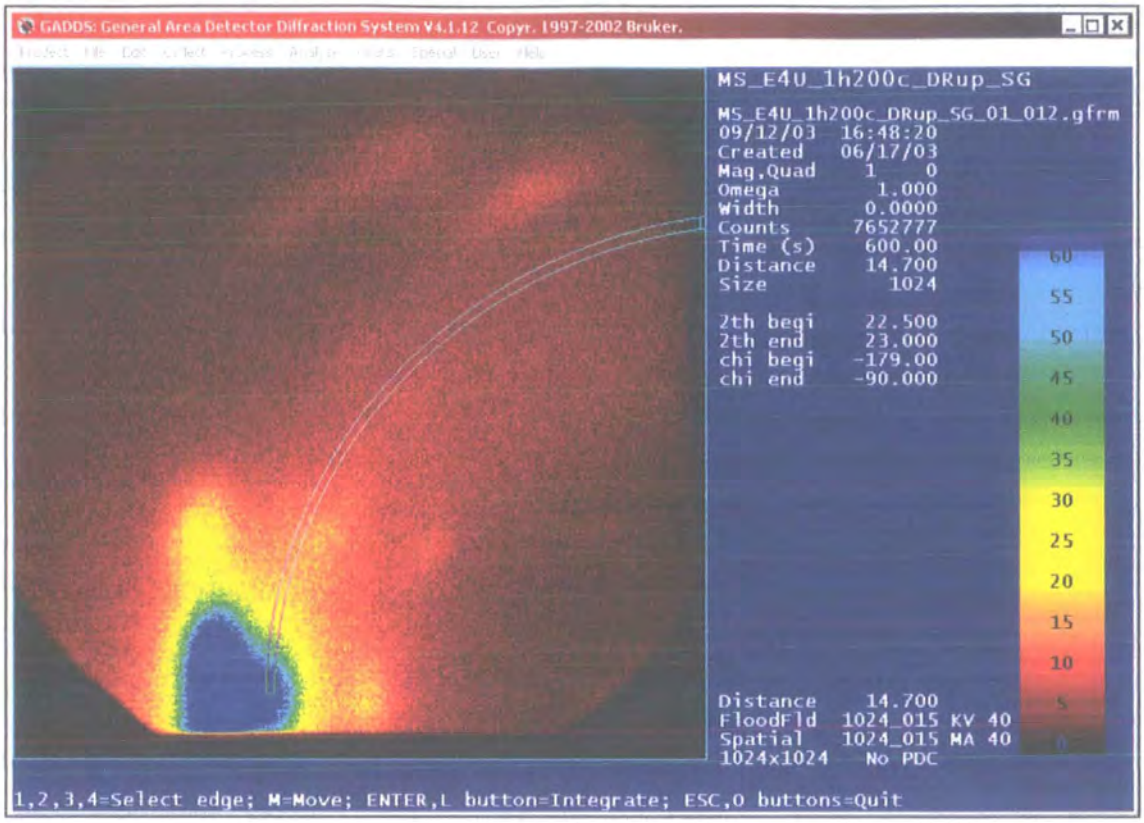

Figure 6-15: An example 2-Theta scan using the GADDS software, where the box indicates the region analysed. For each Chi angle within the box, the intensities of the pixels lying along the specified 2θ range (2θ = 22.5° to 23°) are added.

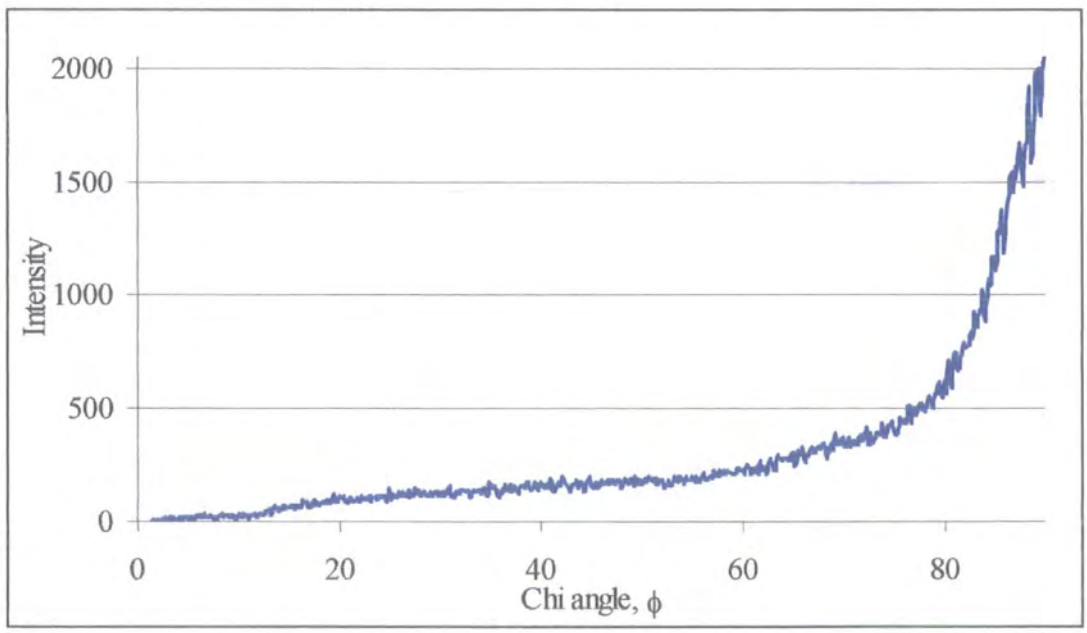

Figure 6-16: The output from the '2-Theta' operation shown in Figure 6-15 (converted to 0-90°).

6.4.4 Orientation calculation from 2D diffraction data

Recall that the $(10\bar{5})$ diffraction signal corresponds to an interplanar direction, which is approximately parallel to the PET chain axis, and hence orientation analysis of this signal from XRD data provides the orientation analysis of the chain axis. However, this convenient $(10\bar{5})$ signal was located at the edge of the observable 2θ range of our setup. Since Wilchinsky showed that crystallite orientation in polycrystalline materials could be calculated using three (hk0) signals[13], several authors have applied this technique to crystalline orientation in PET[3,4,14]. The orientation parameters in this study were thus calculated using the three strong meridional reflections corresponding to the (100), $(1\bar{1}0)$ and (010) diffraction planes using the relation shown for the ASDC of a particular (hkl) signal $\langle\cos^2\sigma_{(hkl)}\rangle$ in Equation 6-11.

$$\left\langle \cos^2 \sigma_{(hkl)} \right\rangle = \frac{\int_0^{\pi/2} I_{(hkl)}(\phi)\sin\phi\cos^2\phi d\phi}{\int_0^{\pi/2} I_{(hkl)}(\phi)\sin\phi d\phi}$$

Equation 6-11

where $I_{(hkl)}(\phi)$ is the measured intensity of the (hkl) reflection at the chi angle φ. The numerator and denominator integrals were calculated using Origin 6 software by determining the areas under the $I_{(hkl)}(\phi)\sin\phi\cos^2\phi$ vs. φ and $I_{(hkl)}(\phi)\sin\phi$ vs. φ plots between 0° and 90°, respectively. Once the ASDCs had been calculated for each of the three reflections, the ASDC between the crystal c-axes and the draw direction was obtained using Equation 6-12.

$$\left\langle \cos^2 \sigma \right\rangle = 1 - 0.8786\left\langle \cos^2 \sigma_{(010)} \right\rangle - 0.7733\left\langle \cos^2 \sigma_{(1\text{-}10)} \right\rangle - 0.3481\left\langle \cos^2 \sigma_{(100)} \right\rangle$$

Equation 6-12

where the 0.8786, 0.7733 and 0.3481 parameters are derived from the values of the triclinic crystal lattice of PET[4,13]. The PET repeat unit lies approximately along the c-axis[1] (see Figure 6-1) and so a determination of the c-axis direction is considered a determination of the chain axis direction. Since the X-ray ASDC was determined using the orientation of the (hk0) diffraction signals, the parameter is representative of the crystallites only. This is in contrast to the infrared ASDCs, which describes the orientation of the chains within both the crystalline and amorphous regions.

6.4.5 X-ray crystallite orientation results above and below the critical angle

The crystallite orientation was calculated using the (hk0) signals for incident angles 0.16° (Frame 006) and 5° (Frame 013) for each of the uniaxially drawn films where τ = 100 nm and 92.6 μm respectively (see Appendix 2 for discussion). This analysis assumes uniaxial sample symmetry and is not applicable to biaxial films, unoriented films or diffraction from uniaxially drawn films in the DRleft sample orientation, which also showed the preferential orientation of the benzene rings parallel to the film surface.

The X-ray ASDC orientation results, denoted $ASDC_{X\text{-}ray}$, for uniaxially drawn PET films are presented in Table 6-4 and Table 6-5. The X, Y and Z ASDCs as determined from the FTIR-ATR experiments on these films are provided for comparison. The FTIR-ATR Y-ASDC describes the orientation of the chain direction in the draw direction and the X-ray ASDC values describe the orientation of the unit cell c-axes of the crystallites into the draw direction. Hence, ASDCX-ray ~ Y-ASDC if the amorphous chains have a similar preferential orientation along the draw direction to that of the crystalline regions. By repeating '2-Theta' scans on the same diffraction pattern with slightly different positions on the (hk0) signals, the calculated ASDCX-ray was

found to vary by 0.01 ASDC units, which is taken as the error of these measurements (see 4.3.4.2 for the FTIR errors). The fraction of TER was calculated using the method described in 6.3.1.2 and is shown in two columns; the fraction of TER at $\theta_l = 0.16°$, and the fraction of TER averaged over the sub-critical angles 0.1° - 0.16° (*'TER avg'*).

Table 6-4: The orientation results determined by GIXD and FTIR-ATR

Full film name	E4U_unheat_DRup	E4U_200cool_DRup	E4U_1h200c_DRup	E4U_75a200cool_DRup
Draw ratio	3.75	3.75	3.75	3.75
Fraction TER at 0.16°	0.307	0.527	0.683	0.965
Fraction TER avg	0.202	0.682	0.803	0.986
Xray results				
Fr'006 $ASDC_{X\text{-ray}}$	0.75 (+/- 0.01)	0.81 (+/- 0.01)	0.83 (+/- 0.01)	0.78 (+/- 0.01)
Fr'013 $ASDC_{X\text{-ray}}$	0.73 (+/- 0.01)	0.76 (+/- 0.01)	0.77 (+/- 0.01)	0.76 (+/- 0.01)
% increase for Fr'006	3.01 %	7.28 %	7.75 %	2.5 %
FTIR-ATR results				
X-ASDC	0.171	0.130	0.126	0.140
Y-ASDC	0.701	0.771	0.770	0.754
Z-ASDC	0.128	0.099	0.104	0.106

Table 6-5: Orientation results for films drawn to 3.75 and 3 draw ratio

Full film name	E4U_75a200cool_DRup	E3U_75a200cool_DRup
Draw ratio	3.75	3.00
Fraction TER at 0.16°	0.965	0.842
Fraction TER avg	0.986	0.937
Xray results		
Fr'006 $ASDC_{X\text{-ray}}$	0.78 (+/- 0.01)	0.84 (+/- 0.01)
Fr'013 $ASDC_{X\text{-ray}}$	0.76 (+/- 0.01)	0.76 (+/- 0.01)
% increase for Fr'006	2.51 %	10.9 %
FTIR-ATR results		
X-ASDC	0.140	0.132
Y-ASDC	0.754	0.767
Z-ASDC	0.106	0.101

6.4.5.1 Analysis of crystallite orientation

For all of these uniaxially drawn films, the ASDCs between the draw direction and the crystallite c-axes are consistently higher for frames collected below the critical angle (τ ~ 100 nm), than those above (τ = 92.6 μm). The percentage increase between the $ASDC_{X\text{-ray}}$ orientation measurements collected above the critical angle (Frame 013, θ_l =

5°) and below the critical angle (Frame 006, θ_l = 0.16°) are also included in Table 6-4 and Table 6-5. This result suggests that the crystallites within the film's surface are more highly oriented into the draw-direction than the crystallites in the bulk. The orientation can be up to 7.75% higher at the sub-micron surface region for the 3.75 draw ratio films. The biggest difference in orientation between surface and bulk regions was observed in the film drawn to 3 draw ratio, which also had the highest X-ray orientation values of all the films, suggesting that no further crystallite orientation typically occurs above this draw ratio value. In this film (Table 6-5), the ASDC between the c-axes and the draw direction is 0.84 for the surface region and 0.76 for the bulk. This is almost an 11 % increase in orientation for the surface material.

From the samples examined in Table 6-4, there is a clear trend that the longer time the 3.75 draw ratio film is heated, the higher the fraction of TER achieved. This could be due to the film becoming more taught with time in the specially made anti-shrinkage frames. This would lead to a flatter surface, which gives a higher TER signal. However, one must be cautious of extrapolating this trend over just four films and this should be the subject of a further study.

It would be intuitive to expect there to be a link between the fraction of TER observed on a specimen and the difference between the 'surface' and 'bulk' measurements, which would be expected for similar heat-treated and stretched samples. No such pattern is observed in these data, because it is not sensible to compare the difference in bulk and surface orientation values from the different heat set samples. To test this dependency further, the analysis should be repeated from more incidence angles just below and just

above the critical angle, in order to achieve different degrees of TER. This would confirm whether higher TER fractions do indeed reveal higher orientation levels towards the surface.

The Y-ASDC values determined using FTIR-ATR spectroscopy, tend to be nearer to the bulk X-ray values than the surface specific measurements. This might be suggesting that the sub-critical angle X-ray diffraction measurement is more surface-specific than the ATR measurement. However, as stated previously, this conclusion would be based on the assumption that the amorphous material is oriented in a similar fashion to the crystallites. It should also be remembered that the FTIR orientation is calculated assuming a full biaxial system whereas the X-ray data assumes uniaxial symmetry, which nevertheless is valid for the particular DRup film geometry used in these studies.

6.5 Further observations of the (hk0) 2θ shifts above and below α_c

The most unusual observations made in this thesis are the 2θ shifts in the intense (hk0) signals for diffraction collected below and above the critical angle for TER (α_c), as typified in Figure 6-12. Similar shifts were also observed for the less intense, non-meridonal signals, but were less easy to observe due to the weakness of many of these signals compared to the background. The 2θ locations of the diffraction signals are determined by the d-spacings within the sample. If the 2θ shift is proven consistent and reproducible, it could reveal that a different crystal structure exists within the surface material compared to the bulk. This has never been observed before and would have been over-looked by previous X-ray experiments on stretched PET films, which have all been performed using transmission geometries[2-5]. This experiment is designed to observe further the nature of the radial 2θ shift at various angles of incidence.

6.5.1 Experimental procedure

Samples were positioned in the beam path using the half-cut beam method. Diffraction images were then collected using the X-ray incident angle progression shown in Table 6-2, which includes incident angles below and above the critical angle for TER. Chi scans were taken from each diffraction image using the usual parameters described in Table 6-1. All 15 Chi scans for each sample were then plotted on the same axes so that they can be easily compared with one another.

The results for this experiment are presented in Figure 6-17 to Figure 6-25. Each of these figures shows the Chi scans corresponding to the diffraction patterns collected at each incident angle for both the DRup (upper graph) and DRleft sample orientations (lower graph). The key next to each graph shows the incident angle in degrees (°).

As previously stated in section 6.2.1, the DRup sample orientation gives rise to a 'fibre diffraction' style pattern and will be subject of the majority of the analysis. The intense (hk0) meridonal signals enable a more easy determination of the signal's 2θ values, than less oriented and hence the less-easily observed above background diffraction arcs obtained in the DRleft orientation. The Chi scans from the DRleft orientation are also included though, for completeness.

Note that, for the data presented in Figure 6-17 to Figure 6-25, many of the Chi scans recorded at $\theta_I = 15°$ show a sharp signal at 2θ ~30°. This is due to diffraction from the underlying (111) planes of the silicon disc, and confirms that at this angle, the entire film depth is probed.

6.5.2 Results of the (hk0) radial shifts for various PET films

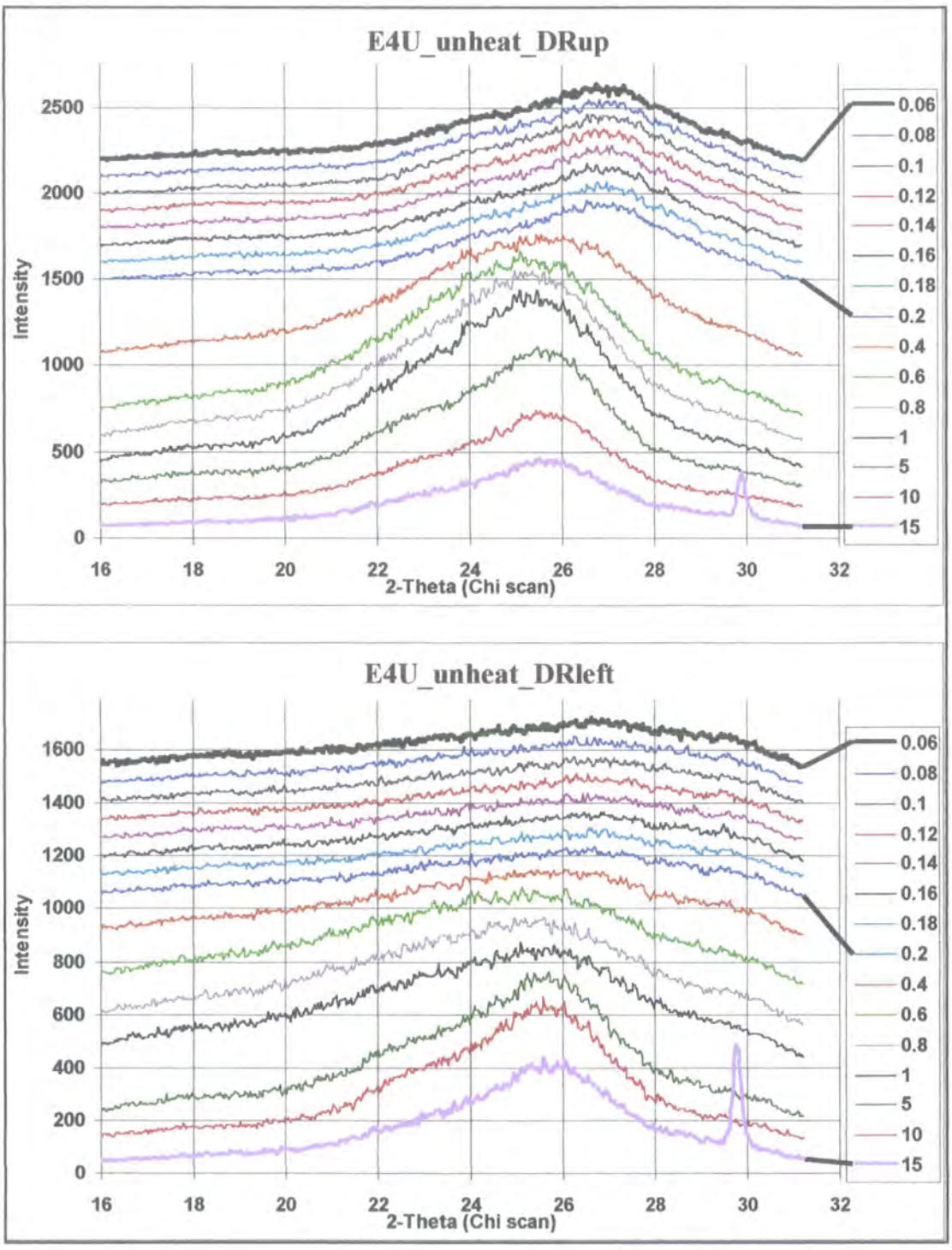

Figure 6-17: E4U_unheat radial positions of (hk0) signals. The estimated fraction of TER for the DRup sample orientation is 0.202.

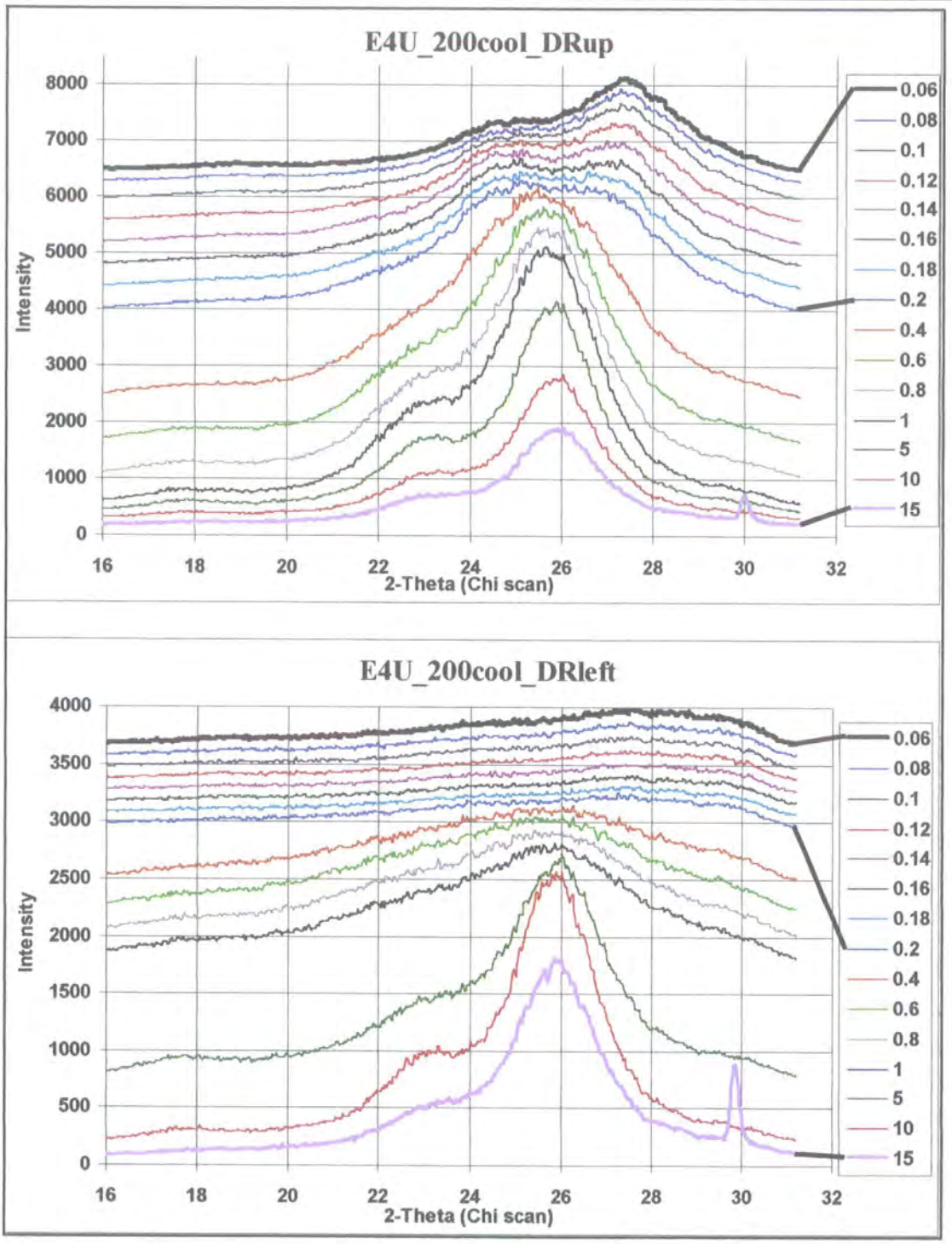

Figure 6-18: E4U_200cool radial positions of (hk0) signals. The estimated fraction of TER for the DRup sample orientation is 0.682.

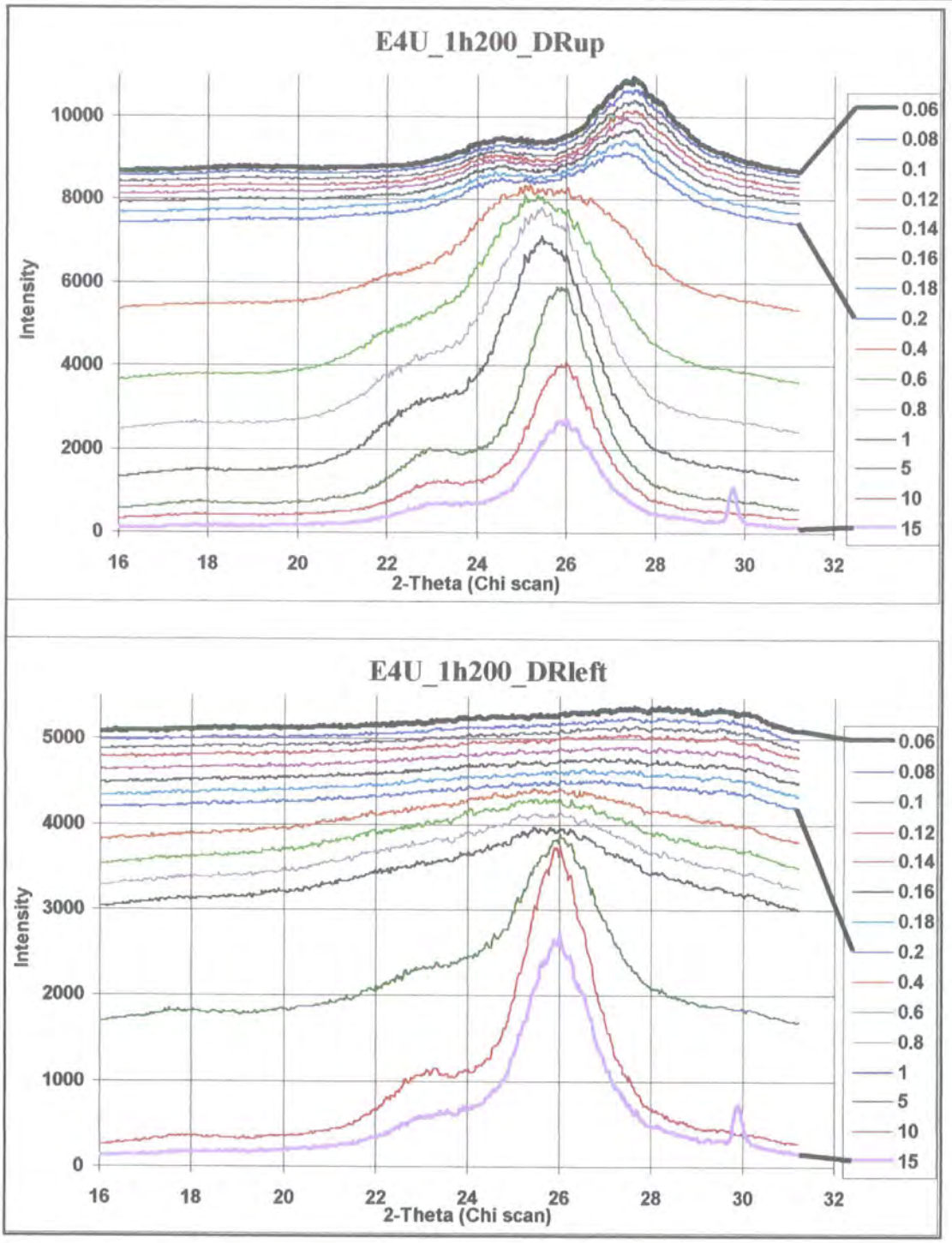

Figure 6-19: E4U_1h200 radial positions of (hk0) signals. The estimated fraction of TER for the DRup sample orientation is 0.803.

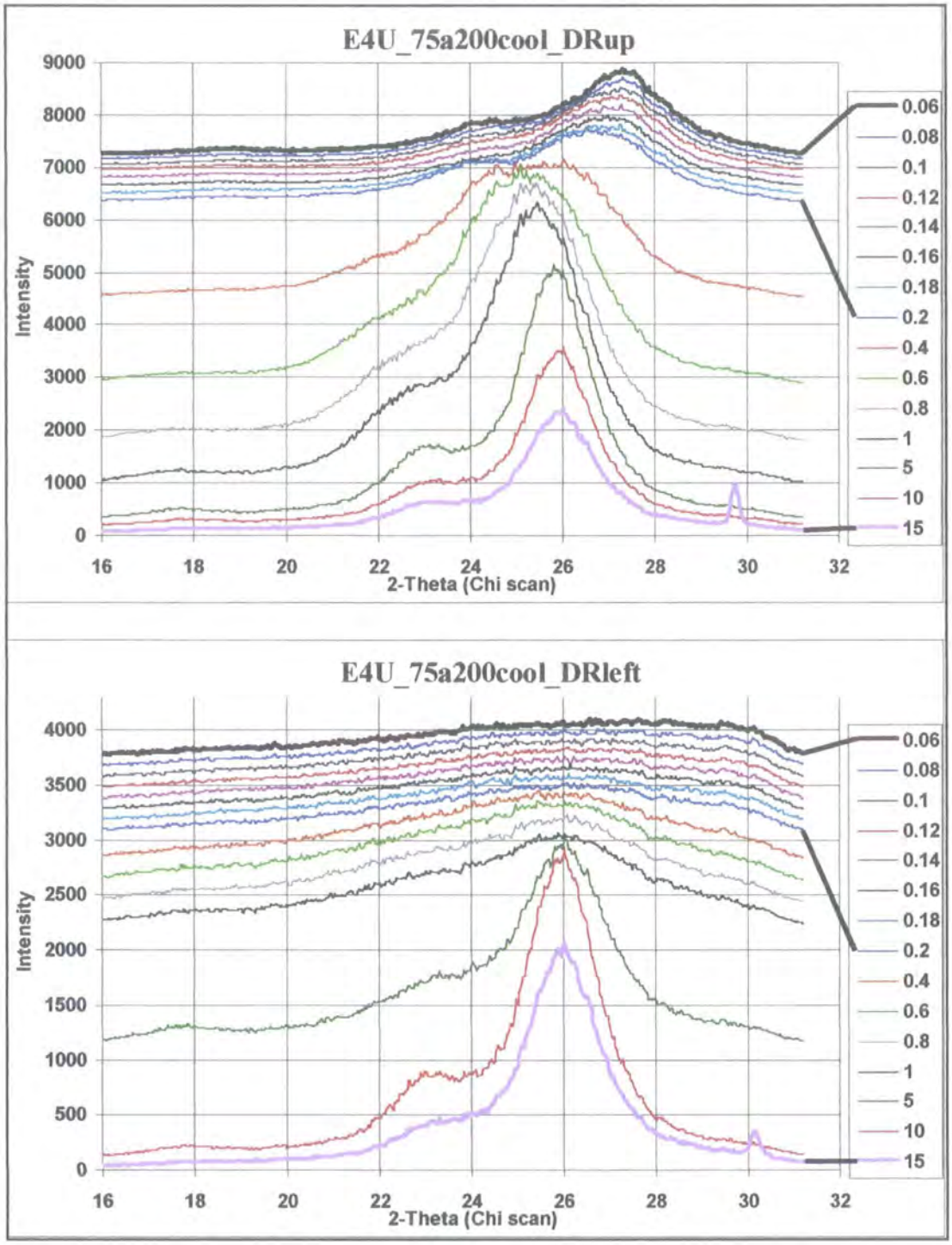

Figure 6-20: E4U_75a200cool radial positions of (hk0) signals. The estimated fraction of TER for the DRup sample orientation is 0.986.

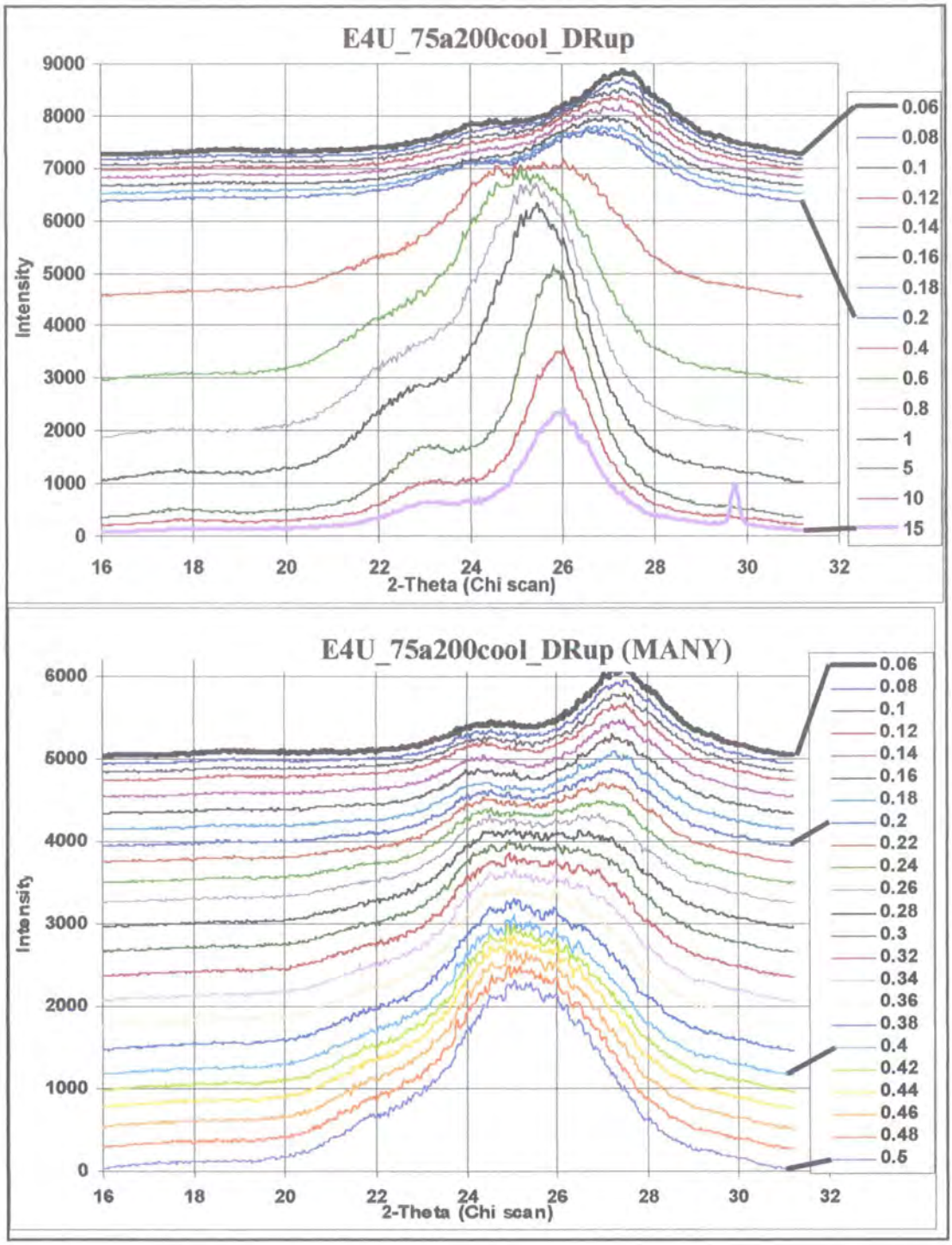

Figure 6-21: E4U_75a200cool_DRup using the standard incident angles shown in Table 6-2 (top graph) and the same sample studied at a later time using a series of angles designed to monitor the transition between $\theta_I = 0.2°$ and 0.4°.

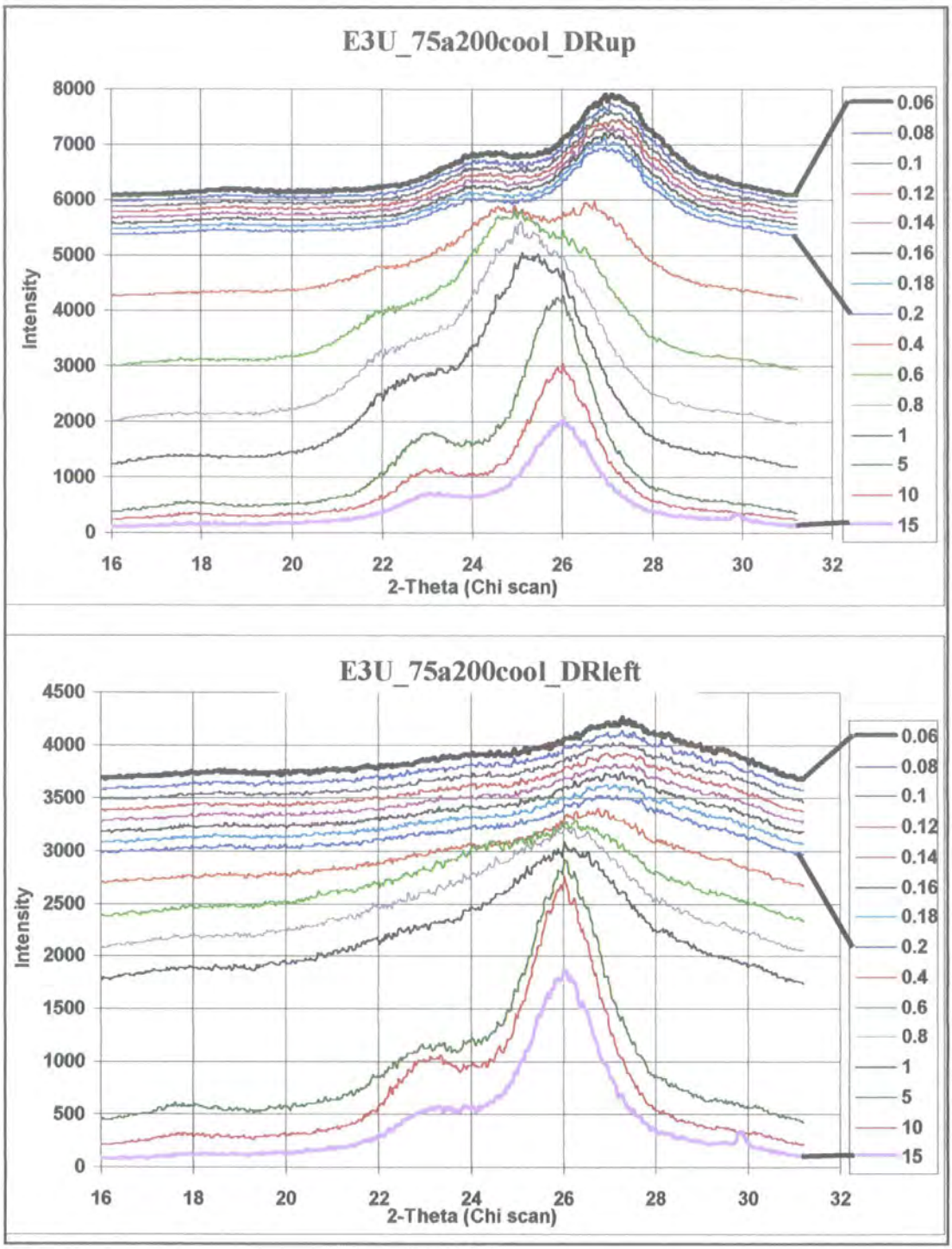

Figure 6-22: E3U_75a200cool radial positions of (hk0) signals. The estimated fraction of TER for the DRup sample orientation is 0.937.

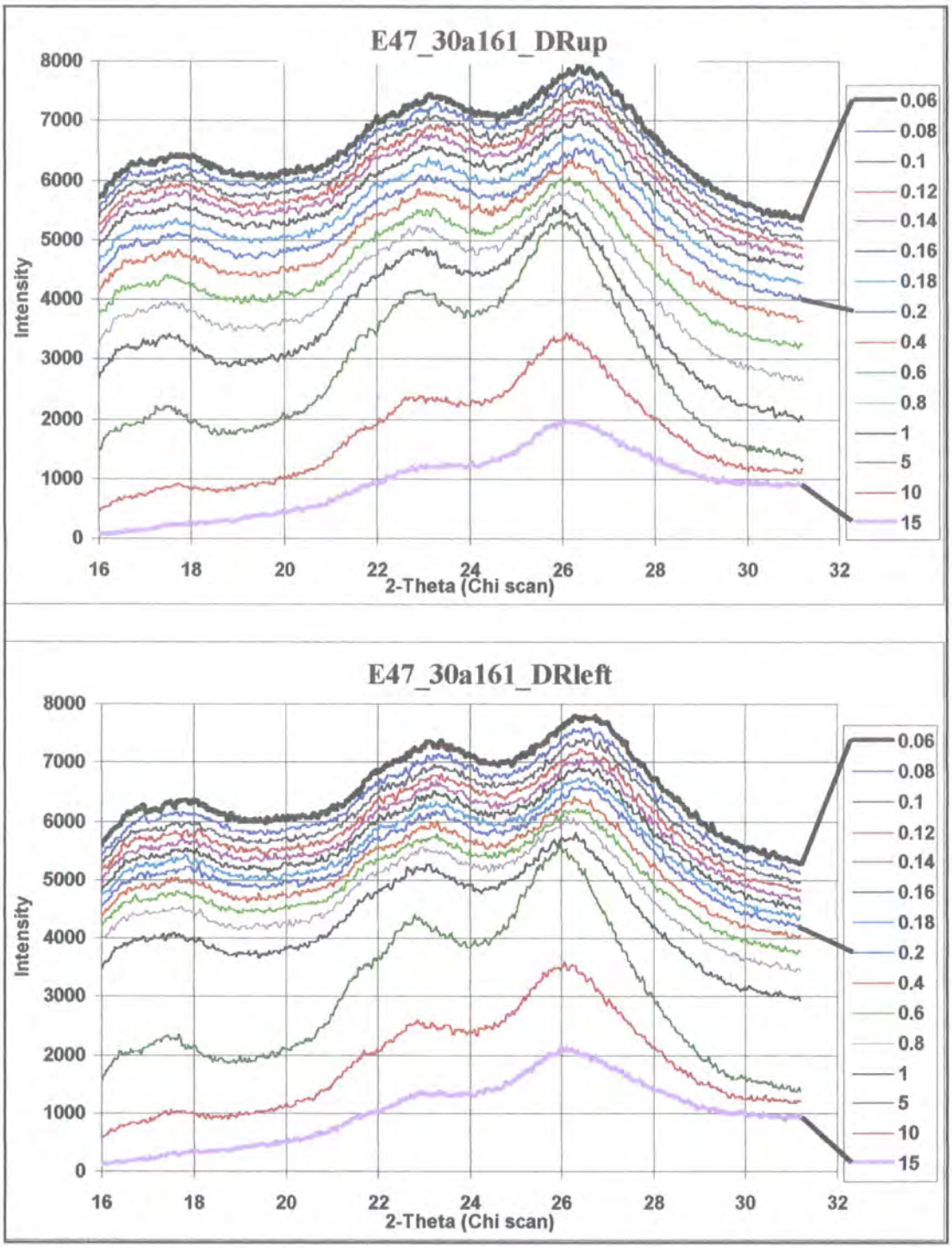

Figure 6-23: E47_30a161 radial positions of (hk0) signals. The estimated fraction of TER for the DRup sample orientation is 0.631.

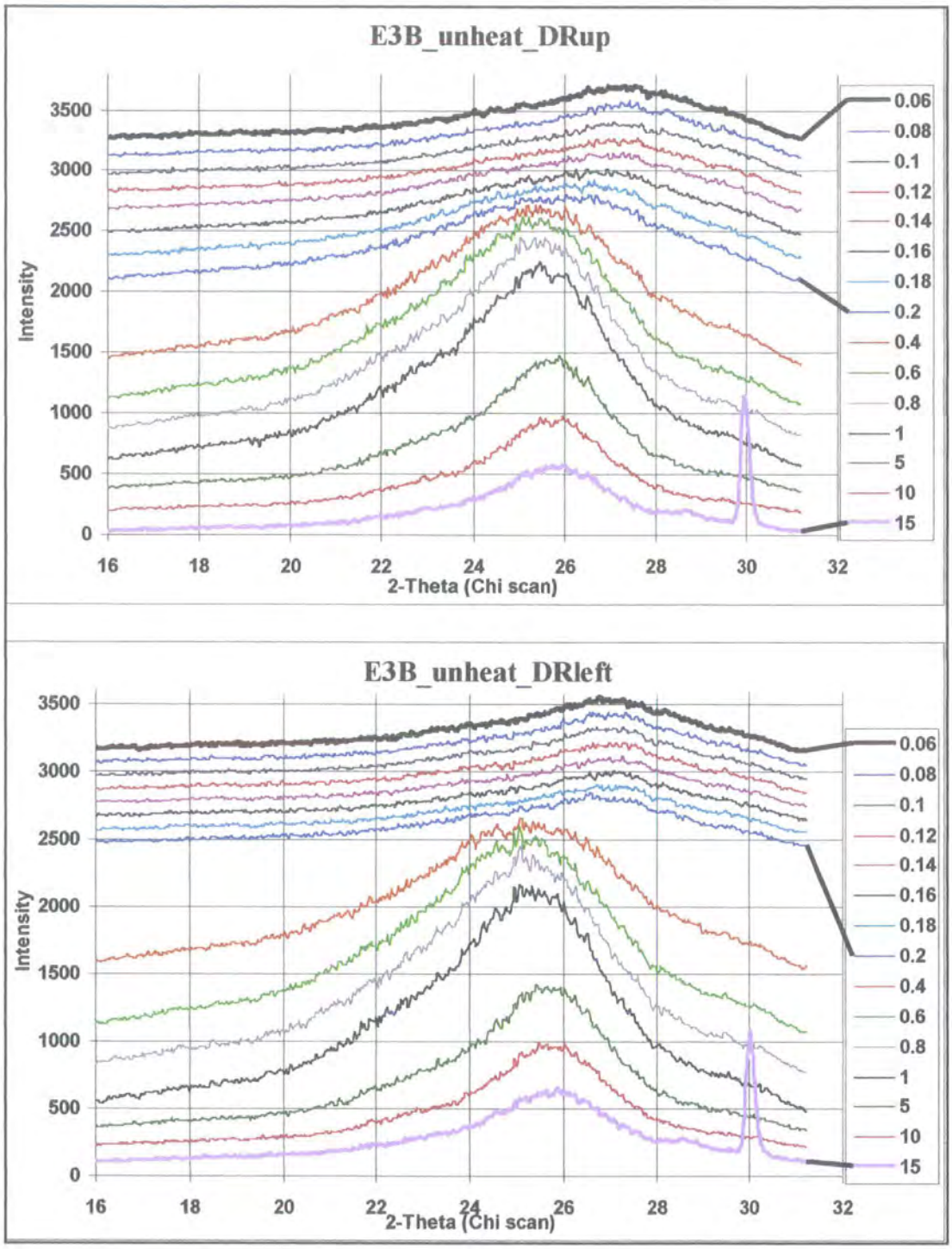

Figure 6-24: E3B_unheat radial positions of (hk0) signals. The estimated fraction of TER for the DRup sample orientation is unavailable for this film.

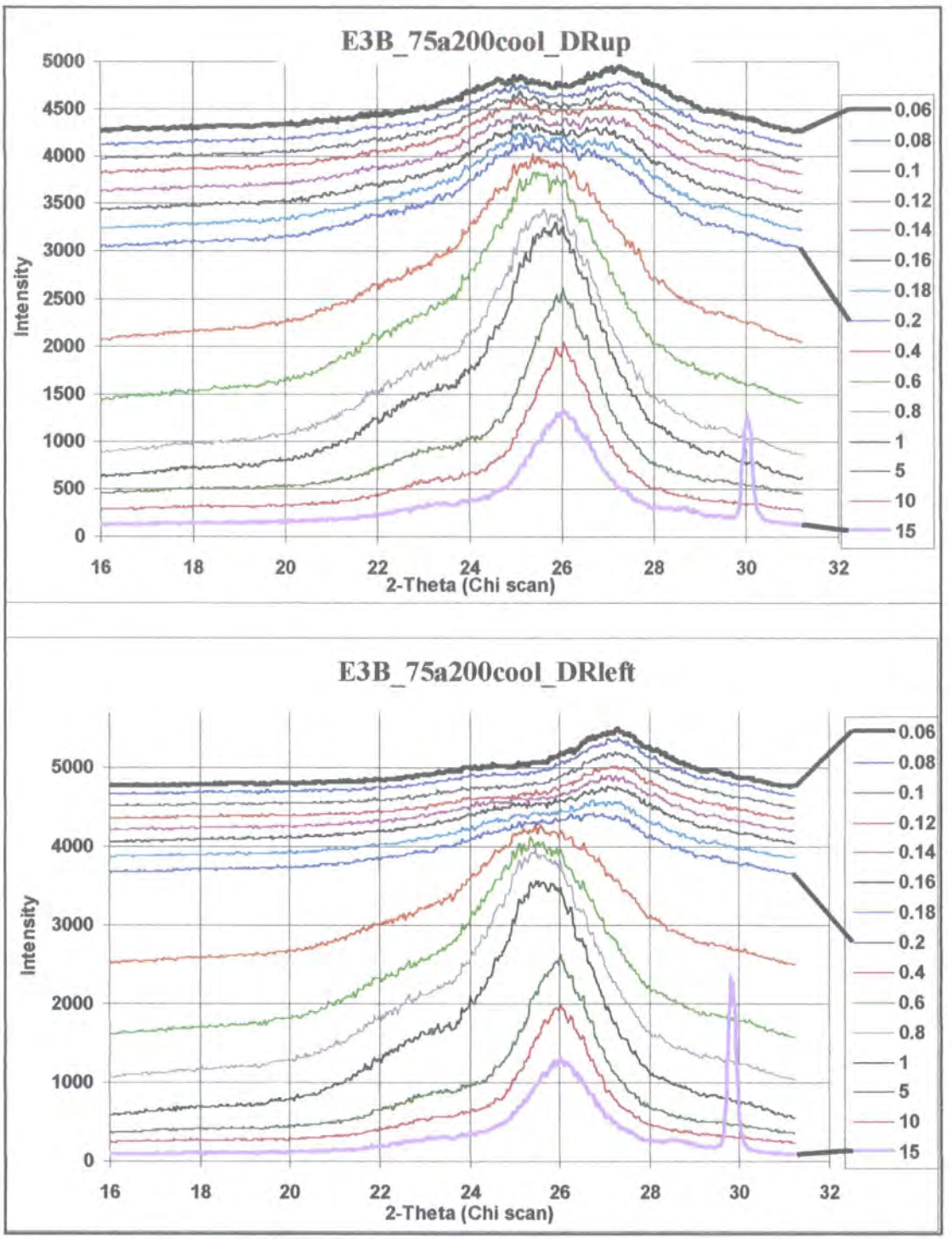

Figure 6-25: E3B_75a200cool radial positions of (hk0) signals. The estimated fraction of TER for the DRup sample orientation is 0.284, and for the DRleft sample orientation is 0.914.

6.5.3 Discussion of shifts in the 2θ position

The first films to be discussed (Figure 6-17 to Figure 6-25) are all drawn to 3.75 draw ratio (DR) on the Long stretcher from the same batch of 0% IPA PET resin (IV = 0.62). These films were subjected to different post-stretch heat setting procedures as discussed in the text.

6.5.3.1 Analysis of (hk0) positions for the PET film -E4U_unheat

The first film analysed (Figure 6-17) was drawn to 3.75 DR on the Long stretcher, but not subjected to the heat-setting procedure in the anti-shrinkage frames. The diffraction patterns from this film did not possess the sharper diffraction signals typical of more crystalline samples, like that in Figure 6-12 which allows scope for the quantitative analysis of crystallite properties. The Chi scan operation results in a broad featureless hump covering the 2θ location of ~20° - 30°. This signal is mainly due to the oriented amorphous phase, which has a roughly Gaussian distribution of spacings between the chains. This is in contrast to the chains within the crystalline regions, where the ordering, and hence interatomic distances, are more regimented producing sharper diffraction signals. There does however appear to be a change in the amorphous signal between the θ_I values of 0.2° and 0.4°. The critical angle for TER is though to be around this angle and thus this transition could be attributed to a change of structure between the surface and bulk material.

The absence of sharp, crystalline, diffraction signals in this unheated film was part of the motivation behind designing and building the anti-shrinkage frame described in the

materials chapter, to produce flat, heat treated films that would have higher crystallinity levels.

6.5.3.2 Analysis of (hk0) positions for PET film - E4U_200cool

This film was drawn to 3.75 draw ratio, placed in a pre-heated vacuum oven at 200°C and allowed to cool slowly under vacuum. Figure 6-18 reveals much stronger (hk0) diffraction signals. There is a clear shift between the signals collected below the critical angle and those collected at larger angles. For θ_I = 0.06° the intense (100) signal is centred at 2θ ~ 27.5°. However, it is clear that the (100) signal shifts to 2θ ~ 26° at θ_I = 1°. The transition between these two extremes is strange, as two intense peaks appear to merge at around θ_I = 0.4. This transition will be discussed in more detail in section 6.5.4.

It is interesting to consider the measured fraction of TER when analysing the Chi scans collected at small incident angles. This will become apparent when comparing Figure 6-18 to Figure 6-19. The observed fraction TER for film E4U_200cool_DRup was 0.682, which is relatively low in comparison to the other films. Hence, the progressive change in the Chi scans between θ_I = .0.06° and θ_I = 0.2° is indicative of the reduced TER, and hence reduced degree of surface probing. For the other films, which show a higher TER fraction at 0.2°, significant surface probing is attained for all angles up to θ_I = 0.2° and hence Chi scans appear similar for these angles.

6.5.3.3 Analysis of (hk0) positions for PET film - E4U_1h200

This film is identical to the previous one except it was heated for one hour at 200°C before it was left to slowly cool under vacuum. This film is thus expected to have a

higher crystallinity than film E4U_200cool. In essence, the radial positions of the (hk0) signals at θ_I = 0.06° and θ_I = 1° are the same as in the previous E4U_200cool film. This shows that this strange shift in radial 2θ position is reproducible across different samples, which adds confidence to the theory of there being a change in structure within the surface region.

For film E4U_1h200_DRup, the fraction of TER averaged over all sub-critical angles was 0.803. There is much less of a change between θ_I = 0.06 and θ_I = 0.2. This shows that the structure probed by the X-rays is essentially the same for all angles below the critical angle, whereas the θ_I = 0.4° data shows a sudden change in the Chi scan shape. As with all the films presented here, it would be difficult to perform an orientation analysis as described in section 6.4.5 on the three (hk0) signals for θ_I = 0.4°, as the three (hk0) components are difficult to separate.

6.5.3.4 Analysis of (hk0) positions for PET film - E4U_75a200cool

This film was heated for 75 minutes at 200°C before being slowly cooled under vacuum. The results of this film are presented in two figures. Figure 6-20 shows the Chi scans from the DRup and DRleft sample orientations as before. The upper graph of Figure 6-21 is identical to the equivalent graph in Figure 6-20, but the lower graph (E4U_75a200cool_DRup MANY) shows the transition between θ_I = 0.06° and θ_I = 0.5° with 0.02° resolution. The motivation behind this was to detail the transitional gap between θ_I = 0.2° and θ_I = 0.4°. The 'MANY' data was collected a month after the original data of Figure 6-20, so this could also be considered a test of the reproducibility of GIXD experiments on drawn polymer samples.

The same 2θ shift is seen for the E4U_75a200cool as the other films. The fraction TER for this film in the DRup position was calculated as 0.986. Again this high level of external reflection results in very similar scans for $\theta_i = 0.06°$ to $\theta_i = 0.2°$ and a sudden shift between $\theta_i = 0.2°$ and $\theta_i = 0.4°$, where the TER falls to zero.

The lower graph in Figure 6-21 shows the transition between surface and bulk measurements in more detail. It can be seen that the θ_i angles between 0.2° and 0.4° show a steady change from the (100) surface signal at 2θ = 27.5° to the strange broad hump central at 2θ ~ 25.8° for incidence angles around 0.3°, whilst at 0.4° the (100) signal occurs at essentially its expected bulk value. A proposed model that could describe these transitional chi scans will be discussed shortly.

6.5.3.5 Analysis of (hk0) positions for PET film - E3U_75a200cool

Film E3U_75a200cool (Figure 6-22) was uniaxially drawn to 3 draw ratio and subjected to the same thermal treatment as for film E4U_75a200cool and thus will be compared to this film during this analysis. Again, a shift can be clearly seen between the diffraction collected below and above the critical angle for TER. Although the radial positions of the (hk0) signals at large angles is the same for the 3 and 3.75 draw ratio films (compare Figure 6-22 and Figure 6-20, respectively), the 2θ positions below the critical angle appear slightly different. For the 3 draw ratio film, the sub α_c (100) signal occurs closer to 2θ = 27° than 2θ = 27.5° as seen for all the draw ratio 3.75 films. This may well suggest that the amount that the 2θ position shifts by is dependant on the amount of

draw in the film. However, only one 3 draw ratio film was analysed in this study and so further studies are required before such conclusions can be confidently stated.

6.5.3.6 Analysis of (hk0) positions for PET film - E47_30a161

This film is different to the others, as it has not been stretched. This film was cut from the cast roll, and the FTIR-ATR study proved that it did not possess any orientation. The amorphous film was heated in the anti shrinkage frames and held for 30 minutes at 161°C to gain high levels of crystallinity. The resulting film was opaque which is known to indicate high levels of spherulitic crystallinity in unoriented PET specimens. The film was also slightly curved, and gave a relatively low TER fraction value of 0.6. The Chi scans recorded below α_c appear to be shifted by less than 0.5° and the bulk measurements recorded above α_c reveal (hk0) signals at the expected positions. However, this shift is far less than those exhibited by the drawn specimens. It would be interesting to repeat this study on a flatter, highly crystalline, unoriented film, but such a flat film may prove difficult to produce.

6.5.3.7 Analysis of (hk0) positions for biaxial PET film

Although the quantitative GIXD orientation analysis is only applicable to uniaxially drawn films, it is useful to look for peak shifting in biaxially drawn specimens. Any peak shifting observed in these films could be of direct interest to industry, as commercial PET films are typically biaxially stretched and heat-set in the film stenter process[15] (see chapter 3). Two films are considered here, which were both drawn biaxially to 2.75 x 2.75 draw ratio on a Long stretcher. Figure 6-24 has had no post-

stretch heating treatment, but the film shown in Figure 6-25 has been subjected to the same thermal treatment as film E4U_75a200cool.

Again, the unheated film shows a lack of sharp, crystalline diffraction signals, which makes the analysis difficult. It does however appear that there is a change between the surface and bulk regions of the film. The heat-setting of the film increases the crystallinity enough for stronger diffraction signals to be observed in Figure 6-25. Here is can be clearly seen that the (hk0) signals shift to higher 2θ locations for measurements taken below the critical angle.

6.5.4 Simulating the change in Chi scans above and below α_c

The shift in 2θ positions for diffraction patterns collected below the critical angle for TER, suggests a change in crystal structure at the surface of the film. Calculations regarding the perturbed crystal structure will be addressed in section 6.6.

The intermediate Chi scans between $\theta_i = 0.16°$ and 1° (typified by $\theta_i = 0.4°$ on Figure 6-21) appear to take on a different form to the scans recorded at $\theta_i = 0.06°$ or 5°. The nature of this transition region may reveal additional information about the nature of the transition between the surface structure and the structure towards the core of the film. For this discussion, two film structures will be considered. In case 1, there is a well-defined boundary between the surface structure and the structure of the bulk. In case 2, the boundary between the two phases is a progressive structural change, as shown schematically in Figure 6-26.

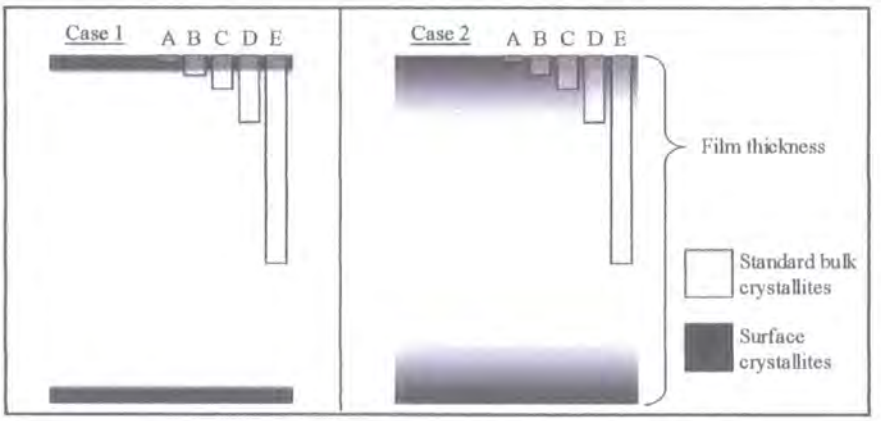

Figure 6-26: Two possible cases for the transition between the surface structure and bulk

The semi-transparent boxes labelled A to E in Figure 6-26 represent different depths probed into the film surface. The measurement would contain structural information averaged over the material contained within each box. In both film systems, depth A would reveal the structure of the surface material only and the signal from depth E would reveal the bulk structure, as the box contains far more bulk than surface material. For case 1, probing at depth C would reveal a signal consisting of half surface and half bulk signals. In contrast, depth C from case 2 would encapsulate a continuous range of signals that would result in a widened diffraction signal.

In Figure 6-27, the transition between the surface and bulk 2θ positions is simulated. The aim is to see if the intermediate Chi scans can be approximated as combination of the Chi scans from above and below α_c. Chi scans from frame 001 and frame 012 are used from the E4U_75a200cool_DRup data set, which correspond to incident angles θ_I = 0.06° and θ_I = 1°. A spreadsheet was then used to calculate spectra that are a combination of these two forms. The curves presented in Figure 6-27 are

1. 100 % frame 001 (Which is the raw Chi scan)
2. 95 % frame 001 + 5 % frame 012
3. 90 % frame 001 + 10 % frame 012 etc. as indicated in the key of Figure 6-27.

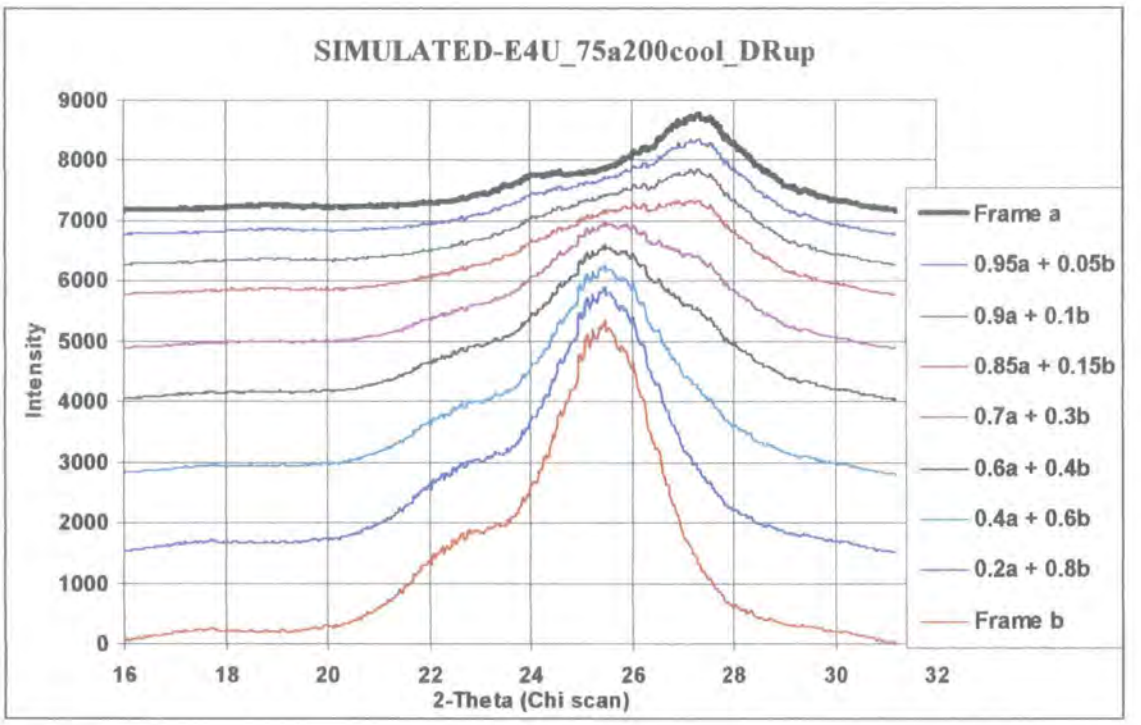

Figure 6-27: Simulating the Chi scans as a combination of two frames, where frame a is $\theta_I = 0.06°$ and frame b is $\theta_I = 1°$ from the data set 'E4U_75a200cool_DRup' as shown in Figure 6-18

The simulation reveals a similar pattern to the actual chi scans recorded in the experiment. This suggests that the data can be modelled as two discrete crystal structures arising from the surface and in the bulk material, rather than a continuous change in crystal structures between the surface and bulk phases. Therefore, the proposed 'case 1' film model shown in Figure 6-26 would appear to be more accurate portrayal than the continuous phase change of 'case 2', although a more quantitative approach is needed to clarify this, which should be the topic of a future study.

6.6 Calculating the unit cell parameters of near-surface crystallites

The inverse relation between d-spacing and diffraction angle in Bragg's law (Equation 6-1) suggests that some or all of the crystal d-spacings within the crystal structure have been *reduced* by some amount, since all the diffraction signals from the GIXD

measurements showed a shift to higher 2θ values compared to the bulk X-ray diffraction measurements. This section aims to quantify the magnitude of this reduction.

For this analysis, the three-draw ratio film data was used (E3U_75a200cool_DRup), as the diffraction peaks were particularly well defined in this case (see Figure 6-28). The frames corresponding to incident angles θ_I = 5° and θ_I = 0.16° were selected to be representative of bulk and surface measurements, respectively. The diffraction peak positions were determined by taking localised 'Chi' and '2-Theta' scans using the GADDS software. A determination of the exact positions was complicated by the fact that some of the signals were low in intensity relative to the amorphous halo and background. This adds measurement errors to the 2θ positions and resulting calculations of the reduced unit cell parameters. The signal indexing was performed using a combination of the simulated diffraction data from chapter 5 and similar attempts by other authors[3,4]. The measured 2θ positions are shown in Table 6-6, where the 'Daubeny' row represents the simulated values from the generally accepted unit cell[1] as described in the *Molecular modelling* chapter.

Table 6-6: The radial (hkl) signal 2θ values above and below the critical angle for the E3U_75a200cool film. The diffraction signal locations are described as either M (Meridonal), off-M (close to Meridian), off-Eq (close to equator) or Eq-M (between equator and meridian).

	1 0 0	**0 1 0**	**1 -1 0**	**1 0 -3**	**0 1 -1**	**1 -1 1**	**-1 1 1**	**-1 1 2**
Location	M	M	M	off-Eq	off-M	off-M	off-M	Eq-M
Daubeny	25.695	17.531	22.544	26.438	16.418	27.841	21.307	24.709
Frame 013	25.8	17.7	22.8	26.5	16.5	27.8	21.8	25.2
Frame 006	27.0	18.8	24.0	27.5	17.5	29.0	22.7	26.2

The diffraction images used to determine the reduced unit cell parameters are shown in Figure 6-28. Superimposed on the θ_I = 5° image are the (hkl) indices as determined by

the Cerius2 simulation. To ensure that the signals had been indexed correctly, they were cross-referenced with the indexing of Göschel *et al.*[4].

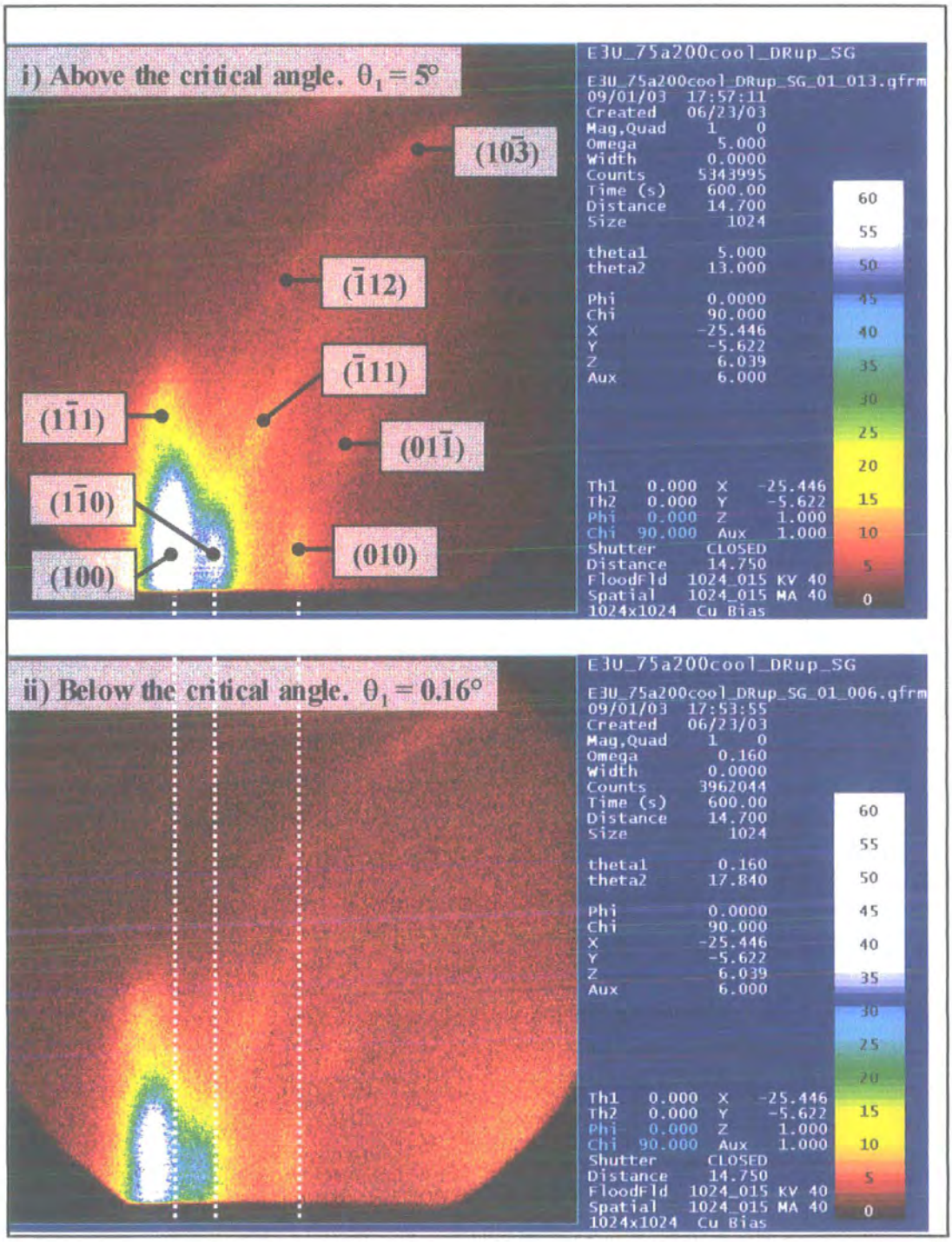

Figure 6-28: Frames 013 (top) and 006 (bottom) used to calculate the reduced unit cell parameters

There are slight discrepancies between the generally accepted 2θ values and the bulk values measured from frame 013. It is uncertain whether this discrepancy is due to a perturbed unit cell or measurement errors.

The reduced unit cell parameters were calculated using a spreadsheet that was designed by the author's Ph.D. supervisor, Dr. Sharon Cooper. The spreadsheet takes the measured signal 2θ values as the input and calculates the unit cell parameters using the relationships between real and reciprocal crystal lattices. The calculated unit cell parameters are compared to the generally accepted unit cell in Table 6-7.

Table 6-7: The calculated unit cell parameters above and below the critical angle

	a	*b*	*c*	α	β	γ
Daubeny	*4.56*	*5.94*	*10.75*	*98.5*	*118*	*112*
Frame 013	4.51	5.87	10.76	99.24	117.87	111.25
Frame 006	4.29	5.51	10.48	99.28	117.43	111.2
% reduction	4.88	6.13	2.60	-0.04	0.37	0.04

In Table 6-7, the '% reduction' row shows the calculated reduction between the measured bulk (Frame 013) and surface crystal structures (Frame 006). The calculation reveals that the α, β and γ parameters are very similar in the surface and bulk crystallites. However, there is a large change in the a, b and c unit cell parameters (with an error of +/- 0.01, resulting from indexing uncertainties) for the crystals residing within the surface material.

6.6.1 A summary of the use of GIXD on drawn PET films

One aim of this thesis was to see if GIXD could be used to extract surface-specific information from *stretched* PET films. The previous GIXD work on polymers was based on the analysis of thin, spin-coated specimens, which were chosen for their

inherently smooth and flat surfaces. This thesis has shown that high levels of total external reflection are achievable for drawn PET films. This suggests that information gathered using grazing incidence angles below 0.2° on more typical industrial film samples could also give structural information from the surface region of the film.

Surprisingly, the highly oriented films in this study show a consistent and reproducible radial shift in 2θ signal position when probed at grazing angles. This phenomenon was not observed for the spin-coated films in the literature[11] and was less observable for the un-stretched films in this study, although this may be due to the lower TER fractions achieved. The shift compared to the bulk can be described by a ~ 2.5 - 6 % reduction in the unit cell parameters for the surface crystallites. This is unusual as the unit cell parameters determined by Daubeny[1] in 1954 are accepted by the vast majority of authors in this field, for all sample thermal histories. One notable exception is Bhatt *et al.*[16], who reported a change in crystal structure in highly drawn commercial PET fibres. Any differences in the results of authors who determine the crystal structure of PET could therefore be due to the sample having slightly different crystal structures, rather than inaccuracies of the chosen characterisation technique. It is known that surface layer contraction can occur most notably for metals, owing to their high surface tension values, which mean that surface atoms bind more strongly to the underlying atoms.

The films studied in this thesis were stretched on a Long stretcher and subsequently heated for relatively long times while clamped taught in a specially-made aluminium frame. Real industrial films produced using the Stenter process are typically biaxially oriented, heat set for only a few seconds and often allowed to contract slightly. The suitability of the GIXD technique described in this thesis to *real* industrial films is not

fully known. Without the extended heat-setting times used to get high crystallinity levels within the films, diffraction signals could not be observed above the oriented amorphous signals. It might be possible to remedy this problem by performing experiments at a synchrotron radiation facility, where X-ray beams of a much higher intensity are available. However, beam time at such facilities is expensive and thus this is not considered a suitable long-term solution. More work is needed to see how useful the GIXD technique is to the less-crystalline industrial films.

6.7 Summary for the X-ray studies

In this chapter, we have shown the following:

1. The orientation in the uniaxially drawn films is consistently higher at the surface than in the bulk, by up to 11 %.
2. There is a good agreement between the orientation values $ASDC_{X\text{-}ray}$ and Y-ASDC determined from the X-ray and FTIR-ATR techniques, with the Y-ASDC values being of comparable, but typically slightly lower value than the $ASDC_{X\text{-}ray}$. This is consistent with the X-rays only probing the crystalline regions and the IR probing both crystalline and amorphous regions.
3. For the more crystalline films, i.e. those that were stretched and heat treated, an easily observable shift to lower 2θ values was observed for the surface region compared to the bulk, corresponding to a ~2.5 - 6 % reduction in the unit cell parameters.
4. The surface 2θ shift was also apparent, to a lesser degree, for the unheated draw ratio 3.75 film, mainly because if had a far lower crystallinity, and a far smaller TER fraction of 0.202 for measurements taken below the critical angle for TER.

5. The surface 2θ shift was only ~0.5° for the (100) diffraction signal for the un-stretched, heat-treated film. (TER fraction was low at 0.631)
6. At present, we cannot unambiguously determine whether the reduction in the unit cell parameters in the surface region of PET films occurs predominantly for uniaxially and biaxially stretched samples, or whether it is a universal feature of the PET films analysed here. The reduction is more apparent for the heat-treated uniaxially and biaxially stretched films, due to their increased crystallinity and flatter nature, which enables a greater degree of TER to be achieved, and hence lend themselves to a more surface-specific analysis.

6.8 References for chapter 6

(1) Daubeny, R. D. P.; Bunn, C. W.; Brown, C. J. *Proc. Roy. Soc. Lon.* **1954**, *A226*, 531-542.

(2) Mahendrasingam, A.; Martin, C.; Fuller, W.; Blundell, D. J.; Oldman, R. J.; Harvie, J. L.; MacKerron, D. H.; Riekel, C.; Engström, P. *Polymer* **1999**, *40*, 5553-5565.

(3) Chaari, F.; Chaouche, M.; Doucet, J. *Polymer* **2003**, *44*, 473-479.

(4) Göschel, U.; Deutscher, K.; Abetz, V. *Polymer* **1996**, *37*, 1-6.

(5) Marco, Y.; Chevalier, L.; Chaouche, M. *Polymer* **2002**, *43*, 6569-6574.

(6) Asano, T.; Calleja, F. J. B.; Flores, A.; Tanigaki, M.; Mina, M. F.; Sawatari, C.; Itagaki, H.; Takahashi, H.; Hatta, I. *Polymer* **1999**, *40*, 6475-6484.

(7) Factor, B. J.; Russell, T. P.; Toney, M. F. *Macromolecules* **1993**, *26*, 2847-2859.

(8) Chang, S.-L. *Journal of Physics and Chemistry of Solids* **2001**, *62*, 1765-1775.

(9) Murthy, N. S.; Bednarczyk, C.; Minor, H. *Polymer* **2000**, *41*, 277-284.

(10) Jensen, T. R.; Balashev, K.; Bjørnholm, T.; Kjaer, K. *Biochimie* **2001**, *83*, 399-408.

(11) Durell, M.; MacDonald, J. E.; Trolley, D.; Wehrum, A.; Jukes, P. C.; Jones, R. A. L.; Walker, C. J.; Brown, S. *Europhysics Letters* **2002**, *58*, 844-850.

(12) Parratt, L. G. *Physical review* **1954**, *95*, 359-369.

(13) Wilchinsky, Z. W. *Journal of Applied Physics* **1959**, *30*, 792.

(14) Göschel, U. *Polymer* **1996**, *37*, 4049-4059.

(15) Hodgson, M. R. In *Chemistry - Ph.D. Thesis*; University of Durham, 2000.

(16) Bhatt, G. M.; Bell, J. P.; Knox, J. R. *Journal of Polymer Science: Polymer Physics Edition* **1976**, *14*, 373-376.

7 Conclusions and further work

7.1 Summary of findings

This thesis contributes more evidence that the surface and near surface regions of PET films can possess significantly different properties to the bulk material. To date, PET films are most commonly characterised using bulk sensitive techniques such as cross-polarizer optical birefringence, transmission XRD and transmission FTIR spectroscopy. Although these measurements can reveal important information in their own right, any discrepancies between the bulk and the sub-micron surface region are overlooked. If the adhesion between polymer laminates fails unexpectedly or if printing inks fail to bind to the PET surface during industrial processing or film conversion, an analysis of the film's surface may help to identify the problem. This work identifies polarised ATR-FTIR spectroscopy as an excellent tool for characterising the molecular orientation within the sub-micron surface region and grazing incidence XRD as being useful for characterising crystal structure and crystallite orientation potentially within the top 10-100 nm of the PET film.

Grazing incidence X-ray diffraction (GIXD) has been applied to drawn PET films for the first time. The intense (hk0) diffraction signals were seen to shift to higher 2θ values by approximately 1.5° for measurements taken below the critical angle of α_C = 0.2°. The weaker (hkl) signals showed a similar, but less easily quantifiable 2θ shift. This unusual observation is reproducible and consistent over the range of films tested and can be accounted for by a change of structure at the sub-micron surface region of

the film. A detailed analysis was performed on the 3 draw ratio film, as the diffraction peaks were particularly well defined in this case. By measuring the positions of these reflections above and below the critical angle, it was calculated that the shift in diffraction peaks can be accounted for by an approximately 5% reduction in the generally accepted *a b* and *c* unit cell parameters of Daubeny *et al.*[1] In other words, the PET chains within the surface crystallites appear to be more closely packed than the bulk crystals towards the centre of the film (However, this study does not rule out the possibility that this effect is due to degradation at the polymer surface). This phenomenon has not been recorded before in this type of system. The previous GIXD work on PET films involved un-oriented spin-cast films on polished silicon wafers. These specimens reportedly do not possess this surface specific structural change. The films used in this study were heat set for long time periods (~ 1 hour), whereas during industrial production in the stenter process, heating times of a few seconds are more common. It was not possible to observe substantial diffraction peaks above background unless the long heating times were employed. However, the samples that were not subjected to the heat-setting process, or not stretched, appeared to show a similar, slightly reduced shift in the amorphous / crystalline diffraction signals.

By taking azimuthal scans of the (100), ($1\bar{1}0$) and (010) signals from diffraction patterns collected below α_c (θ_1 = 0.16°) and above α_c (θ_1 = 5°) it was possible to determine the crystallite orientation for the surface and bulk film material, respectively assuming uniaxial symmetry. In all cases, the orientation of the crystallite c-axes into the draw direction was higher for the surface than the bulk material. This difference was over 10 % in some cases. There was also a very good agreement between the X-ray

determined crystallite orientation ASDC values, and those obtained using FTIR, in which both amorphous and crystalline regions contribute to the measured ASDC values. This suggests that the amorphous regions display similar orientation trends to those of the crystalline regions.

For PET bottles, the near-surface molecular orientation was mapped at regular 20 mm intervals from the bottle top to the bottle base using polarised FTIR-ATR spectroscopy. The ATR accessory used offered a surface selectivity of ~ 0.5 μm so the orientation could be mapped along the inner and outer bottle surfaces independently. The theory of Everall and Bibby[2] was used to extract the orientation parameters from the IR spectra. These calculations were relatively complex as they accounted for normalisation procedures and the full biaxial system symmetry. Data collection was simple but time consuming. In total, 180 IR spectra and backgrounds were required to map each 2-litre bottle in this way. A large spreadsheet was thus designed to part-automate the analysis. The polarised ATR-FTIR technique was repeated for a series of bottles formed after different processing conditions, for different sized bottles and for bottles made from resins containing chemical modifications. Standard bottles (2% IPA) showed two switches in net chain orientation for the material along the outer surface and just one switch for the material along the inner wall. In all cases, the orientation maximum occurs near the base on the inner wall. It was discovered that by heating the bottle preform before the stretch for just five seconds more than the usual time of around one minute, the finished bottle showed greatly diminished levels of orientation. The tensile properties of polymer artefacts are directly related to levels of orientation and crystallinity. Therefore, this work suggests that care must be taken when selecting

stretch-blow processing parameters if bottle performance is not to be compromised. Bottles produced from resin containing 2% t-BIPA showed very similar orientation trends to the well-established 2% IPA alternatives. However, the inclusion of 8% t-BIPA resulted in a bottle, which showed much less orientation throughout its length.

A detailed examination of the 1340 cm^{-1} band revealed that it is erroneous to extract crystallinity values from *orientated* PET films using the equations of Belali and Vigourex[3]. The equation relies on the crystalline regions being unoriented and the amorphous regions consisting of mainly *gauche* conformers. For orientated specimens, however, the numbers of *trans* conformers in the amorphous regions are greatly increased and so the 1340 cm^{-1} band shows an artificially high crystallinity under these circumstances. Artificially high crystallinity values may also be recorded for polarised FTIR studies on oriented crystallites since this thesis demonstrates that the same sample can reveal very small or large 1340 cm^{-1} absorbencies depending on the sample orientation with respect to the spectrometer and the incident IR polarisation. On the other hand, the crystallinity levels in *un-orientated* PET pellets can be easily estimated simply by monitoring the height of the *trans*-specific 1340 cm^{-1} band. The larger this band is relative to the 1410 cm^{-1} normalisation band, the higher the crystallinity within the un-orientated sample.

To date, the 1340 cm^{-1} IR band in PET has been almost exclusively associated with crystallinity determination. This work reveals that for highly drawn PET films and bottles, the 1340 cm^{-1} band yields important orientation information. For the majority of bottles tested, a simple height measurement of the 1340 cm^{-1} band after normalisation by the 1410 cm^{-1} band shows a convincing similarity in orientation trends with the more

meticulous approach of Everall[2,4]. In particular, both methods reveal a higher orientation on the bottle's inner wall than its outer wall. However, the simple 1340 cm^{-1} height method becomes inaccurate for samples with highly uneven crystallinity, such as the bottle blown after too much pre-stretch heating. It can thus be concluded that the height of the 1340 cm^{-1} band is dependant on both the amount of molecular orientation *and* the crystallinity.

7.2 Suggestions for further work

7.2.1 Expanding on the infra-red work

7.2.1.1 Repeat mapping work using a less refractive ATR crystal

The study reported in this work was performed using a highly refractive germanium ATR crystal (n = 4). The penetration depth into the PET surface using this setup is approximately 0.5 μm (see Appendix 2). It should be possible to probe material deeper into the surface if a less refractive crystal is used. The popular "Golden Gate" ATR accessory contains a diamond crystal (n = 2.35) which would be a good choice for future studies as it allows for probing depths of around 2.5 μm. The new orientation mapping could then be compared to the work shown here to give an insight into the nature of the orientation gradient from the outer to the inner bottle surface. However, extra care needs to be taken on the spreadsheet when fitting close baselines to ATR spectra collected using a diamond ATR crystal, as spectral distortion can occur when the refractive index of the sample approaches that of the crystal, violating the conditions required for total internal reflection[2]. This is especially important for highly birefringent polymers like PET, where the orientation and crystallinity can have a marked effect on the refractive index of the specimen.

7.2.1.2 Mapping the chain orientation around the bottle hoop direction

The FTIR-ATR orientation-mapping experiments presented in this thesis were performed by taking measurements at regular intervals along a line connecting the bottle top to the bottle base. It would be interesting to perform similar measurements at regular intervals around the hoop of the bottle. If the bottle expands evenly during the stretch-blow process, it is expected that the orientation would be similar at each position around the hoop. However, orientation gradients around the bottle hoop may indicate otherwise. Possible factors leading to an un-even expansion inside the bottle mould would include preform wall thickness variations and un-even preform heating.

7.2.2 Future X-ray work

7.2.2.1 Synchrotron GIXD studies

The X-ray experiments featured here were performed on a lab-based Brüker D8 system. It would be advantageous to repeat these experiments at a synchrotron radiation facility. The high flux capabilities of the ESRF in Grenoble is capable of producing a micro fine collimated beam, which has been previously been used to collect data from specimens as small as a single strut of a polyurethane foam. For the grazing incidence experiments, the combination of increased synchrotron flux and a much larger proportion of the smaller beam illuminating the sample would result in much stronger diffraction signals.

7.2.2.2 Observations of (hk0) signal shifts at different draw ratios

This work has revealed a reproducible shift in the 2θ positions of diffraction signals for patterns recorded below α_c. The shift from the 3 draw ratio film appears to be slightly less than the shift from the 3.75 draw ratio. It would be interesting to repeat this

experiment on PET films drawn to many more draw ratios to see if the magnitude of the shift depends on the draw ratio.

7.2.3 Using other techniques

It would be interesting to measure the refractive indices in the three primary sample directions using an Abbé Refractometer[5]. It has the capability to measure the refractive index (RI) in the X, Y and Z sample directions which would be useful to feed into the FTIR orientation spreadsheets to improve the accuracy of the orientation parameters. This technique is best suited to liquid samples, but the refractive indices of polymer films can be measured by using a liquid at the sample/prism interface, whose RI falls between that of the sample and the prism. This is required to improve the optical contact between the polymer sample and the glass prism of the refractometer. Although the liquid will perturb the measured RI values, the technique may yield useful results.

7.3 References for chapter 7

(1) Daubeny, R. D. P.; Bunn, C. W.; Brown, C. J. *Proc. Roy. Soc. Lon.* **1954**, *A226*, 531-542.

(2) Everall, N. J.; Bibby, A. *Applied Spectroscopy* **1997**, *51*, 1083-1091.

(3) Belali, R.; Vigoureux, J. M. *Applied Spectroscopy* **1994**, *48*, 465-471.

(4) Everall, N.; MacKerron, D.; Winter, D. *Polymer* **2002**, *43*, 4217-4223.

(5) Ajji, A.; Guèvremont, J.; Cole, K. C.; Dumoulin, M. M. *Polymer* **1996**, *37*, 3707-3714.

Appendix 1 - Calculating the angle between the chain-axis within a PET chain folded lamellae crystal, and the vertical lamellae normal.

This appendix uses crystallographic relationships to explain the results of the FTIR-ATR orientation measurement of the lamellae mat specimen. This experiment is described in section 4.3.4.2 of chapter 4.

The chain folded lamellae crystals are expected to lie flat in the X-Y plane, while each crystal will be randomly oriented about the Z sample axis indicated in Figure A, part i. The triclinic unit cell for PET crystals dictate that the chains within the crystal (which are considered to lie along the c-axis of the unit cell, as shown in chapter 5) will make an angle, θ, with the Z sample axis (see Figure Ai).

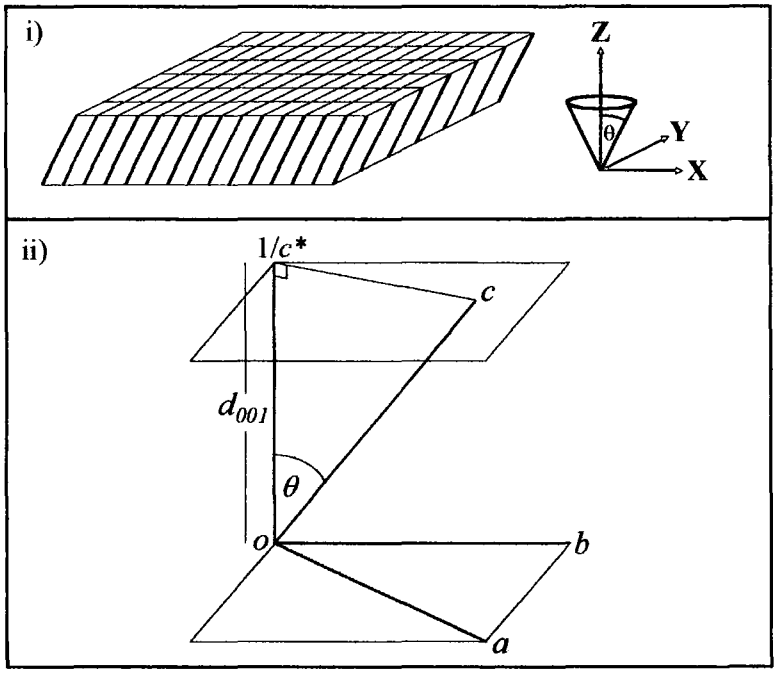

Figure A: Part i) shows a schematic diagram of the chains within a single, perfectly oriented, lamellae crystal (chains represented by black lines, with the chain folds omitted) and the required angle, θ, between the chains and the vertical Z-axis. Part ii) shows the crystallographic relationships that will be used to identify θ.

The reciprocal lattice consists of reciprocal lengths a*, b* and c*, and angles α^* (angle between b* and c*), β^* (angle between a* and c*) and γ^* (angle between a* and b*), such that;

- a* is perpendicular to the b and c real lattice axes, and has a magnitude of $1/d_{100}$ so that a.a* = 1.
- b* is perpendicular to the a and c real lattice axes, and has a magnitude of $1/d_{010}$, so that b.b* = 1
- c* is perpendicular to the b and c real lattice axes, and has a magnitude of $1/d_{001}$, so that c.c* = 1

(Note that c.c* = 1 because c.c* = cos(cc* angle)c/d_{001} but cos(cc* angle) = d_{001}/c, see Figure A, part ii).

The angle between the chain axis and the lamellae normal, θ, is the same as the angle between c and c*. Thus, c* is the vertical lamellae normal, Z, shown in Figure A. The d_{001} spacing of the Daubeny PET unit cell is d_{001} = 8.718 Å and the length of c is 10.75 Å. Therefore, the angle between c and c* is given by Equation A

$$\theta = \cos^{-1}\left(\frac{d_{001}}{c}\right) \qquad \textbf{Equation A}$$

which gives a value of θ = 35.81°. The average squared direction cosine (ASDC) of this angle between the chain axis and the lamellae normal is $\cos^2(35.8)$ which has a value of 0.66. This is in close agreement with the measured value of $\langle\cos^2(yZ)\rangle$ = 0.64, as described in section 4.3 of the FTIR spectroscopy chapter.

Appendix 2- A discussion of the sampling depths involved in the FTIR-ATR and GIXD experiments presented in this thesis

Penetration depth vs maximum sampling depth

The depth probed into the PET surface using both the FTIR-ATR and GIXD experiments are quantified by the depth of penetration (denoted d_p for FTIR-ATR and τ for GIXD). In both cases, an 'evanescent wave' extends onto the sample when the conditions of total *internal* reflection (FTIR-ATR) or total *external* reflection (GIXD) are satisfied.

The d_p value is the depth at which the magnitude of the electric field component has decreased to 1/e of its value at the reflective interface (between the ATR crystal and sample for FTIR-ATR measurements, or between air and the sample for GIXD). In other words, d_p is the depth at which the electric field falls to 36.8 % of its initial value. However, the tail of the evanescent wave extends beyond this and a small component probes the sample at deeper depths. This is demonstrated in Figure 4-1 of the FTIR Spectroscopy chapter. The *maximum* sampling depth achieved is therefore approximately three times the quoted penetration depth, since then the electric field component has decreased to less than 5 % of its value at the reflective interface.

Penetration depths associated with our FTIR-ATR measurements

The depth of penetration associated with the Attenuated Total Reflection technique is discussed in section 4.1.1. Equation 4-1 shows how the d_p value is dependent on the IR wavelength, the angle of incidence and refractive indices of both the ATR crystal and

the sample. This section will calculate the d_p values and approximate maximum sampling depths for our particular system.

The 'Thunderdome' ATR accessory used throughout this study contains a highly refractive Germanium ATR crystal (n_1 = 4) and the angle of incidence within this accessory is fixed at 45°.

The refractive index of a PET film is dependent on factors including the orientation and crystallinity within the sample. Everall and Bibby (see Chapter 4, reference 5) state that this value can range from n_2 = 1.5 to 1.7. The d_p can thus be calculated for each band investigated, for these minimum and maximum sample refractive indices (RI) achievable. The calculations are summarised in Table B.

Table B: The calculated penetration depth (d_p) and approximate maximum sampling depth achieved using our FTIR-ATR setup, for a sensible range of refractive indices found in PET films.

Band (waves/cm)	Wavelength (μm)	Polymer RI	dp (μm)	Max depth (μm)
1410	7.09	1.5	0.47	1.41
1410	7.09	1.7	0.50	1.50
1340	7.46	1.5	0.50	1.49
1340	7.46	1.7	0.53	1.58
1019	9.81	1.5	0.65	1.95
1019	9.81	1.7	0.69	2.07
875	11.43	1.5	0.76	2.28
875	11.43	1.7	0.80	2.41

The determination of molecular orientation using FTIR-ATR spectroscopy in this study was based on measurements of the 1019 cm^{-1} and 875 cm^{-1} bands. The average penetration and maximum sampling depths for these bands (averaged from both the minimum and maximum RI values) are 0.725 μm and 2.178 μm respectively.

Penetration depths associated with our GIXD measurements

Calculations of the X-ray depth of penetration (τ) for various incident angles are presented in Table 6-1 of the X-ray diffraction chapter. For each angle, two τ values are quoted, which refer to situations in which no total external reflection (TER) and 100% TER are achieved in the system. The amount of TER achievable will largely depend on factors including how flat and smooth the sample is. The degree of TER achieved for each sample has been estimated using the technique outlined in section 6.3.1.2.

The exact sampling depth for any given angle of incidence/degree of TER combination is difficult to calculate. For example, if we consider θ_I = 0.16 (from Table 6-1), a perfectly smooth sample, offering 100% TER, will result in a τ value of 9.78 nm. However, if the sample gives 0% TER, the X-rays penetrate over 300 times deeper to τ = 2.96 μm. If the sample gives 99% TER, a small, but highly absorbing component of the radiation penetrates much deeper into the sample than the TER component. It is not fully understood how this non-TER X-ray component affects the overall penetration depth. A more detailed analysis of this phenomenon should therefore be considered in a future study. Although GIXD has scope for probing the first 10 nm of a smooth (spin-coated) PET specimen, it is thought that the sub-α_c measurements presented in this thesis typically probe in the order of hundreds of nanometres (~ 0.1 μm) into the free PET surface.

Therefore, the sampling depths of all sub α_c measurements will be quoted as 100 nm and measurements collected above this angle will be assumed to probe in the manner described in Table 6-1 (See the column labelled 'Assuming no TER (μm)').